Time-Resolved Spectroscopy of Charge-Carrier Dynamics in Metal Halide Perovskites and Other Semiconductors for Photovoltaics

by

Edward Butler-Caddle

Thesis

Submitted to the University of Warwick
for the degree of

Doctor of Philosophy in Physics

Department of Physics
University of Warwick

Submitted April 2023

Contents

List of Figures ii

List of Tables ii

Acknowledgements iii

Declaration iv

List of Publications v

Abstract vii

Abbreviations viii

1 Background 1

- 1.1 Introduction 1
- 1.2 Thesis Overview 3
- 1.3 Theory: Semiconductors and Photovoltaics 5
  - 1.3.1 Fundamentals of Electrons in Semiconductors 5
  - 1.3.2 Photovoltaics 8
    - 1.3.2.1 Thermodynamic Driving Force 8
    - 1.3.2.2 Converting Thermal Energy to Chemical Energy 11
    - 1.3.2.3 Converting Chemical Energy to Electrical Energy 13
    - 1.3.2.4 Photovoltage and Photocurrent 17
    - 1.3.2.5 The Role of the Built-In Field 18
    - 1.3.2.6 Defects and Band Bending at Interfaces 19
    - 1.3.2.7 Solar Cell Optimisation 21
- 1.4 Perovskite Solar cells 22
  - 1.4.1 Overview 22
  - 1.4.2 Charge Transport Layers 23
  - 1.4.3 Spiro-OMeTAD 24
  - 1.4.4 C_{60} and PCBM 25
  - 1.4.5 Band alignment 26
- 1.5 Metal Halide Perovskites 30
  - 1.5.1 Crystal Structure 30
  - 1.5.2 Composition – Bandgap Tuning and Stability 31
  - 1.5.3 Fabrication 32

1.5.4 Computational Studies - Band Structure and Defects 33
1.5.5 Photostability - Single Halides 35
1.5.6 Photostability - Mixed Halides 37
1.5.7 Atmospheric and Chemical Stability 39
1.5.8 Grains 40
1.5.9 Doping 41

2 Experimental Methods 42
2.1 Introduction 42
2.2 THz Spectroscopy 42
2.2.1 THz-TDS and OPTP 42
2.2.2 Relating the Transmission to the Conductivity 43
2.2.3 THz Generation 47
2.2.4 THz Detection 48
2.2.5 Quantifying Photoconductivity 49
2.2.6 Pulse Scheme 52
2.2.7 Delay Stage Choice 53
2.2.8 Data Processing 54
2.3 Absorption 54
2.3.1 Equilibrium Absorption 54
2.3.2 Transient Absorption spectroscopy 58
2.4 Photoluminescence 59
2.4.1 Steady State photoluminesence 59
2.4.2 Time Resolved Photoluminescence 59

3 Modelling Charge-Carrier Dynamics 61
3.1 Introduction 61
3.2 The Basic Semiconductor Equations 62
3.3 Solving the System of Equations 64
3.4 Modelling Recombination Processes 65
3.4.1 One-step Recombination 66
3.4.2 Two-step Defect-Mediated Recombination 67
3.5 Modelling the Spatial Dependence with the Ambipolar Continuity Equation 69
3.5.1 Summary 72
3.6 Analytical Solutions of the Ambipolar Continuity Equation 72
3.6.1 Introduction 72
3.6.2 Separation of Variables 73
3.6.2.1 Interpreting a Product Solution 74
3.6.2.2 Spatial Dimensions 75
3.6.2.3 Temporal Dimension 75
3.6.3 Boundary Conditions 75
3.6.3.1 Spatial Dimension - Hard Wall Boundary Conditions . . . 76
3.6.3.2 Temporal Dimension - Initial Boundary Conditions 76
3.6.3.3 Initial Conditions for Silicon Wafer Measurements 78
3.6.4 Monomolecular Bulk Recombination 79

3.6.5 Monomolecular Surface Recombination 79
3.6.6 Sheet Density - 2D Diffusion Equation 81
3.6.7 Pump-Probe Overlap Integral for the Analytical Solution 81

4 Optical Measurements of Charge-Carrier Dynamics in Perovskite-CTL Bilayers 83
4.1 Introduction 83
4.2 Literature Review - Optical Measurements of Bilayers 84
4.2.1 Introduction 84
4.2.2 TRMC and OPTP on Perovskite-CTL bilayers 85
4.2.3 TA on Bare Perovskite Layers 87
4.2.4 TA on Perovskite-CTL Bilayers 90
4.2.4.1 TA Measuring the Perovskite Carrier Density 90
4.2.4.2 TA Measuring the CTL Carrier Density 92
4.3 Experimental Results 94
4.3.1 Introduction 94
4.3.2 Sample Fabrication 95
4.3.2.1 Solution Preparation 95
4.3.2.2 Deposition 96
4.3.3 Sample Characterisation 96
4.3.3.1 Scanning Electron Microscopy 96
4.3.3.2 Absorption 99
4.3.3.3 Steady State PL 105
4.3.4 Time Resolved Measurements - Overview 106
4.3.5 TRPL 107
4.3.5.1 Methodology 107
4.3.5.2 Results 109
4.3.6 OPTP 111
4.3.6.1 Methodology 111
4.3.6.2 OPTP on PCBM and C_{60} bilayers 114
4.3.6.3 OPTP on Spiro Bilayers 115
4.3.7 Transient Absorption 117
4.4 Conclusion 120

5 Modelling of Charge-Carrier Dynamics in Perovskite-CTL Bilayers 121
5.1 Introduction 121
5.2 Numerical Methods and their Accuracy 122
5.2.1 Numerical Analysis 122
5.2.2 Choice of Numerical Methods 122
5.2.3 Performance 123
5.2.4 Additional Considerations for Semiconductor equations 124
5.3 Finite Differences 124
5.3.1 Finite Difference Expressions 124
5.3.2 Explicit and Implicit Methods for Open Boundary Problems 126
5.3.3 Scharfetter-Gummel Expression for Charge Current 128

5.3.4 Finite Differences Discretisation of Gauss's Law 130
5.3.5 Boundary Conditions for Gauss's Law 131
5.3.6 Thomas Algorithm for Tridiagonal Matrices 133
5.4 Modelling Results 135
5.4.1 Assessing the Accuracy of the Numerical Solution 136
5.4.2 Impact of the Coulomb Force 141
5.4.2.1 Cross-Interface Recombination 144
5.4.3 Modelling with Effective Surface Recombination 145
5.4.4 Global Fitting of the Analytical Solution 148
5.5 Conclusions 149

6 Electronically Delayed Optical Pump Terahertz Probe Spectroscopy 152
6.1 Introduction 152
6.1.1 Previous Versions 153
6.1.2 Alternative Techniques 153
6.2 Experimental Implementation: delays $<$ 1ms 154
6.3 Assessing the Temporal Resolution 155
6.4 Experimental Implementation: delays $>$ 1ms 157
6.5 Carrier Dynamics in Silicon Wafers 159
6.5.1 Impact of Surface Passivation 159
6.5.2 Comparison with PCD 162
6.6 Conclusion 163

7 Conclusion 164
7.1 Future work 166

A *J*-*V* Curve and Equivalent Circuit 167
A.1 J-V curve 167
A.2 Equivalent Circuit 168

B Shockley-Read-Hall Recombination Rate 169

C Equivalence of Methods for Calculating Sheet Density 171
C.1 Integral Over Depth of the Solution to the 3D Diffusion Equation 171
C.2 2D Diffusion Equation 171

List of Figures

1.1 Timeline of Best Research Cell Efficiencies 2
1.2 Fermi-Dirac Distribution and Semiconductor Bandstructure 5
1.3 Electron Cooling and Recombination 7
1.4 Schematic of a p-n Homojunction 9
1.5 Definitions of Energy Quantities 10
1.6 Generation of a Chemical Potential Difference in a Semiconductor 12
1.7 Schematic of a CTL-Heterojunction Solar Cell 15
1.8 Schematic of a p-n Homojunction Solar Cell 16
1.9 Schematic of Band Bending due to Surface Defects 20
1.10 photoelectron Measurements of Perovskite and CTL Band Energies 27
1.11 Cross-Sectional EBIC Measurements of Perovskite Solar Cells 28
1.12 Cross-Sectional KPFM Measurements of Perovskite Solar Cells 29
1.13 Crystal Structure of $MAPbI_3$ 30
1.14 Calculated Defect Formation Energies and Transition Levels 34
1.15 PL Intensity Changes Under Different Atmospheres 36
1.16 Schematic of Photoinduced Halide Segregation 38

2.1 Schematic of OPTP Pump-Probe Overlap and EO Sampling 45
2.2 Schematic of OPTP Setup Used in this Work 50
2.3 Schematic of 4-Pulse Scheme for OPTP 53
2.4 Schematic of Contributions to Steady-State and Transient Absorption Spectra 56
2.5 Schematic of Integrating Sphere Measurements 57

4.1 Example of DAS Analysis of TA measurements 90
4.2 Top Down SEM Images of Perovskite-CTL Bilayers 97
4.3 Cross-Sectional SEM Images of Perovskite-CTL Bilayers 98
4.4 Transmittance and Reflectance of Individual Layers 100
4.5 Transmittance and Reflectance of Perovskite-CTL Bilayers 101
4.6 Determining the Internal Absorbance at High Photon Energies 103
4.7 Steady-State PL Spectra of Perovskite-CTL Bilayers 105
4.8 TCSPC Measurements of the Bare Perovskite Layer 107
4.9 TCSPC of Fullerene Bilayers with 633nm Excitation 109
4.10 TCSPC of Fullerene Bilayers with 405nm Excitation 109
4.11 TCSPC of Spiro Bilayers with 633nm Excitation 110
4.12 TCSPC of Spiro Bilayers with 405nm Excitation 110
4.13 OPTP of PCBM Bilayers with 700nm Excitation 112

4.14 OPTP of Fullerene Bilayers with 460nm Excitation 113
4.15 OPTP of Fullerene Bilayers with 410nm Excitation 113
4.16 OPTP of Spiro Bilayers with 700nm, 410nm or 460nm Excitation 116
4.17 TA Measurements of the Bare Perovskite Layer 118
4.18 TA Measurements of Perovskite-CTL Bilayers 119

5.1 Schematic of Finite Difference and Finite Volume Discretisation 123
5.2 Comparison of Numerical and Analytical Solutions for $S = 0$ 137
5.3 Comparison of Numerical and Analytical Solutions for Large S 139
5.4 Comparison of Numerical and Analytical Solutions for Small S 140
5.5 Numerical Simulations Including the Coulombic Force Without Interface Recombination 142
5.6 Schematic of the Formation of a Double Layer and Possible Interface Recombination Processes 143
5.7 Numerical Simulations Including the Coulombic Force With Interface Recombination 145
5.8 Numerical Simulations Including the Coulombic Force Comparing With and Without Interface Recombination 146
5.9 Fitting an Analytical Solution to OPTP Measurements of C_{60} Bilayers . . . 149
5.10 Fitting an Analytical Solution to OPTP Measurements of PCBM Bilayers . 150

6.1 E-OPTP Measurements of Several Different Semiconductors 155
6.2 Characterising the Jitter and Drift of E-OPTP Measurements 156
6.3 E-OPTP Pulse Scheme for Extended Mode 158
6.4 Schematic of Pump and Probe Beam Profiles and the Silicon Wafers 160
6.5 E-OPTP Measurements of Silicon Wafers 161
6.6 Simulated Carrier Density Profiles in Silicon Wafers 162
6.7 PCD Measurements of Effective Lifetimes in Silicon Wafers 163

A.1 J-V Curve of a Solar Cell 167

List of Tables

4.1 Layer thicknesses from SEM cross-sections 97

Acknowledgements

I would first like to thank my supervisor, Dr. James Lloyd-Hughes, for giving me the opportunity to study for a PhD, and the EPSRC for funding me. I am grateful to James for the time he has given to guiding my projects, helping me in the lab, and reviewing my work. I would also like to thank Dr. Michael Staniforth, Dr. Jack Woolley and Dr. Ben Breeze for training me in the labs and helping when things go awry.

I would like to thank my collaborators who have provided samples for this work: Dr. Imalka Jaywardena at the University of Surrey, and Dr. Anjana Wijesekara, Sophie Pain and Dr. Nicholas Grant at the University of Warwick. I also thank those who have performed supporting measurements for this work: Stephen York, Tom Orton and Ziyi Hu at the University of Warwick.

I am grateful to the members of the THz and Ultrafast Photonics group at the University of Warwick, who have made the department an enjoyable and happy place to work, particularly those with whom I have shared many hours in the office, lab and kitchen.

Finally, I thank my family and particularly my parents, for supporting me through these four years, and encouraging me to follow my interests.

Declaration

This thesis is submitted to the University of Warwick in support of my application for the degree of Doctor of Philosophy. It has been composed by myself and has not been submitted in any previous application for any degree.

The work presented (including data generated and data analysis) was carried out by the author except in the cases outlined below:

- The metal halide perovskite layers, spiro-OMeTAD layers, and PCBM layers were fabricated by Imalka Jayawardena at the University of Surrey.
- The C_{60} layers were fabricated by Anjana Wijesekara at the University of Warwick.
- The perovskite-CTL samples were cut for cross-sectional imaging by Tom Orton at the University of Warwick.
- The scanning electron microscope images were taken by Stephen York at the University of Warwick.
- Atomic force microscopy measurements were performed by Ziyi Hu at the University of Warwick.
- The silicon wafers were prepared and photoconductance decay measurements were performed by Sophie Pain and Nicholas Grant at the University of Warwick.

Parts of this thesis have been published by the author:

- Chapter 6 (Electronically delayed OPTP) was published in Butler-Caddle et al., "Terahertz photoconductance dynamics of semiconductors from sub-nanosecond to millisecond timescales", Appl. Phys. Lett. 122, 012101 (2023).

Publications

The following is a list of the journal articles that I have contributed to during my PhD:

1. Ren, A., Wang, H., Dai, L., Xia, J., Bai, X., **Butler-Caddle, E.**, Smith, J. A., Lai, H., Ye, J., Li, X., Zhan, S., Yao, C., Li, Z., Tang, M., Liu, X., Bi, J., Li, B., Kai, S., Chen, R., Yan, H., Hong, J., Yuan, L., Marko, I. P., Wonfor, A., Fu, F., Hindmarsh, S. A., Sanchez, A. M., Lloyd-Hughes, J., Sweeney, S. J., Rao, A., Greenham, N. C., Wu, J., Li, Y., Cheng, Q., Friend, R. H., Penty, R. V., White, I. H., Snaith, H. J. and Zhang, W., *High-bandwidth perovskite photonic sources on silicon*, Nature Photonics (July 2023)

2. **E. Butler-Caddle**, N.E. Grant, S.L. Pain, J.D. Murphy, K.D.G.I. Jayawardena and J. Lloyd-Hughes, *Terahertz photoconductance dynamics of semiconductors from sub-nanosecond to millisecond timescales*, Appl. Phys. Lett. **122** 012101 (Jan 2023)

3. H. Hempel, T.J. Savenjie, M. Stolterfoht, J. Neu, M. Failla, V.C. Paingad, P. Kužel, E.J. Heilweil, J.A. Spies, M. Schleuning, J. Zhao, D. Friedrich, K. Schwarzburg, L.D.A. Siebbeles, P. Dörflinger, V. Dyakonov, R. Katoh, M.J. Hong, J.G. Labram, M. Monti, **E. Butler-Caddle**, J. Lloyd-Hughes, M.M. Taheri, J.B. Baxter, T.J. Magnanelli, S. Luo, J.M. Cardon, S. Ardo and T. Unold, *Predicting Solar Cell Performance from Terahertz and Microwave Spectroscopy*, Advanced Energy Materials 2102776 (Feb 2022)

4. M.G. Burdanova, G.M. Katybab, R. Kashtiban, G.A. Komandin, **E. Butler-Caddle**, M. Staniforth, A.A. Mkrtchyan, D.V. Krasnikov, Y.G. Gladush, J. Sloan, A.G. Nasibulin and J. Lloyd-Hughes, *Ultrafast, high modulation depth terahertz modulators based on carbon nanotube thin films*, Carbon **173**, 245-252 (Mar 2021)

5. M. Monti, K.D.G.I. Jayawardena, **E. Butler-Caddle**, R.M.I. Bandara, J.M. Woolley, M. Staniforth, S.R.P. Silva and J. Lloyd-Hughes, *Hot carriers in mixed Pb-Sn halide perovskite semiconductors cool slowly while retaining their electrical mobility*, Phys. Rev. B **102** 245204 (Dec 2020)

6. K.D.G.I. Jayawardena, R.M.I. Bandara, M. Monti, **E. Butler-Caddle**, T. Pichler, H. Shiozawa, Z. Wang, S. Jenatsch, S.J. Hinder, M.G. Masteghin, M. Patel, H.M. Thirimanne, W. Zhang, R.A. Sporea, J. Lloyd-Hughes and S. R. P. Silva *Approaching the Shockley-Queisser limit for fill factors in lead–tin mixed perovskite photovoltaics*, J. Mater. Chem. A **8**, 693-705 (Jan 2020)

The results from Chapters 4 and 5 will be combined to make a further journal article.

The following is a list of the conference talks and posters that I have presented during my PhD:

1. Talk: *THz Photoconductivity Dynamics Of Semiconductors From Sub-Nanosecond To Millisecond Timescales*, **E. Butler-Caddle**, N.E. Grant, S.L. Pain, J.D. Murphy, K.D.G.I. Jayawardena and J. Lloyd-Hughes, 47th International Conference on Infrared, Millimeter and Terahertz Waves (IRMMW-THz), Delft, Netherlands (August-September 2022)

2. Talk: *THz Photoconductivity Dynamics Of Semiconductors From Sub-Nanosecond To Millisecond Timescales*, **E. Butler-Caddle**, N.E. Grant, S.L. Pain, J.D. Murphy, K.D.G.I. Jayawardena and J. Lloyd-Hughes, Optical Terahertz Science and Technology (OTST22), Budapest, Hungary (June 2022)

3. Poster: *Comparing Charge Carrier Removal Rates in Perovskite-Transport Layer Heterostructures Using Time-Resolved THz and Optical Spectroscopies*, **E. Butler-Caddle**, K.D.G.I. Jayawardena, and J. Lloyd-Hughes, International Conference on Hybrid and Organic Photovoltaics (HOPV22), Valencia, Spain (May 2022)

4. Talk: *Assessing Charge Carrier Extraction Rates in Halide Perovskite Heterojunctions Using Ultrafast THz and Optical Spectroscopies*, **E. Butler-Caddle**, K.D.G.I. Jayawardena, and J. Lloyd-Hughes, 2021 Virtual MRS Spring Meeting and Exhibit (April 2021)

Abstract

This thesis reports optical measurements and analysis of the charge-carrier dynamics in semiconductor materials and structures that are used in photovoltaic cells. Observing the carrier dynamics in these devices is crucial for understanding the properties that are limiting efficiency, so that improvements can be achieved more quickly through design, rather than trial and error.

In perovskite solar cells, the charge transport layers (CTLs) on either side of the perovskite layer provide the asymmetry required to generate a photovoltage and photocurrent. In this work, the charge-carrier transfer and recombination behaviour at each individual interface is studied by measuring the carrier dynamics when only one interface is present i.e. a bilayer of a perovskite and either an electron transport layer (ETL) or a hole transport layer (HTL). In addition to using optical techniques that are more commonly employed in the literature, optical pump terahertz probe spectroscopy (OPTP) was used to measure the carrier density accurately in the first few nanoseconds, which revealed very different behaviour for fullerene based ETLs and the commonly used HTL, Spiro-OMeTAD. These measurements were then compared to two mathematical models of differing complexity, which provided greater understanding of the measured dynamics. The different behaviours observed at different interfaces have important implications for solar cell design.

A limitation of using OPTP to study semiconductors used in photovoltaics is that the carrier lifetimes are often much longer than the time range of the technique. An electronically delayed OPTP technique (E-OPTP) was developed, that has virtually unlimited time range whilst maintaining sub-nanosecond resolution. An efficient method to sample photoconductance decays longer than the laser repetition period was proposed, and was used to study the impact of surface passivation on the carrier dynamics in silicon. This technique was compared to inductively-coupled photoconductance measurements, which highlighted the superior spatial and temporal resolution of E-OPTP that allows in-plane and out-of-plane diffusion to be studied. The diffusion was modelled using analytical solutions of the ambipolar continuity equation. Overall, this work demonstrates the suitability of this technique for studying semiconductors with long carrier lifetimes.

Abbreviations

AFM	Atomic Force Microscopy
ALD	Atomic Layer Deposition
BC	Boundary Condition
BE	Binding Energy
BGR	Bandgap Renormalisation
BoS	Balance of Systems
CB	Conduction Band
CBM	Conduction Band Minimum
CNL	Charge Neutrality Level
CTL	Charge Transport Layer
CV	Control Volume
CW	Continuous Wave
DAS	Decay Associated Spectra
DFE	Defect Formation Energy
DFG	Difference Frequency Generation
DFT	Density Functional Theory
DSSC	Dye-Sensitised Solar Cell
EAS	Evolution Associated Spectra
EBIC	Electron Beam Induced Currrent
EO	Electro-Optic
E-OPTP	Electronically delayed Optical Pump Terahertz Probe
EPBT	Energy Pay Back Time
ETL	Electron Transport Layer
FD	Finite Difference
F-D	Fermi-Dirac
FE	Finite Element
FF	Fill Factor
FL	Fermi Level
FV	Finite Volume
FWHM	Full Width Half Maximum
GGA/LDA	Generalised Gradient Approximation/Local Density Approximation
GSB	Ground State Bleach
HLI	High Level Injection
HOMO	Highest Occupied Molecular Orbital
HTL	Hole Transport Layer
IE	Ionisation Energy
IRF	Instrument Response Function
IRT	Instrument Response Time
ISHE	Inverse Spin Hall effect
JDOS	Joint Density of States
KPFM	Kelvin Probe Force Microscopy
LCOE	Levelised Cost of Electricity
LLI	Low Level Injection
LUMO	Lowest Unoccupied Molecular Orbital
LVL	Local Vacuum Level
MHP	Metal Halide Perovskite
MPP	Maximum Power Point
NIR	Near Infra-red
NMR	Nuclear Magentic Resonance
ODE	Ordinary Differential Equation
OPTP	Optical Pump Terahertz Probe
OR	Optical Rectification
PCA	Photoconductive Antenna
PCD	Photoconductance Decay
PDE	Partial Differential Equation
PES	Photoemission Spectroscopy
PIA	Photo-Induced Absorption
PL	Photoluminescence
PMT	Photo-Multiplier Tube
PV	Photovoltaic
QFL	Quasi-Fermi Level
QWP	Quarter Wave Plate
SEM	Scanning Electron Microscopy
SG	Scharfetter-Gummel
SOC	Spin-Orbit Coupling
SQ	Shockley-Queisser
SRH	Shockley Read Hall
SVL	Surface Vacuum Level

TA	Transient Absorption
TAC	Time-to-Amplitude Converter
TAS	Thermal Admittance Spectroscopy
TCO	Transparent Conducting Oxide
TCSPC	Time Correlated Single Photon Counting
TDMA	Tridiagonal Matrix Algorithm
THz-TDS	Terahertz Time Domain Spectroscopy
TRMC	Time Resolved Microwave Conductivity
TRPL	Time Resolved Photoluminescence
TRTS	Time Resolved Terahertz Spectroscopy
VB	Valence Band
VBM	Valence Band Maximum
WF	Work Function
XPS	X-ray Photoelectron Spectroscopy

Chapter 1

Background

1.1 Introduction

Photovoltaic generation of electricity is a vital alternative to the current dependence on fossil fuels for generating energy, whose combustion emits greenhouse gases and whose reserves are finite [1]. Photovoltaic cells on the other hand do not emit greenhouse gases except in the fabrication and installation processes, and this carbon footprint will be rapidly reduced as fossil fuels are removed from these processes [2]. It has been predicted that to limit global warming to 2°C, photovoltaics will supply at least 30% of electricity by 2050, by which time electricity will be an even larger share of total energy consumption [3] as transport and heating is electrified. The key to increasing the commercial deployment of photovoltaics (PV) is the reduction of the levelised cost of electricity (LCOE is the average cost of electricity production over the lifetime of the generator). The LCOE of photovoltaics has dropped dramatically in recent years and is now comparable to or better than coal and gas [2, 4–7].

Silicon solar cells currently dominate the market [4] due to their high power conversion efficiency (PCE ~26% for research cells [8], see Fig.1.1) and their order of magnitude lower manufacturing costs than the only more efficient alternative, GaAs [9]. For silicon, the cost of the module contributes a minority of the LCOE [10] so reductions in module cost have contributed less to the reduction of the LCOE than improvements in power conversion efficiency have[11]. Furthermore, the Balance of System costs (BoS), which includes costs such as land, installation, and connection to the grid, are difficult to reduce so increasing the efficiency without significantly increasing the module cost is one of the most effective routes to reducing the LCOE [2, 4].

Another PV technology that could potentially achieve an economically attractive LCOE is the perovskite solar cell. Perovskite solar cells were first reported in 2009 [12] and their efficiencies have risen rapidly to become comparable to those of silicon cells after just a decade of research [8]. This rapid improvement suggests the possibility of their efficiency surpassing that of silicon, however the stability of perovskite solar cells remains the largest barrier to commercial deployment [13]. Perovskite-silicon tandem cells have also been investigated as a quick route to increase the efficiency of deployed modules[2], as silicon is cheap and well established, and the bandgaps of perovskite and silicon are well suited for tandem operation [14]. Efficiencies of over 32% for research cells have been

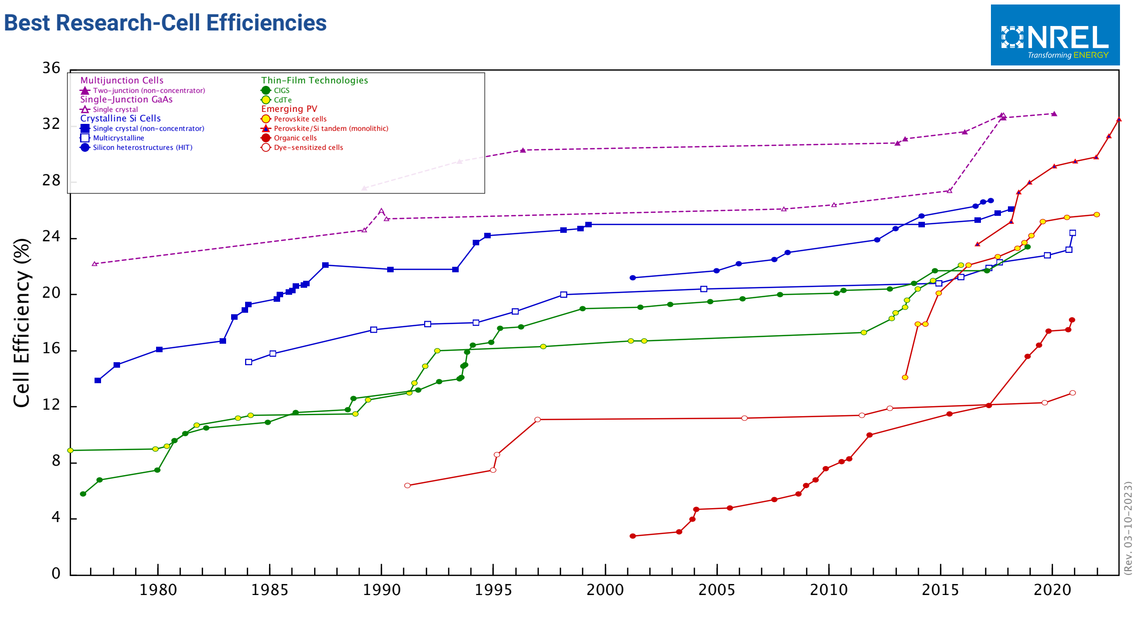

Figure 1.1: The best research cell efficiencies for a selection of technologies, measured under Standardised Test or Reporting Conditions by independent recognised test labs and collated by the National Renewable Energy Laboratory. Perovskite cells are represented by red circles filled with yellow, and perovskite on silicon tandem cells are represented by red triangles. This plot is courtesy of the National Renewable Energy Laboratory, Golden, CO.

achieved[8].

Perovskite solar cells employ a layer of metal halide perovskite to absorb the sun's electromagnetic radiation, which is fabricated by low energy processes meaning deployed cells would potentially have lower energy pay back times (EPBT) than silicon [15]. The high efficiencies of perovskite solar cell can be attributed to the perovskite layer's advantageous properties of strong light absorption [16, 17], low exciton binding energies [18] and long carrier diffusion lengths [19].The perovskite layer does not function as a photovoltaic by itself, but is sandwiched between two layers called charge transport layers (CTLs). The properties of these indispensable layers and the junctions they form with the perovskite light absorber have an enormous influence on device performance. Part of this thesis investigates the behaviour of these junctions through optical spectroscopy.

Non-radiative recombination of photoexcited electrons and holes reduces the PCEs of photovoltaics below their theoretical limit (the Shockley-Queisser radiative limit [20, 21]), and reducing this loss has been key to the improvement of efficiencies. These recombination processes need to be observed and understood so that they can be minimised, and a wide range of techniques have been used to study them. A common approach to studying recombination is to photogenerate electrons and holes in the material and then monitor their recombination either under steady state conditions, or as a function of time after pulsed photogeneration (a transient/time-resolved measurement). Contactless techniques are favoured as contacts influence the measurement and these effects are hard to disentangle. The main time-resolved contactless techniques for studying silicon are time resolved microwave conductivity [22–25] or an inductance coil eddy current technique[26–28], called photoconductance decay (PCD). However, the temporal and spatial resolution of these techniques are limited, and so this work introduces a modified optical-pump terahertz probe technique with superior capabilities. This technique can be used to study the electron and hole recombination and transport in semiconductors that are used in a wide range of technologies, not just photovoltaics.

1.2 Thesis Overview

Chapter 1 summarises the theoretical background of photovoltaic cells, and then reviews perovskite solar cells and the halide perovskite material itself. It will be explained how a photovoltage and photocurrent are generated by certain asymmetries in the device structure, such as by employing CTLs, and what properties of the materials and their interfaces should be optimised in order to maximise power conversion efficiency. This explanation includes a description of the thermodynamic driving force for the processes that return the system to equilibrium, and thus drive the carrier dynamics that are studied in this work. The development of perovskite solar cells is summarised and particular attention is applied to the properties of the CTLs that have been selected for study in this work due to their high performance and thus prevalence in research literature. Finally, metal halide perovskites will be introduced and the properties that are advantageous and or detrimental to their use in photovoltaics will be highlighted, providing context for the choice of perovskite used in this study. Particular attention will be applied to the properties that are relevant to optical spectroscopy techniques and the interaction of the perovskite with a CTL.

Chapter 2 describes the experimental techniques used in this work. Steady state absorption and photoluminescence measurements are used to characterise the samples and then time resolved measurements are used to measure the charge carrier dynamics. Time resolved terahertz spectroscopy measurements are also used to measure charge carrier dynamics, and since an extension to this technique is presented in chapter 6, this technique will be described in more detail. For all techniques, the relations between carrier densities and the different spectroscopy signals are presented.

Chapter 3 presents the mathematical models used to simulate and thus understand the carrier dynamics measured in the experiments. In this thesis, these models are solved both analytically and numerically, and this chapter derives the analytical solutions for the different boundary conditions relevant to the experiments in this work.

Chapter 4 presents the results of optical spectroscopy measurements of bilayers consisting of a lead halide perovskite and an organic CTL. Previous investigations of similar bilayers from the literature will be reviewed. This doctoral work employed both steady state and time resolved measurements of absorption and photoluminescence. Optical pump-THz probe spectroscopy (OPTP) is also used to monitor the population dynamics and due to a simpler data interpretation is analysed with a mathematical model.

Chapter 5 presents simulations of the population dynamics measured by OPTP using a model that incorporates Gauss's law to account for Coulombic forces between electrons and holes. The numerical method for solving this model is presented, and the solutions are compared to the experimental observations. The experimental data is also compared to an analytical solution of a simplified continuity equation that describes some of the measurements very well.

Chapter 6 presents an improvement to optical pump-terahertz probe spectroscopy, that allows the photoconductance dynamics to be measured over an unlimited time range rather than just the first few nanoseconds. This improved technique replaces mechanical delay stages with an electronic delay generator and is referred to as electronically delayed OPTP, i.e. E-OPTP. The temporal performance of this improved technique will be characterised, and an efficient method for measuring decays longer than the laser repetition period is presented. This method is compared to inductively-coupled eddy current techniques by measuring surface passivated silicon wafers with the two techniques. This comparison highlights the superior spatial and temporal resolution of E-OPTP that allows in-plane and out-of-plane diffusion to be studied. This charge carrier diffusion is modelled using analytical solutions of the ambipolar continuity equation.

1.3 Theory: Semiconductors and Photovoltaics

In order to understand the role of CTLs in perovskite solar cells and how they can be optimised, the physics of photovoltaic energy conversion will be reviewed. In a photovoltaic cell, the energy of solar photons is absorbed by the conducting electrons in a semiconductor, and therefore the relevant physics for the cell is the dynamics of these conducting electrons, which includes transitions between electronic states and the spatial transport of electrons. The thermodynamic driving force for these processes is reviewed in this chapter, but the mathematical model of these dynamics is described in chapter 3. The absorption of light by the semiconductor electrons will be discussed in the context of light absorption experiments in section 2.3. In this chapter, before discussing photovoltaics, the relevant fundamentals of semiconductors are defined.

1.3.1 Fundamentals of Electrons in Semiconductors

Solid state materials can have electronic states that are delocalised over the entire material, and there may be many states with the same energy (degenerate) [29]. There may be an energy range E_g for which there are no electronic states, which is a bandgap separating bands of electronic states. The bandstructure (Fig. 1.2b) is a plot of the electronic state energies versus their momentum, and the density of states, DoS or $g(E)$, is the number of states (per unit volume) within the energy range dE (Fig. 1.2c). Near the band edges, the bands are approximately parabolic and the density of states per energy in a 3D crystal has a square root dependence on energy. When the CB minimum and VB maximum are at the same momentum vector **k**, this is called a direct bandgap, otherwise it is called indirect (e.g. silicon). In some semiconductors the band extrema (edges) are at **k**=0 (Γ point), but for perovskites some calculations have suggested the band extrema are not at

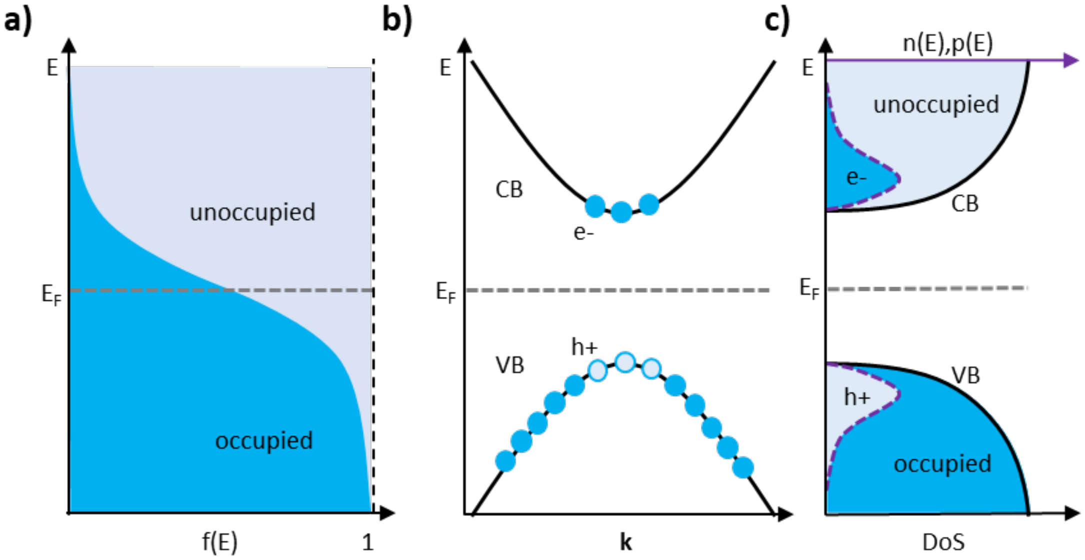

Figure 1.2: a) The Fermi-Dirac distribution $f(E)$. b) The bandstructure near the conduction band (CB) and valence band (VB) edges for a direct bandgap. c) Black lines represent the density of states (DoS) with respect to energy, with blue and grey areas representing occupied and unoccupied states respectively. The purple dashed lines show the electron and hole densities as functions of energy.

k=0 [30, 31]. The electrons occupy this distribution of states according to the Fermi-Dirac (F-D) distribution, which describes the fraction of states at each energy that are occupied (Fig. 1.2a).

$$f(E) = \frac{1}{e^{\frac{E-E_f}{k_BT}} + 1}$$

The Fermi level E_F is the energy that has 50% occupancy of the states at that energy, and for semiconductors it is in the bandgap (note the term Fermi energy is specifically the Fermi level at zero temperature). If the energy scale ignores electrostatic potential, then E_F simplifies to chemical potential μ (see section 1.3.2.1).

Although electrons are in delocalised states, so are "free", conducting electrons are those at energies where occupation is partial, neither 0 or 1 (i.e. the transition range of the F-D function). The band of states below and above the Fermi level are called the valence band (VB) and conduction band (CB) in crystalline materials, or HOMO and LUMO in molecular materials (the highest occupied and lowest unoccupied molecular orbitals respectively). The flux of particles and charge due to the motion of electrons in the VB, is equivalent to the fluxes due to the motion of the unoccupied states in the VB, if they are attributed a positive charge, hence they are called holes. Similarly, the removal of electrons from the VB is equivalent to injection of holes into the VB. The energy scale for holes in the VB is inverted compared to the energy scale for electrons. The density of electrons in the CB and holes in the VB have the symbols n and p respectively, and are referred to as charge carriers (or just carriers).

An electron-hole pair may form a bound state called an exciton, which lowers the energy of the pair by an amount called the exciton binding energy. If this binding energy is small compared to thermal energy k_BT, then most electron-hole pairs will be unbound. In a later section it will be explained that in "3D" perovskites, electron-hole pairs are expected to be unbound at room temperature.

The electron distributions in the CB and VB can be in equilibrium with each other because electrons can transition between them, creating or destroying holes in the VB (see Fig. 1.3). The excitation of an electron from the VB to the CB adds an electron to the CB and a hole to the VB, so is called a generation process, whereas the reverse process is called recombination. At equilibrium, the transition rates between the bands are balanced. Electrons can absorb or emit the transition energy in the form of electromagnetic radiation (photons), lattice vibrations (phonons) or by exchanging energy with another electron (Auger process). Momentum must be conserved for every transition. Transition rates between states are proportional to the density of occupied electron states that are losing electrons and the unoccupied electron states receiving the electrons, and similarly for the other species involved i.e. the phonon and photon states. The proportionality constant between a transition rate and the densities of species involved is called a rate constant. Generation and recombination rates have dimensions of particles per unit volume per unit time, but are sometimes referred to as fluxes or particle currents (electrical/charge current is the particle current times particle charge), even though these have the dimensions of particles per *area* per time.

Phonon energies are much smaller than the bandgap so band-to-band transitions

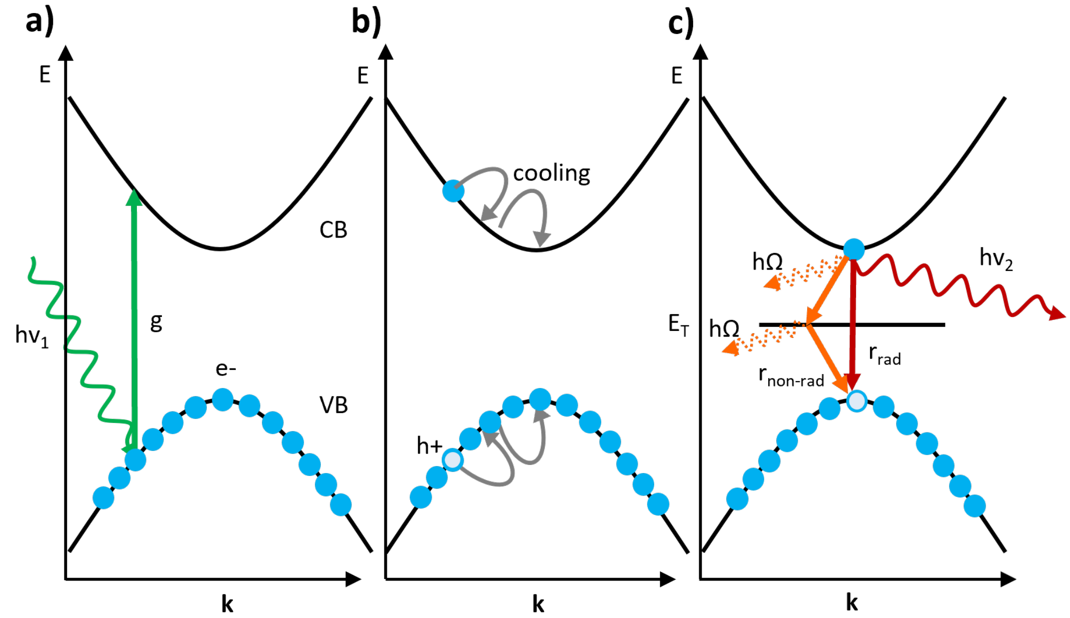

Figure 1.3: a) Electrons excited from the valence band (VB) to the conduction band (CB) by absorbing a photon of energy $h\nu_1$, leaving holes in the VB. b) Electrons and holes relax i.e. cool toward lower energy states in their bands by phonon emission (holes have inverted energy scale). c) Electrons recombine with holes either in one-step (radiatively) emitting a photon with energy $h\nu_2$, or in two-steps via a defect state (non-radiatively), emitting phonons in each step, with energy $h\Omega$.

would require the simultaneous emission/absorption of many phonons, with the correct combination of momenta, so are very unlikely i.e. the process has a small rate constant. Therefore, almost all band-to-band transitions involve photons or an Auger process, but Auger processes require three electrons/holes, and so only have significant rates at high carrier densities.

Alternatively, localised states within the bandgap provide intermediate states for a sequential two step transition between bands (see Fig. 1.3c). For phonon-mediated transitions, the rate constant for transitions between a band and a localised state is higher than for between bands, because the former has a smaller energy gap. Localised states that are close in energy to one band edge have a very high rate constant for transitions to/from that band, but a low rate constant for transitions to/from the other band, so the two-step transition from one band to the other has very low probability. For a localised state near the middle of the gap, for which there is an intermediate transition probability to both bands, the probability of a two-step transition is much higher.

A point modification to the periodic lattice creates a localised state whose energy may be in the bandgap and represents an electron or hole bound to the point modification. Substituting an atom for one with a different valency (called an electronic dopant atom) not only changes the distribution of states with respect to energy (new localised states), but also changes the number of electrons in the system, shifting the Fermi level of the Fermi-Dirac distribution. If the number of electrons is increased (a donor type dopant), then the Fermi level of the F-D distribution is shifted up in energy towards the CB, and so its range of partial occupancy has greater overlap with the CB than the VB. This increases the number of conducting electrons in the CB, n, more than it decreases of the number of conducting holes in the VB, overall increasing $n + p$ and thus the conductivity. This is called n-type doping. Whilst $n + p$ increases, the law of mass action dictates that the product np is not changed

$$np = N_c N_v e^{\frac{-E_g}{k_B T}} = n_i^2$$

where N_c and N_v are constants called the effective band density of states. This is valid when the bands are parabolic with respect to energy and when the Fermi level is more than $k_B T$ from the band edges (called non-degenerate), so that in the bands the F-D distribution can be approximated as the Boltzmann distribution.

1.3.2 Photovoltaics

A photovoltaic cell converts the thermal energy of the sun's black body radiation into the chemical energy of electron-hole pairs in a light absorbing material, which is then converted into the electrical energy of a charge current [32]. In order to understand why and how these conversions occur, the thermodynamics that governs what processes can occur in nature, and thus in a photovoltaic, is briefly reviewed first.

1.3.2.1 Thermodynamic Driving Force

A natural process increases the entropy, S, of the universe while conserving the energy of the universe - the 2^{nd} and 1^{st} laws of thermodynamics - which can be divided into a system and its surroundings [33]. For processes inside the system, natural processes correspond to decreasing a thermodynamic potential energy of the system, such as the Gibbs Free energy (the magnitude of the decrease is equal to thermal energy of any entropy generated by the process, TS). Therefore, this minimisation condition dictates what processes can occur.

Minimisation of the thermodynamic potential energy is also the principle that drives two subsystems (i.e. regions of a larger system) to equilibrate their state potentials (distinct from thermodynamic potential energy), such as temperature T or chemical potential μ, by exchanging energy. For example, a familiar case is that heat (thermal energy) will transfer from a hotter body to a colder body to equilibrate their temperatures, or a dissolved solute will diffuse from regions of high concentration to low concentration, to equilibrate concentration, which is one constituent of chemical potential (this transports chemical potential energy). A different situation occurs in an electron gas, in which electrons carry both chemical and electrical "matter"[33] i.e. particle number and charge. This means the chemical and electrical potentials, μ and ϕ, may not equilibrate individually. The minimised thermodynamic potential energy corresponds to a distribution in which the combined electrochemical potential η is uniform. An example of this is p-doped and n-doped layers of the same material, which when connected form a p-n junction (see Fig. 1.4). Before being connected they have the same electric potential (i.e. both neutral) but different chemical potentials, so different electrochemical potentials. When they are connected, electrons will flow reducing the chemical potential difference and building up an electric potential difference, until the electrochemical potential is uniform. This electric potential difference that exists at equilibrium is called a built-in potential difference (or field) and will occur whenever two materials with different electrochemical potentials are connected, including metal-semiconductor junctions. Since each material is expected to be neutral before contact (i.e. same electric potential), the electrochemical potential difference between the isolated materials is entirely due to the chemical potential difference.

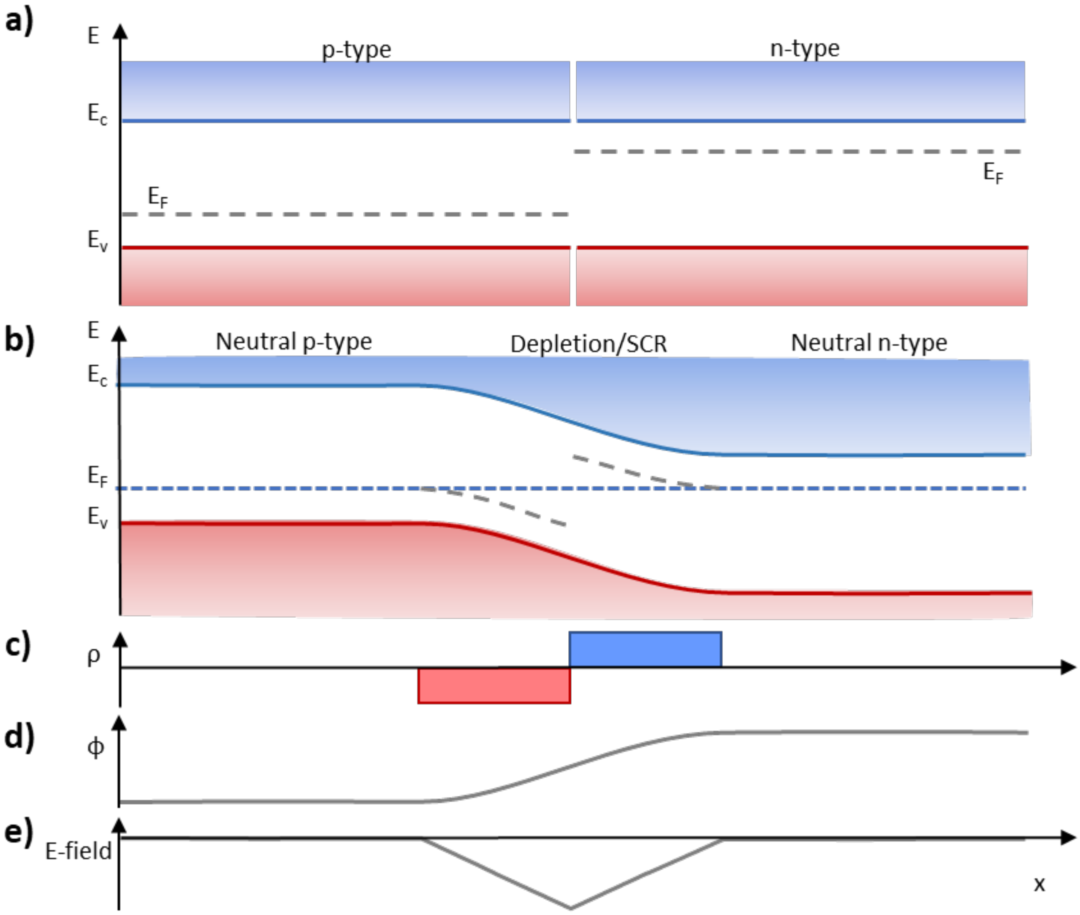

Figure 1.4: Schematic of a p-n homojunction. a) p-type and n-type doped layers of the same material prior to contact - the electric potentials are the same but the chemical potentials and thus electrochemical potentials E_F are different. b) When contacted, electrons flow to equilibrate the electrochemical potential, resulting in an electric potential difference and thus band bending, that balances the chemical potential difference. c) A space charge $\rho(x)$ exists due to carriers being depleted leaving fixed ions. d) The electric potential profile $\phi(x)$. e) The electric field profile $E(x)$.

From the discussion above, it can be seen that when studying charge-carrier transport, it is crucial to realise that transport is driven by gradients in the electrochemical potential, rather than the chemical or electrical potentials individually. This corresponds to carriers moving in the direction such that Free energy decreases, and entropy is generated. Transport that is driven by gradients of chemical potential only is called diffusion, and transport driven by gradients of electric potential only is called drift. Therefore, the total current when both gradients exist is often decomposed into drift and diffusion, components, but this is merely a mathematical decomposition, there is only one current and it flows due to the gradient of the electrochemical potential ([32]). It can be shown that the electrochemical potential of an electron gas is equivalent to the Fermi level parameter in the Fermi-Dirac distribution[32], so the discussion is often in terms of Fermi levels.

Overall, energy conversion devices use differences in state potentials (e.g. temperature or chemical potential) to drive processes that convert energy from one form to another [33]. In a solar cell, the difference in temperature of the sun's radiation and the lattice is used to convert thermal energy into chemical energy i.e. a difference in chemical potential. This is a heat engine. Then the difference in chemical potential is used to convert chemical energy into electrical energy [33].

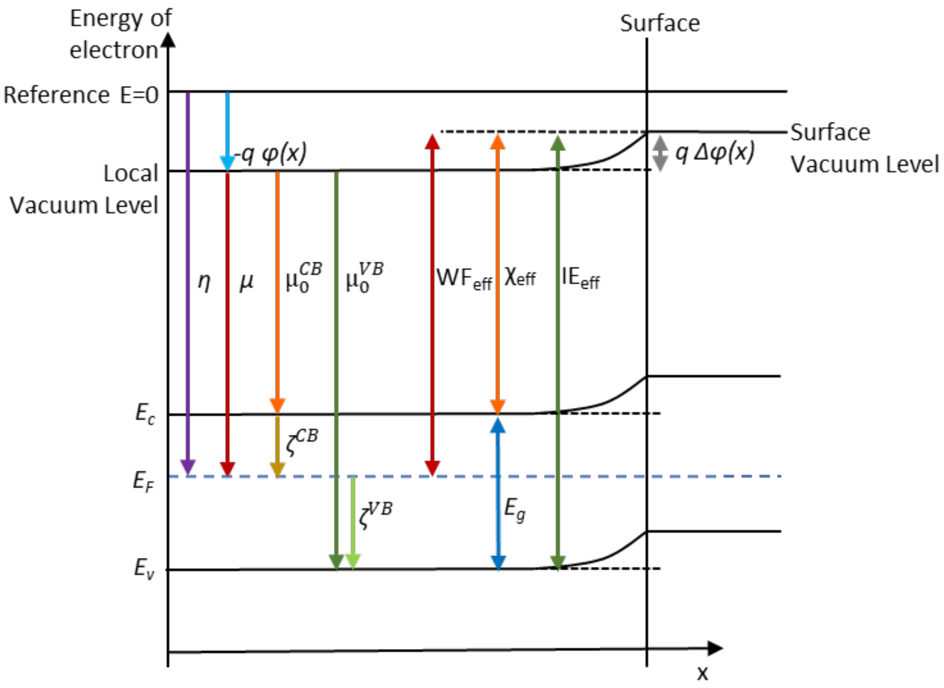

Figure 1.5: Different energy quantities in semiconductors as defined in the text, plotted on the energy scale of an electron (holes have an inverted energy scale). Potentials are quantities per particle, so are multiplied by particle number to get energy (electric potential ϕ is also multiplied by particle charge). One sided arrows indicate an absolute quantity (i.e. signed) relative to the start of the arrow. Double sided arrows indicate magnitudes (i.e. not signed).

Many different energy or potential quantities have been referred to, and so their definitions will now be clarified. The chemical potential is the energy per particle (energy is $N\mu$) and the electric potential is the energy per particle per particle charge (energy is $NZq\phi$ where q is the elementary charge and $Z = -1$ for electrons and $Z = +1$ for holes). Fig. 1.5 shows definitions of potentials and energies per electron. The energies are relative to an arbitrary zero reference, which is usually taken as a point infinitely far from the semiconductor such that it's presence is not felt, i.e. any electric potentials have decayed to zero. The local vacuum level (LVL) represents the electrostatic potential energy relative to the zero reference and ignores the crystal potential that cause the bandstructure. The LVL can be defined both inside and outside the crystal. The surface vacuum level (SVL) is the energy of an electron that is unbound from the crystal potential i.e. just outside its surface. A sharp jump in LVL over atomic distances between the inside and outside of the surface is termed a surface dipole. The SVL may differ from the VL at infinity due to slowly decaying electric potentials. Variations of LVL inside the crystal over length scales greater than atomic distances is termed band bending and occurs due to net space charge.

The crystal potential creates the bandstructure that lowers the energy of the electrons relative to the LVL, and the two band edges E_c and E_v are lower in energy than the LVL by the electron affinity, χ, and the ionisation energy, IE, respectively. χ and IE are not absolute energies but are magnitudes of energy differences so are not signed (indicated by double headed arrows in Fig. 1.5). χ and IE are uniform within a single material phase, so E_c and E_v are parallel to LVL.

The electrochemical potential η or equivalently the Fermi Level E_F, is composed of the electric potential ϕ (LVL relative to zero) and the chemical potential μ (E_F relative to LVL). The chemical potential is composed of the concentration dependent and independent parts, where the concentration independent part μ_0 is the phase dependent part, i.e. due to the crystal potential that creates the bandstructure. The concentration independent part is E_c or E_v relative to LVL (so χ or IE), and the concentration dependent part ζ is E_F relative to either E_c or E_v (this is defined as a signed quantity). At equilibrium, the populations in the CB and VB are in equilibrium with each other with the same chemical (and thus electrochemical) potentials

$$\mu_{CB} = \mu_{VB} = \mu$$

where

$$\mu_{CB} = \mu_0^{CB} + \zeta^{CB} = E_c + k_B T \ln\left(\frac{n}{N_c}\right) \tag{1.1}$$

$$\mu_{VB} = \mu_0^{VB} - \zeta^{VB} = E_v - k_B T \ln\left(\frac{p}{N_V}\right) \tag{1.2}$$

It will shortly be seen that the populations in the CB and VB can have different chemical (and thus electrochemical) potentials, $\mu_{CB} \neq \mu_{VB}$, when n and p do not have their equilibrium values. To be clear, the value of this μ_{VB} is using the energy scale of electrons, i.e. is negative relative to the zero reference.

The work function, WF is the magnitude (not signed) of the E_F relative to the LVL. When photomeission spectroscopy is used to measure χ, IE and WF as the energy difference between SVL and E_c, E_v and E_F respectively, these measured differences will include surface dipoles, so the measured quantities are labelled as effective.

1.3.2.2 Converting Thermal Energy to Chemical Energy

The first step in a photovoltaic is to transform thermal energy into chemical energy, which requires a material with a gap in its density of electronic states, i.e. a semiconductor [32]. This step is equivalent to the operation of a heat engine in that the electrons receive heat from a source, the sun, and then transfer it to a cooler sink, the ionic lattice (in reality it also radiates some heat into surroundings other than the lattice).

The sun emits radiation that has a continuous spectrum approximately following the spectrum of a black body. This population of photons has the temperature of the emitting body and it carries entropy and thermal energy (TS), but the photons have zero chemical potential. Due to these properties of black body radiation, when a gas of electrons with a uniform continuous density of states absorbs solar radiation (see Fig. 1.6a,b), the absorbed thermal energy increases the temperature of the gas, but the Fermi level (chemical potential) is not changed. The electron gas will transfer the excess thermal

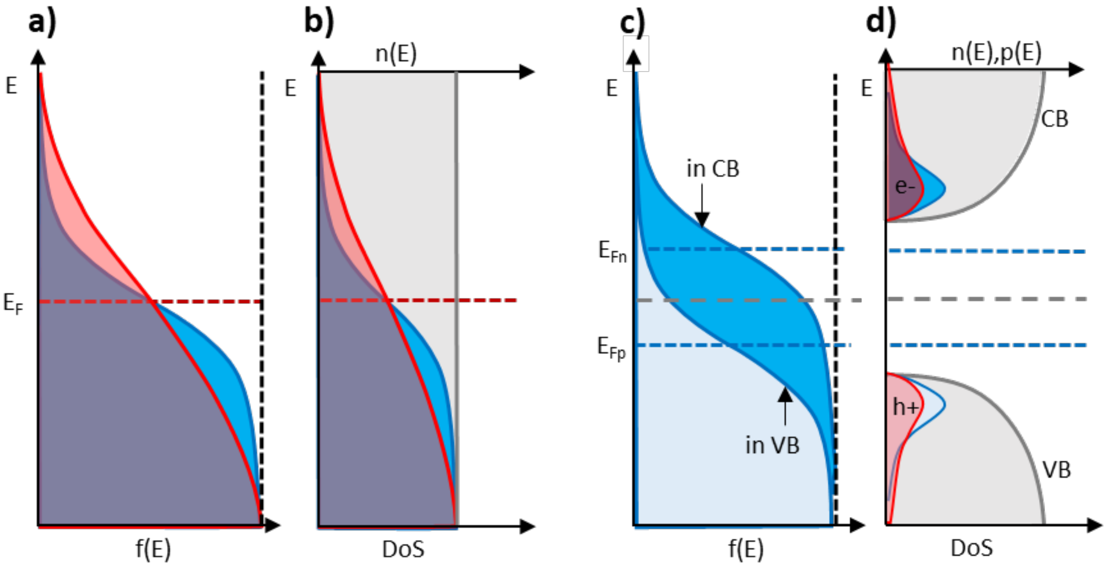

Figure 1.6: a) The Fermi-Dirac occupation function, $f(E)$, for two different temperatures (red=hotter). b) The density of states (DoS) for a material with a uniform continuous DoS (grey), and the electron density as a function of energy after absorbing thermal energy from the sun (red). c) For a material with a bandgap (a semiconductor), the Fermi-Dirac occupation function is shown for the electrons in the CB (blue) and the holes in the valence band (grey-blue) following photoexcitation across the bandgap and once these populations have cooled close to the lattice temperature, resulting in their quasi-Fermi levels (E_{Fn} and E_{Fp}) splitting. d) The DoS for a semiconductor (grey), and the electron and hole densities as functions of energy, with raised temperature following photoexcitation (red), and then after cooling to the lattice temperature (blue).

energy to the lattice by scattering with the lattice (i.e. phonon emission) to equilibrate their temperatures (photon emission can also carry away heat). In contrast, when there is a bandgap (see Fig. 1.6c,d), the processes which exchange electrons between the bands are very slow (recombination takes ns to ms) compared to the cooling of the electrons (fs to ps), which means the electrons in each band return to their original lattice temperature without the population of the bands returning to their original values. Changing the number of particles in a band without changing the temperature corresponds to changing the chemical potential of the particles in the band. Defining a chemical potential and temperature for the population in a band assumes the population is in quasi-equilibrium within the band, whilst not being in equilibrium with the population in the other band. The band population can reach quasi- equilibrium by electron-electron scattering. This quasi-equilibrium state in each band slowly evolves (hence only quasi-equilibrium) until the two bands equilibrate.

Since the upper band (CB) has an increased electron population and the lower band (VB) has a decreased electron population, the chemical potentials have changed in opposite directions, so there is a separation of the chemical potentials for each band. The total chemical potential of the populations in the two bands is increased, so a photoexcited electron-hole pair has excess chemical energy compared to the equilibrium state where this pair has recombined. When the electron-hole pair recombines, the excess chemical energy must be emitted and is carried away by the emitted photon, which is in contrast to photons emitted from continuous DoS (e.g. the photons from the sun that excited the electron-hole pair), which carry no chemical potential [34]. The chemical energy that is emitted when an electron moves from a band with high chemical potential μ_{CB} to a band with low chemical potential μ_{VB} is, to first order, equal to $\mu_{CB} - \mu_{VB}$.

Overall, the solar energy has partly been transferred to the lattice, and partly transformed into the additional chemical potential energy of an excited electron relative to the empty state in the VB it would otherwise occupy $(\mu_{CB} - \mu_{VB})$. When the excess population of the bands is larger due to more intense photoexcitaton, this increases the separation of the chemical potentials, so each electron-hole pair that is recombined or is removed carries more chemical potential energy (the corollary is that electron-hole pair recombination or removal reduces the chemical separation).

An electron and hole are generated in the same location so have the same electric potential, but due to their opposite charge their electrical energies are opposite, so the pair has no net electrical energy. Therefore, the electrochemical energy of the pair is initially just the chemical energy of the pair. If the pair is spatially separated, their electric potential energy increases. The separate electrochemical potentials, i.e. Fermi levels, for the two bands are called quasi-Fermi levels (QFLs), denoted E_{F_n} and E_{F_p}, so the excess chemical energy of the pair is $E_{F_n} - E_{F_p}$, also called the QFL splitting. The excitation of an electron from the VB to the CB can instead be thought of as photogeneration of a new CB electron and a new VB hole from nothing, $null \rightarrow e + h$. In this view, the increase in chemical potential is $\mu_e + \mu_h$, where these values are relative to the chemical potential of the null state before creation of the pair, and the energy scale of holes is used for μ_h, which is inverted compared to the electron energy scale due to the opposite charge and particle number of holes. Splitting of the QFL corresponds to positive μ_e and positive μ_h.

During steady state operation of a solar cell (the rate of photogeneration of electron-hole pairs equals the rate of their removal), the temperature of the electron gas is only slightly increased above the lattice temperature because the transfer of thermal energy to the lattice is a fast process. Ohmic resistance during transport to the contacts is another form of heat dissipation to the lattice.

1.3.2.3 Converting Chemical Energy to Electrical Energy

Following photoexcitation, this excited state of the system will proceed to minimise its thermodynamic potential energy by returning the excited electron from the CB to the VB, thus recombining with its corresponding hole, and emitting the electrochemical energy of the pair out of the electron gas. The driving force for these processes is the electrochemical potential difference between the two bands. The electrochemical energy of the pair can be emitted in a number of ways.

Recombination processes within the device (internal) such as radiative recombination or defect mediated recombination emit the electrochemical energy as photons and phonons respectively. In photovoltaics, the electrochemical energy is converted to the electrical energy of a charge current in a circuit, which can do work (i.e transform to other forms of energy). An electron is extracted from the CB and a hole is extracted from the VB (equivalent to an electron injected into the VB), so the pair is extracted. For a net charge current to flow, electrons and holes must be extracted in opposite directions, otherwise if the electron and hole are transported in the same direction, the chemical energy is just transported rather than converted into electrical energy. One way to guide extraction in opposite directions is to use selective membranes on two sides [32, 35, 36] i.e. making extraction of a carrier in one direction favourable over another, which is modifying the kinetics of the two processes. In this work it is referred to as kinetic asymmetry. Under illumination, the QFLs in the absorber layer are split, and so carriers will flow to the contacts where the Fermi Levels are lower (holes have inverted energy scale), but the selective membranes allow the flow of only one carrier type to each contact. The driving force for net flow of a carrier to one side can be viewed as diffusion towards a sink on one side, with diffusion to the other side blocked.

For example, a selective membrane for the absorber can be another semiconductor (so a heterojunction) that has the energies of its CB and VB aligned relative to those in the absorber layer, such that the carriers in one band of the absorber cannot be extracted because there is an energy barrier for this process, whereas carriers in the other band of the absorber layer can be extracted because there is no such barrier (see Fig. 1.7). These kinetic barriers are used in dye sensitised solar cells (DSSCs). This implies the selective layers should have larger bandgaps than the absorber layer, so are here referred to as bandgap layers. A large bandgap can be beneficial in minimising the generation that takes place in the selective layer itself, which is undesirable as the unwanted carrier is on the wrong side of the selective barrier and is not blocked from reaching the contact. Fig. 1.7 illustrates the operation of these bandgap layers or CTLs, considering the simplified scenario in which all the layers have the same Fermi level when isolated, so when connected no band bending occurs. This has required that the equilibirum Fermi levels in the ETL and HTL are not mid-gap, i.e. they are n-type and p-type doped respectively. In principle, bandgap layers can be very selective but interfaces between different materials often have a high density of localised states which increases recombination and reduces the extraction of electrical energy. It should be noted that bandgap layers are often doped in favour of the extracted carrier, in order to maximise the chance of the carrier reaching the contact (maximising the diffusion length).

The most commercially deployed structure is a p-n homojunction (see Fig. 1.4 and Fig. 1.8), which uses a single material so avoids the high density of defect states associated with heterojunctions. The single material is divided into two regions with different doping, and equilibration of the Fermi level/electrochemical potential by carrier transfer results in a region at the interface which is depleted of carriers. In this depletion region the charge of the immobile dopant ions is no longer neutralised by the mobile carriers, so there is a space charge region with a built-in field, and the bands (LVL, E_C, E_V) are sloped (called bending). Either side of the depletion region, there are two neutral, field-free regions (flat bands), and the majority carrier in these regions has a longer recombination lifetime than the minority carrier, because the majority carrier has lower probability of encountering a recombination partner (minority carriers), and vice versa. Therefore, carriers have longer diffusion lengths (average distance they diffuse before recombining) when they are in a region in which they are the majority carrier, and vice versa. When illumination generates electron-hole pairs, they are driven towards the side where they are the majority (explained further below), and then extracted at the metal contact. Due to the short diffusion lengths

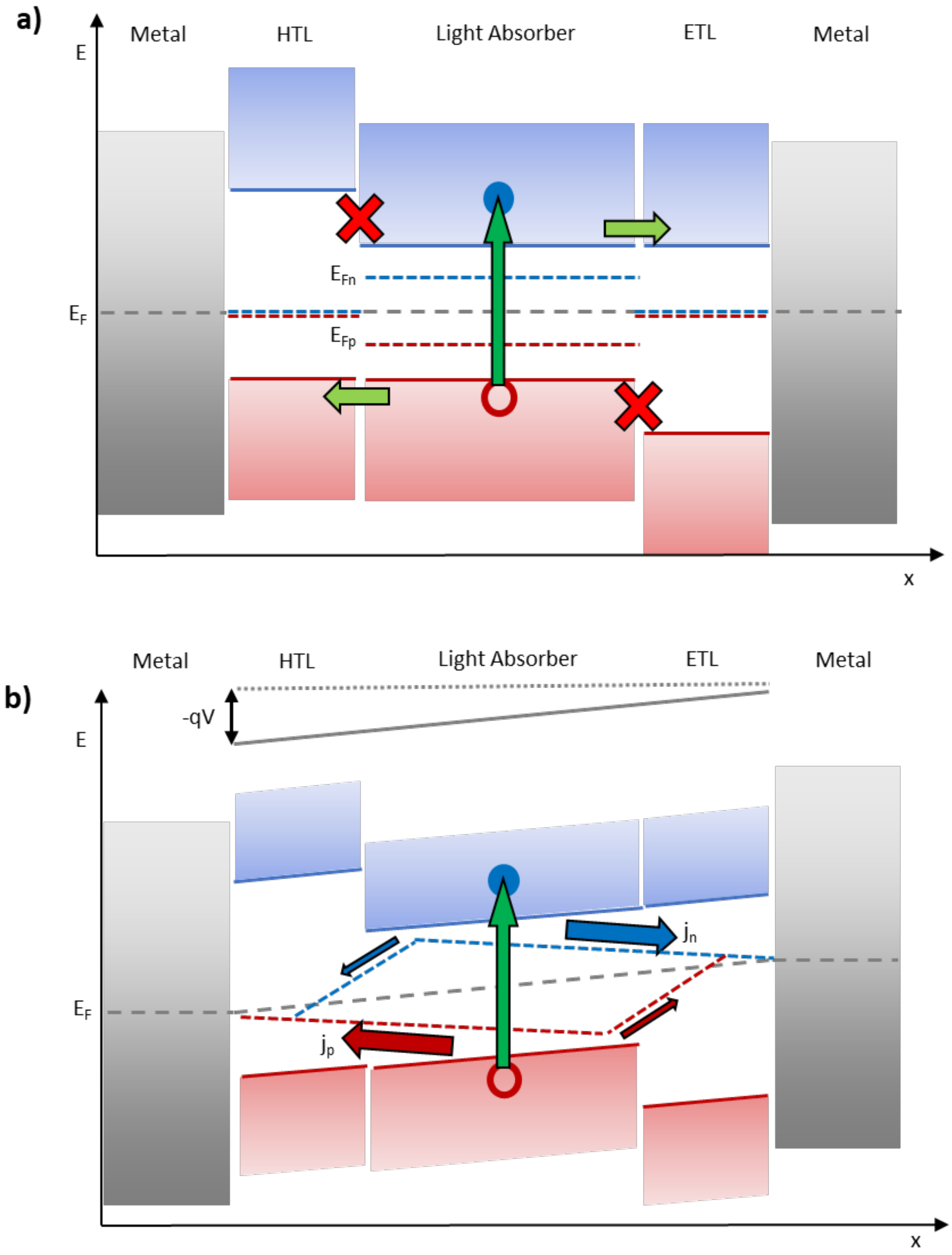

Figure 1.7: a) The structure of a solar cell employing layers with larger bandgap either side of the light absorbing layer (called bandgap layers or CTLs), whose band energies are aligned such that only carriers from one band can be extracted at each interface. This diagram considers the simplified scenario in which all the layers have the same Fermi level when isolated, so when connected, no band bending occurs. Under illumination, the quasi-Fermi Levels (QFLs) in the absorber layer are split, and so carriers will flow to the CTLs where the Fermi Levels are lower (holes have inverted energy scale). b) Under steady state conditions, there is an accumulation of electrons at one contact and holes at the other, giving a splitting of the Fermi Levels in the two metal contacts, called the photovoltage, V. The gradient of QFLs indicates the direction of flow, and the magnitude of the flow (which is not simply the magnitude of the gradient) is given by the size of the arrows, j_n and j_p. Note that the direction of net current within the device is opposite to the photovoltage. In the CTLs, the QFL for the blocked (minority) carrier converges towards the QFL of the extracted (majority) carrier as few blocked carriers will enter the CTL and those that do will mostly recombine before reaching the contact, since they are minority carriers.

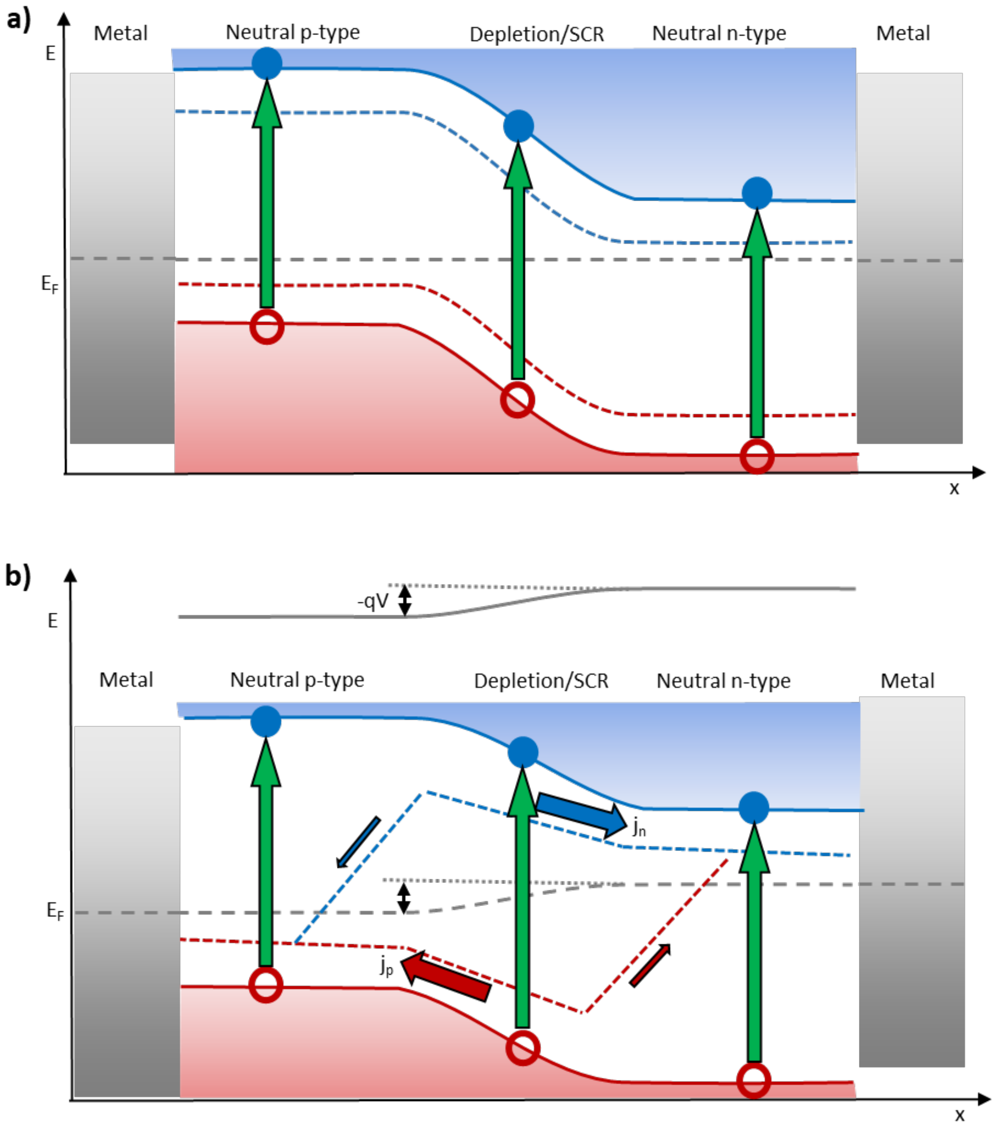

Figure 1.8: a) A p-n junction in the moment immediately following spatially uniform photoexcitation and before any carrier motion. At each position, the quasi-Fermi Levels are shifted more for the minority carriers than for majority carriers, resulting in gradients following the built-in band bending. b) Under steady state conditions, there is an accumulation of electrons at one contact and holes at the other, giving a splitting of the Fermi Levels in the two metal contacts, called the photovoltage, V. The gradient of the QFLs indicates the direction of flow, and the magnitude of the flow (which is not simply the magnitude of the gradient) is given by the size of the arrows, j_n and j_p. Note that the direction of net current within the device is opposite to the photovoltage. In the neutral regions, the QFL for the blocked (minority) carrier converges towards the QFL of the majority carrier as any minority carriers which enter the neutral regions from the depletion region will mostly recombine before reaching the contact.

of minority carriers, only minority carriers generated within a diffusion length of the depletion region will reach the depletion region, where they will cross to the side where they are majority carriers and have long diffusion lengths, and thus can reach the contact. These p-n junctions have been interpreted as selective membranes with the selectivity due to their conductivity [36], but later works have attributed the driving force for current in p-n junctions to the photoinduced changes in the chemical potential gradients [37], which will be discussed below.

Whilst a homojunction avoids interface states between different materials, some materials cannot be doped to form p-n junctions. However, the metal contacts themselves can form band-bending junctions as they will in general have different electrochemical potentials to the semiconductor, so will induce a band bending region near the interface. Unfortunately, it is difficult to find metals that will form interfaces that are as selective as doping junctions or CTL junctions. The CTLs are also likely to induce band bending junctions and so the CTLs should have electrochemical potentials that result in favourable band bending, and this can be manipulated by doping the CTLs, whilst remembering that the doping should enhance the diffusion length of the extracted carrier.

1.3.2.4 Photovoltage and Photocurrent

A photovoltaic device under steady state conditions generates a photovoltage, V, which is a difference in the electron QFL at the electron extracting contact, and the hole QFL at the hole extracting contact. At a metal contact, the electron and hole QFLs in the semiconductor converge into a single FL, because a metal has no bandgap, so the photovoltage is also equivalent to the difference between the FLs of the two metal contacts. In both CTL-heterojunction and p-n homojunction cells, it is the minority QFL that converges towards the majority QFL, in the CTL and neutral regions respectively. This is because minority carriers extracted into the CTL or the neutral region have short diffusion lengths, so their population decreases towards the contact due to recombination. Recombination changes the populations equally, but causes a greater change in the QFL for the minority carrier than the majority carrier, due to its logarithmic dependence on density, and hence the minority QFL converges to the majority QFL.

The formation of a photovoltage can be understood as follows. Under steady state illumination, carriers are generated in the absorber layer (so the Fermi level in the absorber is split into quasi-Fermi levels) and then a selective transport structure like the ones above results in the electron current to one contact being greater than to the other, and similarly for holes in the other direction. These currents are driven by electrochemical gradients from the absorber layer towards the contacts. The net flow of a photogenerated carrier towards a contact leads to an accumulation of the carrier near the contact which modifies the carrier's electrochemical potential there. Since electrons and holes have net flow to opposite contacts, the electrochemical potential of electrons is raised at one contact, and the electrochemical potential of holes is lowered (using electron energy scale) at the other contact, giving a quasi-Fermi level splitting between the contacts. This is the photovoltage that drives current through the circuit. The slower the extraction, the greater the accumulation at the contacts, and thus the greater the photovoltage. This QFL difference that drives current through the circuit looks like it might drive a current backwards through the device. However, the gradients of the QFLs do not show the absolute value of the current, only the driving force. So although the QFLs will have gradients in the wrong direction in parts the device, these currents are small compared to the currents in parts of the device where the QFL has a gradient in the correct direction, so there is a net current in the correct direction (see Fig.1.7 and 1.8).

To maximise the electrical power extracted, the product of the current density J and the electrochemical energy of the pairs, i.e. the photovoltage V, must be maximised. Increasing the extraction rate reduces the steady state populations in the bands, so reduces the quasi-Fermi level splitting and thus the photovoltage. Similarly, reducing the extraction rate increases the steady state population and thus the recombination rate, which reduces the fraction of carriers that are extracted. So the maximum extracted power occurs for a particular extraction rate, which is controlled by varying the load. How the current and voltage vary as the load is varied between zero and infinity is the $J-V$ curve, and is sometimes modelled as the superposition of ideal circuit elements, i.e. an equivalent circuit (see Appendix A). Recombination reduces the current that can be extracted and also reduces the carrier populations and thus photovoltage. So to maximise power conversion, recombination needs to be minimised. Radiative recombination cannot be avoided as it is the inverse of photon absorption. Other forms of recombination can be minimised, such as by reducing the density of defects.

1.3.2.5 The Role of the Built-In Field

It is commonly stated that the built-in electric field in a p-n junction drives the separation of photogenerated electrons and holes, probably because its electric force acts in the same direction as carrier flow under short circuit operation. A number of publications have sought to clarify the driving force and concluded that this is not the case. For example, solar cells exist without this built-in field e.g. DSSCs which have nanometre thickness so no space charge can develop to give such a built-in field [32]. Hypothetical p-n junctions can be simulated which have no built in field and they still operate as solar cells (this comprises a gradient of materials which all have the same Fermi level and bandgap, but the band energies E_C and E_V vary gradually across the junction) [32]. Similarly, it can be simulated that the photovoltage can be greater than the built-in voltage giving a net electric field in the opposite direction to current extraction. Furthermore, an electric field stores electric potential energy, and if it accelerates charges and does work, it must dissipate this finite energy [32]. Therefore, whilst a built-in field stores the energy released by a capacitor, it cannot account for the continuous current generation under illumination, which is instead an energy conversion process. Moreover, an electric field is conservative so cannot do work by moving a charge around a loop [37], another form of energy must be dissipated.

For devices with built-in fields, at equilibrium there are chemical and electric potential gradients that balance each other so that the electrochemical potential is uniform. Before spatial separation of the electron hole pair, uniform generation does not change the electrical potential gradient but modifies the chemical potential gradient, resulting in a net electrochemical gradient [37, 38]. This can be viewed as the driving force for separation and is illustrated in Fig. 1.8. This additional chemical potential gradient is because chemical potential is logarithmic in concentration so a uniform increase in concentration will increase chemical potential more in regions where the equilibrium concentration is lower. The gradients of electrons and holes are in opposite directions leading to a net charge current. The subsequent separation of the electron-hole pair will result in electrical potential gradients which oppose further separation, but a net charge current still occurs if the chemical potential gradient outweighs the opposing electrical potential gradient.

For the neutral regions either side of the space-charge region in a p-n junction, the chemical potential (i.e. concentration) is uniform within each region, but different between the two sides (which at equilibrium is balanced by the built-in electric potential difference). For each carrier type, uniform illumination changes the chemical potential of one carrier type more in one region than in the other, so an additional difference in chemical potential is induced for each carrier type, which will drive carrier flow.

A built-in field in a p-n junction can be viewed as consequence of forming a chemical potential gradient at equilibrium [35]. It is the non-uniformity of the equilibrium chemical potential (specifically the concentration dependent component of it) that provides the asymmetry to drive electrons and holes in opposite directions.

Since the depletion region experiences an additional *gradient* of chemical potential under uniform illumination, it can be useful to increase the width of this region compared to the neutral regions. This is achieved by inserting an intrinsic region between the two doped regions, called a p-i-n junction. The intrinsic region has a low density of carriers and dopant ions so cannot screen the built in electrostatic and chemical potential differences between the two doped layers either side. However, in regions that are less doped, like this intrinsic layer, recombination is increased as the np product will be greater. Therefore, a wide depletion region should be avoided if recombination rate constants are high [14]. Conversely, the doping process itself may increase the recombination rate constants (more defects) and so a wider intrinsic region is favoured.

Real devices may employ both built-in fields (i.e. chemical potential asymmetry) and bandgap layers (i.e. kinetic asymmetry) to induce net flow of electrons to one side and holes to the other side. Most devices will have built in fields as the individual layers will usually have different Fermi levels, and the presence of localised states at surfaces or interfaces creates built-in fields near these surfaces interfaces.

1.3.2.6 Defects and Band Bending at Interfaces

Since this work considers processes at the interface between two materials, the physics of interfaces will be briefly summarised [39, 40], with a focus on band-bending at the interface. For a crystalline semiconductor, a surface disrupts the periodic structure causing deviations from the band structure that occurs in the bulk. For example, atoms at the surface have fewer neighbouring atoms resulting in“dangling bonds” which are localised states that can have energies in the bandgap. Furthermore, surface contamination or the presence of another material (i.e. an interface) can result in more localised states. These localised states are concentrated in a thin layer at the surface/interface. The effect of these surface/interface states can be approximated by considering an initially isolated surface/interface layer that has a different density of states distribution to the bulk and has its own Fermi level (called charge neutrality level, CNL) that may be different to the bulk

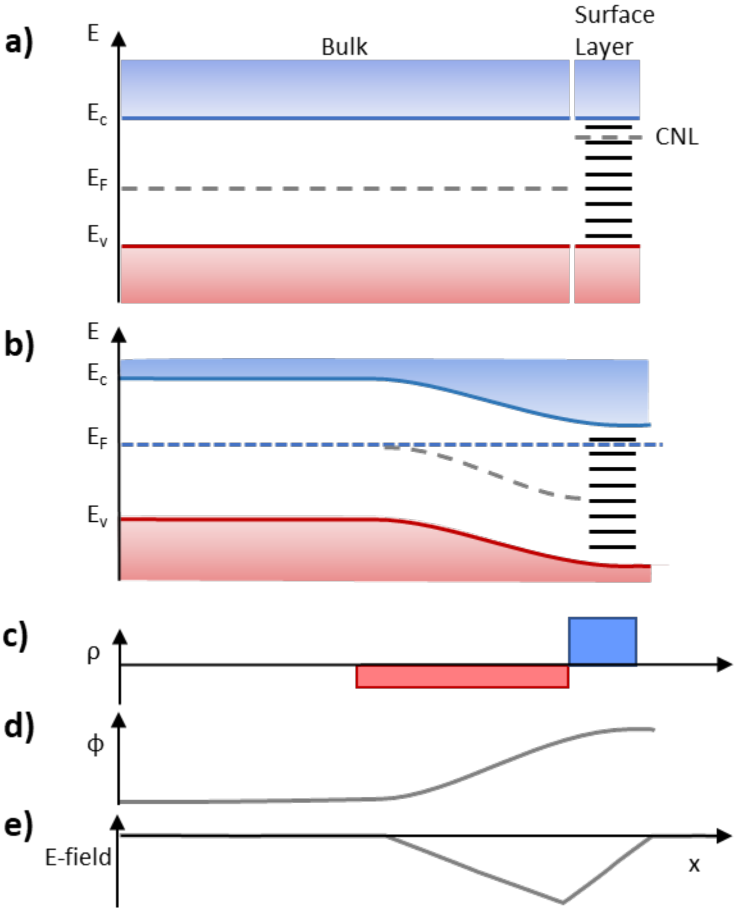

Figure 1.9: a) The bulk and the surface defect layer prior to contact, showing defects (black lines) spread over a range of energies. The electric potentials are the same but the chemical potentials are different, so the Fermi level in the bulk and the surface layer (called charge neutrality level CNL) are different. b) When contacted, electrons flow to equilibrate the Fermi-Level and the CNL, resulting in an electric potential difference that balances the chemical potential difference. c) The space charge $\rho(x)$ due to carriers being depleted leaving fixed ions. d) The electric potential profile $\phi(x)$. e) The electric field profile $E(x)$.

(see Fig.1.9). Similarly, at the interface between two materials there will be an interface layer with localised states that may be different to those for the surfaces of the separate materials, i.e. the interface is not simply a superposition of two surfaces. Both the surface layer and bulk are initially neutral, so the difference in electrochemical potential is only in their chemical potentials. When the layer is contacted with the bulk, the electrochemical potentials equilibrate by the flow of electrons resulting in a net charge in the surface layer and a charged region in the semiconductor. The gradient of electrical potential near the surface, is called band bending. Before connecting the layers, if the Fermi level of the bulk is closer to the majority band than the CNL, then there will be a depletion region near the surface, and the opposite results in an accumulation region (more heavily doped). Fermi level pinning refers to the density of interface states being very large such that the CNL does not move very far when equilibrating with the bulk, and the equilibrated Fermi level is pinned to the CNL. A metal has a high density of states compared to a semiconductor so at a metal-semiconductor junction the metal will often pin the Fermi level.

1.3.2.7 Solar Cell Optimisation

From the above it can be seen that after the thermal energy of the photons is absorbed, some is transferred to the lattice during cooling, with the remainder becoming chemical energy some of which is transferred to the lattice by non-radiative recombination and some is emitted by radiative recombination. The remainder is converted into electrical energy. It is very difficult to prevent cooling losses as this is a very fast process (although there are efforts to develop hot-carrier solar cells that extract the carriers with elevated temperatures[41]). A tandem cell comprises a cell with a large bandgap light absorber in front of a cell with a low bandgap, so that the high energy photons photons absorbed by the top cell lose less energy due to cooling to the band edge. In each individual cell, only the amount that is lost through recombination can be modified. The rate *constant* for radiative recombination cannot be modified (although changing the load will change the radiative recombination rate/current for given illumination), but the rate *constant* for non-radiative recombination can be minimised. For example, by choosing a material with a lower defect capture coefficient, or for a given material, fabricating it with a lower density of defects.

Minimising the defect density corresponds to minimising the chance of recombining at a defect whilst travelling to the contact, or maximising the average distance that carriers travel without recombining. Therefore, it can be viewed as maximising a survival length, which can be approximated with a diffusion length (the characteristic length carriers diffuse within a certain time $\sim \sqrt{Dt}$ which in this case is the recombination lifetime). Therefore the film thickness is limited to be on the order of the diffusion length or less, however it must also be thick enough to absorb most of the solar radiation, so has a lower limit of the absorption depth. As a rule of thumb, for an efficient device, the diffusion length should be greater than the absorption depth, and the thickness should be in between.

The selectivity of the contacts should also be maximised, to prevent carriers from reaching the wrong contact. When carriers reach the wrong metal contact, they effectively recombine with the opposite carrier immediately (the quasi-Fermi levels in a metal converge into a single Fermi level as there is no bandgap that inhibits equilibration). So non-ideal selectivity can also be categorised as a non-radiative recombination loss. Indeed the famous Shockley Quiesser (SQ) limit on the maximum efficiency of a single junction solar cell [20] is derived by assuming that recombination other than the unavoidable radiative recombination is eliminated, and the contacts are perfectly selective. The SQ limit is the power conversion efficiency for the case of perfect conversion of the chemical energy that remains after carriers have cooled to the temperature of the lattice. The SQ limit is at the highest level of abstraction, which means it provides minimum information on how to optimise the design [21].

Furthermore, the distribution of the defects and the transport kinetics also play a major role in determining the recombination current. It is likely that transport across an interface will be slowed compared to transport in the bulk, which will lead to a relative accumulation of carriers near this transport bottleneck during operation. This increases the recombination current in this region, so transport bottlenecks should be minimised and the defect density in the vicinity of bottlenecks is particularly important to minimise. This is why band alignment and the interface defect density are so influential.

1.4 Perovskite Solar cells

1.4.1 Overview

Having reviewed the theoretical operation of photovoltaic cells, the history and design of perovskite solar cells (PSCs) will be briefly introduced, with particular attention applied to the CTL materials employed in PSCs. This is followed by a more detailed summary of the CTL materials studied in this work, which were chosen due to their high performance and corresponding prevalence in the literature.

Organic-inorganic metal halide perovskites (MHPs) have been known about since the 1890s [42] and were studied crystallographically in the 1970s [43]. In the 1990s organic-inorganic MHPs were investigated for use in optoelectronics, mostly with 2D crystal structures which have enhanced luminescence [44, 45] compared to 3D structures (dimensionality is described later). Researchers in Japan [46, 47] first reported the successful use of MHPs as the light absorbing sensitiser in dye sensitised solar cells (DSSCs), first with $\mathrm{MAPbBr_3}$ [48] and then with $\mathrm{MAPbI_3}$[49] (where MA is methylammonium). They used MHPs with 3D crystal structures since they have a smaller bandgap and broader absorption across the solar spectrum compared to 2D structures. With a liquid electrolyte, an efficiency of 3.8% for $\mathrm{MAPbI_3}$ was achieved in 2009 [12], and then an increase to 6.5% in 2011 [50] by increasing the loading of the perovskite. However, the perovskite was quickly dissolved in the liquid electrolyte so solid state hole transporting materials were investigated [51], and efficiency jumped to 10.9% [52] by using a solid state hole transporting material, spiro-OMeTAD (and $\mathrm{MAPbI}_x\mathrm{Cl}_{1-x}$ perovskite). Spiro-OMeTAD (2,2',7,7'-Tetrakis[N,N-di(4-methoxyphenyl)amino]-9,9'-spirobifluorene) will be discussed in section 1.4.3. This device used an insulating mesoporous-$\mathrm{Al_2O_3}$ scaffold rather than the electron trasporting mesoporous-$\mathrm{TiO_2}$, indicating that the perovskite itself has a sufficiently large electron diffusion length to be used as a thicker layer rather than just a sensitiser. This led to investigations of devices incorporating a solid capping layer of perovskite on top of the mesoporous scaffold [53] or even without a mesoporous scaffold [53, 54], and now planar perovskite layers are universally incorporated (with or without mesoporous layer).

Due to their origin in DSSCs, the standard perovskite solar cell consisted of a perovskite layer as the light absorber, sandwiched between two bandgap layers, the hole and electron transport layers (HTL and ETL). Unsurprisingly, there has also been research into forming p-n homojunctions within the perovskite layer. There have been reports of p-n homojunctions in perovskite layers where doping is due to intrinsic defects, whose type and density are controlled by varying the stoichiometry [55, 56]. However, their efficacies as p-n junctions [57] and stability against ion migration has been questioned [58]. Extrinsic electronic doping by heterovalent ions has also been investigated [59], such as substituting of Pb^{2+} with Bi^{3+} [60], but Bi^{3+} was later found to detrimentally increase the defect density [61–63]. Computational studies suggest extrinsic doping will result in the formation of intrinsic defects that will compensate the extrinsic dopants i.e. the formation of intrinsic defects that dope oppositely to the extrinsic dopant [63]. Therefore, instead of p-n homojunctions, perovskite solar cells have so far relied on using bandgap layers called CTLs, to provide asymmetry. Whilst CTLs can increase the series resistance, devices without them have much worse performance [64, 65].

The broadest classification of perovskite cell structures is division into standard or inverted structures. This refers to whether the illuminated side of the cell extracts electrons (n-side) or holes (p-side). The CTLs are usually doped to enhance the diffusion length of the extracted carrier, and the perovskite layer is close to intrinsic, which leads to the names n-i-p or p-i-n for these two structures (n-i-p indicates illumination on the n-side).

1.4.2 Charge Transport Layers

The CTLs should have large bandgaps with one band energetically aligned to a perovskite band and the other CTL band offset relative to the other perovskite band in order to present an energetic barrier to extraction. The extracting CTL band may have a small offset that presents an energy barrier to back transfer from the CTL into the perovskite. However, if a carrier transfers to a band with a lower energy, it will lose some energy (ultimately emitted to the lattice), and the quasi-Fermi level of the carriers reaching the contact is reduced, and thus also the voltage. A correlation between energy offset and V_{OC} has been observed [66].

The Fermi level of the CTL should be such that it creates favourable band bending at the interfaces with the perovskite, and a large Fermi level difference between the two CTLs will create a large built-in potential difference across the perovskite layer. If the perovskite carrier density is low enough, it will not be able to screen the built-in potential difference and there will be a non-zero field throughout the thickness, like a silicon p-i-n homojunction. However, if there is a large density of mobile ions, then they will screen the field, confining the potential drop to the interfaces and leaving the bulk of the perovskite field free [57, 58, 67]. Clearly, the band energy offsets and electric potential profile in the device is crucial to performance, but measuring these is difficult and prone to errors (see section 1.4.5).

Practical considerations for CTLs include whether a uniform layer with controlled thickness can be deposited without damaging the underlying layers. A layer with pinholes allows shorting between the contact and absorber (and possibly unwanted chemical diffusion and reactions). The deposition process should not damage underlying layers, for example it should avoid using high temperatures or solvents that dissolve the underlying layer [68] (high temperature processes also increase cost and energy pay-back time). Similarly, it must be considered whether the CTL allows layers to be deposited on top, for example for solution deposition, the hydrophobicity of the underlying layer is important [69, 70]. Thus, the order of deposition is important. Deposition processes must also be scalable to be acceptably inexpensive. Furthermore, the stability to degradation of the layers under environmental conditions is a necessary requirement.

Due to their origin in DSSCs, perovskite solar cells originally employed mesoporous TiO_2 as an ETL in n-i-p cells and this has remained popular [71], as it is suggested to increase the interfacial contact, and also increase the light absorption in the perovskite by increasing light scattering. SnO_2 is an increasingly popular choice for the ETL since in their crystalline forms, SnO_2 has a higher mobility than TiO_2 (250 vs 1 cm^2/s), a wider bandgap that reduces parasitic absorption (3.8 vs 3.0 eV), and is more chemically, thermally and UV stable [72]. The fullerene molecule and its derivatives such as PCBM

([6,6]-Phenyl-C61-butyric acid methyl ester) are also commonly employed in n-i-p devices, either instead of the metal oxide or coated on top of the metal oxide. They are also frequently used for p-i-n devices, since they can be deposited on top of the perovskite without high temperature processes.

The organic molecule Spiro-OMeTAD has been the dominant hole transporting material in DSSCs since 1998 [73, 74] and similarly in n-i-p perovskite solar cells since their inception [12, 75]. Alternatives for n-i-p devices include P3HT (Poly[3-hexylthiophene-2,5-diyl]) and PTAA (Poly[bis(4-phenyl)(2,4,6-trimethylphenyl)amine]), and for p-i-n architectures, other organic HTLs such as PEDOT:PSS (Poly[3,4-ethylenedioxythiophene]: poly[styrenesulfonate]) or inorganics such as CuI, CuSCN and NiOx are used [76].

This work focusses on CTLs that can be deposited on top of the perovskite layer, so HTLs for n-i-p devices and ETLs for p-i-n devices. This means that the perovskite layer can be deposited on the same substrate for all samples, which avoids any differences in the perovskite film due to growth on different substrates. For this work, the HTL Spiro-OMeTAD and the ETLs C_{60} and its derivative PCBM are chosen due to their high performance and thus prevalence in the literature.

1.4.3 Spiro-OMeTAD

Spiro-OMeTAD is a solution processable small molecule (containing TPA, triphenylamine) which consists of two extended π systems connected by an sp^3 atom [75]. The spiro link aligns the π systems perpendicularly which increases solubility and disfavours aggregation or crystallisation (increasing T_g the glass transition temperature) [77], although it is still susceptible to crystallisation under heating [75]. Molecular alignment (crystallisation) with significant π-π stacking provides carrier pathways which are beneficial to mobility if oriented correctly, but this alignment reduces solubility and the more crystalline films have poorer interfacial contact than amorphous films [66]. However, the mobility of spiro-OMeTAD is very low as the propeller structure has large intermolecular distances and so oxidising additives have been found to be indispensable for achieving good performance [66].

There are three additives commonly used to improve performance, Li-TFSI, tBP and cobalt salts[66, 75]. Li-TFSI salt is used to induce oxidation of spiro-OMeTAD when exposed to air, which increases the p-doping [78]. This will increase the recombination lifetime for holes and thus their diffusion length. It is also suggested to increase mobility, as with optimal air exposure the mobility increased by up to two orders of magnitude, to $2 \times 10^{-2}\text{cm}^2/\text{Vs}$ [79].

The second additive, 4-tert-butyl-pyridine (tBP), was used as an additive for spiro-OMeTAD in DSSCs where it is believed to adsorb onto the TiO_2 surface reducing recombination there [80, 81]. In perovskite solar cells it is found to be a morphology controller that prevents the phase separation of spiro-OMeTAD and the Li-TFSI, which increases the uniformity of the layer [82]. It has also been suggested to p-dope the perovskite near the surface, which results in band bending at the interface which is favourable for hole extraction and thus enhances device performance [83]. However, after 1000 hours in the dark, the tBP gradually evaporates leading to agglomeration of Li-TFSI, which is hygroscopic, and so these agglomerations become voids [82]. The hydrophilic nature of spiro-OMeTAD (with Li-TFSI and tBP) [84] is also detrimental to stability of perovksite. Pinholes have actually been used to explain the performance enhancement of devices upon exposure to air, as Li-TFSI is usually concentrated at the bottom of a freshly deposited film, but upon exposure to and penetration by H_2O, Li-TFSI can redistribute and improve performance [79, 85]. However, for longer exposures pinholes accelerate degradation[86]. It has been suggested that tBP corrodes the perovskite layer[87] and reduces the glass transition temperature of spiro-OMeTAD[88].

The third type of additive is Co(III) based salts such as FK102 [89] and FK209 [90] that are used as additional oxidisers to increase the p-doping of the spiro-OMeTAD. In the rest of this thesis, spiro-OMeTAD will be referred to as Spiro for brevity.

1.4.4 C_{60} and PCBM

The fullerene molecule C_{60} and its derivatives, such as PCBM, are commonly used ETLs in both p-i-n and n-i-p devices, having previously been very popular as the electron acceptor in organic heterojunction solar cells [91]. C_{60} can be vapour or solution deposited and the derivatives such as PCBM have additional groups added in order to increase the solubility so that they can be solution deposited [92, 93] (they are also less suitable for vapour deposition as a result of reduced thermal stability [94]). In n-i-p devices, fullerenes have been used as an interlayer between metal oxides such as TiO_2 and SnO_2, and the perovskite layer[68, 95–97], or have been used as an ETL by themselves [96, 98]. In these n-i-p devices care must be taken to use solvents that do not dissolve the fullerene when depositing subsequent layers. Fullerene layers are found to quench the steady state photoluminescence (PL) intensity and accelerate the decay of time resolved PL more quickly than metal oxide [68, 96, 97], suggesting faster electron extraction. Fullerene interlayers on top of metal oxide layers are proposed to create a more favourable band alignment with the perovksite CB than without the fullerene [68, 96]. The metal oxide is proposed to act as a better hole blocker due to its wider bandgap, and has fewer pinholes that can create shunt paths [96].

Furthermore, fullerenes deposited on top of the perovskite layer in p-i-n cells are found to reduce defect densities as observed by thermal admittance spectroscopy (TAS), presumably at the perovskite surface and grain boundaries [99]. TAS also suggests that PCBM and C_{60} passivate defects with different energy levels. A combination of a spin coated PCBM layer and evaporated C_{60} layer therefore reduced defect density the most, and is also suggested to give more complete coverage. The supression of hysteresis by using fullerenes has been attributed to this defect passivation, and also the reduction of iodine migration along grain boundaries, which is thought to be the dominant migration pathway [100]. Xu et al.[101] even mixed PCBM into perovskite precursor which reduced hysteresis, and they propose the PCBM accumulates in the grain boundaries. They performed density functional theory (DFT) simulations showing that the PCBM reduced the defect density and made the defect energy level shallower. C_{60} and PCBM are both hydrophobic [102], so should enhance the stability of the perovskite layer in air by protecting it from moisture.

Both C_{60} and PCBM are observed to have energetic disorder, a tail of electronic states going into the bandgap. Shao et al [103] observed this tail in PCBM from impedance spectroscopy, and Schulz et al.[104] observed a tail of states at the VB in C_{60} by photoelectron spectroscopy. Schulz et al. suggested that the combination of the small bandgap of C_{60} (and PCBM) and the tail of states above the VB, reduces the energy offset between the C_{60} and perovskite VBs and thus may allow some hole extraction into the ETL. This will be relevant for the interpretation of the results in this work. Indeed, the wide bandgap bathocuproine (BCP) is commonly used as an interlayer between the fullerene and the electrode, possibly to increase hole blocking[105]. Furthermore, C_{60} has a bandgap of only 1.7eV so the layer thickness should be minimised, and so using an additional hole blocking layer will also help to provide a physical barrier (e.g. to avoid shorting between the perovskite and metal contact, or chemical ingress).

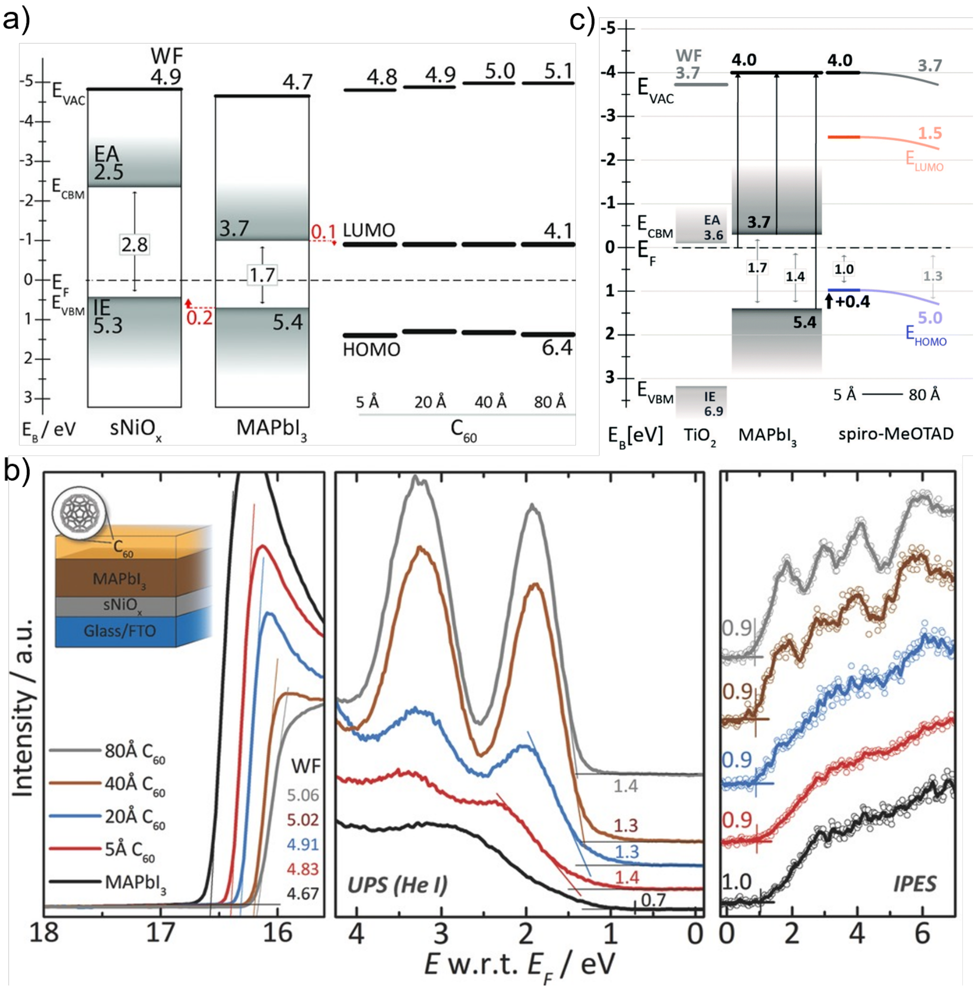

Figure 1.10: a) The band alignment of C_{60} deposited incrementally on $MAPbI_3$, derived from photoelectron measurements, b) The ultraviolet PES spectra (left and middle) and the inverse PES spectra (right) for C_{60} grown on the device stack shown in inset. A significant tail of states above the valence band edge is observed. c) The band alignment derived from photoelectron measurements of Spiro-OMeTAD deposited incrementally on $MAPbI_3$. Reproduced from refs. [106] and [104].

1.4.5 Band alignment

The alignment of the perovskite and CTL bands is crucial to the device operation and to the interpretation of the data presented in this work. The band energies relative to the Fermi level are commonly measured with photoelectron spectroscopies (PES), but predicting the band alignment of different layers from measurements of individual layers is very unreliable, for example due to the presence of interface dipoles. Instead, band alignment at buried interfaces can be measured by incremental deposition of the layers, and early works by Schulz et al. confirmed that Spiro[106] and C_{60} [104] have energy bands that are well aligned for the extracted carrier and have large energy barriers for the other carrier (see Fig.1.10). Helmman et al. [107] performed incremental deposition and compared dark and illuminated conditions to identify where band bending occurs, and found it was always at the HTL interface, which is consistent with their observation that the perovskite is n-doped. They further showed that when the HTL is Spiro, the band bending is inside the Spiro layer itself (they co-deposited Spiro-OmeTAD and the additive Li-TFSI), and when the HTL is NiOx, the band bending is in the $MAPbI_3$. However, the properties of the perovskite layer have been shown to be very sensitive to fabrication conditions (see section 1.5), and so the results observed for incremental deposition are not necessarily representative of samples fabricated by other methods. An alternative to incremental deposition, is cross-sectional measurements, which due to the low spatial resolution of PES require tapered cross-sections[108]. Cross-sectional PES can map the electrostatic potential through the film by looking at the energy shifts of emission peaks for individual elements. Again, the band bending is found to be inside the Spiro layer in the dark, and the perovskite layer is n-type [108].

Electron beam induced current (EBIC) cross-sectional maps have also been used to try to understand the electric potential profile and thus operating mechanism of perovskite

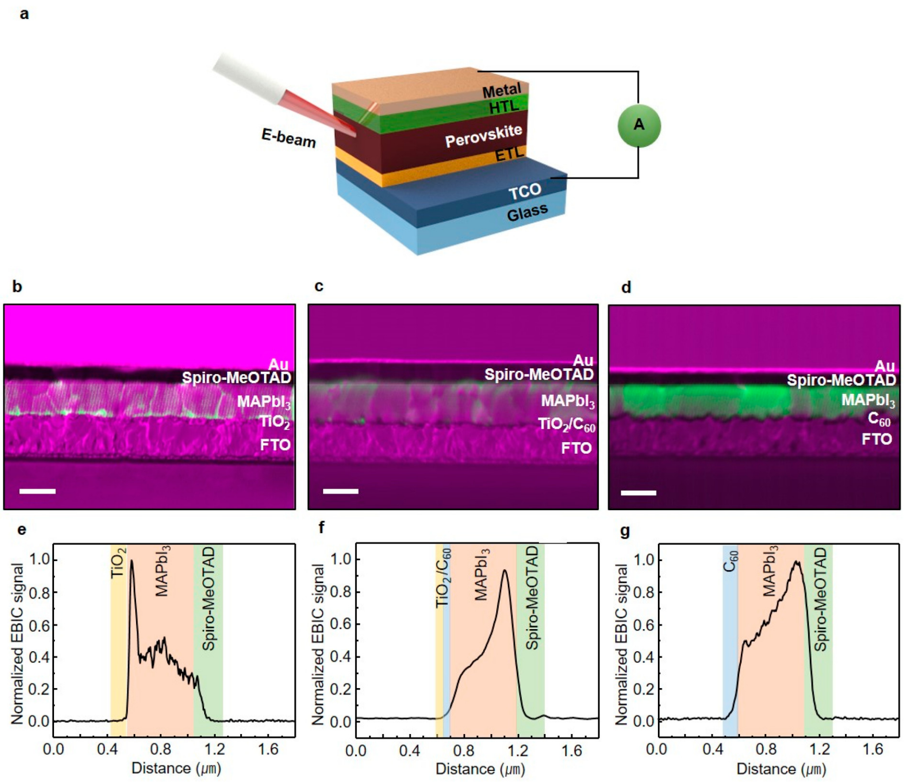

Figure 1.11: Cross-sectional electron beam induced current (EBIC) measurements of different device stacks. a) A schematic of the technique. b)-d) Maps of the induced current (green) for different devices stacks. e)-g) Line profiles of b)-d) showing a significant difference between devices with and without C_{60} layers. Reproduced from ref. [109].

solar cells. It maps the current extracted for electrons injected at different positions, and large currents are attributed to gradients in electric potential in the region of injection, so this is an indirect way of measuring the electric potential. Some work[110] has suggested that there are spikes in current extraction, and thus band bending, near both CTL interfaces (although the efficient extraction could just be correlated with proximity to the interface). Byeon et al. [109] (see Fig.1.11) showed slightly different results: extraction is greatest for injection near the TiO_2 interface only, and then switches to the spiro-OMeTAD interface when TiO_2 is replaced with C_{60}. This highlights that there are variations in the literature. Edri et al.,[110] showed that removing the HTL reduced extraction efficiency for carriers injected near the hole contact, highlighting the importance of the HTL for extracting holes and blocking electrons. A limitation of EBIC is that it cannot measure dark conditions, and cannot simulate illumination through the transparent conducting oxide (TCO) layer as would occur in operation. It has also been shown to induce degradation during the line scanning process.

Kelvin Probe Force Microscopy (KPFM) cross-sections can measure the variation in electric potential through the device, for both dark and illuminated conditions [109, 111–115]. It should be noted that KPFM is very sensitive to surface band bending, and

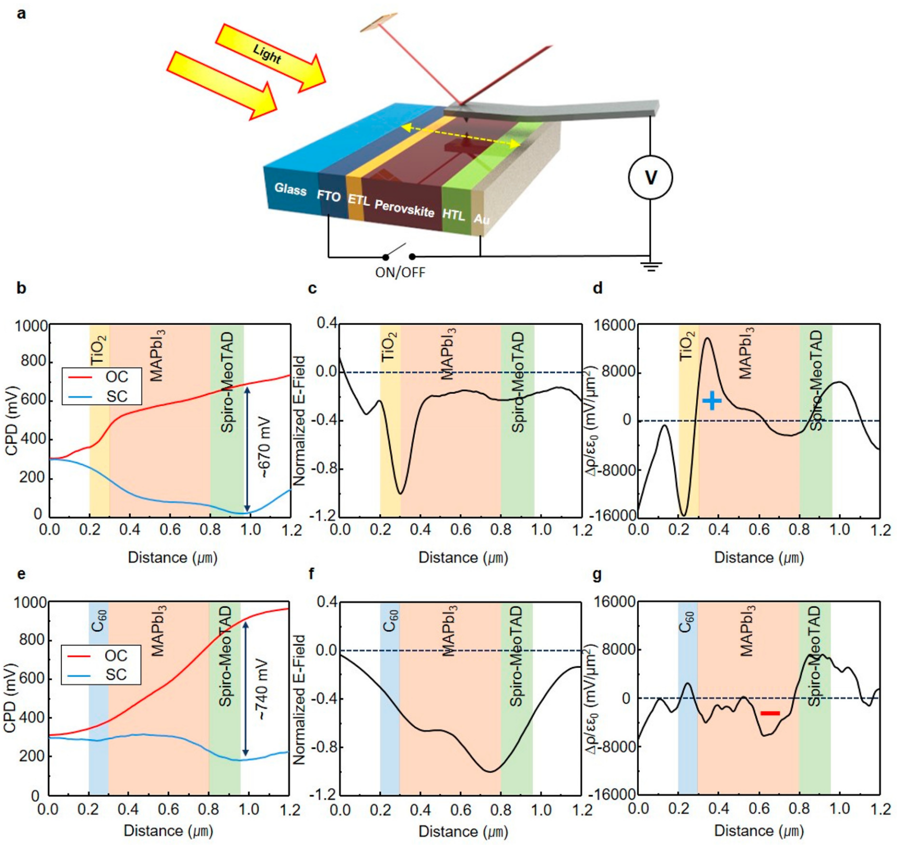

Figure 1.12: Cross-sectional Kelvin probe force microscopy (KPFM) measurements of different device stacks. a) A schematic of the technique. b),e) The measured contact potential difference (CPD) under illumination for open-circuit (OC) and short-circuit (SC) conditions, for two device stacks. The CPD is depends on the local work function, and thus maps the electric potential. c),f) The E-field for OC conditions, calculated from the gradient of the CPD at OC. d),g) The charge distribution calculated from the difference between the CPD for OC and SC conditions. Reproduced from ref.[109].

thus depends on the preparation of the surface and atmospheric contamination, which may vary across the surface being measured. The potential profile in the dark indicates where the built in fields are located, and the change in the profile between dark and illuminated conditions can indicate accumulation of charge under illumination. Byeon et al. [109] performed both EBIC and KPFM (see Fig.1.12) for devices with spiro-OMeTAD as the HTL, and either TiO_2 or C_{60} as the ETL. They concluded that with TiO_2 there is band bending at the TiO_2 interface, which at open circuit accumulates charges, whereas with C_{60} the band bending and open-circuit charge accumulation is at the spiro-OMeTAD interface. Early works did not consider the possibility of changes in ionic distribution when illumination or circuit conditions are changed, and thus considered the charge accumulation to be unbalanced of extraction of electrons and holes. Later works have been able to show that the time scale for accumulation is indicative of ion migration instead[113, 116, 117]. This ion migration has been used to explain hysteresis in J-V scans, as the transport, extraction and recombination of electrons and holes will change when the electric potential changes due to ion migration. This highlights that perovskite solar cells do not have fixed electric profiles as for silicon, but rather depend on the history of previous conditions. Therefore, due to ion migration, the electric profile during operation is difficult to predict.

Overall, whilst coarse estimates of the band alignment and band bending between the perovskite layer and the CTL can be made (i.e. similar band energies or large offsets), more precise estimates are difficult as the measurement techniques are very sensitive to the particular conditions and must be performed and interpreted carefully. In particular, the presence of ion migration complicates interpretation, and the poor reproducibility of samples limits the ability to apply conclusions from one study to others.

1.5 Metal Halide Perovskites

Having introduced perovskite solar cells and the crucial CTL materials, the properties of the metal halide perovskite material itself will now be reviewed, with particular attention to the properties that are relevant to PV cells and the optical spectroscopy measurements employed in this work.

1.5.1 Crystal Structure

Perovskite is the name of a crystal structure first observed in the mineral $CaTiO_3$ [118], and it is one of the most common structures for ternary and quarternary compounds [119]. These compounds have the formulae ABX_3 and A_2BCX_6 and consist of corner sharing BX_6 octahedra (a B anion surrounded by 6 X ions), and a single A cation occupying the (12-fold coordinated) gaps. The charge of the cation balances the charge of the octahedra. The highest symmetry perovskite structure is cubic, but the symmetry can be lowered by rotations or distortions of the BX_6 octahedra or translations of the A or B site cations[120]. For example, $MAPbI_3$ (where MA = methylammonium) is cubic above 330K, tetragonal between 160 and 330K, and orthorhombic below 160K [120, 121]. All perovskite crystals have the same network topology but the degree of tilting and distortions of the octahedra may vary[119]. The combination of elements that can assume this structure is principally constrained by steric factors and charge balance [118].

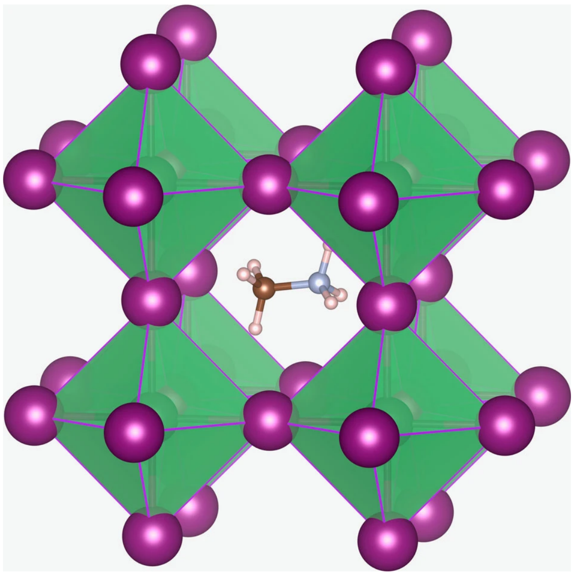

Figure 1.13: The structure of $MAPbI_3$: purple spheres are iodine atoms in the X-sites, the green octahedra surround lead atoms in the B-sites, and the methylammonium cation occupies the A-sites. The figure is reproduced from ref. [122].

For organic-inorganic metal halide perovskites, the X-anion is a monovalent halide ion, the A-cation is a monovalent organic cation and so a divalent B-cation satisfies charge balance, usually either Pb or Sn. Alternatively, a B-cation that can have the charge states +1 or +3 can occupy alternate B-sites to satisfy charge balance, and in a similar manner a quarternary compound (double perovskite) contains two B-cations with +1 and +3 states respectively.

Regarding steric factors, considering the ions to be rigid spheres, Goldschmidt [123] proposed that ions in perovskite structures arrange so that "the number of anions surrounding a cation tends to be as large as possible, subject to the condition that all anions touch the cation" [124]. This has been termed the "no-rattling" principle, i.e. that the spheres are just touching with no room to move. It corresponds to conditions on two dimensionless factors that are functions of the ionic radii, the tolerance factor and the octahedral factor. The tolerance factor must be $t < 1$, with cubic structures occurring for $0.9 < t < 1$ and lower symmetry structures for $t < 0.9$ [125]. Indeed it is empirically found that most 3D perovskites have a tolerance factor of $0.8 < t < 1$ [118]. Predicting the existence of compounds based off these steric factors has been shown to be 80% accurate [119]. This work focusses on 3D perovskites with the structure described as above, but other dimensionalities exist, such as 2D perovskites in which the network of corner-sharing octahedra is interrupted by sheets of organic cations, leaving sheets of octahedra networks that can be one or more octahedra thick, referred to as n=1,2,3, etc. (3D corresponds to $n = \infty$).

1.5.2 Composition – Bandgap Tuning and Stability

$MAPbI_3$ and $MAPbBr_3$ were the first perovskites to be used in DSSCs and the best efficiencies were for $MAPbI_3$, which is partly due to its smaller bandgap (1.57 vs 2.29eV)[90] absorbing more of the solar spectrum. Attempts to alloy the halides were reported soon after, and stable phases across a wide range of alloying ratios could be formed with a continuously varying bandgap energy, both with MA [90] or with FA (formamidinium) as the A-site cation[126]. This range includes the ideal value for the top layer in a 2-layer tandem (and for layers in tandems with even more layers) [127, 128]. FA based perovskites were found to have a lower bandgap (1.47eV)[129, 130], closer to the optimum for single junction cells, and also have higher stability to heating than MA (but not moisture)[131], as MA appears to be quite volatile and more acidic so more prone to react with iodine [132]. However, the perovskite phase of $FAPbI_3$ that is stable at annealing temperatures is only metastable once cooled to room temperatures, so gradually converts into a non-perovskite phase, which is accelerated by humidity [121, 125, 131]. This highlights that phase stability can be a more serious weakness than chemical reactions. This phase instability has been attributed to the larger FA cation giving a tolerance factor that is too large [125].

Alloying FA based perovskites with smaller A-site cations such as Cs can tune the tolerance factor,[125] reducing the phase transition temperature and thus increasing the stability of the perovskite phase at room temperature, which also makes it less sensitive to moisture. The alloying of Cs or MA into FA based perovskites has also been suggested to modify the interaction between the A-site cation and the octahedra [133, 134], and the enhanced stability of the perovskite phase is also attributed to entropic stabilisation[135]. Alloying the A-site cation also varies the bandgap. One of the most stable compositions $Cs_{0.05}(FA_{0.83}MA_{0.17})_{0.95}Pb(I_{0.83}Br_{0.17})_3$, commonly referred to as “triple cation”, is used in this work as it has been widely used in research due to its phase purity, temperature and humidity stability, and reproducibility [136]. Nuclear magnetic resonance (NMR) studies have confirmed Cs is incorporated into MA and FA based perovskites[137], whereas other dopants such as K and Rb are not.

For the pure inorganic halide perovskites using Cs cations, the smallest bandgap for lead-based materials is E_g=1.73 eV for $CsPbI_3$ (so suitable for tandem cells) and has been used to make PV cells[126]. However, similar to $FAPbI_3$, the perovskite phase of $CsPbI_3$ is only stable at high temperatures[125, 138], which in this case is due to the small Cs cations giving a tolerance factor that is too small.

1.5.3 Fabrication

A large variety of methods can be used to form perovskite materials in different forms, such as powders, nanocrystals, polycrystalline films, or single crystals. For present designs of PSCs, a thin film is required, and the most common methods are either solvent based or vapour based [139], or a combination of both [140]. Research laboratory devices have active areas on the order of 1cm^2 but commercial devices require uniform fabrication of larger areas and many solution or vapour based methods have been employed [141]. The morphology of the films have an enormous impact on the performance of the device, as incomplete coverage, small grains and non-uniform thickness are detrimental.

The simplest technique for fabricating lab-scale films is spin-coating, in which a solution containing dissolved components of the perovskite compound (a precursor solution) is dropped onto a spinning substrate so that the precursor solution has continuous coverage over the substrate. Crystallisation of the dissolved components may occur upon contact with the substrate, which provides nucleation sites, or may be delayed until the substrate is annealed. In either case, annealing will evaporate the solvent causing the solution to saturate and crystallisation to occur. Solvent based processes can be either one step, in which all the components are dissolved in a single solution, or two step, in which a solution containing the metal halide is spin-coated first to form an inorganic framework, followed by deposition of an organic-halide solution to form the final perovskite composition.

A significant increase in performance can be attributed to an improvement to the one step method, called anti-solvent quenching [142, 143]. The components are dissolved in solvents such as DMF, DMSO and NMP that form intermediates with the components preventing them from crystallising upon deposition. Consequently, this initial deposition results in a layer of this intermediate coating the substrate, and then whilst the substrate is still spinning, a solvent in which the components are not soluble and is miscible with the precursor solvent, called anti-solvent, is dropped onto the substrate reducing the solubility of the components so that they crystallise. This sudden and uniform drop in solubility results in crystals that cover the entire substrate, with a more uniform size distribution.

This highlights that interactions within the precursor solution have an enormous impact on the resulting thin film, and a wide range of solvents and additives have been used to control this[143], and even the atmospheric humidity[131]. Many of the highest performing MA based perovskites in the early years were fabricated with Cl in the precursor, and this has been attributed to it modifying the crystallisation process and thus morphology[144]. Furthermore, Buin et al. [145] found that using $PbCl_2$ and $Pb(Ac)_2$ in the precursor solution instead of PbI_2 reduces defect density, which they attribute to the removal of lead-iodide complexes from the solution, which would otherwise template for certain defects in the crystalline structure. Controlling the concentration of colloids in the solution by using hydrohalic acids has been shown to influence the size of the grains [146].

In addition to polycrystalline films, single crystals can be grown [147]. Single crystals have much lower defect densities and lack grain boundaries[148], so might be expected to perform better than polycrystalline devices, but less research has been done since they are not as quick and simple to fabricate. They still cannot be made as thin as polycrystalline films [149], but they have longer diffusion lengths so the upper limt on thickness imposed by the diffusion length is not as strict. Efficiencies are improving but may be limited by high density of surface defects, shown to be 6x higher than for polycrystalline [149].

Solid fabrication routes, such as grinding together powders of the components, can be used to ensure that there is no solvent residue in the final material and are useful for studies such as solid state NMR [150], and have even been used to make devices [151].

1.5.4 Computational Studies - Band Structure and Defects

Computational studies of perovskite structures, are vital for interpreting the origin of experimentally observed properties and behaviours. The band structures of MHPs have been simulated by density functional theory (DFT) and there is a consensus that the VB is dominated by the 5p orbitals of iodine with a smaller contribution from Pb $6s^2$ orbitals, and the CB is dominated by the Pb 6p orbitals[152].

The accuracy of the computational simulation depends on the implementation of DFT. Even et al. [153] and Du et al. [154] propose that the agreement between bandgaps measured experimentally and those calculated by GGA/LDA (generalised gradient ap-

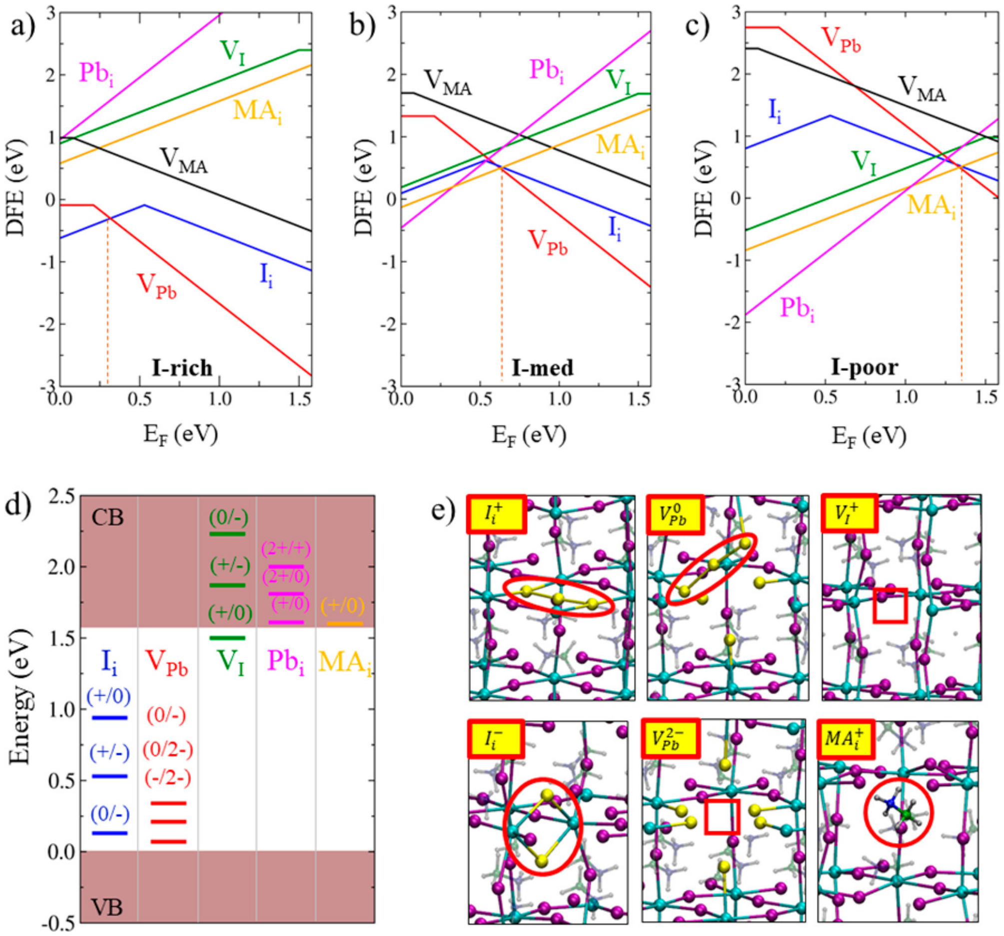

Figure 1.14: a),b),c) Defect formation energies (DFEs) calculated from DFT using the most accurate version of DFT for this calculation (HSE06-SOC with $\alpha = 0.43$, including dispersion corrections through the DFT-D3 method, for a 2x2x2 super cell with PA corrections), for three different conditions. d) The calculated thermodynamic ionisation (transition) levels. e) Structures of some of the defects. Reproduced from ref. [155].

proximation/local density approximation) versions of DFT is due to the cancellation of the bandgap overestimation by excluding spin-orbit coupling (SOC) and the bandgap underestimation by using GGA/LDA. A more severe consequence of this inaccuracy is that the positions of the CB minimum (CBM) and VB maximum (VBM) are calculated as higher in energy than they should be, so the positions of the defect state transition levels (defined below) relative to the band edges - and thus the character of the defects - are incorrect. SOC is usually left out as it is computationally expensive, but it has a significant effect due to the heavy Pb and I atoms[152–154].

Non-radiative recombination occurs via defect states in the bandgap and many different ways of reducing non-radiative recombination have been reported, from modifying the composition or fabrication conditions discussed above, to the inclusion of additives such as potassium [156] or post-deposition surface treatments such as Lewis bases [157, 158]. Computational studies are important for understanding how these modifications change the defect density or type, and provide guidance on further improvements. For intrinsic point defects such as vacancies, interstitials and anti-site defects, DFT has been used to calculate the defect formation energies (DFE), which depend on the chemical potentials of the constituents (i.e. concentrations) during film formation, and so multiple conditions e.g. I-rich vs I-poor are simulated. The defect formation energy is also a function of the Fermi level of the material and the Fermi level that the material actually assumes (native Fermi level) is taken as the one which gives overall charge neutrality. Therefore, the doping of the perovskite is related to the prevalence of different point defects. The most common defect types for the chosen processing conditions are those with the lowest formation energy at the native Fermi level that is calculated.

The transition levels of the defects are also calculated, which are the values of the Fermi levels at which the defects would change charge state by capturing or releasing an electron when the Fermi level is varied. A transition from charge state a to b is denoted (a/b). As mentioned previously only transition levels near the middle of the bandgap facilitate recombination by capturing an electron and hole, whereas transition levels close to the band edges will capture only one type of carrier.

Through a detailed comparison of different approaches to DFT simulations, Meggiolaro and de Angelis [155] identify best practice for estimating the DFEs, and summarise the results for $MAPbI_3$ in I-rich, I-poor and I-medium conditions, which are shown in Fig. 1.14. These predictions are compared to experimental observations in order to assess their accuracy. Under I-rich conditions, the most stable defects (low DFE) are positively charged iodine interstitials I_i^+ and lead vacancies V_{Pb}, which pin the Fermi level closer to the VB giving p-doping. Credibility for these predictions is provided by the fact that the same calculations predicted that the presence of I_2 molecules at the surface and in the bulk should form the same defects and thus p-doping, and this p-doping was experimentally observed for exposure to I_2 gas [159, 160]. The positive $\mathrm{I_i^+}$ can trap electrons $(+/0$ transition) forming a neutral interstitial, but this is associated with lattice rearrangements making it a metastable state which it inhibits recombination. This agrees with the observation that defects can trap electrons for a long time leading to hole doping [161], and resulting in PL lifetimes that are much shorter than the photoconductivity lifetimes[162, 163], as the electron trapping quenches PL, but leaves holes which provide photoconductivity. The low formation energy of lead vacancies implies a tendency to form metallic lead, which has been observed by x-ray photoelectron spectroscopy (XPS) for illuminated or heated samples [164]. The deeper transition levels of $\mathrm{V_{Pb}}$ defects have low cross-sections, which reduces their detrimental effect on performance.

Under I-medium conditions, the most stable defects are also iodine interstitials (but negatively charged $\mathrm{I_i^-}$) and lead vacancies ($\mathrm{V_{Pb}}$), with the addition of positive MA interstitials $\mathrm{MA_i^+}$, which together also p-dope the perovskite. Under I-poor conditions, the most stable defects are the same as for I-medium, but the Fermi level is pinned to give n-doping.

Overall, it is predicted that in $MAPbI_3$, iodine interstitials will dominate recombination, with some contribution from lead vacancies. Neutron diffraction studies show that disorder is due to iodine interstitials [165], confirming that this type of defect is common.

Du et al. [154] (also using hybrid with SOC) predict that Br and Cl atoms prefer to substitute an interstitial I atom rather than substituting a lattice I atom. Br and Cl interstitials are predicted to have transition levels which are closer to the VB (more shallow) meaning there are fewer deep traps which would explain the increased PL lifetimes for Br doped samples reported in that paper[166], and may contribute to improvements by Cl doping, although Cl has also been shown to impact the crystallisation and thus morphology[144]. This mechanism may be relevant to the high performance of triple cation compositions that employ a fraction of Br at the X-site.

1.5.5 Photostability - Single Halides

One of the most concerning properties of MHPs for use in optoelectronics is the modification of their properties under illumination, such as a change in photoluminescence intensity, or for mixed IBr compositions, segregation into different phases. These effects are very important for the optical spectroscopy techniques used in this work.

For pure ternary compositions such as $MAPbI_3$ (where no phase segregation is possible), whether PL emission intensity increases or decrease under illumination has been shown to be sensitive to the atmospheric environment and illumination wavelength, and is found to be partially reversible. An example is of this effect is shown in Fig.1.15. There is consensus that PL enhancement is strong in the presence of oxygen, and the enhancement is removed by switching to oxygen-free atmosphere such as nitrogen or vacuum [167–170]. This suggests that a photochemical reaction with oxygen passivated defect states and that this reaction is partially reversible. One simulation showed that oxygen leads to oxidation of negative iodide interstitials I_i^-, forming iodine compounds, but this is only weakly favoured hence the reversibility [155, 171]. Importantly, it shifts the 0/- transition 0.25eV closer to the VB, reducing its recombination effect. Another simulation study showed that the formation of superoxide species (compounds containing O_2^-) under illumination can passivate defects [169, 170]. However, other work argued that these superoxide species can also trigger gradual degradation of the perovskite[172, 173].

The effect of moisture on PL has less consensus, with lab air containing moisture either enhancing PL[169], quenching PL [168], or having no effect [167] in different reports. Moisture has been found to form hydrates at the surface [174], which may affect the defect density at the surface. Whilst water and oxygen may modify the defect density over seconds and minutes, both oxygen [172] and [173] and moisture [175] have been found to degrade the perovskite over longer time scales of hours and days.

Quitsch et al. [176] reported that PL intensity grows whilst illuminated with wavelengths above 520nm, but PL decreases when illuminating with wavelengths below 520nm (in lab air and even with a PMMA capping layer). This threshold is similar to the absorption edge of PbI_2, so they propose light absorption by residual PbI_2 leads to degradation, possibly by generating I_2 since I_2 gas was found to degrade the perovskite [177].

Photoinduced changes occur even in vacuum, where the role of oxygen and water can be excluded. Motti et al [178] have proposed that there are competing PL enhancement and decline mechanisms, that are related to long lived carrier traps and iodine chemistry, and involve ion migration. Under vacuum, the evolution of PL intensity under continuous wave (CW) illumination was observed to depend on temperature which suggests thermally activated processes are responsible for both PL enhancement and decline. Similarly, the PL intensity was observed to depend on the repetition period of pulsed illumination, growing under low duty cycles or declining for higher duty cycles. This shows that there are competing mechanisms. The dark period of 1ms for low duty cycles is longer than the observed trapping lifetime of a carrier, so the effects cannot be attributed to cumulative

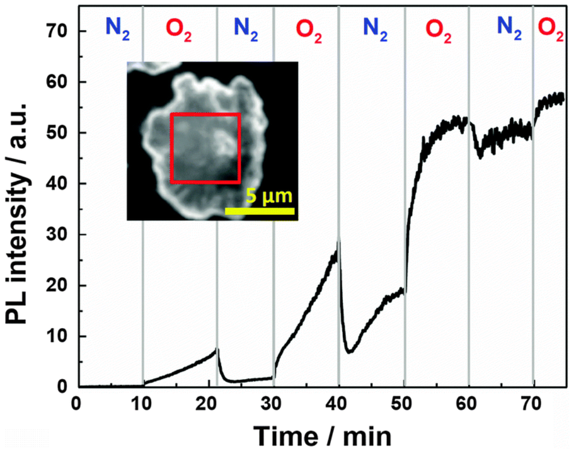

Figure 1.15: The PL intensity from MAPI$_3$ illuminated at 0.2Wcm^{-2} is switched between N$_2$ and O$_2$, highlighting the dependence on exposure history. Reproduced from ref. [167].

saturation of carrier traps, and is instead attributed to a process involving ion migration. Computational studies suggest a possible mechanism, whereby electrons can remain trapped in iodine defects for long times, and that this can induce annihilation of Frenkel defects (which will reform slowly in the dark, meaning the effect is cumulative). The competing PL decline mechanism is enhanced for higher temperatures, higher duty cycles of illumination, shorter wavelengths (including for MAPbBr$_3$ for which the bandgap of PbBr$_2$ is too large to absorb suggesting PbI$_2$ is not dominant cause in MAPbI$_3$), and for one sided illumination (which is known to drive halide segregation [179]). This suggests PL decline also occurs by mechanism involving ion migration, and that a higher density of occupied electron traps favours PL decline. Computation suggests a possible mechanism, whereby the encounter of two occupied electron traps will form I$_2$, which is stable when at the surface where there are undercoordinated Pb ions, so will migrate to the surface leading to further defect formation in the bulk, thus degrading the perovskite and PL intensity. This proposed mechanism is supported by the observation that passivation of the surface by oxygen containing molecules such as PEO is found to eliminate the PL decline effect. This coincided with a reduction in the release of I$_2$ into hexane, implying a reduced migration of I$_2$ to the surface due to passivation of surface sites by the PEO. This work highlights that measurements are sensitive to atmosphere but also the illumination conditions, and the history of exposure.

1.5.6 Photostability - Mixed Halides

Mixed I-Br compositions are appealing due to the ability to tune the bandgap energy to the optimum for the top cell in a tandem device. However, a photoinduced change particular to mixed I-Br compositions is the tendency for the original PL peak to diminish whilst a new lower energy PL peak emerges under illumination (see Fig.1.16), which was first reported for pure MA compositions[180] and then for pure FA compositions [181]. There is a consensus that this is due to the mixed halide material segregating into small volumes of I-rich composition that have a smaller bandgap, and thus carriers will collect in this region (specifically holes due to a raised VB[106]), meaning that radiative recombination is enhanced in these regions and reduced elsewhere. The smaller bandgap of these regions

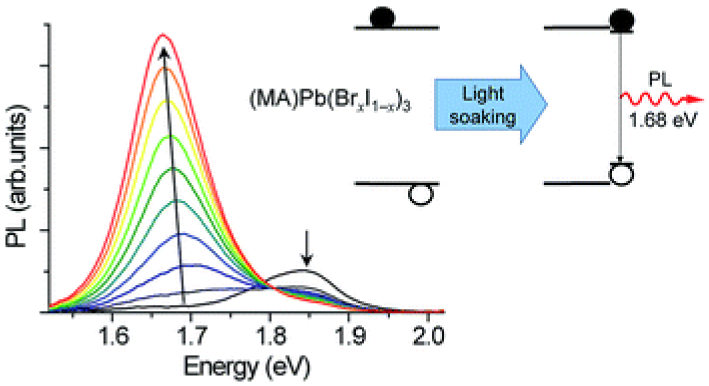

Figure 1.16: The PL spectra for a MAPb(I$_x$Br$_{1-x}$)$_3$ film with $x = 0.6$ (over 45 s in 5 s increments under 457nm, 15 mW cm^{-2} light), and the proposed mechanism of segregation into I-rich regions with a raised valence band (VB) from which low energy PL is emitted. Reproduced from ref. [180].

means the new PL peak is at a lower energy - this is the characteristic fingerprint of segregation. This photoinduced effect has been found to be mostly reversible in the dark. Segregation into phases with different halide composition must occur by halide migration, and indeed the migration of iodide ions under illumination has been directly observed [182] and computational studies predict the halide ions have lower barriers to migration than other ions [122, 183–186]. Alloying of the A-site cation that improves the crystal stability and crystalline quality appears to also increase the stability against segregation [146, 187–189]. In this work, triple cation compositions are used which are less susceptible to phase segregation and indeed segregation was not observed.

The driving force for this segregation is debated, but several works have attributed it to the presence of photoexcited carriers rather than heating [179, 190–195]. This is supported by the observations that electrical injection induces segregation[196], and segregation is reduced by increasing the extraction rate of carriers out of the perovskite in a full device[197].

Knight et al.[198] proposed a mechanism for segregation that explains the observed dependence on illumination conditions. The sensitivity of the perovskite surface to the surrounding atmosphere will also be present for mixed halides and so will overlap with attempted observations of segregation, complicating the interpretation and leading to varied results. The authors attempted to distinguish these two phenomena in their work. They observed that when alternating between 15 seconds of illumination and 30 minutes in the dark, the I-rich PL peak grows under illumination but disappears in the dark, consistent with the literature. Vacuum and air environments gradually decrease and increase the PL intensity respectively over multiple cycles (both the I-rich and the Br-rich PL peaks), consistent with trends seen for pure halides. Under nitrogen or a thick PMMA coating in vacuum, the PL intensity remains stable over multiple cycles (PMMA does not suppress changes as efficiently under air, indicating some permeability). Therefore, the authors focussed on PMMA coated samples in vacuum to exclude atmospheric effects. They photoexcited the sample with CW illumination of different intensities and for different times to achieve the same total number of photons for each intensity, and found segregation (as measured by PL peaks) was greater for low intensity illumination. Consequently they propose segregation is driven by carrier trapping, since a larger fraction of the photoexcited carriers will be trapped for low intensity illumination as the steady state carrier densities are lower. By considering this mechanism, plots of the segregation degree versus illumination time for different intensities can be scaled to have the same curve for all intensities (featuring a delayed onset and saturation at long times), lending credence to their hypothesis. In the literature, segregation behaviour under pulsed illumination appears to be sensitive to parameters of the pulse sequence such as pulse repetition rate[184], but here the authors show that this can be explained by the fraction of carriers that are captured by traps. They propose that it is electrons that are trapped as long-lived electron trapping has been observed [161] and predicted by computation [155]. Furthermore, they propose that the formation of I-rich region leads to positive feedback, as the higher VB of I-rich regions funnels holes into these regions and away from trapped electrons, and segregation is driven by the local electric fields of the separated carriers. Belisle et al.[199] also propose that carrier induced electric fields drive halide migration, suggesting that net trapping of electrons in surface states creates such fields.

1.5.7 Atmospheric and Chemical Stability

The largest barrier to deployment of perovskite solar cells is the stability of the material. As mentioned previously, thermodynamic structural instabilities are a serious problem for some compositions, but even for thermodynamically stable compositions, degradation can be induced by heating, illumination or environmental molecules such as water and oxygen, or a combination.

There are reports that moist atmospheres cause reversible formation of hydrated phases in the dark[174], but irreversible degradation under illumination[200, 201], and that illumination without moisture hardly causes any degradation over long periods[201]. This suggests that illumination and moisture work together to cause degradation. Condensation of water however does cause irreversible degradation[174], so the material is not stable to humidity over longer timescales even in the dark[175]. Ahn et al. [201] showed that irradiating the perovskite with positive N_2 ions or negative H_2 ions in the dark does not cause degradation unless moisture is present, suggesting that it is the combination of excess charge and moisture that causes this degradation mechanism, rather than photons. They propose the mechanism involves two steps: first there is reversible hydration, then the local electric field of the trapped charges causes lattice distortion which triggers irreversible degradation. They also found that the combination of oxygen and charged ions without moisture does not cause degradation, although the presence of oxygen does accelerate degradation by the combination of moisture and charged ions. Ahn et al. also found that a mixed $MA_{0.6}FA_{0.4}PbI_{2.9}Br_{0.1}$ composition degrades more slowly, again showing the improved stability of certain alloys.

This degradation by trapped charges is also proposed to explain the observation that applying an electric field using contactless electrodes does not induce degradation, but in a device degradation is observed to occur at the interface to the CTLs, as there will be a high density of trapped charges at the interface[201]. Furthermore, for a ETL-HTL pairing of TiO_2 and Spiro, degradation is at the TiO_2 interface, but for a pairing of C_{60} and Spiro the degradation is at the Spiro interface, which suggests C_{60} reduces the density of interface defects and/or has faster extraction of carriers than TiO_2. This degradation pattern was also observed by Byeon et al [109], who compared KPFM measurements at open and short circuit to reveal charge accumulation at the interfaces.

In addition to atmospheric molecules, the other layers in a full device can contribute to perovskite degradation as halides react with metal electrodes (Al and Ag are more reactive than Au) and spiro-OMeTAD allows metal diffusion into the perovskite[202]. Yang et al. [184] and Christians et al. [200] both found that spiro-OMeTAD made perovskite degradation in humid atmospheres worse, and Yang et al. found that removing the Li-TFSi additive helped stability.

1.5.8 Grains

Thin films used in solar cells are polycrystalline so have grain boundaries which may impact performance. Microscopic measurements have found that PL intensity varies between grains[203], even for wide field illumination[204], but is homogeneous within grains. This has been attributed to variations in defect density between grains and inhibited transport across grain boundaries, although the ease of transport across grain boundaries has been found to vary. Chen et al. [140] proposed that during annealing MAI evaporates from grain boundaries leaving PbI_2 phases, and ultraviolet photoelectron spectroscopy (UPS) measurements showed that PbI_2 has a higher CB and lower VB than $MAPbI_3$ (type-I junction), so forms an energy barrier to both electrons and holes. Time-resolved microwave conductivity (TRMC) studies of films with different grain sizes also find that grain boundaries limit in-plane transport of carriers (but do not increase non-radiative recombination)[163]. Therefore, to avoid the formation of boundaries to vertical transport, it is desired to form films with grains that are large enough to extend through the entire thickness of the film.

The literature has conflicting conclusions whether grain boundaries are detrimental[204] or beneficial[203, 205, 206] or neither[207]. Grain boundaries are expected to have dangling bonds and therefore a large concentration of point defects and they also provide pathways for external species to enter and possibly cause degradation. Indeed, grain boundaries have been observed to be a starting point for degradation[201], and provide pathways for ion migration[100]. The observations that polycrystalline films have higher trap densities[208] than single crystals[148] and that PL is dimmer at grain boundaries[204] have led to the belief that grain boundaries have higher rates of non-radiative recombination. On the other hand, in other polycrystalline materials used in PV, such as CdTe and CIGS, the grain boundaries are found to be beneficial by enhancing minority carrier collection[209, 210], as band bending at the grain boundaries attracts one carrier type and repels the others reducing the recombination rate. Several papers observed band bending at grain boundaries in perovskites, which they propose has a similar beneficial effect[110, 140, 203, 205, 206]. Yun et al. [206] performed contact-atomic force microscopy (c-AFM) measurements and found that under illumination the current is larger at the grain boundaries (and not correlated to height), so they are providing efficient charge collection pathways. The grain boundaries themselves therefore may not have higher recombination, but local PL intensity may instead be reduced by carrier separation. Some works have found a lack of correlation between grain size and recombination rates[163], suggesting they are not a dominant factor.

1.5.9 Doping

The doping level (i.e. the equilibrium Fermi level), in perovskites has a significant impact on the solar cell device as it will affect the band bending that occurs at equilibrium, and also the recombination rates and thus diffusion lengths. Intrinsic defects are predicted to dope perovskites and the type and degree of doping will depend on the type and density of defects[155]. The doping/Fermi level has been found to be influenced by the fabrication conditions such as precursor stoichiometry, and also by the substrate which can affect crystal growth and cause charge transfer between the perovskite and substrate[211, 212]. Exposure to iodine vapour has been shown to p-dope the perovskite[159], highlighting the sensitivity of the doping level to stoichiometry and defect density. Doping is also sensitive to atmosphere as Shin et al. [213] showed that oxygen can change the perovskite material from intrinsic to p-doped, which was attributed to oxygen occupying iodine vacancies.

The Fermi level is often measured by photoelectron spectroscopy but since the emission energies measured by photoelectron experiments are severely affected by surface band bending, Zu et al. [214] argued that they will be unintentionally varied by background illumination, leading to varying results. Using intense illumination to flatten the bending they found that most compositions in fact are p-type in bulk with surface bending giving possibly n-type surface. But a later work by Hellmann et al. [107] argued that Zu et al. incorrectly attributed the band bending to the surface, and incremental deposition of the perovskite and comparing dark and illuminated measurements revealed that the bending was at the interface to the HTL substrate. Instead they concluded that vacuum deposited $MAPbI_3$, and spin coated $FAPbI_3$, $CsFAPbI_3$, $MAFAPbI_3$, $CsMAFAPbI_3$, are all n-type on both the ETL SnOx and the HTL NiOx. They suggest that literature reports of intrinsic $MAPbI_3$ on HTLs should be interpreted as n-type $MAPbI_3$ with unnoticed surface band bending.

To determine the doping density, Pena-Camargo et al.[67] emphasised the use of a combination of different techniques to avoid systematic errors in each. For example, measurements at low frequencies such as Hall effect[211] may detect mobile ions as well as electrons. The work arrives at an upper limit of electronic doping density for $MAPbI_3$ and mixed-cation perovskites. Their work determines that the doping density is not large enough to screen built-in fields between electrodes/contact layers [57], but mobile ions have high density so may do so. Walsh et al. [215] suggest that the reason that the measurements of carrier concentrations have been so low considering the low formation energy of defects is due to Schottky defects whereby donors and acceptors can cancel each other, called compensation. Indeed Steirer et al. [216] showed that the release of MA and I leaving vacancy pairs does not have significant impact on the Fermi level, consistent with compensation.

Chapter 2

Experimental Methods

2.1 Introduction

This chapter describes the experimental techniques used in this work. Steady state absorption and photoluminescence (PL) measurements are used to characterise the perovskite-CTL bilayer samples, and then time-resolved absorption and PL measurements are used to measure the charge carrier dynamics. Optical-pump terahertz-probe (OPTP) spectroscopy is used to measure the carrier dynamics in both the perovskite-CTL bilayers, and in chapter 6 an electronically delayed version of OPTP (E-OPTP) is developed in order to extend the time range of the technique. Therefore, OPTP is described in more detail than some of the others, but the development of the E-OPTP method is described in chapter 6. The relations between carrier densities and the different spectroscopy signals are presented in the current chapter.

2.2 THz Spectroscopy

2.2.1 THz-TDS and OPTP

The transmission of electromagnetic radiation through a material can be used to determine information about the complex permittivity of that material[217–220]

$$\tilde{\epsilon}(\omega) = \epsilon_1(\omega) + i\epsilon_2(\omega) = \tilde{n}^2(\omega)$$

where the complex refractive index is composed of the real refractive index n and extinction coefficient $\kappa(\omega)$

$$\tilde{n}(\omega) = n(\omega) + i\kappa(\omega)$$

so

$$\tilde{\epsilon}(\omega) = [n^2(\omega) - \kappa^2(\omega)] + i[2n(\omega)\kappa(\omega)]$$

The complex permittivity includes the response to electric fields of both the ions and the electrons. There are many resonances with energies in the THz frequency range, and in semiconductors these include phonons, excitons and free carrier absorption (intra-band transitions)[217–220]. The absorption by free charge carriers (i.e. electrons and holes) means that THz radiation can be used to study free carriers, and also the change in free carrier density after photoexcitation by an optical pump pulse, i.e. a pump-probe measurement.

THz time-domain spectroscopy (THz-TDS) refers to measuring the electric field of THz pulses in the time domain. Compared to continuous wave (CW) radiation, pulses have a broad spectrum, allowing the spectrum of transmission and thus the spectrum of permittivity to be obtained using a single radiation source. The advantage of measuring the electric field in the time domain is that it keeps phase information, so Fourier transforming the transmitted pulse yields the complex transmission spectrum, which can be related to the complex permittivity spectrum. Thus the spectrum of both the real refractive index $n(\omega)$ and extinction coefficient $\kappa(\omega)$ are obtained.

Performing THz-TDS measurements at different times after photoexcitation with an optical pump pulse, is referred to as either time-resolved THz spectroscopy (TRTS) or optical-pump terahertz probe (OPTP). This measures the pump-induced change in the permittivity, $\Delta\tilde{\epsilon}$, as a function of pump-probe delay. This is a 2D scan because as well as varying the delay between the THz pulse and the detection pulse that samples the field of the THz (the THz-detection delay), the delay between the pump pulse and the THz probe pulse is also varied (the pump-probe or pump-THz delay). Measuring the full THz pulse at each pump-probe delay can give spectral information at each pump-probe delay time, although the analysis must be done carefully, particularly if properties change during the probe pulse[221–224]. If only a single time in the THz pulse is measured for each pump-probe delay, this is a 1D scan as only the pump-probe delay is varied - some researchers use the name OPTP to refer to only this 1D scan, and refer to the 2D scan as TRTS. In this work, only the results of 1D pump-probe scans are presented and are referred to as OPTP measurements.

2.2.2 Relating the Transmission to the Conductivity

In order to determine the material's complex permittivity $\tilde{\epsilon}(\omega)$ from a THz transmission measurement, the incident and transmitted THz pulses must be related in terms of the material's permittivity $\tilde{\epsilon}(\omega)$. In the time domain, the transmitted field, $E_t(t)$, is a convolution of the incident electric field, $E_i(t)$, and the transfer function, $T(t)$

$$E_t(t) = [E_i * T](t)$$

so it is the transfer function that contains information about the permittivity. If the fields can be Fourier transformed to the frequency domain, the relation becomes a product

$$\tilde{E}_t(\omega) = \tilde{E}_i(\omega)\tilde{T}(\omega) \tag{2.1}$$

where the transfer function, $\tilde{T}(\omega)$, contains the permittivity $\tilde{\epsilon}(\omega)$ (note that in the frequency domain these functions are complex, indicated by the tilde). This transformation of a convolution in time to a product in the frequency domain relies on the transfer function $T(t)$ being the same for the duration of the incoming field $E(t)$. Working in the frequency domain makes it much easier to rearrange the expressions to isolate a particular factor, such as the sample's permittivity, compared to dealing with convolutions in time. For example, to determine the permittivity of a single layer, the expressions for the transmitted field with and without this layer, $\tilde{E}_{samp}(\omega)$ and $\tilde{E}_{ref}(\omega)$ are compared.

Specifically, taking the ratio of the transmitted fields will cancel out common terms in the transfer functions $\tilde{T}_{samp}(\omega)$ and $\tilde{T}_{ref}(\omega)$, and also cancels out the common factor $\tilde{E}_i(\omega)$

$$\begin{aligned}\frac{\tilde{E}_{samp}(\omega)}{\tilde{E}_{ref}(\omega)} &= \frac{\tilde{E}_i(\omega)\tilde{T}_{samp}(\omega)}{\tilde{E}_i(\omega)\tilde{T}_{ref}(\omega)} \\ &= \frac{\tilde{T}_{samp}(\omega)}{\tilde{T}_{ref}(\omega)}\end{aligned}$$

Similarly, in the frequency domain the measured field, $\tilde{E}_{meas}(\omega)$, is a product of the actual field, $\tilde{E}_{act}(\omega)$, and the instrument response function (IRF), $\tilde{H}(\omega)$ (whereas in the time domain it is a convolution),

$$\tilde{E}_{meas}(\omega) = \tilde{E}_{act}(\omega)\tilde{H}(\omega)$$

so the IRF is cancelled out when taking the ratio of two measurements [223]. Overall, this ratio in the frequency domain leaves an expression containing the desired quantity $\tilde{\epsilon}(\omega)$, which can then be solved for. In order to determine the unknown $\tilde{\epsilon}(\omega)$ of the sample from this expression, the sample $\tilde{\epsilon}(\omega)$ should be the only unknown in the expression. However this inversion problem may not have an analytical solution, in which case it must be done numerically, e.g. via Newton-Raphson. Limiting cases which have analytical solutions are often used, and are discussed below. For the case of 2D OPTP, the comparison of the transmitted THz for pump-on and pump-off is related to the photoinduced change in the transfer function, and thus the photoinduced change in the permittivity. However, if the properties of the material are changing during the propagation of the THz pulse, the analysis becomes much more complicated [221–224].

The expressions for the transfer function in terms of permittivity are now derived. For each frequency component, an expression for the transmitted field (Eq.2.1) can be derived by dividing the propagation path into sections of uniform permittivity and then considering the phase delay and absorption occurring during propagation through each section

$$e^{i\tilde{n}\omega d/c} = e^{in\omega d/c}e^{-\kappa\omega d/c}$$

(where d is the thickness), as well as the (complex) transmission and reflection coefficients, $\tilde{t}_{jk}(\omega)$ and $\tilde{r}_{jk}(\omega)$, at the interfaces between different layers j and k[225, 226]. Summations of Fabry-Perot reflections in each layer are also included, giving a factor of

$$\sum_p \left(\tilde{r}_{kl}\tilde{r}_{kj}e^{2i\tilde{n}\omega d/c}\right)^p$$

where p is the number of back and forth reflections inside layer k between layers j and l.

In certain limiting cases, such as a thick substrate and a thin sample (shown in Fig.2.1), an analytically invertible expression can be derived [226–229]. If the *substrate* is thick, the first Fabry-Perot echo due to the substrate will not overlap with the original pulse. The data can be truncated to remove the Fabry-Perot reflections which simplifies the substrate Fabry-Perot summation term. The extra distance of the reflections is $2d_{sub}$ (d_{sub} is thickness), which should be greater than length of the THz pulse, which is on the order of the wavelength λ for single-cycle pulses – therefore the substrate should be thicker

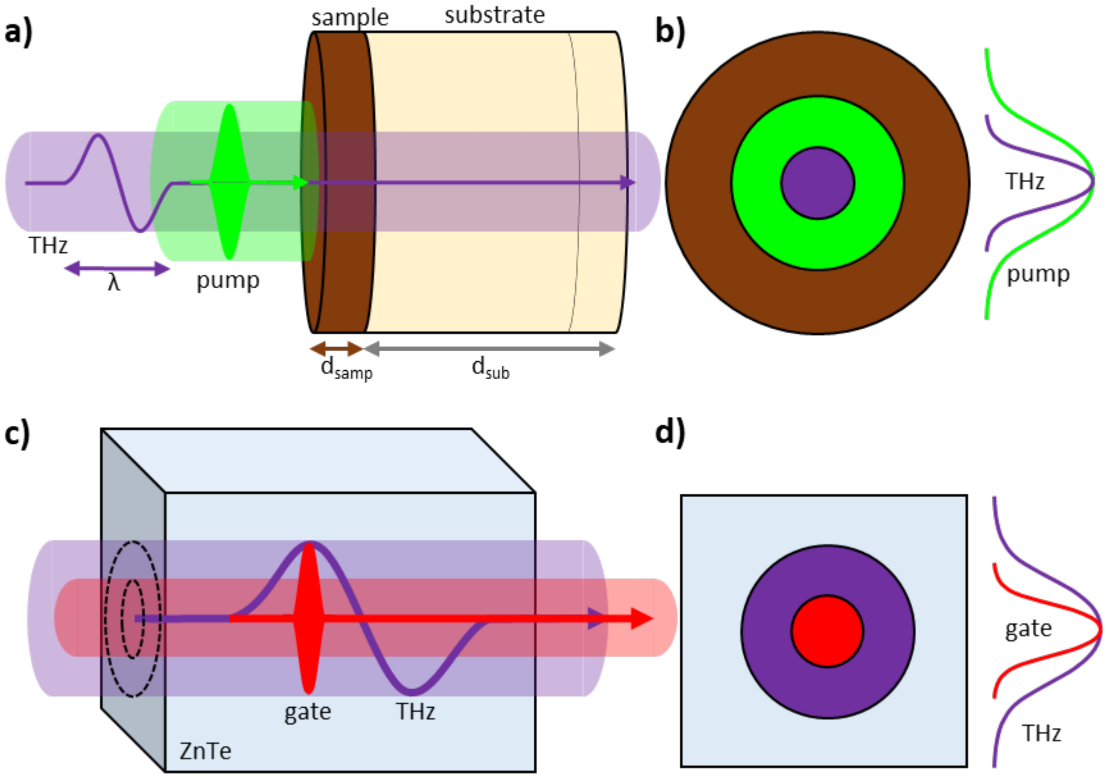

Figure 2.1: a) Schematic of an optical pump terahertz probe (OPTP) measurement (pump is green, THz is purple), for a thin sample ($d_{samp} \ll \lambda$) on a thick substrate ($d_{sub} \gg \lambda$). b) The spatial overlap of the optical pump's intensity cross-section and the THz probe's electric field strength cross-section at the sample position. c) Schematic of electro-optic sampling in a non-linear crystal such as ZnTe (gate is red, THz is purple). d) The spatial overlap of the THz probe's electric field strength cross-section and the gate beam's intensity cross-section (red) at the electro-optic detection crystal. The relative widths of the gate and THz pulses may be different to what is shown (see section 2.2.5).

than the wavelength $d_{sub} \gg \lambda$. Effectively the reflection of the pulse from the second side of the substrate (and subsequent echoes) is not recorded and so is a loss.

Similarly, if the *sample* is thin, all the Fabry-Perot echoes from this layer will overlap and so are all recorded. This simplifies the sample's Fabry-Perot summation term as the sum to infinity is $1/(1 - \tilde{r}_{kl}\tilde{r}_{kj}e^{2i\tilde{n}\omega d_{samp}/c})$. This condition requires that the sample layer must be much thinner than the length of THz pulse, so thinner than the wavelength $d_{samp} \ll \lambda$.

This expression still contains sinusoids and exponentials, which can be simplified under the small angle approximation if the argument $\tilde{n}\omega d_{samp}/c \ll 1$. The thin sample condition $d_{samp} \ll \lambda$ is equivalent to $n\omega d_{samp}/c \ll 2\pi$ (where n is $\Re(\tilde{n})$), so is a similar condition. Overall, assuming the layer in front of the sample has $\tilde{n}_{sup} = 1$, this yields

$$\frac{\tilde{E}_{samp}(\omega)}{\tilde{E}_{ref}(\omega)} = \frac{1 + \tilde{n}_{sub}}{(1 + \tilde{n}_{sub}) - i(\tilde{n}^2 + \tilde{n}_{sub})\omega d_{samp}/c}$$

which can be rearranged for $\tilde{\epsilon} = \tilde{n}^2$.

The calculated permittivity is the sum of lattice permittivity and permittivity due to conductive charges,

$$\tilde{\epsilon}(\omega) = \tilde{\epsilon}_L(\omega) + \frac{i\tilde{\sigma}(\omega)}{\omega\epsilon_0}$$

where $\tilde{\sigma}(\omega)$ is the conductivity. Assuming permittivity is dominated by conducting charges, the measured permittivity can be wholly attributed to conduction, giving

$$\tilde{\sigma}(\omega) = -i\omega\epsilon_0\tilde{\epsilon}(\omega) \tag{2.2}$$

This measured conductivity spectrum is often interpreted with the Drude model in which charge carriers are free but scatter with average lifetime τ_s that randomises their momentum [29]. This corresponds to a drag force proportional to their momentum times the scattering rate $\Gamma = 1/\tau_s$. The equation of motion in terms of electron momentum ($d\mathbf{p}(t)/dt = -q\mathbf{E}(t) - \mathbf{p}(t)/\tau_s$) for a sinusoidal driving electric field $\mathbf{E}(t) = \Re[\tilde{\mathbf{E}}_0(\omega)e^{-i\omega t}]$ and thus sinusoidal momentum $\mathbf{p}(t) = \Re[\tilde{\mathbf{p}}_0(\omega)e^{-i\omega t}]$ yields the complex amplitude $\tilde{\mathbf{p}}_0(\omega)$. From $\mathbf{j}(t) = -Nq\mathbf{p}(t)/m^*$ and $\mathbf{j}(t) = \Re[\tilde{\sigma}(\omega)\mathbf{E}_0(\omega)e^{-i\omega t}]$, the conductivity is

$$\sigma(\omega) = \frac{Nq^2}{m^*}\frac{\tau_s}{1 - i\omega\tau_s} = \frac{Nq^2\tau_s}{m^*}\left(\frac{1}{1+\omega^2\tau_s^2} + i\frac{\omega\tau_s}{1+\omega^2\tau_s^2}\right) \tag{2.3}$$

If the measured frequencies are $\omega \ll 1/\tau_s = \Gamma$, then in this frequency range the real part is constant ($Nq^2\tau_s/m^*$) and the imaginary part is negligible.

To determine the photoinduced change in the layer's permittivity, the transmitted field with and without pump illumination are measured, $\tilde{E}_{\text{on}}(\omega)$ and $\tilde{E}_{\text{off}}(\omega)$ [225, 227, 228, 230]. In this case, under the same thin sample thick substrate conditions, an expression containing the difference between the photoexcited and dark permittivity can be derived by considering the fractional change in the transmitted field $(\tilde{E}_{\text{on}} - \tilde{E}_{\text{off}})/\tilde{E}_{\text{off}}$ (often denoted as $\Delta\tilde{E}/\tilde{E}$), rather than just the ratio of the transmitted fields. The expression is further simplified in the case that $\Delta E/E \ll 1$, yielding

$$\frac{\tilde{E}_{\text{on}} - \tilde{E}_{\text{off}}}{\tilde{E}_{\text{off}}} = \frac{i\omega d_{samp}}{c}\frac{(\tilde{n}^{*2} - \tilde{n}^2)}{(1 + \tilde{n}_{sub})}$$

where the superscript * indicates the property of the photoexcited sample. Again, assuming that there is no photoinduced change in the lattice permittivity, the photoinduced change in permittivity is attributed to the change in permittivity of conducting charges,

$$(\tilde{n}^{*2} - \tilde{n}^2) = \frac{i(\tilde{\sigma}^* - \tilde{\sigma})}{\omega\epsilon_0}$$

This gives

$$\Delta\tilde{\sigma}(\omega) = -\frac{(1 + \tilde{n}_{sub}(\omega))}{Z_0 d_{samp}}\frac{\Delta\tilde{E}(\omega)}{\tilde{E}_{\text{off}}(\omega)} \tag{2.4}$$

Moving the thickness d_{samp} to the other side of the equation shows that $\Delta\tilde{E}/\tilde{E}$ is proportional to $\Delta\tilde{\sigma}_s(\omega) = d_{samp}\Delta\tilde{\sigma}(\omega)$, which is the sheet photoconductance (the photoconductivity integrated over the the thickness of the layer) for a layer with uniform photoconductivity through its thickness, as considered in this derivation. For samples in which the photoconductivity varies with depth, this can be approximated as a series of thin layers with different photoconductivity. It can be shown that the variation of photoconductivity with respect to depth has negligible impact on the total transmission change[217, 221, 222], and it actually only depends on the integral of the photoconductivity over the thickness, i.e. the sheet photoconductance $\Delta\tilde{\sigma}_s(\omega)$. Therefore, in the relations in section 2.2.5, the $\Delta\tilde{\sigma}(\omega)$ and carrier density n can be replaced with $\Delta\tilde{\sigma}_s(\omega)$ and n_s.

To use this frequency domain relation, the full temporal pulse must be measured and then Fourier transformed. For the case of 2D OPTP, measuring the temporal profile of the THz pulse at each pump-probe delay is time consuming and requires careful analysis [221–224]. The full temporal pulse is not required when photoexcitation simply attenuates the transmitted THz waveform independently of frequency, with negligible phase delay at any frequency, i.e. a flat and real photoinduced change in the transfer spectrum (for example, if the change is due to photoconductivity with a broad Drude-like spectrum). In this case, measuring a single time in the temporal profile of the THz pulse is sufficient to determine the photoinduced change in the transfer spectrum (it is described by a single uniform and real value). For other cases, the measurement at only a single time in the THz waveform cannot be easily related to the photoinduced change in the transmission spectrum.

In this work, the metal halide perovskite materials have a photoconductivity spectrum that is real and uniform across the measured frequency range [231] (using the Drude model this corresponds to a short scattering time $\sim$fs [231]), so only 1D pump-probe scans are necessary. The measured fractional change in transmission is not a function of frequency, so is denoted $\Delta E/E$. From Eq.2.4, this is also true for photoconductivity and photoconductance, which are therefore simply denoted $\Delta\sigma$ and $\Delta\sigma_s$.

2.2.3 THz Generation

THz radiation is generated by charges accelerating on femtosecond timescales, so for table-top sources, femtosecond pulsed lasers are used to induce charge acceleration. Two of the most common techniques for generating THz pulses from femtosecond laser pulses are photoconductive antennae (PCA) and optical rectifcation (OR) in non-linear crystals - these techniques employ the acceleration of free charges and bound charges respectively.[217–220]. As the pulse fluence (energy per pulse per area) of the femtosecond laser is increased, the magnitude of the photoinduced current burst in a small area PCA will begin to saturate. Therefore, for amplified laser systems, such as the one used in this work, OR in non-linear crystals is favoured as the the saturation mechanisms occur at higher pulse fluences (such as absorption of THz by carriers generated by two-photon absorption). For non-linear crystals, the THz generation and detection bandwidth is limited by phonon resonances which absorb THz (5-8THz for ZnTe). Recently spintronic emitters have been introduced, which do not suffer from this limitation.

In this work, both non-linear crystals (ZnTe) and spintronic emitters have been used to generate THz. The femtosecond laser pulse is generated by a Spitfire Ace amplified Ti:Sapphire laser system (Spectra Physics), outputting 13mJ pulses with a centre wavelength of ~800nm at a repetition rate of 1kHz. In this system, a MaiTai Ti:Sapphire oscillator laser (800nm centre wavelength, 80MHz repetition rate) seeds two consecutive regenerative amplification stages, that are each pumped by an Ascend diode-pumped solid state Q-switched laser (527nm centre wavelength, 1kHz repetition rate). The pump beams with different wavelengths are derived from the femtosecond laser via wavelength conversion in an optical parametric amplifier (Light Conversion TOPAS).

In non-linear crystals the process can be viewed as difference frequency generation (DFG) between frequencies in the femtosecond laser pulse that differ by ~ 1 THz. Alternatively, it can be considered that for each longitudinal position in the pulse's envelope, there is DFG between the two photons of the same frequency giving a DC field, known as optical rectification (OR), and the strength of this DC field follows the intensity profile of the laser pulses envelope (although it will be distorted due to frequency dispersion effects).

In a spintronic emitter, the laser pulse is directed at normal incidence into a nanometre thick stack of a ferromagnetic layer and a non-magnetic layer, positioned in an applied magnetic field in the plane of the layers [232, 233]. This results in a pulse of charge current in the non-magnetic layer that is aligned to the magnetic field i.e. in the plane of the material, which emits a broad spectrum pulse of electromagnetic radiation. This process can be explained as follows [234]. The ferromagnetic material has an equilibrium magnetisation as a function of temperature (decreasing with increasing temperature). The applied magnetic field orients it within the plane of the layer. Rapidly increasing the temperature with a laser pulse means the magnetisation will also need to change (decrease). This demagnetisation occurs by spins flipping, or by a current of net spin polarisation out of the material into a neighbouring layer. In this neighbouring layer, since the spin current has a net polarisation, the inverse spin hall effect (ISHE) results in a net charge current, aligned to the net spin polarisation, i.e. in the plane of the layers. The ISHE effect is quasi-instant, meaning the charge current has a rise time that is similar to the duration of the femtosecond laser pulse, so the full bandwidth available from the short laser pulse envelope is exploited. The emitted THz spectrum can extend up to 30THz at 10% amplitude[232]. Pt and W have the largest ISHE effect so give the largest current and THz emission, but with opposite polarisation because they have opposite spin hall angles. So they are put on opposite sides of the ferromagnetic layer so that their polarisations add constructively (reversing the direction of the spin current reverses the direction of the charge current). Varying the layer thicknesses has shown that the spin current and charge current occur within 1nm of the interface, so only thin layers are needed.

2.2.4 THz Detection

Both PCA and non-linear crystals can be used to measure the electric field of the THz pulse as a function of time, where the time resolution is because a femtosecond laser pulse is used to gate the detection mechanism on and off, hence this pulse is called the detection or gate pulse. When non-linear crystals are used to detect the electric field, it is called electro-optic detection/sampling. ZnTe crystals are used in this work. The gate pulse is usually split off from the laser pulse that is used to generate the THz. When the electric field of the THz pulse passes through a non-linear crystal (specifically those without inversion symmetry), a birefringence is introduced that is linearly proportional to the THz field strength - the Pockel's effect. The gate pulse, which travels collinearly with the THz pulse, experiences this birefringence and so its polarisation will be modified and measured. This change in polarisation is linearly proportional to the field strength that induced the birefringence.

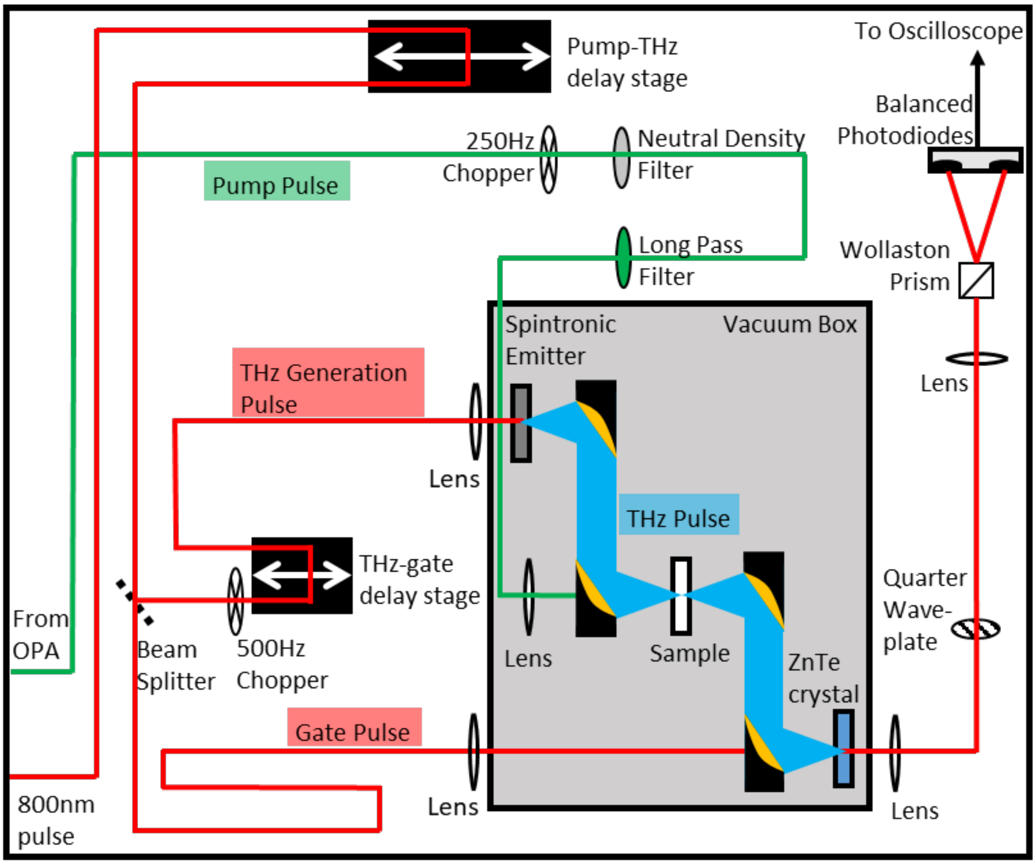

Figure 2.2: The optical pump terahertz probe (OPTP) setup used in this work. The wavelength of the pump pulse coming from the optical parametric amplifier (OPA) can be varied.

This polarisation change is detected by passing the gate pulse through a quarter wave plate (QWP) and then a Wollaston prism, which directs the two orthogonal polarisation components of the gate pulse onto separate photodiodes (see Fig.2.2). In a typical setup, the gate pulse has linear polarisation and the optical axis of the QWP is aligned such that, without any THz present at the detection crystal, this linearly polarised pulse becomes circularly polarised by passing through the QWP. This means the two orthogonal linear components have equal amplitudes. The two photodiodes are connected to a balancing circuit, such that the difference in the currents is converted to a voltage. Without any THz at the detector crystal, this difference should be zero when the QWP optical axis is correctly aligned – aligning the QWP is called balancing the photodiodes. The THz induced birefringence causes the optical pulse to become slightly elliptically polarised, and so the two components separated by the Wollaston prism have different amplitudes and the two photodiodes output different currents. Overall, the voltage is linearly proportional to the change in polarisation and is therefore linearly proportional to the THz field strength at the detector crystal.

2.2.5 Quantifying Photoconductivity

To measure photoconductivity (or the sheet photoconductance), one must determine the fractional change in the transmitted field, $\Delta E/E$, that is induced by photoexciting the sample. This is *equal* to the fractional change in the measured voltage, $\Delta V/V$, since the proportionality constant between voltage and transmitted field cancels out when considering a dimensionless ratio, such as the fractional change.

$$\frac{\Delta V}{V} = \frac{\Delta E}{E} \propto \Delta\sigma$$

EO sampling measures the THz field integrated over its cross-section weighted by the intensity profile of the gate pulse (see Fig.2.1). In the detection crystal, the gate pulse can be chosen to have a spot size larger than the THz pulse (which is focussed into the detection crystal to increase the field strength and thus the induced birefringence), so that there is roughly equal weighting across the THz cross-section. However, this will mean that only part of the gate's cross-section experiences birefringence, so the balanced photodiode voltage will not be as large compared to if the gate beam waist was smaller than the THz beam waist.

Positions in the THz cross-section that have greater field strength will cause greater birefringence and thus contribute more to the balanced photodiode voltage, i.e. positions with high field strengths have greater weighting. Therefore, photoinduced fractional changes in transmission $\Delta E/E$, have greater weighting if they occur at positions in the THz cross-section that have higher field strength. So the fractional change in voltage, $\frac{\Delta V}{V}$, is equal to an integral over the sample plane of the fractional change in THz transmission, $\frac{\Delta E}{E}(x, y)$, weighted by the profile of the THz field strength incident on the sample, $E_i(x, y)$ (it is also weighted by transverse profile of the detection beam intensity but that can be treated as uniform if in the detection crystal plane the gate beam is much wider than the THz)

$$\begin{aligned} \frac{\Delta V}{V} &= \int \frac{\Delta E}{E_{\text{off}}}(x, y)\, |E_i^{norm}|(x, y)dxdy && (2.5) \\ &\propto \int \Delta\sigma(x, y)|E_i^{norm}|(x, y)dxdy && (2.6) \\ &= \langle\Delta\sigma\rangle_T && (2.7) \end{aligned}$$

where $|E_i^{norm}|(x, y)$ is the profile of the incident THz field strength normalised such that integrating over the cross-section gives 1. The proportionality between $\Delta E/E$ and $\Delta\sigma$ from Eq.2.4 has been invoked. Overall, the measured signal $\Delta V/V$ is proportional to a weighted spatial average of the photoconductivity. The cross-sectional profiles of the incident THz field strength, $E_i(x, y)$, and of the initial photoconductivity, $\Delta\sigma(x, y, t = 0)$, can be measured by performing knife-edge scans of the THz and pump beams respectively. The sum of the electron and hole mobilities (at THz frequencies) can be estimated if the initial average carrier density is estimated, which will be shown next.

The conductivity is the product of the carrier density and the mobility,

$$\sigma(x, y) = qn(x, y)\mu_e + qp(x, y)\mu_h$$

(assuming an average mobility for each band) and the photoconductivity is the photoinduced *change* in conductivity,

$$\Delta\sigma(x, y) = q[n^*(x, y)\mu_e^* + p^*(x, y)\mu_h^*] - q[n(x, y)\mu_e + p(x, y)\mu_h]$$

(where * denotes photoexcited properties), which could be due to a change in the carrier densities or mobilities. If it is assumed that the mobilities do not change, and that the photoexcited electron and hole densities are equal, then

$$\Delta\sigma(x,y) = q\Delta n(x,y)(\mu_e + \mu_h) \tag{2.8}$$

The sum mobility at THz frequencies, $\mu_e + \mu_h$, at $t = 0$ can be extracted using this relation since the initial $\Delta\sigma$ is calculated from Eq.2.4, and the initial $\Delta n(x,y)$ can be calculated from power and knife-edge measurements. Using Eq.2.8, then Eq.2.5 becomes

$$\begin{aligned}\frac{\Delta V}{V} &\propto (\mu_e + \mu_h) \int \Delta n(x,y) |E_i^{norm}|(x,y) dxdy \\ &= (\mu_e + \mu_h)\langle \Delta n \rangle_T\end{aligned}$$

where $\langle \Delta n \rangle_T$ is referred to as the pump-probe overlap integral. The total number of carriers generated, N_T, is the number of photons incident per pulse (the pulse energy divided by the photon energy, W_{pulse}/W_{photon}) multiplied by the fraction that are absorbed, $1 - T - R$ (R and T are the fractions of incident power that are reflected or absorbed) and the fraction of these that generate carriers, Φ (called the yield or branching ratio). Overall,

$$N_T = \Phi(1 - T - R)\frac{W_{pulse}}{W_{photon}}$$

$\Delta n(x,y)$ is normalised such that

$$\int \Delta n(x,y) dxdy = N_T$$

In this work, the pump beams of different wavelengths used for the perovskite-CTL bilayer measurements, were derived from the amplified femtosecond laser by wavelength conversion in an optical parametric amplifier. For some of the E-OPTP measurements, a fibre laser was used. These beams all have 2D Gaussian intensity profiles. For a 2D Gaussian profile,

$$\Delta n(x,y,) = N_T \frac{1}{2\pi\sigma_x\sigma_y} e^{-\frac{x^2}{2\sigma_x^2}} e^{-\frac{y^2}{2\sigma_y^2}}$$

However the diode laser used for some of the E-OPTP measurements can have a top hat profile in one dimension and a Gaussian profile in the other, so

$$\Delta n(x,y) = N_T \frac{1}{w\sqrt{2\pi}\sigma} e^{-\frac{y^2}{2\sigma_y^2}}$$

where w is the diameter of the top hat.

The THz probe has a 2D Gaussian profile, with width σ_T in both the x and y directions. It is normalised such that

$$\int_a^b \int_c^d E_T^{norm}(x,y) dxdy = 1$$

which gives

$$E_T^{norm}(x,y) = \frac{1}{2\pi\sigma_T^2} e^{\frac{-(x-x_0)^2}{2\sigma_T^2}} e^{\frac{-(y-y_0)^2}{2\sigma_T^2}}$$

If the pump profile is a 2D Gaussian with $\sigma_x = \sigma_y = \sigma_p$, the pump-probe overlap integral is

$$\langle \Delta n \rangle_T = \frac{N_T}{2\pi(\sigma_T^2 + \sigma_p^2)}$$

If the pump profile is a top hat in one direction (width w), Gaussian in the other (width σ_p), the pump-probe overlap integral is

$$\langle \Delta n \rangle_T = \frac{N_T}{w\sqrt{2\pi}\sqrt{\sigma_p^2 + \sigma_T^2}}$$

When considering time resolved changes of the sheet photoconductance, it must be remembered that the signal that is recorded is an average over the area of the probed region, and so the time evolution of the recorded signal is an average of the time evolution for different positions in the probed cross-section. If the time evolution varies across the probed area, this makes it more difficult to interpret the time evolution of the measured signal. Indeed, the normalised decay shape is in general different for different initial densities, except for the particular case that the decay process is monomolecular across the whole range of densities. Therefore, it is preferred to photogenerate carriers uniformly in the probed region, both with respect to the in-plane dimensions and the out-of-plane (depth) dimensions, so that the spatial dependence does not need to be accounted for, and the recorded signal is simply and directly related to this uniform density. This is why the cross-sectional area of the probe is chosen to be several times smaller than the cross-sectional area of the pump, so that it probes a region over which the sheet carrier density is almost uniform.

2.2.6 Pulse Scheme

In both THz-TDS and OPTP, as well as measuring the THz pulse transmitted through the sample (and the reference substrate for THz-TDS), a reference measurement with no THz at the detector crystal, called THz-off, is also recorded in order to account for any non-zero offsets in the EO sampling signal when the THz pulse is absent. The THz field strength, E, is the difference between THz-on and THz-off measurements. It is important to account for the non-zero offsets in this way, because for both THz-TDS and OPTP, the ratio of different measurements is the quantity of interest (e.g. Eq.2.4), so any systematic non-zero offsets in the signals would distort this ratio. Furthermore, since the non-zero offset may vary over successive shots (due to fluctuations in the femtosecond laser's fluence or pointing), this should be accounted for by measuring the THz-off signal as frequently as possible. Therefore, alternating measurements of THz-on and THz-off are recorded, by blocking alternate THz pulses with a mechanical chopper - this accounts for slow drifts but not shot-to-shot fluctuations.

THz-TDS employs this repeating 2-pulse scheme (THz-on and THz-off) to repeatedly measure the THz field strength transmitted through the sample, E_{samp}, or through

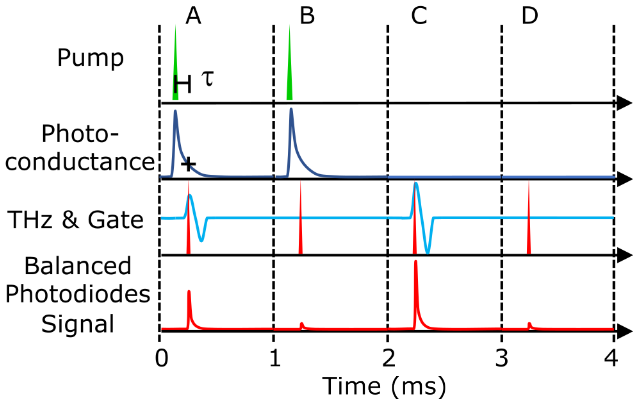

Figure 2.3: The 4-pulse scheme used in optical pump terahertz probe (OPTP) measurements. The photoconductance decay is sampled at the point indicated by the cross, with pump-probe delay τ.

the reference substrate, E_{ref}, but in a pump-probe measurement (OPTP), a repeating 4-pulse scheme is used to repeatedly measure pairs of E_{on} and E_{off}, as shown in Fig.2.3. E_{on} is determined from the difference between by measuring THz-on and THz-off with the pump on $(A - B)$, and E_{off} is the difference between THz-on and THz-off with the pump off $(C - D)$. Separate THz-off measurements for pump-on and pump-off (B and D) are used since the pump excitation of the sample may generate THz itself, which would not be accounted for by pulse D (pump-off). This 4 pulse scheme can be achieved by modulating the THz beam on and off alternatively i.e. a 50% duty cycle at half the frequency of the repetition frequency, and modulating the pump beam with a 50% duty cycle at a quarter of the laser's repetition frequency.

2.2.7 Delay Stage Choice

The arrival time of THz pulse and the detection pulse in the detector crystal is controlled by a delay line: one of the mirrors in the beam path is a retroreflector on a stage that moves parallel to the propagation of the beam, changing the path length (see Fig.2.2. Similarly, the relative arrival time of the THz pulse and the pump pulse at the sample is controlled by a second delay line. The beam path must be aligned very precisely parallel to the stage axis, otherwise the beam's position on the detector or sample will vary as the stage is moved. Since the pump beam's alignment is frequently changed (for example when changing the wavelength), its path does not include a delay stage. Instead, a delay stage is used in the path of the 800nm beam before it is split into generation and detection portions, so that moving this stage changes the delay of both of these pulses relative to the pump pulse. The other delay stage is in the detection beam's path, to vary its delay relative the THz beam.

2.2.8 Data Processing

In this work, due to the presence of outliers - caused by the laser pulse power occasionally fluctuating with a frequency component that matches the repetition frequency of the 4-pulse scheme (250Hz for 4 × 1ms pulse pattern) – the median and the 68th percentile width are sometimes used in place of mean and standard deviation, as they are more robust to outliers.

2.3 Absorption

2.3.1 Equilibrium Absorption

The absorption coefficient for a particular frequency of light, $\alpha(\omega)$, is the fraction of light intensity absorbed per length of propagation through the material. The absorption of energy occurs when the electromagnetic wave induces transitions of an electron from an initial state (energy E_i) to an empty final state with higher energy (E_f). Only a quantised amount of energy can be absorbed (a photon), which is related to the light's frequency, $E = \hbar\omega$. If the transition is instead to an empty state with lower energy, then this results in the creation of a photon, so stimulated emission rather than absorption. For an electromagnetic wave propagating through a material, the rate of transitions per unit time per unit volume from an occupied state to an unoccupied state separated by energy $\hbar\omega$, $\Gamma_{i\to f}(\omega)$, can be calculated using time-dependent perturbation theory, when the perturbation by the electromagnetic wave is weak (i.e. the transition probability is low) [39, 235–238]. This is called Fermi's Golden Rule, commonly written in the form[1]

$$\Gamma_{i\to f} = \frac{2\pi}{\hbar}|M_{if}|^2\delta(E_f - E_i - \hbar\omega) \tag{2.9}$$

where

$$|M_{if}|^2 = |\int \psi_f^*(\mathbf{r},t)\mathcal{H}'\psi_i(\mathbf{r},t)d\mathbf{r}|^2 = | < \psi_f|\mathcal{H}'|\psi_i > |^2 \tag{2.10}$$

is called the transition matrix element, $\mathcal{H}'$ is the Hamiltonian of the time-dependent perturbation, and ψ_i and ψ_f are the initial and final wavefunctions. In a real system, this rate must be multiplied by the probability that the initial state is occupied, $f(E_i)$, the probability that the final state is unoccupied, $1 - f(E_f)$ [35, 39]. For a pair of states, the transition probabilities for absorption or stimulated emission are the same, but the rate of absorption is higher since the probability of occupation of the lower state is higher, giving a net absorption rate [39, 235].

For the perturbing Hamiltonian, often a semi-classical approach is used in which the perturbing electromagnetic field is treated as a classical wave, whereas the electron is described by quantum Bloch states [235–237]. The total Hamiltonian $\mathcal{H}$ in the presence of an electromagnetic wave is found by replacing the momentum operator $\mathbf{p}$ in the time-independent (no light present) Hamiltonian, $\mathcal{H}_0$, with $\mathbf{p} - q\mathbf{A}$, where $\mathbf{A}(\mathbf{r},t) = \mathbf{A_0}e^{i\mathbf{q}.\mathbf{r}-\omega t}$ is the vector potential of the light wave (considered to be a plane sinusoidal wave with wavevector $\mathbf{q}$). This results in a perturbation $\mathcal{H}'$ compared $\mathcal{H}_0$ that is proportional to $\mathbf{A}.\mathbf{p}$, which is inserted into $|M_{if}|^2$. The transition matrix element is thus proportional to the light intensity and thus the photon density. Spontaneous emission does not depend on the light intensity and its rate can be considered as stimulated emission by the zero-point energy of the quantised electromagnetic field, i.e. the semi-classical approach cannot account for it.

$|M_{if}|^2$ is non-zero only when the frequency ω and momentum $\mathbf{q}$ of the light matches

---

[1] When there is a continuum of final states, this rate is multiplied by the density of final states $g(E_f)$ and integrated over the final state energy E_f.[238]

the frequency difference $\omega_f - \omega_i$ and momentum difference $\mathbf{k}_f - \mathbf{k}_i$ of the two states, i.e. energy and momentum are conserved by the transition (also other symmetries such as parity must be conserved, giving other selection rules) [236–238]. The energy conservation contained within the matrix element is often written explicitly using the delta function in Eq. 2.9.

Usually, the wavevector of the light is small compared to the spatial extent of the system, so the $e^{i\mathbf{q}\cdot\mathbf{r}}$ in the vector potential can be approximated as 1, i.e. $\mathbf{q}$ is approximated as zero. Therefore, the initial and final states must have the same momentum, so transitions are vertical in energy vs. momentum. In this case, the perturbation Hamiltonian, $\mathcal{H}'$, becomes equivalent to the energy of an electric dipole in the electric field of the light, hence this is called the electric dipole approximation [39, 235–238].

The *total* absorption rate (per unit volume) of a photon with a particular energy/frequency is the sum of the absorption rate for each pair of states. The sum can be limited to only pairs of states for which the transition matrix element is non-zero, i.e. those transitions that conserve energy, momentum and other symmetries. Since optical transitions are vertical, there is a unique one-to-one pairing between states in the VB and

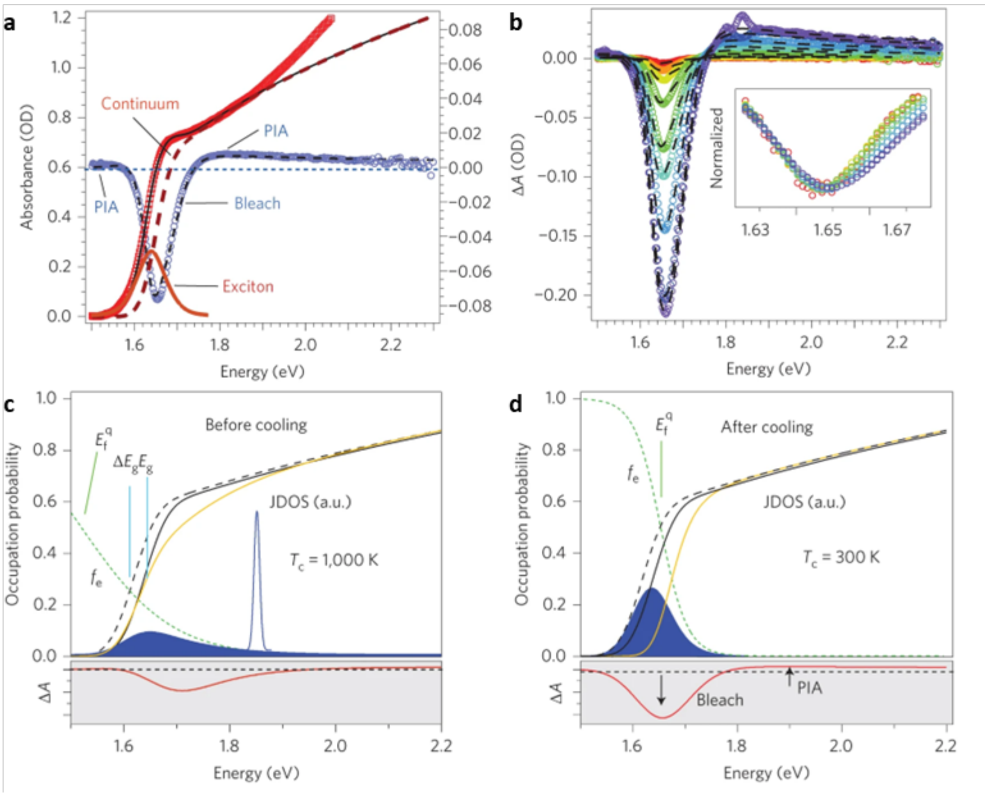

Figure 2.4: a) A typical measured equilibrium/steady state absorption spectrum (red squares) and a corresponding transient absorption (TA) spectrum (blue circles) recorded at 10ps pump-probe delay, for a metal halide perovskite. The equilibrium spectrum is fit with Elliot theory and the exciton and continuum contributions are indicated. The TA spectrum comprises a ground state bleach, a broad photoinduced absorption (PIA) above the bandgap, and a narrower PIA below the bandgap (it is small at this pump-probe delay). b) The TA spectra at different delay times, with the narrowing of the GSB due to cooling highlighted in the inset. c), d) Schematic of the different contributions to the difference spectra (red) due to bleaching (yellow) of the JDOS (black), before cooling (c) and after cooling (d). Reproduced from two figures in ref.[184].

CB that conserve energy and momentum, so the density (per photon energy) of pairs of states separated by $\hbar\omega$, called the joint density of states JDOS ($\hbar\omega$), has a square root dependence on photon energy for interband transitions near the band edges. If the transition matrix element is approximately equal for all interband transitions near the band edges, then the absorption coefficient has a square root dependence on photon energy.

For many perovskite samples, the absorption spectrum near the band edge does not simply follow the square root shape predicted for transitions between parabolic bands, but features enhanced strength near the band edge. The shape of the absorption spectrum can be described by the Elliot formula [17, 184, 239, 240], which includes the exciton resonance just below the band edge, and a uniform enhancement of the square root continuum (see Fig.2.4a). This spectrum is often convoluted with a broadening function, where the spectral broadening can be homogeneous or inhomogeneous. The observation of an excitonic resonance in the absorption, and also that the PL and stimulated emission overlap with this resonance does not necessarily mean excitons are present[241]. If free electrons and holes were non-interacting (ideal gas like) then emission at an exciton resonance can only be from excitons. But because the semiconductor's delocalised electrons are a strongly interacting many–body system, the emission should instead be thought of as a transition from a state of N to $N-1$ electron-hole pairs. The recombination of an unbound pair emitting a photon with energy of an exciton recombination (so less than the band-to-band transition energy) can conserve energy because the remaining energy is transferred to the many-body system (i.e. through carrier-carrier interactions).

The exciton binding energy (BE) is a measure of the strength of the interaction between electron-hole pairs, and has been used to estimate the fraction of carriers that are bound at a given temperature and density using the Saha-Langmuir equation [242] The exciton BE has been estimated either by fitting the equilibrium absorption spectrum with Elliot theory[17, 184, 239, 240], or by fitting the change in the PL linewidth with temperature [242]. However, the excitonic feature in the absorption spectrum is broadenened and overlaps with the continuum absorption, especially at room temperature, giving large uncertainty to the Elliot fitting. Alternatively, the exciton BE can be estimated, from THz absorption [243, 244] or electro-absorption spectroscopies[245, 246]. High field magneto-absorption measurements have been suggested to be the most accurate as there are fewer free parameters in the fitting of the data [18] and the exciton BE for $MAPbI_3$ was found to be 16meV at 4K reducing to 10-12meV at 161K, just at the phase transition[247]. It has been suggested that at higher temperatures the dielectric constant increases and thus reduces the exciton binding energy compared to low temperatures[30], as suggested by the magneto-absorption results. At room temperature, the exciton BE has been measured by 2D electron spectroscopy, extracting a value of 12meV [248]. The THz and electro-absorption measurements gave similar values as well[245, 246]. Overall, the exciton binding energy seems to be much lower than thermal energy at room temperature, 25meV, suggesting most electron-hole pairs are unbound.

Other evidence for excitons being predominately dissociated at room temperature comes from the observation that PL comes from unbound carriers. For example, Saba et al. [249] showed that the initial PL intensity and time integrated PL intensity after pulsed excitation scales quadratically with fluence (below a certain intensity) so must be due to

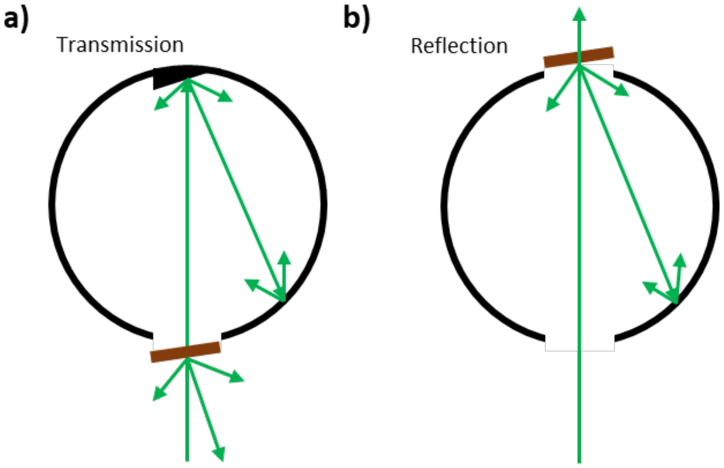

Figure 2.5: A schematic of a transmission measurement and reflection measurement using an integrating sphere. For the reflection measurement, the sample is mounted at a small angle to the incident beam so that the specular reflection is collected by the sphere. The sample is mounted at the same angle for the transmission measurement as well.

the recombination of unbound carriers. Chen et al. [250] observed that there is some PL emitted above the bandgap energy before carriers completely cool to the band edge, which is attributed to free carriers recombining.

In this work the absorption spectra were measured using a spectrophotometer (Perkin Elmer Lambda 1050) with an integrating sphere module. The sphere has a spectrally uniform, diffusely reflective coating so that any light inside of it is internally reflected and is eventually incident on a detector at the base. The sample's transmission is measured by placing the sample in the aperture where the light enters the sphere, so that light that is transmitted, including scattered transmission, will enter the sphere and be detected (see Fig.2.5). The sample's reflection is measured by placing the sample in an aperture at the back of the sphere so that transmitted light is not collected and light that is specularly or diffusely reflected is collected in the sphere. The absorbed intensity is the incident intensity minus the transmitted and reflected intensities.

$$I_A = I_0 - I_T - I_R = I_0(1 - T - R)$$

where $T = I_T/I_0$ is the transmittance and $R = I_R/I_0$ is the reflectance.

2.3.2 Transient Absorption spectroscopy

Transient absorption (TA) spectroscopy measures the sample's change in transmittance of a broadband pulse of light as a function of time after pulsed photoexcitation of the sample. The broadband pulse is spectrally resolved yielding an absorbance difference spectrum, $\Delta A(\lambda)$ or optical density difference spectrum $\Delta OD(\lambda)$ (the distinction is that absorbance is defined as the natural logarithm of the transmittance $A = -\ln(T)$ and optical density is defined as the decadic logarithm of transmittance $OD = -log_{10}(T)$). The broadband pulse is generated by focussing a pulse from the Ti:Sapphire amplified laser (described above) into a 2mm CaF_2 window to generate a white light continuum (the window is continuously translated to prevent damage). The white light spectra were measured shot-by-shot using an Avantes spectrometer (Avaspec 1650 Fast USB) consisting of a grating and a multi-pixel CCD.

The principle of TA spectroscopy is that photoexcitation temporarily changes the absorption coefficient compared to its equilibrium value. This is because photoexcitation decreases the occupation of the lower states and increases the occupation of upper state, thus decreasing the number of pairs of states that can absorb photons, called bleaching of the absorption. For a semiconductor, the bleaching of transitions at or just above the bandgap energy is often called the ground state bleach (GSB). The different contributions to the difference spectrum $\Delta A(\lambda)$ are shown in parts c) and d) of Fig.2.4 (reproduced from [184]), which shows the bleaching (yellow) of the JDOS (black) due to the carrier density (blue area), resulting in the difference spectra (red). After photoexcitation the JDOS is also shifted in energy (dashed black), which results in the photoinduced absorption (PIA) at energies above the GSB, which will be discussed in section 4.2.3. Immediately after photoexcitation, the transitions that have absorbed pump photons will no longer be able to absorb the probe photons, and absorption is decreased/bleached at the energy of the photoexcitation (indicated by the blue line). However, on the timescale of femtoseconds (so faster than the IRF), electrons in the CB and the holes in the VB can move to other states in their bands (by scattering), achieving a Fermi-Dirac distribution (green dashed line) within each band. Then as the population cools (by scattering with the lattice), these distributions change shape, which causes the bleaching spectrum to change. This cooling takes place on the time scale of picoseconds [251]. After the carrier cooling has taken place, the spectral shape of this bleach will change more slowly and the amplitude will decay with time as recombination proceeds. A higher density of excited carriers will result in a stronger bleach, but also the bleach will extend to high photon energies as the QFL in each band will be deeper in their respective bands. Therefore, the difference spectra measured by TA gives significant information about the carrier dynamics. This spectrally resolved information is recorded in a single shot, so is not an additional burden unlike for spectrally resolving the THz pulse at each pump-probe delay (i.e. a 2D TRTS scan) with the OPTP setup used here.

2.4 Photoluminescence

2.4.1 Steady State photoluminesence

Photoluminescence (PL) is the emission of photons from a sample following absorption of photons by the sample. The emission intensity is proportional to the product of the electron and hole densities in the CB and VB respectively $I \propto np$, so gives information about the carrier densities. The intensity also depends on what fraction of the carriers recombine radiatively rather than non-radiatively, thus contains information about the competing recombination processes. The PL spectrum is related to the distribution of the electrons and holes with respect to energy.

In this work, both steady state PL and time resolved PL are measured using a Horiba Jobin Yvon (HJY) Fluorolog-3 fluoro-spectrometer. For steady state measurements, the sample is illuminated continuously with a Xenon lamp, with the wavelength range selected using a Czerny-Turner monochromator: the lamp light is collimated onto a diffraction grating that angularly disperses the light which is then focussed onto a slit. The grating is rotated to vary the wavelength range that passes through the slit, and into the sample chamber. The PL emitted from the photoexcited sample is collected by mirrors and focussed onto the entrance of a HJY iHR320 spectrometer. This spectrometer consists of a Czerny-Turner monochromator that is used to select the wavelength range of the light that passes through a final slit in front of the detector, which is a Hammamatsu R982P photomultiplier tube (PMT). The width of the slit determines the spectral resolution.

2.4.2 Time Resolved Photoluminescence

Time resolved photoluminescence (TRPL) is measured by time correlated single photon counting TCSPC[252]. Electronics are usually not fast enough to allow a single-shot measurement of the fluorescence intensity as a function of time after a pulse of photoexcitation, i.e. continuous recording (the streak camera is one exception). Also, the fast photodetectors which one might use may not be sensitive enough to measure the low intensity emission of some samples. TCSPC circumvents these issues, achieving high temporal resolution and sensitivity, by measuring multiple cycles of excitation and emission to accumulate a TRPL curve. This enables the use of more sensitive photodetectors which would be too slow to use for a single shot measurement.

In TCSPC, the sample is repeatedly photoexcited with low fluence pulses such that the probability of two photons reaching the detector following each photoexcitation is close to zero. This corresponds to a single photon reaching the detector for a few percent of the excitation pulses, i.e. a count rate of a few percent. The time delay between photoexcitation and the arrival of each photon is recorded and used to build up a histogram of the number of photons arriving within narrow time bins. A time-to-amplitude converter (TAC) produces a voltage corresponding to the time between the excitation and the detection (using a voltage ramp). If two photons reach the detector within one cycle, the TAC will not record the arrival of the second photon, and so if this occurs these later photons will be underrepresented meaning the lifetime will be underestimated. This is why the count rate is kept below two percent of the excitation pulses.

The temporal resolution can be improved by measuring the instrument response function and iteratively reconvoluting this with a mathematical model until the result converges on the measured data. This is thus model dependent. The instrument response function is obtained by measuring the photons from the excitation source which are scattered off the sample to the detector. This measurement of the instrument response function (IRF) can be called the "prompt". In this work, the PL decays are much longer than the prompt ($\sim$2ns), and so iterative reconvolution to improve the temporal response has no benefit.

In this work, TCSPC is performed using the Fluorolog-3 with the same PMT, but illuminating the sample with pulsed diode sources (HJY N-405L and N-635L) with centre wavelengths of 405nm and 633nm and pulse energies of $\sim$3.4 and $\sim$1.7 pJ/pulse respectively (pulse durations <200ps but the IRF is longer $\sim$2ns). For 45 degree incidence and minimum spot sizes of $\sigma \sim 50\mu$m, the maximum pulse fluences are 26 and 10 nJ/cm^2 for 405nm and 633nm excitation respectively. The repetition period is varied depending on the pump-probe delay window being measured, which is chosen to ensure the PL intensity decays to zero before the next pump pulse arrives (typically 1-10μs). The timing electronics are provided by a HJY FluoroHub.

Chapter 3

Modelling Charge-Carrier Dynamics

3.1 Introduction

In this thesis, the experimental results are compared with solutions of mathematical models of the charge carrier dynamics. The output of the model is compared to the data to see if the model is physically accurate, and to determine correct values of the model's parameters for these specific experiments.

Models that are simple enough to be solved analytically, are usually simplified approximations of the actual system and whilst an analytical solution can be studied to give qualitative insight, they may not give accurate quantitative insight ([253]). Models that are constructed to be more accurate in order to give quantitative insight, often cannot be solved analytically so must be solved numerically.

In this work, the measurements of silicon wafers in Chapter 6 will be compared to solutions of a model that can be solved analytically, whereas the perovskite-CTL bilayers in Chapter 4 are compared to both a simplified model that can be solved analytically, and a more detailed model that can only be solved numerically.

The experimental conditions for the perovskite-CTL bilayers mean that the semiconductor equations can be solved in 1D, considering only the depth dimension of the layers, denoted x in this chapter. This is because the cross-sectional width of the pump beam is much larger than the absorption depth of the pump beam in the perovskite film (and also the silicon wafers), so the photogenerated carrier density varies with respect to the in-plane dimensions y and z much more slowly than with respect to the depth dimension x. Consequently, diffusion in the in-plane direction is much slower than in the out-of-plane (depth) dimension. For the perovskite layers, the in-plane diffusion is slow compared to carrier recombination, so the in-plane profile does not change significantly during the decay of the carrier population. However, for the silicon samples, it will be seen that in-plane diffusion must be accounted for.

This chapter presents the mathematical models used to simulate and thus understand the measured carrier dynamics. In this thesis, these models are solved both analytically and numerically, and this chapter derives the analytical solutions for the different boundary conditions relevant to the experiments in this work.

3.2 The Basic Semiconductor Equations

The carrier density is both temporally and spatially varying, and controlled by the continuity equation ([29]) that expresses conservation of particle number. Terms representing the rate of generation, g_{tot} or recombination, r_{tot} of carriers can also be added, giving the continuity equation

$$\frac{dc}{dt} + \nabla \cdot \mathbf{j}_c - g^c_{tot} + r^c_{tot} = 0$$

where $\mathbf{j}_c$ is the particle flux/current for charge carrier with density c. For electrons and holes, the particle flux/current is related to the charge current by $\mathbf{J}_n = (-q)\mathbf{j}_n$, $\mathbf{J}_p = (q)\mathbf{j}_p$. Therefore,

$$\frac{dn}{dt} - \frac{\nabla \cdot \mathbf{J}_n}{q} - g^n_{tot} + r^n_{tot} = 0$$

$$\frac{dp}{dt} + \frac{\nabla \cdot \mathbf{J}_p}{q} - g^p_{tot} + r^p_{tot} = 0$$

The continuity equations for electrons and holes describe the change in density at each position due to transport, recombination and generation. The continuity equations are coupled as the recombination rates can depend on the density of the other carrier. Transport can be driven by electric fields, which can be externally applied, or arise due to the spatial distribution of charges: electrons $n(\mathbf{r})$, holes $p(\mathbf{r})$, ionised donor atoms $N_D(\mathbf{r})$, and ionised acceptor atoms $N_A(\mathbf{r})$

$$\rho_f(\mathbf{r}) = q(-n(\mathbf{r}) + p(\mathbf{r}) - N_D(\mathbf{r}) + N_A(\mathbf{r}))$$

The fields arising from these charges are described by Gauss's law

$$\nabla \cdot (\epsilon_r(\mathbf{r})\mathbf{E}(\mathbf{r})) = \frac{\rho_f(\mathbf{r})}{\epsilon_0}$$

The electric field $\mathbf{E}(\mathbf{r})$ is minus the gradient of the electric potential $V(\mathbf{r})$

$$\mathbf{E}(\mathbf{r}) = -\nabla V(\mathbf{r})$$

and the material permittivity $\epsilon_r(\mathbf{r})$ (in general a tensor) accounts for the polarisation induced by the fields from the charges, which partially screens these fields. If the permittivity is isotropic (so scalar) and uniform within the domain of interest, then Gauss's law has the form of the Poisson equation

$$\nabla \cdot \mathbf{E}(\mathbf{r}) = \frac{\rho_f(\mathbf{r})}{\epsilon_0 \epsilon_r}$$

This Poisson equation contains the electron and hole densities so is coupled to the continuity equations for electrons and holes, forming a system of 3 coupled equations, called the basic semiconductor equations. These three coupled equations have the two densities, $n(\mathbf{r}, t)$ and $p(\mathbf{r}, t)$, and the potential $V(\mathbf{r}, t)$, as the dependent variables, although a different but equivalent set can be chosen (QFLs instead of densities). These dependent variables are functions of the independent variables, spatial position $\mathbf{r}$ and time t. In one dimension, the vector notation can be dropped and the vector components along this dimension is considered.

$$\frac{\partial\left(\epsilon_r(x)\frac{-\partial V(x,t)}{dx}\right)}{\partial x} = \frac{\rho_f(x,t)}{\epsilon_0} \tag{3.1}$$

$$\frac{\partial n(x,t)}{\partial t} = \frac{1}{q}\frac{\partial J_n(x,t)}{\partial x} + g^n_{tot}(x,t) - r^n_{tot}(x,t) \tag{3.2}$$

$$\frac{\partial p(x,t)}{\partial t} = -\frac{1}{q}\frac{\partial J_p(x,t)}{\partial x} + g^p_{tot}(x,t) - r^p_{tot}(x,t) \tag{3.3}$$

An expression for the charge current J_c must be derived, where c indicates a generic carrier type. This can be derived from the semi-classical Boltzmann Transport Equation (BTE) ([29, 39, 254]) which considers the occupation function, to yield J_c as the gradient of the Fermi level.

$$J_c = c\mu\nabla E_F$$

where the mobility μ ($= v/E$) is equivalent to $q\langle\tau\rangle/m$ where $\langle\tau\rangle$ is the mean scattering lifetime. The derivation of this BTE charge current makes a number of assumptions about the conditions in the material (such as the relaxation time approximation) and it is valid for semiconductor structures with features much larger than the mean free path of electrons (the mean distance they travel between scattering events). This has been estimated as 0.8 nm for $\mathrm{MAPbI_3}$ [255] and 20 nm for silicon [227], which are both much smaller than dimensions of the layers in this work (perovskite ~500 nm and silicon ~700μm). For electrons in the CB,

$$J_n = n\mu_n\frac{\partial E_{F_n}}{\partial x}$$

where

$$E_{F_n} = E_c + k_BT\ln\left(\frac{n}{N_c}\right)$$

and

$$E_c = -q\phi - \chi$$

For holes in the VB,

$$J_p = p\mu_p\frac{\partial E_{F_p}}{\partial x}$$

where

$$E_{F_p} = E_v - k_BT\ln\left(\frac{p}{N_v}\right)$$

and

$$E_v = -q\phi - \chi - E_g$$

Some of these quantities were defined in Fig.1.5. Using these relations, the current can be written explicitly in terms of the dependent variables n, p, and V

$$J_n = qn\mu_n\left(-\frac{\partial V}{\partial x}\right) - n\mu_n\frac{d\chi}{dx} + qD_n\frac{\partial n}{\partial x} - \frac{n\mu_nk_BT}{N_c}\frac{dN_c}{dx} \tag{3.4}$$

$$J_p = qp\mu_p\left(-\frac{\partial V}{\partial x}\right) - p\mu_p\frac{d\chi}{dx} - p\mu_p\frac{dE_g}{dx} - qD_p\frac{\partial p}{\partial x} + \frac{p\mu_pk_BT}{N_v}\frac{dN_v}{dx} \tag{3.5}$$

(the identity $\frac{\partial(\ln(n(x)))}{\partial x} = \frac{1}{n}\frac{\partial n}{\partial x}$ has been used). For the case of Boltzmann statistics, (e.g. non-degenerate) the diffusion coefficient is given by the Einstein relation, $D_n = \frac{\mu_n k_B T}{q}$, $D_p = \frac{\mu_p k_B T}{q}$. For other statistics, it is given by a generalised Einstein relation, which enhances the diffusion coefficient compared to the Einstein relation for Boltzmann statistics ([256, 257]). These expressions show that the spatial variation in the band edge DoS (N_c and N_v), or the band edge energies (χ and $\chi + E_g$) give effective fields that can drive current. This is because it is the gradient in chemical potential, not just concentration, that drives "diffusive" current, and the chemical potential is composed of a material dependent component and a concentration dependent component.

For a uniform material, Eq.3.4 and Eq.3.5 simplify to the more familiar "drift-diffusion" form,

$$J_n = qn\mu_n E + qD_n \frac{\partial n}{\partial x} \tag{3.6}$$

$$J_p = qp\mu_p E - qD_p \frac{\partial p}{\partial x} \tag{3.7}$$

The general form of the drift-diffusion particle flux rather than charge current is (remember $J_n = -qj_n$, $J_p = qj_p$)

$$j_c = c\mu_c E - D_c \frac{\partial c}{\partial x}$$

3.3 Solving the System of Equations

The semiconductor equations are non-linear if they contain a drift term ($c\mu E$), since this is a product of two dependent variables (c and V), or they contain a recombination or generation term that is a product of carrier densities (e.g. radiative recombination, see section3.4). It is very difficult to find analytical solutions for non-linear equations, but an analytical solution for the carrier distribution can be found if these non-linearities are removed, which occurs if the neutrality approximation [29] applies (see section 3.5) and the recombination rate is a linear function of density (see section 3.4).

If the spatial dependence is ignored, the system of 3 partial differential equations (PDEs) called the basic semiconductor equations, reduces to just the two continuity equations with time as the only independent variable, so they are ODEs called rate equations. The rate equation itself may contain non-linear terms, and when multiple processes occur simultaneously, analytical solutions are difficult to find. Neglecting the spatial dependence is often an approximation that is applied to model experiments, and this is called the 0D model. When it comes to fitting a solution to the data (i.e. finding the parameter values which give the simulated solution which most closely resembles the data), if there are too many free parameters in the model, then there may be more than one set of parameter values that fit the data, rather than just one unique set. Often a simplified model with a minimal number parameters is used, called the k_1-k_2-k_3 or ABC model [258]. It assumes the electron and hole carrier densities are equal, and the different recombination processes are assumed to be proportional to a power of this balanced carrier density, yielding the rate equation

$$\frac{dn}{dt} = k_1 n + k_2 n^2 + k_3 n^3$$

Often the monomolecular (linear) recombination rate $k_1 n$ is attributed to defect mediated two-step recombination, and the bimolecular recombination rate $k_2 n^2$, is attributed to radiative one-step recombination. However, the next section will show that both processes can give rates which are either monomolecular or bimolecular.

It should be noted that if a linear recombination rate constant, k_1, is spatially non-uniform, e.g. increased at a surface, a 0D model can still be used if the spatial distribution of carriers does not change shape during the time range of interest, only its amplitude changes i.e. a stationary distribution[259]. In this case there is an effective k_1 that includes both surface and bulk recombination and is a function of the diffusion coefficient.

3.4 Modelling Recombination Processes

The carrier creation or annihilation processes in the continuity equations are the interband transition processes that were introduced in section 1.3.1. Quantitative models for their rates (generation g and recombination r) are now presented. At equilibrium, the total rates g_{tot} and r_{tot} balance and are denoted $G_{tot} = R_{tot}$. The total rates will usually include multiple different processes, which will be addressed individually below. Excess illumination is an increase in g_{tot}, and will cause an increase in r_{tot}, and for prolonged illumination may reach a steady state $g_{tot} = r_{tot}$. After excess illumination is terminated, g_{tot} is reduced to just G_{tot}, and r_{tot} remains greater than R_{tot} until equilibrium is reached.

The total carrier densities under non-equilibrium conditions, n and p, are a sum of the equilibrium densities n_0 and p_0, and the excess densities n_e and p_e : $n = n_0 + n_e$ and $p = p_0 + p_e$. The decay of the excess density (n_e and p_e) towards equilibrium is given by the net recombination rate (net means recombination minus generation) that is in excess of the net rate at equilibrium,

$$(r_{tot} - R_{tot}) - (g_{tot} - G_{tot}) = r_{tot} - g_{tot}$$

since $R_{tot} - G_{tot} = 0$.

The rate of change of density c due to recombination is a function of the density, c, so can be written in the form [260]

$$\frac{dc}{dt} = -kc = -\frac{c}{\tau_c}$$

This is assigning an effective monomolecular rate constant or lifetime to the decay rate, regardless of whether the decay is monomolecular. When the lifetime τ_c (or rate constant $k = 1/\tau_c$) depends on c (so not monomolecular), this contributes a non-linear term to the rate equation.

Since the equilibrium density c_0 is not a function of time,

$$\frac{dc}{dt} = \frac{dc_e}{dt}$$

so the dependent variable of the rate equation is just the excess density c_e rather than the total density c.

The condition of balanced excess densities, $n_e = p_e$, is often required to simplify the rate equations from their most general form into simpler forms which can be easily interpreted or solved analytically. The rates for the individual processes will now be considered, first for one-step recombination and then for two-step recombination via an intermediate defect state.

3.4.1 One-step Recombination

The rate of one-step recombination is proportional to n and p, and annihilates electrons and holes in pairs so

$$r^n_{rad} = r^p_{rad} = Bnp$$

This rate is the spontaneous emission rate discussed in section 2.3, where the factors n and p come from the occupation probabilities and densities of states of the bands, and the coefficient of proportionality B contains the transition matrix element. As mentioned previously, these one step transitions are dominated by radiative transitions, so the suffix "rad" is used, and any radiationless transitions (phonon emission) can be incorporated as a small modification to the radiative rate [260]. Reabsorption of radiative recombination can either excite transitions across the bandgap (so contribute to g_{tot}), cause intraband transitions, or stimulate further radiative recombination. Photon reabsorption is very dependent on sample geometry[260], and the effect of reabsorption is usually absorbed into an effective rate constant for radiative recombination, which describes the rate of radiative recombination that results in photons escaping the sample [260].

In the limiting case that radiative band-to-band transitions are the only process possible, ($r^c_{tot} = r^c_{rad}$ and $g^c_{tot} = g^c_{rad}$) electrons and holes are only created or annihilated in pairs ($g^n_{tot} = g^p_{tot}$ and $r^n_{tot} = r^p_{tot}$), so under excess illumination, the excess electron and hole densities will balance, $n_e = p_e$. In this case a simple expression for the net recombination rate in excess of the equilibrium rate ($R = G = Bn_i^2$) can be derived [260]. With illumination switched off (i.e. there is no excess generation rate, so $g_{rad} = Bn_i^2$), the excess net recombination rate is $(r_{rad} - g_{rad}) = B(np - n_i^2)$. Since in the considered scenario, $n_e = p_e$, this rate can be written in a simple form that allows easy interpretation

$$(r_{rad} - g_{rad}) = Bn_e(n_0 + p_0 + n_e) \tag{3.8}$$

In particular, in this scenario the excess rate can be written in the form

$$(r_{rad} - g_{rad}) = -k_{rad}n_e = -\frac{n_e}{\tau_{rad}}$$

where the lifetime of the excess carriers $n_e = p_e$ is

$$\frac{1}{\tau_{rad}} = B(n_0 + p_0 + n_e)$$

This rate constant or lifetime depends on excess density n_e, so this process is a non-linear term in the rate equation for n_e ($= p_e$). For excess densities lower than the majority equilibrium density, $n_e \ll n_0$ (for n-type), called low level injection (LLI), the lifetime is independent of excess density n_e and so the process becomes linear in excess density again. Thus, at late times in a transient measurement where radiative recombination is dominant, the decay of density becomes mono-exponential. However, at earlier delay times, n_e may be larger than the majority equilibrium density, $n_e \gg n_0$ (for n-type), meaning the decay rate is bimolecular and the decay is hyperbolic [260]. For excess densities in between these two limiting cases, the decay of the excess density is a superposition of a monomolecular and bimolecular processes. If other processes occur that do not maintain $n_e = p_e$, the expressions for the excess net recombination rate $(r_{tot} - g_{tot})$ become more complicated.

3.4.2 Two-step Defect-Mediated Recombination

Two-step recombination via intermediate defect states is more complex, as the occupation of a third level is now included (the localised states associated with defects). A defect state can capture a carrier from either band and emit a carrier to either band, where the rate is proportional to the available densities of the species involved. For example, for electron capture into a defect state, the rate is proportional to the density of occupied CB states, n, and the density of unoccupied defect states, $N_T(1 - f_T)$ (where $f_T = f(E_T)$), with a constant of proportionality called the capture coefficient C_n,

$$r^n_{cap} = C_n n N_T(1 - f_T)$$

The capture coefficient C_n is the product of thermal velocity and the capture cross-section $C_n = v\sigma_n$ [39, 254]. C_n is proportional to the transition matrix element as discussed in section 2.3 (note that when the transition is by phonon absorption/emission rather than photon absorption/emission, a different Hamiltonian is used in the transition matrix element).

Whilst photogeneration and one-step (radiative) recombination generate or annihilate a pair of electrons and holes meaning n_e and p_e are always equal (assuming one-step recombination is dominant), two-step recombination via a defect state may cause n_e and p_e to differ, as there may be accumulation of electrons or holes in the defects. This would invalidate the neutrality approximation used to derive analytical solutions to the spatially dependent problem (see section 3.5), and means the rate equations do not have easy to interpret forms.

During transients, the occupation of defect states will change during the period immediately after pulsed injection, but may then reach a quasi-steady state during part of the transient, before later changing as it returns to equilibrium occupation[260]. The imbalance of n_e and p_e during the transient is only significant if the defect density is large, and the degree of accumulation of electrons or holes in the defects is large. The accumulation depends on relative strengths of the four capture and emission coefficients of the defect. Shockley and Read showed that $n_e \simeq p_e$ is valid whenever density of defects N_T is small compared to any of n_0, p_0, n_T, p_T [261]. n_T and p_T are the electron and hole densities if $E_F = E_T$ (see Appendix B), so to be small E_T should be far away from the band edge energies.

A single expression describing the rate of this two step process can be found for steady state conditions, i.e. the net capture rate of electrons from the CB and holes from the VB are balanced, and thus the defect occupation is constant. This steady state rate is called the Shockley Read Hall rate and is derived in Appendix B (but is only valid for the limit of small trap density or small injected density[260]). Outside of steady state this expression does not apply.

$$r_{SRH} = \frac{np - n_i^2}{\tau_c^n(p + p_T) + \tau_c^p(n + n_T)}$$

where $\tau_c^n = \frac{1}{C_n N_T}$ and $\tau_c^p = \frac{1}{C_p N_T}$ are called the capture lifetimes for electrons and holes. n_T and p_T are the electron and hole densities when the Fermi level equals the trap energy E_T.

Again, under conditions where $n_e \simeq p_e$, the expression can be written in a more interpretable forms

$$r_{SRH} = \frac{n_e(n_0 + p_0 + n_e)}{\tau_c^n(p_0 + n_e + p_T) + \tau_c^p(n_0 + n_e + n_T)}$$

Expressing this rate as $r_{SRH} = n_e/\tau_{SRH} = k_{SRH}n_e$ gives

$$k_{SRH} = 1/\tau_{SRH} = \frac{(n_0 + p_0 + n_e)}{\tau_c^n(p_0 + n_e + p_T) + \tau_c^p(n_0 + n_e + n_T)}$$

When the excess density is much larger than the equilibrium densities (HLI) and the constants n_T and p_T, $n_e \gg n_0, p_0, n_T, p_T$, then

$$k_{SRH} = 1/\tau_{SRH} = \frac{1}{\tau_c^n + \tau_c^p}$$

Alternatively, if the excess density is much smaller than the equilibrium densities $n_e \ll n_0, p_0$, i.e. low level injection (LLI), then

$$k_{SRH} = 1/\tau_{SRH} = \frac{(n_0 + p_0)}{\tau_c^n(p_0 + p_T) + \tau_c^p(n_0 + n_T)}$$

In both of these limiting cases, the SRH rate constant (k_{SRH}) or lifetime (τ_{SRH}) is independent of the balanced excess density n_e, so the process is monomolecular and the decay is exponential. For densities in between, the lifetime takes an intermediate value that varies with density.

For a doped material, low level injection (LLI) results in a SRH rate constant/lifetime equal to the minority carrier capture time (provided n_T and p_T are small). For example, for LLI in n-type $p_0, n_e \ll n_0$ (and $n_T, p_T \ll n_0$),

$$k_{SRH} = 1/\tau_{SRH} = \frac{1}{\tau_c^p}$$

For LLI in p-type $n_0, n_e \ll p_0$ (and $n_T, p_T \ll p_0$),

$$k_{SRH} = 1/\tau_{SRH} = \frac{1}{\tau_c^n}$$

3.5 Modelling the Spatial Dependence with the Ambipolar Continuity Equation

There is no analytical solution for the general case of the three coupled and usually non-linear PDEs Eq.3.1-3.3 (the basic semiconductor equations), where the charge currents are given by Eq.3.6 and Eq.3.7. An analytical solution can be found by making the neutrality approximation, which is that the density of electrons and holes are approximately equal at all places and times [29]. The validity of this approximation with regard to net accumulation of carriers in defects was mentioned in the previous section ($n_e \simeq p_e$ is valid whenever density of defects N_T is small compared to any of n_0, p_0, n_T, p_T [261]). Although an applied field or a difference in diffusion coefficients will tend to separate the electrons and holes, only a small difference in the electron and hole densities compared to the absolute densities is necessary to generate sufficient internal field (i.e. due to electron and hole separation) to keep the oppositely charged carriers together. Thus the neutrality approximation is usually valid ([29]). If $n_e = p_e$ everywhere, then the Poisson equation does not need to be solved. $n_e = p_e$ also allows the two continuity equations to be written in terms of the same dependent variable, n_e or p_e. The two equations for a single dependent variable can thus be combined into a single equation. The effect of the small internal fields that attract electrons and holes is included implicitly in this equation. Recalling that the continuity equations Eq.3.2 and 3.3 are

$$\frac{\partial n}{\partial t} = \frac{\frac{\partial J_n}{\partial x}}{q} + g^n_{tot} - r^n_{tot}$$

$$\frac{\partial p}{\partial t} = \frac{-\frac{\partial J_p}{\partial x}}{q} + g^p_{tot} - r^p_{tot}$$

and the charge currents are given by Eq.3.6 and Eq.3.7

$$J_n = qn\mu_n E + qD_n \frac{\partial n}{\partial x}$$

$$J_p = qp\mu_p E - qD_p \frac{\partial p}{\partial x}$$

The continuity equations written explicitly in terms of the dependent variables n and p are

$$\frac{\partial n}{\partial t} = \mu_n \frac{\partial (nE)}{\partial x} + D_n \frac{\partial^2 n}{\partial x^2} + g^n_{tot} - \frac{n}{\tau^n_{\text{tot}}} \tag{3.9}$$

$$\frac{\partial p}{\partial t} = -\mu_p \frac{\partial (pE)}{\partial x} + D_p \frac{\partial^2 p}{\partial x^2} + g^p_{tot} - \frac{p}{\tau^p_{\text{tot}}} \tag{3.10}$$

The total recombination rate has been expressed in terms of density and an effective monomolecular total rate constant/lifetime. This total rate may be the result of more than one recombination process, for example for carrier c

$$\frac{c}{\tau^c_{\text{tot}}} = \frac{c}{\tau^c_{SRH}} + \frac{c}{\tau^c_{rad}}$$

The total density for charge carrier with density c is the equilibrium density plus the excess density, $c = c_0 + c_e$, where c_0 is constant, so $\frac{\partial (c_0)}{\partial t} = 0$. It will also be assumed that the sample is homogeneous, so c_0 is uniform, and $\frac{\partial (c_0)}{\partial x} = 0$. Therefore, the two continuity equations Eq.3.9 and Eq.3.10 can be written in terms of the excess densities, n_e and p_e. The total generation rate for carrier c is the equilibrium rate G^c_{tot} plus the excess rate ${g'_{tot}}^c$: $g^c_{tot} = G^c_{tot} + {g'_{tot}}^c$. G^c_{tot} equals the equilibrium recombination rate, $G^c_{tot} = R^c_{tot} = c_0/\tau^c_{\text{tot},0}$, where $\tau^c_{\text{tot},0}$ is the total lifetime at equilibrium, and the excess generation rates for electrons and holes are equal, ${g'_{tot}}^{n} = {g'_{tot}}^{p}$, since photoexcitation generates an electron-hole pair. Using these identities and applying the product rule to $\frac{\partial(c_e E)}{\partial x}$ gives

$$\frac{\partial n_e}{\partial t} = \mu_n \left(\frac{\partial n_e}{\partial x} E + n \frac{\partial E}{\partial x} \right) + D_n \frac{\partial^2 n_e}{\partial x^2} + g'_{tot} - \left(\frac{n}{\tau^n_{\text{tot}}} - \frac{n_0}{\tau^n_{\text{tot},0}} \right) \tag{3.11}$$

$$\frac{\partial p_e}{\partial t} = -\mu_p \left(\frac{\partial p_e}{\partial x} E + p \frac{\partial E}{\partial x} \right) + D_p \frac{\partial^2 p_e}{\partial x^2} + g'_{tot} - \left(\frac{p}{\tau^p_{\text{tot}}} - \frac{p_0}{\tau^p_{\text{tot},0}} \right) \tag{3.12}$$

The neutrality approximation is that $n_e = p_e$. Therefore, equations 3.11 and 3.12 can be combined and $\frac{\partial E}{\partial x}$ eliminated leaving

$$\frac{\partial n_e}{\partial t} = -\mu^* \frac{\partial n_e}{\partial x} E + D^* \frac{\partial^2 n_e}{\partial x^2} + g'_{tot} - \frac{n_e}{\tau^*_{\text{tot}}} \tag{3.13}$$

where

$$\mu^* = \frac{(n-p)\mu_n \mu_p}{n\mu_n + p\mu_p} = \frac{(n_0 - p_0)\mu_n \mu_p}{n\mu_n + p\mu_p} \tag{3.14}$$

$$D^* = \frac{(n+p) D_n D_p}{n D_n + p D_p} \tag{3.15}$$

$$\frac{n_e}{\tau^*_{\text{tot}}} = \frac{n}{\tau^n_{\text{tot}}} - \frac{n_0}{\tau^n_{\text{tot},0}} = \frac{p}{\tau^p_{\text{tot}}} - \frac{p_0}{\tau^p_{\text{tot},0}} \tag{3.16}$$

The combined equation 3.13 has the form of a continuity equation (except $\frac{\partial(cE)}{\partial x}$ has become $E\frac{\partial(c)}{\partial x}$), but the parameters describing drift, diffusion and recombination are now ambipolar parameters μ^*, D^* and τ^*. The electric field E is a sum of the internal fields and the externally applied fields, however the internal fields can usually be neglected as they have small *direct* influence on the spatial distribution of the excess carriers compared to diffusion or external fields - their effect is included implicitly in the ambipolar diffusion equation.

The ambipolar continuity equation Eq.3.13 cannot be solved analytically unless the equation is linear, which requires that the ambipolar parameters are independent of excess density. [1] For example, for an intrinsic material, $n_0 = p_0$,

$$\mu^* = 0$$

and

$$D^* = \frac{2 D_n D_p}{D_n + D_p}$$

μ^* is zero because it represents the drift mobility of the ambipolar density, which is neutral when $n_0 = p_0$ and $n_e = p_e$, and hence is not accelerated by an electric field.

For low level injection (LLI) in a doped semiconductor, ambipolar D^* and μ^* are also independent of excess density, and are equal to those of the minority carrier. For LLI in p-type ($n_e, n_0 \ll p_0$)

---

[1] In Eq.3.13, the electric field E is not a function of the excess carrier density n_e (i.e. the dependent variable), which means the drift related term is linear when $\mu*$ is independent of excess density n_e. In contrast, in the individual continuity equations Eq.3.2 and 3.3, E is a function of the dependent variable ϕ, which makes the drift related term non-linear.

$$\mu^* = \frac{-p_0\mu_n\mu_p}{p_0\mu_p} = -\mu_n$$

$$D^* = \frac{p_0 D_n D_p}{p_0 D_p} = D_n$$

For LLI in n-type ($n_e, p_0 \ll n_0$)

$$\mu^* = \frac{n_0\mu_n\mu_p}{n_0\mu_n} = \mu_p$$

$$D^* = \frac{n_0 D_n D_p}{n_0 D_n} = D_p$$

For LLI, the ambipolar total lifetime is also independent of density. This is because for both the majority and minority carriers, their SRH and band-to-band lifetimes are both independent of density. In the LLI case, the ambipolar total lifetime is equal to the total lifetime of the minority carrier. This can be seen by considering Eq.3.16 and recognising that the lifetime for the minority carrier is not changed significantly because the density of majority carriers is not changed significantly. For example, for p-type $\tau^n_{\text{tot}} = \tau^n_{\text{tot},0}$, so

$$\begin{aligned}\frac{n_e}{\tau^*_{\text{tot}}} &= \frac{n}{\tau^n_{\text{tot},0}} - \frac{n_0}{\tau^n_{\text{tot},0}} \\ &= \frac{n_e}{\tau^n_{\text{tot},0}}\end{aligned}$$

or for n-type $\tau^p_{\text{tot}} = \tau^p_{\text{tot},0}$, so

$$\begin{aligned}\frac{n_e}{\tau^*_{\text{tot}}} &= \frac{p}{\tau^p_{\text{tot},0}} - \frac{p_0}{\tau^p_{\text{tot},0}} \\ &= \frac{n_e}{\tau^p_{\text{tot},0}}\end{aligned}$$

For high level injection (HLI) $n_e \gg n_0, p_0$, the situation is the same as for an intrinsic material

$$\mu^* = \frac{(n-p)\mu_n\mu_p}{n_e\mu_n + n_e\mu_p} = 0$$

$$D^* = \frac{2D_n D_p}{D_n + D_p}$$

Regarding the ambipolar total lifetime, for both majority and minority carriers the SRH lifetime is independent of density for HLI, but the radiative lifetime is not, meaning the ambipolar total lifetime is not independent of density if the radiative rate is significant, such as in direct semiconductors with low defect densities. However, for indirect semiconductors the radiative rate will make a small contribution to the total rate, so the ambipolar total lifetime may be independent of density.

3.5.1 Summary

Overall, assuming $n_e = p_e$ (the neutrality approximation) and that n_0 and p_0 are spatially uniform, means that the spatially dependent carrier dynamics can be described by a single differential equation for the excess densities $n_e = p_e$, called the ambipolar continuity equation. The ambipolar continuity equation Eq.3.13 cannot be solved analytically unless the equation is linear, which requires that the ambipolar parameters are independent of excess density. This has been shown to be the case for an intrinsic semiconductor, or for the limiting cases of high-level or low-level injection in doped semiconductors.

In Chapter 4, measurements of the carrier dynamics in perovskite-CTL bilayers are reported. The CTLs are expected to selectively extract one type of charge carrier, thus resulting in charge separation that violates the neutrality approximation. Therefore, these dynamics were modelled (see Chapter 5) using numerical solutions of the semiconductor equations Eq.3.1-3.3 (where the charge currents are given by Eq.3.6 and Eq.3.7). It was concluded that the dynamics are consistent with very small charge separation across the interface, and thus the neutrality approximation was valid and the ambipolar continuity equation could be applied. This could be solved analytically by treating the recombination process at the interface as monomolecular, and this give excellent fits to the measurements.

In Chapter 6, measurements of the photoconductance decay of silicon wafers are reported. The neutrality approximation is expected to be valid for these wafers, so the ambipolar continuity equation was used to model the diffusion of carriers in order to understand how diffusion impacts the measured photconductance signal.

3.6 Analytical Solutions of the Ambipolar Continuity Equation

3.6.1 Introduction

As mentioned previously in section 3.5, under the neutrality approximation, the system of 3 PDEs that describes the carrier distribution as a function of space and time (Eq.3.1-3.3 supplemented with Eq.3.6 and Eq.3.7), reduces to a single ambipolar continuity equation, which in 1D is

$$\frac{\partial n_e}{\partial t} = -\mu^* \frac{\partial n_e}{\partial x} E + D^* \frac{\partial^2 n_e}{\partial x^2} + g' - \frac{n_e}{\tau^*_{\text{tot}}}$$

The combined equation has the form of a continuity equation (except $\frac{\partial(cE)}{\partial x}$ has become $E\frac{\partial(c)}{\partial x}$), but the parameters describing drift, diffusion and recombination i.e. mobility, diffusion coefficient, lifetime, are now ambipolar parameters, denoted by *. The ambipolar continuity equation only has analytical solutions when the equation is linear, which requires that the ambipolar parameters are independent of excess density.

For the silicon wafers reported in Chapter 6, the only fields that are present are due to the field effect passivation, and are confined to a very short depth near the surface, and so can be treated as boundary conditions to the bulk of the wafer, in which there are no fields. Therefore, in the bulk the continuity equation is simply

$$\frac{\partial n_e}{\partial t} = D^* \frac{\partial^2 n_e}{\partial x^2} - \frac{n_e}{\tau^*_{\mathrm{tot}}}$$

The boundary conditions for the passivated sample are considered to be hard walls, whereas the non-passivated surface has additional surface recombination. If the recombination is treated as linear in density (monomolecular), an analytical solution of this continuity equation can be derived and used to model the data. The analytical solution is derived by separation of variables and the solution is derived here, first without bulk recombination so it is just the diffusion equation. Bulk recombination can be included as a simple extension to this solution, but surface recombination requires a different solution.

3.6.2 Separation of Variables

In 3D, the diffusion equation is

$$\frac{\partial n(t,x,y,z)}{\partial t} = D\left(\frac{\partial^2 n(t,x,y,z)}{\partial x^2} + \frac{\partial^2 n(t,x,y,z)}{\partial y^2} + \frac{\partial^2 n(t,x,y,z)}{\partial z^2}\right) \tag{3.17}$$

Certain PDEs such as the diffusion equation can be solved by "separation of variables" [262], which effectively splits the PDE into a summation of ODEs (ODEs are usually quite routine to solve), and the ODE solutions are combined together to give the PDE solution. The "separation of variables" method results in solutions that have a separable product form. This form is a product of functions that are functions of one independent variable only, one for each independent variable (i.e. for each dimension). For the 3D diffusion equation, the form of a product solution is:

$$n(t,x,y,z) = X(x)Y(y)Z(z)T(t) \tag{3.18}$$

Inserting this into the 3D diffusion equation (Eq.3.17) yields:

$$\frac{1}{DT(t)}\frac{\partial T(t)}{\partial t} = \frac{1}{X(x)}\frac{\partial^2 X(x)}{\partial x^2} + \frac{1}{Y(y)}\frac{\partial^2 Y(y)}{\partial y^2} + \frac{1}{Z(z)}\frac{\partial^2 Z(z)}{\partial z^2} \tag{3.19}$$

Each term is function of one variable only, so for the expression to be true over a domain rather than just a single point, each term must be a constant:

$$-\mu = -l^2 - m^2 - n^2 \tag{3.20}$$

These constants are called "separation constants", and the algebraic relation between them is called the "separation equation". Each term in Eq. 3.19 is an ODE, for example

$$\frac{\partial T(t)}{\partial t} + \mu D T(t) = 0 \tag{3.21a}$$

$$\frac{\partial^2 X(x)}{\partial x^2} + l^2 X(x) = 0 \tag{3.21b}$$

Where the ODEs involve second derivatives, it is common for the separation constant to be defined with a power of two. Similarly, the separation constants are usually defined with minus to make the ODEs have conventional form.

The ODEs in the spatial dimensions and temporal dimension are both eigen-equations, in which the eigen-values in the spatial dimensions are the separation constants $-l^2$,$-m^2$,$-n^2$, and in the temporal dimension is $-\mu D$. The ODE solutions are therefore eigenfunctions and each distinct eigenvalue gives a different eigenfunction. For each spatial ODE, the spatial boundary conditions for that dimension determine what values of the eigenvalues/separation constants are possible.

The general solution to one of the ODEs is a weighted sum of the possible solutions (eigenfunctions), for example for the x dimension,

$$X(x) = \sum_{p=1}^{\infty} a_p X_p(x) \tag{3.22}$$

where a_p is the weighting coefficient. The letter p is used to index the value of the separation constant/eigenvalue. So an individual solution to the PDE is the product solution:

$$n_{pqr}(t,x,y,z) = X_p(x)Y_q(y)Z_r(z)T_{pqr}(t) \tag{3.23}$$

where p,q,r, are used to index the value of the separation constants for each of the three dimensions,$-l_p^2$,$-m_q^2$,$-n_r^2$, which must satisfy $-\mu_{pqr} = -l_p^2 - m_q^2 - n_r^2$.

For an N-dimensional PDE (i.e. N independent variables), there are N separation constants linked by one equation. This means $N-1$ separation constants can vary freely (i.e. are independent) and the remaining one is dependent on the others via the equation. The separation constants for the spatial dimensions (l_p^2,m_q^2,n_r^2) are chosen to be independent, and the separation constant for the temporal dimension (μ_{pqr}) depends on them via the separation equation (so is indexed/labelled with pqr). This is convenient as it will be shown that the spatial separation constants/eigenvalues are constrained to discrete values by the spatial boundary conditions (BCs), whereas the temporal separation constant/eigenvalue can take continuous values, and are then constrained to discrete values by the separation equation (Eq.3.20).

The general solution to the PDE is a weighted summation of all the allowed PDE solutions (allowed means the separation equation Eq.3.20 is satisfied):

$$n(t,x,y,z) = \sum_{i=1}^{\infty} c_i n_i(t,x,y,z) = \sum_{p=1}^{\infty}\sum_{q=1}^{\infty}\sum_{r=1}^{\infty} c_{pqr} X_p(x)Y_q(y)Z_r(z)T_{pqr}(t) \tag{3.24}$$

where $c_i \equiv c_{pqr}$ is a weighting coefficient. All the multiplicative coefficients inside $X_p(x)$, $Y_q(y)$, $Z_r(z)$, $T_{pqr}(t)$ can be gathered into c_{pqr}. The temporal BC (an initial condition) is applied to this general solution as a final step to find the weighting coefficients c_{pqr}.

3.6.2.1 Interpreting a Product Solution

The PDE's product solution is a linear combination of product terms $\sum T(t)S(\mathbf{r})$, each of which describes a spatial shape $S(\mathbf{r})$ that is independent of time but whose amplitude changes according to the $T(t)$ term in the product. These $S(\mathbf{r})$ can be called spatial modes, which sum to give a resultant spatial shape. Each mode $S(\mathbf{r})$ has a different $T(t)$, so their amplitudes change at different rates, hence the resultant shape changes with time.

3.6.2.2 Spatial Dimensions

The separated ODEs in the spatial dimensions have the form

$$\frac{d^2}{dx^2}X(x) = vX(x) \tag{3.25}$$

where eigenvalue v equals the separation constant, e.g. $-l^2$ for the x-dimension. The ODE is a self-adjoint operator, so its eigenvalues are real and its eigenfunctions $X(x)$ are orthogonal and form a complete set. Therefore, the general ODE solution Eq.3.22 ($X(x) = \sum_{p=1}^{\infty} a_p X_p(x)$) is a Fourier Series. The different eigenvalues allowed by the boundary conditions are indexed with p, so $v_p = -l_p^2$. In this text, index $p = 0$ will always correspond to eigenvalue $v_p = -l_p^2$=0.

The general 1D solution Eq.3.22 has explicit form :

$$X(x) = Ax + B + \sum_{p=1}^{\infty} C_p \cosh(\sqrt{v_p}x) + D_p \sinh(\sqrt{v_p}x) \tag{3.26}$$

Before boundary conditions are applied, the summation is over real eigenvalues $v_p = -l_p^2$, both positive and negative, which is equivalent to summing over real and imaginary positive values of l_p.

$$X(x) = Ax + B + \sum_{p=1}^{\infty} C_p \cos(l_p x) + D_p \sin(l_p x) \tag{3.27}$$

In this explicit form, the eigenfunction for the eigenvalue with index $p = 0$ ($v_p = -l_p^2 = 0$), is outside the summation because it has a different form, so the summation starts at $p = 1$.

3.6.2.3 Temporal Dimension

The temporal ODE

$$\frac{\partial T(t)}{\partial t} + \mu D T(t) = 0$$

(where $-\mu$ is the separation constant, $-\mu D$ is the eigenvalue) has solution

$$T(t) = T(0)e^{-t\mu D}$$

where $\mu > 0$ gives exponential decay; $\mu = 0$ gives constant $T(t)$; $\mu < 0$ gives exponential growth, which is unphysical. The time dimension is an initial value problem (IVP), so has an open boundary, and the eigenvalues are not limited to discrete values. In the PDE solution (Eq.3.24), the $T_{pqr}(t)$ are

$$\begin{aligned} T_{pqr}(t) &= E_{pqr} e^{-t\mu_{pqr} D} \\ &= E_{pqr} e^{-t(l_p^2 + m_q^2 + n_r^2)D} \end{aligned}$$

3.6.3 Boundary Conditions

The spatial boundary conditions determine the values of the unknown parameters, i.e. the eigenvalues, and the initial condition determines the values of the coefficients c_{pqr} in

Eq.3.24.

The case considered here is a rectangular domain with the boundaries orthogonal to the coordinate directions, i.e. lines with a constant value of one coordinate. This makes applying boundary conditions much simpler: the ODE in each dimension has a boundary condition that is independent of the other dimensions, so the ODE problems can be solved individually, rather than simultaneously.

Separation of variables requires homogeneous PDEs, and that all BCs are homogeneous except for one - for transients, it is the temporal dimension that is not homogeneous. The case considered here is hard wall boundary conditions in each spatial dimension, which means that the flux normal to the boundary (direction $\hat{n}$) is zero: $j_{\hat{n}} = 0$. Since the flux is $j_{\hat{n}}\hat{n} = -D\frac{\partial n(t,x,y,z)}{\partial \hat{n}}\hat{n}$ this means $\frac{\partial n(t,x,y,z)}{\partial \hat{n}} = 0$, which is a homogeneous Neumann condition. Since each spatial dimension has the same boundary conditions, the solution will have the same form. The derivation for the x-dimension will be shown.

3.6.3.1 Spatial Dimension - Hard Wall Boundary Conditions

Applying hard wall boundary conditions on a rectangular domain in the x dimension, $\frac{\partial X_p(x)}{\partial x} = 0$, gives

$$l_p = \frac{p\pi}{L_x}$$

so the general solution to the ODE is:

$$X(x) = B + \sum_{p=1}^{\infty} C_p \cos(\frac{p\pi}{L_x}x) \tag{3.28a}$$

$$= \sum_{p=0}^{\infty} C_p \cos(\frac{p\pi}{L_x}x). \tag{3.28b}$$

where p are only real positive integers. The $p = 0$ term, $X_p(x) = B$, can be included in the summation, since $C_p \cos(\frac{p\pi}{L_x}x) = \text{constant}$ for $p = 0$.

The solution in the y and z dimensions are the same except the boundaries are at $y = L_y$ and $z = L_z$ instead of $x = L_x$

3.6.3.2 Temporal Dimension - Initial Boundary Conditions

After the spatial boundary conditions are applied, the temporal boundary conditions are applied to the resulting summation of product solutions (Eq 3.24) to find the coefficients for this summation, c_{pqr}. The explicit form after spatial boundary conditions have been applied is:

$$n(t,x,y,z) = \sum_{p=0}^{\infty} \cos(l_p x) \sum_{q=0}^{\infty} \cos(m_q y) \sum_{r=0}^{\infty} \cos(n_r z) e^{-t(l_p^2+m_q^2+n_q^2)D} c_{pqr} \tag{3.29}$$

where $l_p = \frac{p\pi}{L_x}$, $m_q = \frac{q\pi}{L_y}$, $n_r = \frac{r\pi}{L_z}$, and p, q, r are real positive integers. It is simpler to combine all the coefficients into a single coefficient c_{pqr}.

By comparing the initial distribution to the general solution, the unknown coefficients, c_{pqr}, can be found. The initial condition $n(x, y, z, 0)$ is equated to the solution at

$t = 0$:

$$n(x, y, z, 0) = \sum_{p=0}^{\infty} \cos(l_p x) \sum_{q=0}^{\infty} \cos(m_q y) \sum_{r=0}^{\infty} \cos(n_r z) c_{pqr} \tag{3.30}$$

However, this is one equation with many unknown coefficients. The fact that the general solution is a summation of orthogonal functions, i.e. a Fourier series, can be used to isolate a single coefficient at a time. Multiplying by one of these product terms and integrating over multiple dimensions, eliminates all terms except that which matches the multiplying term.

For example, multiplying Eq.3.30 by one of the product terms, $\cos(\frac{a\pi x}{L_x}) \cos(\frac{b\pi y}{L_y}) \cos(\frac{c\pi z}{L_z})$, whose index values are $p = a$, $q = b$, $r = c$ and then integrating over all the dimensions gives

$$\begin{aligned} \int_0^{L_x} \int_0^{L_y} \int_0^{L_z} & \cos(\frac{a\pi x}{L_x}) \cos(\frac{b\pi y}{L_y}) \cos(\frac{c\pi z}{L_z}) n(x, y, z, 0) dxdydz \\ &= \int_0^{L_x} \int_0^{L_y} \int_0^{L_z} \cos(\frac{a\pi x}{L_x}) \cos(\frac{b\pi y}{L_y}) \cos(\frac{c\pi z}{L_z}) \\ &\qquad c_{pqr} \sum_{p=0}^{\infty} \cos(\frac{p\pi x}{L_x}) \sum_{q=0}^{\infty} \cos(\frac{q\pi y}{L_y}) \sum_{r=0}^{\infty} \cos(\frac{r\pi z}{L_z}) dxdydz \end{aligned} \tag{3.31}$$

The right side of Eq.3.31 is simply:

$$c_{abc} \frac{L_x}{2} \frac{L_y}{2} \frac{L_z}{2} \tag{3.32}$$

when $a, b, c > 0$. A factor of $\frac{1}{2}$ is removed for each index (a, b and/or c) that is zero.

Considering the left side of Eq.3.31, the initial condition has a product form $n(x, y, z, 0) = AX_{init}(x)Y_{init}(y)Z_{init}(z)$, which means the integrals in each dimension can be calculated independently.

$$A \int_0^{L_x} \cos(\frac{a\pi x}{L_x}) X_{init}(x) dx \int_0^{L_y} \cos(\frac{b\pi y}{L_y}) Y_{init}(y) dy \int_0^{L_z} \cos(\frac{c\pi z}{L_z}) Z_{init}(z) dz \equiv I_x(a) I_y(b) I_z(c)$$

The initial distribution is normalised using a factor A, such that the integral over the whole spatial domain matches the total number of carriers that are injected, N_T.

$$\int_0^{L_x} \int_0^{L_y} \int_0^{L_z} n(x, y, z, 0) dxdydz = A \int_0^{L_x} X_{init}(x) dx \int_0^{L_y} Y_{init}(y) dy \int_0^{L_z} Z_{init}(z) dz = N_T$$

Overall, the left side of Eq.3.31 is the product of normalising amplitude A and the three integrals above, $I_x(a)$, $I_y(b)$, $I_z(c)$. Therefore, Eq.3.31 can be written as

$$AI_x(a) I_y(b) I_z(c) = c_{abc} \frac{L_x}{2} \frac{L_y}{2} \frac{L_z}{2} \tag{3.33}$$

Note a factor of $\frac{1}{2}$ is removed for each index (a, b and/or c) that is zero. So the unknown coefficients c_{abc} are found by rearranging this expression to give

$$c_{abc} = A \frac{2}{L_x} I_x(a) \frac{2}{L_y} I_y(b) \frac{2}{L_z} I_z(c) \tag{3.34}$$

This is performed for many values of a, b, and c, and then the coefficients c_{abc} are substituted as c_{pqr} in the final solution (Eq.3.29)

$$n(t,x,y,z) = \sum_{p=0}^{\infty} \cos(l_p x) \sum_{q=0}^{\infty} \cos(m_q y) \sum_{r=0}^{\infty} \cos(n_r z) e^{-t(l_p^2+m_q^2+n_r^2)D} c_{pqr} \tag{3.35}$$

3.6.3.3 Initial Conditions for Silicon Wafer Measurements

For the initial conditions used in the measurement of the silicon wafers in Chapter 6, the evaluation of the integrals on the left side of Eq.3.31, $I_x(a)$,$I_y(b)$,$I_z(c)$, is shown here.

The initial condition is:

- In the x direction, $X_{init}(x)$ is Gaussian $X_{init}(x) = e^{-\frac{(x-(L_x/2))^2}{2\sigma^2}}$
- In the y direction, $Y_{init}(y)$ is a top hat of width w centred on $\frac{L_y}{2}$, so constant between $\frac{L_y}{2} - \frac{w}{2}$ and $\frac{L_y}{2} + \frac{w}{2}$
- In the z direction, $Z_{init}(z)$ is an exponential decay, $Z_{init}(z) = e^{-\alpha z}$, where α is the absorption coefficient.

The normalising amplitude coefficient is therefore

$$A = \frac{N_T \alpha}{(1 - e^{-\alpha L_z}) w \sqrt{2\pi}\sigma \operatorname{erf}(\frac{L_x}{2\sqrt{2}\sigma})} \tag{3.36}$$

The integrals on the left side of Eq.3.31 are as follows. In the x-dimension:

$$\begin{aligned} I_x(a) &= \int_0^{L_x} \cos(\frac{a\pi x}{L_x}) e^{-\frac{(x-(L_x/2))^2}{2\sigma^2}} dx & (3.37) \\ &= \frac{1}{2}\sqrt{\frac{\pi}{2}}\sigma(1+e^{i\pi a}) e^{-\frac{(\pi a(\pi\sigma^2 a + iL_x^2))}{2L_x^2}} \left(\operatorname{erf}(\frac{L_x^2 - 2i\pi\sigma^2 a}{2\sqrt{2}L_x\sigma}) + \operatorname{erf}(\frac{L_x^2 + 2i\pi\sigma^2 a}{2\sqrt{2}L_x\sigma}) \right) & (3.38) \end{aligned}$$

The first bracketed term equals 2 for even values of index a and equals 0 for odd values of a. In the exponential term, the second part of the exponent gives a repeating sequence, starting from index $a = 0$, of 1,-i,-1,i,... . The error functions both ≈ 1 for $L_x \gg \sigma$ (5cm $\gg$ 1mm). Overall, only the even a terms are non-zero and these are real, so

$$I_x(a) = \sqrt{2\pi}\sigma e^{-\frac{\pi^2 a^2 \sigma^2}{2L_x^2}} (-1)^{\frac{a}{2}}$$

In the y-dimension:

$$I_y(b) = \int_{\frac{L_y}{2}-\frac{w}{2}}^{\frac{L_y}{2}+\frac{w}{2}} \cos(\frac{b\pi y}{L_y}) dy = \frac{2L_y \cos(\frac{b\pi}{2}) \sin(\frac{b\pi w}{2L_y})}{b\pi}$$

for $b > 0$. For odd b, $I_y(b) = 0$. For $b = 0$, the integrand is 1 and $I_y(b) = w$.

In the z-dimension:

$$\begin{aligned} I_z(c) &= \int_0^{L_z} \cos(\frac{c\pi z}{L_z}) e^{-\alpha z} dz & (3.39) \\ &= \frac{L_z^2 \alpha(-\cos(\pi c) e^{-\alpha L_z} + 1)}{L_z^2 \alpha^2 + \pi^2 c^2} & (3.40) \end{aligned}$$

For the silicon wafer measurements, αL_z is large so the exponential tends to zero, leaving

$\frac{L_z^2\alpha}{L_z^2\alpha^2+\pi^2c^2}$. Since αL_z is large, this is approximately $\frac{1}{\alpha}$.

3.6.4 Monomolecular Bulk Recombination

The separation of variables method described above for the diffusion equation without recombination, can be easily extended to account for monomolecular recombination with a spatially uniform rate constant. The continuity equation is then

$$\frac{\partial n(t,x,y,z)}{\partial t} = D\left(\frac{\partial^2 n(t,x,y,z)}{\partial x^2} + \frac{\partial^2 n(t,x,y,z)}{\partial x^2} + \frac{\partial^2 n(t,x,y,z)}{\partial x^2}\right) - kn(t,x,y,z) \tag{3.41}$$

A solution with product form, $n(t,x,y,z) = X(x)Y(y)Z(z)T(t)$, is substituted in to give

$$\frac{1}{DT(t)}\frac{\partial T(t)}{\partial t} = \frac{1}{X(x)}\frac{\partial^2 X(x)}{\partial x^2} + \frac{1}{Y(y)}\frac{\partial^2 Y(y)}{\partial y^2} + \frac{1}{Z(z)}\frac{\partial^2 Z(z)}{\partial z^2} - \frac{k}{D} \tag{3.42a}$$

Each term must be a constant, so the separation equation becomes

$$-\mu = -l^2 - m^2 - n^2 - (k/D) \tag{3.43}$$

Including monomolecular bulk recombination adds a constant to the separation equation, but in contrast to the other constants which are eigenvalues of ODEs, it has a single value. It appears in the final solution where the separation constant for the temporal solution is written in terms of the separation equation.

$$\begin{aligned} T_{pqr}(t) &= E_{pqr}e^{-t\mu_{pqr}D} && (3.44)\\ &= E_{pqr}e^{-t(l_p^2+m_q^2+n_r^2+(k/D))D} && (3.45)\\ &= E_{pqr}e^{-t(l_p^2+m_q^2+n_r^2)D}e^{-kt} && (3.46) \end{aligned}$$

The e^{-kt} can be factored out, so this is exactly the same as multiplying the solution without recombination by e^{-kt}. This is because the process $\frac{\partial n}{\partial t} = -kn$ is linear in density, so it applies the same fractional rate to all positions regardless of density, so the whole 3D distribution changes by a uniform scaling.

3.6.5 Monomolecular Surface Recombination

In the previous section 3.6.4, the recombination constant k was considered to be uniform throughout the material, including at the surface, meaning hard wall boundary conditions were considered: $j_{\hat{n}}\hat{n} = -D\frac{\partial n(t,x,y,z)}{\partial \hat{n}}\hat{n} = 0$, which is a homogeneous Neumann condition. However, for many materials the recombination constant is increased at the surface, and in this work this is relevant for the silicon wafers without surface passivation, or for perovskite-CTL bilayers in which the interface behaves as a recombination centre, which is observed for PCBM and C_{60} bilayers. This increased recombination constant at the surface is incorporated into the analytical model as a boundary condition. For example, on the left boundary at $z = 0$

$$j_{\hat{n}}\hat{n} = -D\frac{\partial n(t,x,y,z)}{\partial \hat{n}}\hat{n} = -Sn(t,x,y,z)\hat{n}$$

where S is an (unsigned) constant called the surface recombination velocity with units of ms^{-1} (the minus sign is for the left boundary of a domain, $z = 0$). This is a homogeneous Robin condition, which for the left boundary in the z-dimension ($z = 0$) is written as

$$j_z|_{z=0}\hat{z} = -D\left.\frac{\partial Z(z)}{\partial z}\right|_{z=0}\hat{z} = -S_{LHS}Z(z)|_{z=0}\hat{z}$$

so

$$\left.\frac{\partial Z(z)}{\partial z}\right|_{z=0} = HZ(z)|_{z=0}$$

where $H = \frac{S_{LHS}}{D}$. For the examples in this work, the left boundary is assigned a surface recombination constant and the right boundary is assigned a hard wall condition. Applying these boundary conditions to the solution Eq.3.27, ($Z(z) = Az + B + \sum_{r=1}^{\infty} C_r\cos(n_r z) + D_r\sin(n_r z)$ where $-n_r^2$ is the rth separation constant) yields

$$\tan(n_r L_z) = H/n_r$$

which is a transcendental equation - it cannot be rearranged for n_r. The solutions n_r can be found numerically by finding the roots of $\tan(n_r L_z) - H/n_r = 0$. This is the form of the solution for $S > 0$ (the solution for $S = 0$ was considered in sections 3.6.3 and 3.6.4). Therefore, n_r is never zero, and so it is chosen to only consider indices $r > 0$ (to be consistent with sections 3.6.3 and 3.6.4 where $n_0 = 0$). The solution $Z_r(z) = C_r\cos(n_r z) + D_r\sin(n_r z)$ can be re-written as

$$Z_r(z) = \gamma_r\cos(n_r(L_z - z))$$

where $\gamma_r = \frac{C_r}{\cos(n_r L_z)}$. So the general solution in this dimension is

$$Z(z) = \sum_{r=1}\gamma_r\cos(n_r(L_z - z)) \tag{3.47}$$

This solution for $Z(z)$ can be incorporated into a 3D product solution with the coefficients γ_r absorbed into the 3D coefficients c_{pqr}. The work in this thesis considers cases where only the 1D solution is required. For the 1D continuity equation, the separation equation is just $-\mu_r = -n_r^2$. The coefficients γ_r are found as follows.

The coefficients for this Fourier series, γ_r, are found by considering the initial condition $n(0, z)$ expressed as a Fourier series solution, and using orthogonality of the terms. The initial condition is an exponential decay $n(0, z) = e^{-\alpha z}$. Expressing the initial condition as a Fourier series and then multiplying by one of the product terms, $\cos(n_r(L_z - z))$, whose index value is $r = a$, and then integrating over the z-dimension gives

$$\int_0^{L_z}\cos(n_a(L_z - z))n(z, 0)dz = \int_0^{L_z}\cos(n_a(L_z - z))\sum_{r=1}^{\infty}\gamma_r\cos(n_r(L_z - z))dz \tag{3.48}$$

which is evaluated as

$$\frac{\alpha\cos(n_a L_z) - \alpha e^{-\alpha L_z} + n_a\sin(n_a L_z)}{\alpha^2 + n_a^2} = \gamma_a\left(\frac{L_z}{2} + \frac{1}{4n_a}\sin(2n_a L_z)\right) \tag{3.49}$$

This equation is rearranged for γ_a, and this is performed for multiple values of the index a. The final solution is

$$n(t,z) = \sum_{r=1} Z_r(x)T_r(t) \tag{3.50}$$

$$= \sum_{r=1} \gamma_r \cos(n_r(L_z - z))e^{-t(n_r^2)D} \tag{3.51}$$

3.6.6 Sheet Density - 2D Diffusion Equation

In this work, the experiment (OPTP) measures a signal that is proportional to the integral over thickness (z-dimension) of the carrier density, which is the sheet density, $n_s(t,x,y)$. This means that the product solution for the density $n(t,x,y,z)$ can be analytically integrated over depth z to give a 2D product solution for the sheet density, $n_s(t,x,y)$. If a closed form expression for this integration is possible, then this 2D sheet density solution can be evaluated instead of the 3D solution. This is distinct from solving the 2D diffusion equation. It is quicker to evaluate the expression for the sheet density than the expression for the density, which is beneficial for fitting the model to data.

For the case that the recombination is either ignored or is linear with uniform rate constant (so no increased rate constant at the surface), then the sheet density can be modelled by the 2D diffusion equation in the x-y plane (with the sheet density $n_s(t,x,y)$ as the dependent variable). This is distinct from the general case described just prior, in which the 3D diffusion equation is solved and then this 3D solution is analytically integrated to get a 2D solution for the sheet density. The 2D equation is sufficient in these particular cases because the distribution in the z-dimension does not affect the evolution of the sheet density. This is because when recombination is linear in density and the rate constant is uniform, then this applies a uniform scaling everywhere in the domain, so the particular distribution in the z-dimension does not influence the decay of the sheet density. However, if the surface has a different rate constant to the bulk then a full 3D solution is required as the distribution in the z-dimension does affect the decay rate.

3.6.7 Pump-Probe Overlap Integral for the Analytical Solution

The signal measured by OPTP is proportional to the pump-probe overlap integral of the sheet density, that is given by:

$$\langle n_s \rangle_T = \int\int n_s(x,y)E_T^{norm}(x,y)dxdy$$

where

$$E_T^{norm}(x,y) = T_0 e^{\frac{-(x-x_0)^2}{2\sigma_T^2}} e^{\frac{-(y-y_0)^2}{2\sigma_T^2}}$$

represents the normalised shape of the THz pulse. This pump-probe overlap integral can decay due to recombination or in-plane diffusion out of the probe region. If the latter effect is not significant, then the cross-sectional profiles of the probe and carrier density do not change with time, and the overlap can be calculated at just one time, using the initial density profile. If in-plane diffusion is significant, then the overlap integral must be calculated for each delay time. This integral can be performed on the analytical solution for sheet density $n_s(t,x,y)$, either the 2D Fourier series solution $n_s(t,x,y)$, or for cases with surface recombination, on the 3D solution $n(t,x,y,z)$ integrated over thickness. For example, for the 2D solution

$$\langle n_s \rangle_T = \int\int n_s(x,y) E_T^{norm}(x,y) dxdy \tag{3.52a}$$

$$= \int_0^{L_x} \int_0^{L_y} c_{pq} \sum_{p=0}^{\infty} \cos(l_p x) \sum_{q=0}^{\infty} \cos(m_q y) e^{-t(l_p^2+m_q^2)D} T_0 e^{\frac{-(x-x_0)^2}{2\sigma_T^2}} e^{\frac{-(y-y_0)^2}{2\sigma_T^2}} dxdy \tag{3.52b}$$

This is evaluated to give

$$\langle n_s \rangle_T = c_{pq} \sum_{p=0}^{\infty} \sum_{q=0}^{\infty} I_x(p).I_x(q).T_0 e^{-t(l_p^2+m_q^2)D}$$

where the I_x integral was stated in Eq.3.38. I_x integrals have analytical solutions, which are just scalars so this expression for the overlap $\langle n_s \rangle_T$ is much quicker to evaluate than evaluating the expression for the distribution $n_s(x,y)$ at a large number of x and y positions and then integrating this numerically. The computational speed is particularly useful when iteratively fitting the model to the data.

Chapter 4

Optical Measurements of Charge-Carrier Dynamics in Perovskite-CTL Bilayers

4.1 Introduction

In perovskite solar cells, charge transport layers (CTLs) on either side of the perovskite layer provide the asymmetry that gives photovoltaic action. To maximise power conversion efficiency, the extraction selectivity of these layers must be maximised and the recombination at the interfaces must be minimised. Therefore these electrical properties need to be studied and understood. Optical measurements of these electrical properties are preferred, because the contacts required for electrical measurements can influence the results, whereas optical measurements are contactless. Furthermore, whilst measurements of full device stacks will be closest to operational conditions, it is difficult to distinguish the behaviour of each layer and interface. Measurements of bilayers comprising the perovskite light absorber and a CTL, which can only be done optically, enable single interfaces to be studied. Compared to a full device, a bilayer has a reduced built-in field and lacks the second CTL that draws one carrier type away from the first CTL, so carrier distributions will be different. However, bilayers enable rate *constants* to be extracted more easily, and these should still be applicable to the full device. Hence optical measurements of these bilayers are attractive and are studied in this work.

Electronic recombination and transport across the interface can be measured by optical techniques in which the absorption or emission of radiation is related to the electron and hole densities, such as time resolved PL, transient absorption (TA) or OPTP. All of these techniques can in principle measure the charge carrier density in both the perovskite layer and the charge transport layer, however the perovskite layer usually gives the largest signal. For all techniques, the number of carriers transported to the CTL may only be a small fraction of the number that are excited in the perovskite layer, so any OPTP, TA and TRPL signals from the CTL will be smaller than from the perovskite. For OPTP, the signal is proportional to the charge carrier mobility at THz frequencies and this is often much smaller for carriers in the CTLs, so carriers in the perovskite layer will contribute a larger $\Delta E/E$ signal. For Spiro-OMeTAD the carrier mobility is thought to be $10^{-5} - 10^{-3}$cm^2/Vs for thin films [263–266], depending on the measurement technique and sample fabrication (10^{-3}cm^2/Vs for single crystals [267]), and for PCBM the mobility is thought to be 1 cm^2/Vs or less [268–270], whereas for perovskite thin films the THz sum mobility is found to be tens of cm^2/Vs [271]. Indeed, in this work layers of the CTLs on quartz were photoexcited above their bandgap using a wavelength of 410nm and no photoconductivity signals from these layers were observed via OPTP at the experimental fluences. In transient absorption measurements, the features related to the perovskite and CTL may be at different energies allowing them to be distinguished. Similarly for TRPL, the PL spectral peak may be at a different energy for the perovskite and CTL, although the CTL has a much lower radiative efficiency.

This chapter presents optical spectroscopy studies of bilayers consisting of a lead halide perovskite and an organic charge transport layer. This work employs both steady state and time resolved absorption and photoluminescence techniques, where time resolved techniques are used to monitor the charge carrier population in the perovskite layer as a function of time. Optical pump-THz probe spectroscopy is also used to monitor the population dynamics and due to a simpler data interpretation is analysed with a mathematical model. The population dynamics measured by OPTP are simulated using a model that incorporates Gauss's law to account for Coulombic forces between electrons and holes. The numerical method for solving this model is presented, and the solutions are compared to the experimental observations. The experimental data is also compared to an analytical solution of a simplified continuity equation that describes some of the samples very well. Prior to presenting the experimental data and analysis, an overview of previous reports in the literature of time resolved measurements of bilayers is presented and the different analysis approaches are reviewed.

4.2 Literature Review - Optical Measurements of Bilayers

4.2.1 Introduction

The impact of adding a CTL to the perovskite layer, such as additional carrier extraction or recombination, can be studied by observing its influence on the population decay in the perovskite, or by observing the population change in the CTL, i.e. a direct measurement of extraction (as mentioned previously, the signal in the CTL is often much smaller). Investigations reported in the literature have unsurprisingly focussed on the most popular materials, so CTLs such as TiO_2 (mesoporous or compact), PCBM, C_{60}, and Spiro-OMeTAD, and in the early years, perovskite compositions such as $MAPbI_3$ or $MAPbI(_{1-x}Cl_x)_3$. However, the results reported in the literature have significant variation, which is due to a number of factors that are discussed in the following.

Firstly, measurements of the perovskite's charge carrier population (an indirect measurement of extraction) often study the decay of a signal over picoseconds to nanoseconds, whereas measurements of the CTL's population often measure small signals where only the timescale of the signal rise can be quantified. Therefore, they are reporting different quantities. For most interfaces at least some extraction may occur very quickly, because some carriers will be photoexcited immediately adjacent to the interface and immediately after photoexcitation the driving force for extraction (quasi-Fermi level differences between perovskite and CTL) will be largest. However, after the initial extraction, the gradients in Fermi level will be reduced, and the remaining carriers will be further from the interface, so the removal rate may become transport limited. Indeed, in the literature, the direct measurements of the CTL population, if they are to be believed, report extraction within hundreds of femtoseconds, whereas monitoring the decay of the perovskite population gives extraction times of hundreds of picoseconds to nanoseconds. It is to be expected that a good CTL will be able to have some very fast extraction, but since many CTLs show this fast extraction yet have widely different performance, then it is more useful to study how extraction proceeds after this initial extraction, when the driving force is reduced. In this work it is suggested that continued decay at later times is a sign of interface recombination.

Secondly, measurements on the same nominal materials do not always agree well because the materials can actually be quite different, for example the quality of the layers or the exact composition of alloys may vary. This may lead to differences in the densities of interface states or the doping levels, which will both have a large impact on the measurements of bilayers, as well as the performance of devices.

Furthermore, the literature results can disagree even if the materials are hypothetically exactly the same. This is because when different experimental conditions are used, the data cannot be directly compared, only the parameter values extracted by fitting a model to the data can be compared, and these fit results will only agree for different conditions if the model is very accurate. However, models are usually simplifications, and also require many parameters to be specified that may not be known very accurately (such as fluences or thicknesses). Furthermore, even if the experimental conditions are the same, using two different simplified models could extract different results from the same data. For example, in time resolved measurements the carrier density as a function of time is modelled to different degrees of complexity. In most works a zero dimensional (0D) model is used that does not account for spatial distribution of densities or defects, whereas in other works this spatial dependence is incorporated in the model, and so the physical meaning of the extracted recombination rate constants can differ.

In the following, the different conclusions in the literature will be summarised, and factors which may be causing these differences will be highlighted, which includes the sample variations, the measurement conditions, and the data analysis.

4.2.2 TRMC and OPTP on Perovskite-CTL bilayers

One of the main techniques used in this work is OPTP, and this has been used in a limited number of previous studies of bilayers. Due to their relevance, these works will be reviewed in more detail, and the differing conclusions reached in these studies are highlighted here.

In 2015, Ponseca et al. used TRMC and OPTP to study $MAPbI_3$ with Spiro or PCBM coated on top, using 590nm excitation.[272] For both techniques the signal is related to the carrier density in the perovskite layer only. The authors observed that with (undoped) Spiro on top, the initial amplitude was reduced to 1/3 compared to the plain perovskite sample, which they attribute to the fast extraction of holes within the rise time (sub-ps for OPTP). The signal amplitude suggests that if all holes are removed within the rise time, the electrons remaining in the perovskite have half the mobility of the holes.

This is in contrast to their previous paper[273] where they observed a reduction in initial amplitude for a perovskite-CTL bilayer incorporating the electron extractor meso-TiO_2, (400nm excitation) and by similar reasoning concluded that the remaining holes had half the mobility of the electrons. These contradictory conclusions derived from the initial amplitudes highlight that the initial carrier density generated in the perovskite may not have been well controlled. In the earlier work, [273] the meso-TiO_2 sample was compared to meso-Al_2O_3, and since the particles used to form the meso-layer are different sizes, this may have resulted in different amounts of light scattering and volume fraction of perovskite. In the later work [272], the Spiro layer itself could have been parasitically absorbing some of the 590nm pump which was incident through the Spiro layer (although changes in reflection and transmission were accounted for), or the perovskite layer itself may have differed between the reference and Spiro sample, as their supplementary information (SI) shows poor substrate coverage with 4μm thick crystals, suggesting poor fabrication quality. Good fabrication recipes were not well established at this time.

The authors found that the normalised decay shape for the Spiro sample was the same as for the plain perovskite reference, and under the assumption of complete hole extraction within the rise time, they attributed this matching decay shape to possible hole doping in the perovskite. This would mean the hole population in the perovskite would not be significantly affected by the extraction of photoexcited holes, so the recombination dynamics in the perovskite would not be affected.

For the PCBM bilayer, they observed a continuous decay without a plateau, so the extraction does not slow down as electrons accumulate in the ETL, which they attributed to interface recombination across the interface, between extracted electrons and remaining holes preventing accumulation of extracted electrons in the CTL. This cross-interface recombination would be enhanced by possible p-doping in the perovskite.

They support the p-doping hypothesis with work by Hutter et al.[162], who argued that a monoexponential decay observed in TRPL data indicates doping (although there are multiple explanations for monoexponential decay, see section 3.4), and that decays for $MAPbI_3$ samples could only be fit by including doping. Also, they suggested it is the hole mobility that is lower as hole masses are reported to be higher. However, the materials in the work of Hutter et al. [162] were fabricated by a different process, so conclusions from this work are less applicable to the work of Ponseca et al.[272].

In 2017, Hutter et al. [274] performed TRMC on perovskite-CTL bilayers for which the $MAPbI_3$ layer was vapour deposited, which should be much more reproducible allowing a more reliable comparison of the bilayer and perovskite reference samples. The minimum resolution of TRMC is a few nanoseconds, so extraction within this time would reduce the initial amplitude. They observed that the initial amplitude was lower with Spiro on top, and the decay was slowed down compared to the plain reference sample for all fluences and wavelengths. They attributed this slower decay to fast hole extraction within the rise time (nanoseconds for TRMC), which would extend the lifetime of the remaining electrons provided cross-interface recombination was low. The small reduction in initial amplitude suggests electron mobility was 5 times larger than the hole mobility, contradicting their previous work [162, 273]. The authors argued that their previous observation[162] that the decay shape was instead the same for the Spiro bilayer and the reference was because doping was much higher in that case, so extracting photoexcited holes did not extend the lifetime of the remaining electrons, as it did in this later work. In the later work,[274] they also observed that the initial amplitude for the bare perovskite sample grew sub-linearly with fluence whereas the initial amplitude grew linearly with fluence for Spiro. The sub-linear relation for the reference was attributed to increased higher order recombination during the rise time (nanoseconds) for higher fluences, since higher order recombination increases super-linearly with carrier density. For Spiro, the linear relation was attributed to fast hole extraction which inhibits the super linear increase in recombination.

In the later work[274], PCBM and C_{60} had greatly reduced initial amplitude which was attributed to fast decay within the rise time (nanoseconds), whereas other fullerene variants had only slightly reduced initial amplitude, which was attributed to their CBs being higher causing electron extraction to be slower.

Overall, the conflicting conclusions in these works show the current uncertainty in this area, and the need to carefully control the photogenerated density in the perovskite layer in order to make reliable conclusions from the initial amplitude of the signal (i.e. whether there is decay within the instrument response time, <1ps).

4.2.3 TA on Bare Perovskite Layers

Transient absorption (TA) setups are more common than OPTP and have thus been more widely used to study perovskite-CTL bilayers. However, interpreting TA data and relating it to carrier density is more challenging than for OPTP, and the wide variety of approaches contributes to the variety of conclusions in the literature. To understand the variations and uncertainties in the literature reports of TA measurements on bilayers, the varying interpretations of TA measurements on bare perovskite layers are summarised first.

One measure of carrier density is to look at the amplitude of the ground state bleach (GSB). However, in addition to bleaching by changes in state occupation, there are other effects that determine the TA difference spectrum, meaning a more detailed analysis is required. Indeed Pydzinksa et al.[275] pointed out that the initial amplitude of the TA difference signal (ΔOD) at a single probe wavelength is sublinearly related to fluence, and instead it is the initial amplitude of the integral over energy of the TA features that is linearly related to the fluence. This is because the integral can account for the changing shape of the TA spectrum with respect to time delay, whereas for a single probe wavelength, the changing spectral shape slows the rise time of this signal, with a slower rise for higher fluences. The transient curves from these two methods are most different at early times, when the spectral shape is changing the most, which will be discussed below. However, many papers study the transient at a single wavelength only, so the first ∼10ps are probably less reliable.

An alternative to using a single probe wavelength is to consider the width of the ground state bleach (GSB) with respect to energy (so similar to an integral), since a higher density of excited carriers gives band occupation, and thus bleaching, up to high energies. The GSB width was found by Manser et al.[276], to increase in proportion to $n(t=0)^{2/3}$ (the initial density $n(t=0)$ was estimated from the pump fluence), as expected from the Burstein Moss model[277]. However, they observed a density threshold above which this increase occurs, so this measure cannot be used at low fluences. Others have reported that the bleach width grows linearly with fluence [275], highlighting the low precision of this measure.

The photoinduced change in the transmission spectrum is not only determined by changes in occupation such as the GSB, but by other effects as well, meaning more detailed analysis is required to extract a signal that is proportional to carrier density. The spectrum near the band edge is not as simple as just a GSB, as a narrow photoinduced absorption (PIA) is observed at energies just below the GSB, and a broad PIA is observed above the GSB. The sub-gap PIA is widely attributed to a uniform redshift of the absorption spectrum in the presence of photoexcited carriers. This is due to either bandgap renormalisation (BGR) [184, 240], or the electroabsorption/Stark effect resulting from correlated electron-hole pairs setting up strong local electric fields [278]. If the equilibrium absorption coefficient increases monotonically with energy, a redshift of the spectrum results in an increased absorption coefficient (a PIA) at all energies, so this could also explain the broad PIA above the bandgap. The redshift gives a greater PIA in the range where the absorption spectrum changes steeply with energy, i.e. the bandgap energy, consistent with the strong sub-gap PIA. Yang et al.[184] found that both PIA features (sub-gap and broad above gap) grow as $n^{1/3}$ which is consistent with BGR, whereas an alternative interpretation of free carrier absorption is expected to grow as n^1. If the equilibrium absorption spectrum is not monotonically increasing with energy, but has an absorption enhancement near the bandgap due to electron-hole correlations, the redshift of the spectrum will result in decreased absorption at the original energy of the absorption peak, so a "derivative" shape is expected (the derivative of a single peak).

Mathematical modelling of these features is necessary for extracting a carrier density, but also for testing the accuracy of the interpretation. Price et al.[240] and Yang et al.[184] both used the Elliot formula and considered photoexcitation to modify the equilibrium absorption by state filling, i.e. bleaching. Price et al.[240] considered changes in the degree of reflection due to changes in the real refractive index, whereas Yang et al.[184] included a BGR induced shift in the continuum contribution, and the exciton resonance contribution was bleached and broadened (but not shifted by BGR). Some works have attributed the spectral changes over the first few picoseconds to exciton dissociation which removes the Stark effect [278, 279], whereas Price et al.[240] and Yang et al.[184] attribute the changes to carrier cooling, which reduces the bleach at high energies and increases the bleach at low energies.

The measured transmission is expected to change due to photoinduced changes in absorption, but there is disagreement about the degree to which photoinduced changes in the reflection and transmission at interfaces contribute to changes in the measured transmission. Liu et al.[280] measured the change in reflection and suggest that that the derivative shape they observe contributes to the PIA in the transmission measurement, and will be more significant for films with more scatter (since grain sizes are in the range of tens of nm to microns, larger grains in this range will have more scatter of visible wavelengths). Also, they observe the refection feature has a different decay time to the absorption features (this is because reflection at an interface is more sensitive to the density at the interface, rather than the total density through the thickness), which will complicate interpretation of the transmission spectra.

Price et al.[240] determined the change in real refractive index and thus reflection by estimating a change in the absorption coefficient from the TA data, and then using Kramers-Kronig relations to estimate the change in the real refractive index. However, Tamming et al.[281] argue that this method is model dependent and that not accounting for scatter will lead to large errors. Instead they used a white light interferometer to determine the real refractive index change under illumination, and then the change in absorption coefficient was calculated using Kramers-Kronig relations. The calculated transmission and reflection spectra match the measurements, in amplitude as well as shape. They conclude reflection clearly has some effect on transmission spectrum at the band edge, but at higher energies it is weak, so they believe the broad PIA is instead due to BGR, not reflection.

Furthermore, Gosh et al.[282] compared samples with different degrees of scatter (thin films and nanocrystals) and predicted that if the change in reflectivity were the dominant cause of the broad PIA, the thin film and nanocrystals would have transmission changes with opposite signs. However, this was not observed, indicating the change in absorption is the dominant cause of the broad PIA.

Overall, these works highlight that relating the TA data to carrier density is not trivial, as BGR and carrier cooling must be considered and the impact of changes in reflection will depend on the particular sample.

In the works discussed above, the TA features are fit to physical models, but two alternative approaches are forms of global analysis called decay associated spectra (DAS) and evolution associated spectra (EAS) (or EADS and DADS for difference spectra) [283], that do not require an a priori model of the data. DAS involves fitting the time resolved

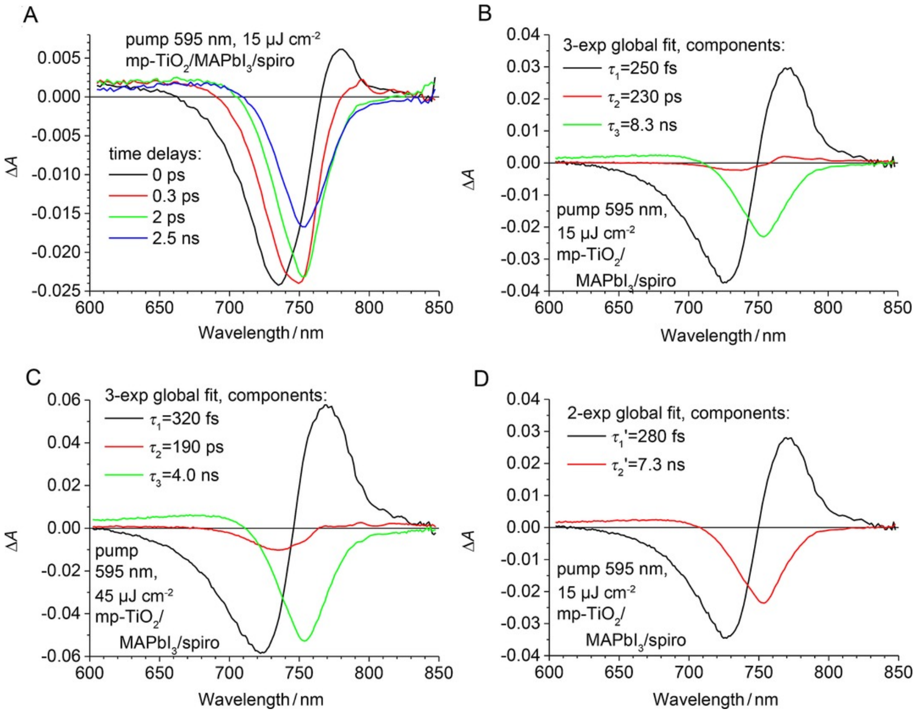

Figure 4.1: Example of DAS analysis of TA measurements of a perovskite layer. a) The TA difference spectra at selected delay times. b),c) Fits using 3 DAS spectra with monoexponential lifetimes of each spectrum indicated, for two different pump fluences. d) Fits using 2 DAS spectra. Reproduced from Ref.[279]

spectra using a sum of a few different spectra, each covering the full spectral range, that each have maximum amplitude at $t = 0$ and then decay in amplitude monoexponentially, but with different lifetimes. EAS considers sequential spectra, with the second spectrum rising with the decay lifetime of the first spectrum, so that the first spectrum evolves into the second, and so on. This approach has been used to model perovskite transient absorption spectra by a number of groups [279, 284–287]. For example, Pydzinksa et al.[279] used three spectra for DAS modelling (see Fig.4.1). One component has a slow decay and resembles a bleach due to state filling, and another component has a very fast decay and has a derivative shape centred around the bandgap, consistent with a redshift of the absorption spectrum. There is another component with an intermediate lifetime, which is suggested to be a component that compensates for the inaccuracy of using just two spectra that decay monoexponentially, and indeed becomes more significant for higher intensities where the recombination becomes less monoexponential (due to the increased contribution of bimolecular recombination).

This method is quite useful for distinguishing overlapping spectral features that have different decay rates, and whose spectral shape does not change with time [283]. However, it seems less appropriate for modelling solid state semiconductors in which the spectral features associated with certain effects change with time. This modelling approach does not connect the spectral shape to a physical model, but simply tries to distinguish the lifetimes of different features.

4.2.4 TA on Perovskite-CTL Bilayers

For bilayer samples, TA measurements have been used to monitor not only the carrier density in the perovskite layer but also in the CTL. These will be reviewed in turn in this section.

4.2.4.1 TA Measuring the Perovskite Carrier Density

For bilayer samples, the population in the perovskite layer can be measured and the effect of the CTL can be included in the model of population dynamics as population removal, whose rate is proportional to the population i.e. monomolecular. In the vast majority of works, the electron and hole populations are not distinguished in the model, even though removal only effects one carrier type. This approach therefore treats the electron and hole populations as equal (like in the ABC model) and so might be viewed as assuming that any selective extraction of one carrier type is closely followed by cross-interface recombination to decrease the population of the remaining carrier. The processes at the interface are likely to be more complex than modelling the interface extraction rate as linear in density, but it is an approximation that can be used to get an approximate timescale for the process and enables quantitative comparison of different materials.

Some models in the literature [19, 288, 289] include the spatial dependence of the carrier densities and so distinguish bulk and surface/interface effects and also the time taken for transport of carriers towards surface/interfaces. On the other hand, for models that disregard this spatial dependence, i.e. 0D models, the extracted effective rate constants/lifetimes will contain within them the effects of both bulk and surface recombination, and the transport processes. For example, DAS and EAS are inherently 0D models, but Pydzinska et al.[279] have attempted to distinguish bulk and surface effects in their DAS analysis.

Pydzinska et al.[279] considered a 0D model, and performed DAS as mentioned previously. The monoexponential decay lifetime for the bleach-like spectral component was found to be a function of intensity, i.e. bimolecular process), and extrapolating to zero intensity is assumed to provide the lifetime for the monomolecular processes. This monomolecular lifetime is considered to be a combination of the bulk and surface defect-mediated recombination. The fitted monomolecular recombination constant k_1 is a sum of the rate constants for the contributing monomolecular processes, so comparing samples with different interfaces allows the contribution of each interface to be determined. For Spiro, they found the Spiro interface contributed a rate constant equivalent to a lifetime of 15ns ($\tau = 1/k$), which was much slower than other CTLs they tested, such as 5ns for CuSCN, even though Spiro gives better device performance. This highlights that a fast surface rate is not necessarily good, as it may be related to detrimental recombination rather than extraction, so must be interpreted carefully. Since the timescale of nanoseconds is similar to the timescale for diffusion through these layers, the authors acknowledged that the transport time could be contributing to all their observed surface rates.

In a later study[275], the same authors compared this analysis to the commonly used approach of fitting the decay to a ABC/k_1-k_2-k_3 rate equation (with negligible k_3) [258] and found that both models give the same k_1 lifetimes, giving credence to the fitted k_1, but the k_2 lifetimes slightly differ. This later work studied PCBM bilayers, for which they found an additional surface decay lifetime of 3.5ns - so again on a timescale of nanoseconds.

A different approach to distinguishing bulk and surface rates was reported by Zhou et al[287]. They also performed EADS analysis but compared both TA and transient reflection (TR) measurements of the bilayers, illuminating through the CTL. Whilst TA is sensitive to carriers at all depths, TR is sensitive to carriers near the interface, so diffusion away from the interface will also cause the signal to decay. For 400nm excitation, PCBM reduces the initial amplitude of the TA signal, which was attributed to parasitic absorption rather than fast extraction, whereas for TR the initial amplitude was increased by adding PCBM, which was attributed to the PCBM's refractive index. For TA, an additional decay rate for the PCBM bilayer kicks in after 100ps, whereas for TR, both PCBM and Spiro accelerate the sub-ps decay. They assume that diffusion away from the surface cannot be faster by introducing a CTL (although band bending at the interface would change the carrier transport), and propose that sub-ps extraction/recombination is occurring and that only TR is sensitive enough to detect these changes in density at the interface. PCBM and Spiro had no effect on the sub-ps decay when excited with 600/710nm, which was attributed to carriers being less concentrated near the interface, so there was less sub-ps extraction.

Some literature reports have included the spatial dependence in the modelling. The first works on bilayers in 2013 by Stranks et al.[19] and Xing et al.[288], performed both TRPL and TA. In both works they considered that the CTL had an infinite removal rate for one carrier type (so zero density at the interface), and the bulk recombination rate was determined from the measurements without the CTL. Stranks et al. excited the perovskite layer on the opposite side to the CTL, and the analytical solution for this diffusion equation with bulk recombination and zero interface density was fit to the data for the bilayers by varying the diffusion coefficient. The diffusion coefficient was attributed to only the carrier that was extracted. This may not be very physical, since the electrons and holes do not diffuse independently because they are Coulombically attracted (so one should instead consider the ambipolar mobility), and also the approximation of infinite extraction rates may not be applicable.

Leng et al.[289] took a similar analysis approach to their TA measurements, modelling independent diffusion of each carrier type rather than ambipolar diffusion, except the extraction at the interface was included as a finite rate (rather than a boundary condition). They also allowed electrons and holes to have different weightings for their contribution to the bleach. The rates for extraction at the interface were 6ps for PCBM and 8ps for Spiro, significantly faster than the signal decay rates, confirming their suggestion that the nanosecond decay dynamics they observed were transport limited.

4.2.4.2 TA Measuring the CTL Carrier Density

To measure the population in the CTL rather than the perovskite, a number of papers have studied the near-infrared (NIR) region in order to probe an energy range where the perovskite does not have strong absorption. However, since these features are weak compared to the GSB of the perovskite, changes in the perovskite transmission in this energy range due to changes in the reflection of the probe at interfaces will be more problematic than they were when considering the strong perovskite GSB. Due to the thicknesses of the layers, the NIR region is often dominated by thin film interference, so is sensitive to variations in thickness [203, 290]. A number of papers [273, 291–294] have reported features in the NIR for the plain perovskite layer, that are attributed to changes in absorption. However, measurements on different insulating substrates give contrasting results – for glass substrates [292–294] the NIR features are PIAs, but for meso-Al_2O_3 substrates [273, 291] the NIR feature is a bleach.

For plain perovskite layers on glass substrates, Zhai et al.[294] saw a broad PIA centred on 1500nm that appears within the instrument response time. They pointed out that it matches the energy difference between the GSB and a high energy bleach feature of the perovskite, so if the high energy bleach is attributed to an intergap transition involving a deeper sub-band, then this NIR feature is possibly a transition between a pair of bands on the same side of the bandgap. Also on glass substrates, Jimenez et al. [292] observed a PIA around 1200nm, and Dursun et al. [293] observed a broad PIA from 850-1400nm, which decays over few picoseconds. On the other hand, on meso-Al_2O_3 substrates, Grancini et al.[291] observed a broad *bleach* centred on 1400nm that appears within the instrument response time (IRT). These disagreements could be explained by different amounts of reflection for a flat perovskite layer on glass versus perovskite penetrated into meso-Al_2O_3. However, Ponseca et al.[273] observed a bleach at 970nm within the IRT for both glass and meso-Al_2O_3 substrates, further adding to the inconsistencies. These inconsistencies highlight that the NIR region is less reproducible and is possibly sensitive to differences in reflection for different sample geometries. Any features due to changes in the CTL will overlap with these inconsistent features from the perovskite and substrate making it difficult to correctly distinguish them.

For Spiro, it has been shown that oxidising the Spiro molecules (equivalent to accumulation of holes) gives a broad increase in absorption in the NIR region centred on 1400nm [295, 296]. Therefore, a number of works have attributed a PIA in the NIR to hole extraction into the Spiro. For example, Makuta et al.[295] found that when a Spiro layer was added to the perovskite, a broad PIA from 1000-2500nm is observed that was not observed for Spiro by itself or when meso-TiO_2 was added to perovskite. Grancini et al.[291] found that for perovskite on meso-TiO_2, the bleach at 1000-1200nm becomes a PIA when Spiro was added. Dursun et al.[293] found that both plain perovskite and the perovskite-Spiro bilayer gave a broad PIA from 880-1400nm that decayed over picoseconds, but it decayed more slowly when Spiro was present, which was attributed to holes being extracted into the Spiro and contributing a long lived PIA. Marchioro et al.[297] performed TA measurements with lower time resolution and over a much longer delay window and found that only the Spiro bilayer gave a PIA feature at 1400nm. Adding TiO_2 caused the signal to last longer which was attributed to opposite carriers being more effectively separated by the presence of both CTLs, which slowed down recombination.

Charge injection into the CTL also gives TA features in the visible range, where interference effects may be less significant, but any features will overlap with the broad PIA and high energy bleach features of the perovskite layer. The HOMO-LUMO transition in Spiro gives a strong absorption at 400-450nm, which is expected to be bleached by carrier extraction. However, oxidising Spiro molecules have been shown to increase the absorption across this range which may counteract the bleach at 400-450nm, as well as giving an additional absorption in the neighbouring range 450-550nm[291] These Spiro features would overlap with the high energy bleach in the perovskite, so Brauer et al.[285] subtracted the TA spectra taken with and without Spiro, to find the Spiro does give a GSB rather than a PIA at 400-450nm, plus the expected PIA at 450-500nm. Piatkowksi et al.[298] and Grancini et al.[291] have also observed the bleaches around 500nm when Spiro layers are added. For PCBM, the absorption feature for the HOMO-LUMO transition is also in the blue spectral region, and so PIA features in this region in the presence of PCBM have been attributed to electron extraction into the PCBM[286].

Overall, it is clear that most features that could possibly be attributed to the CTL may overlap with features related to changes in the perovskite, and so misidentification is possible. One concerning trend is that all of the features attributed to changes in the CTL appear within the instrument response time (IRT), and some of them have decays over the first few picoseconds. This is also true for other CTLs not mentioned above such as PEDOT:PSS[286]. These changes are attributed to charge extraction within the IRT followed by decay. However, the instant rise suggests the features may instead be due to parasitic absorption of the photoexcitation by the CTLs, although some studies rule this out as the features are not observed when photoexciting the CTLs by themselves (e.g. in ref.[286]). The instant rise also suggests the features could be partially or entirely related to overlapping perovksite features that are expected to be rise instantaneously. The changes of the suggested CTL features over the first few picoseconds match the time scale for carrier cooling in the perovskite, or for recombination at the very high photoexcitation fluences used in these experiments (noted by Pydzinksa et al.[279]), suggesting the features may not have been fully disentangled from the overlapping perovskite features that change over this time scale.

Even if the suggested features really are due to charge in the CTLs, the small size of the features and the difficulty of disentangling them from the overlapping perovskite features means their dynamics will have large uncertainty, and most conclusions have been limited to identifying their rapid rise, and then either their disappearance over a few picoseconds or persistence over a few nanoseconds. Measuring the large features associated with the perovskite layer allows more quantitative analysis of the decay dynamics.

4.3 Experimental Results

4.3.1 Introduction

This work studies the commonly used CTLs, C_{60}, PCBM and Spiro-OMeTAD (with additives Li-TFSI, tBP and FK209), all of which were deposited on top of a triple-cation lead perovskite layer with mixed I-Br composition, $(FA_{0.83}MA_{0.17})_{0.95}Cs_{0.05}Pb(I_{0.83}Br_{0.17})_3$ (samples with pure I_3 composition were also investigated, $(FA_{0.83}MA_{0.17})_{0.95}Cs_{0.05}PbI_3$). This triple-cation composition has been mentioned previously as one with high crystallinity, reproducibility and stability, including against phase segregation [136]. As well as their stability, the mixed I-Br composition is particularly relevant due to its bandgap (PL data in this work indicates ~1.63eV) being close to the ideal for the top junction in a 2-junction tandem PV cell (~1.75 eV for a silicon bottom junction [14]).

The dynamics of the carrier density in the perovskite layer following pulsed photoexcitation are measured using TCSPC, TA and OPTP. In the literature, TCSPC and TA are much more frequently used to study the effect of CTLs on the perovskite carrier population than OPTP. As mentioned previously, OPTP has advantages over TA because the signal is simply a weighted sum of the electron and hole densities, whereas it is more difficult to reliably relate the TA spectrum to carrier density.

Time-resolved PL measurements (usually using TCSPC) is commonly used to track changes of carrier density with time, and is a useful complement to the OPTP and TA techniques as it measures over time delays greater than just 3ns, and can detect much lower densities of carriers. The PL signal is proportional to the product of n and p (not a sum), so the excess PL following photoexcitation requires some careful interpretation. For example, the excess PL signal in the simplest case of $n_e = p_e$ (i.e. insignificant accumulation in traps), is proportional to $n_e^2 + (n_0 + p_0)n_e$, not just n_e^2 (see Eq. 3.8). The dependence of PL intensity on the product of densities means the PL signal depends on the spatial overlap of the electron and hole densities, so if they are spatially separated (e.g. by electric fields) then the PL intensity is reduced, which might be misinterpreted as a reduction of carrier density.

Compared to OPTP and TA, TCSPC measurements are more sensitive to illumination or atmosphere related changes in the defect density. This is because at the low pump fluences and thus low excess carrier densities used in TCSPC setups, the total recombination rate will be dominated by defect mediated recombination, and thus sensitive to the defect density. On the other hand, OPTP and TA use higher pump fluences meaning that carrier densities are much higher during the 3ns delay window following photoexcitation, so trap-mediated recombination will contribute a smaller fraction of the total decay rate and so the total rate is less sensitive to defect density. The sensitivity to defect density means that for TCSPC vastly different decay rates can be measured on the same sample at the start of an experimental session and at the end, because the defect density (particularly at the surface) may change during the course of the session (see section1.5.5). The particular decay rate for any measurement will depend on the history of the sample. This means the measurements must be performed carefully to acquire reproducible results, which will be discussed in more detail further below.

Due to the considerations outlined above and in the previous section regarding the interpretation of the TRPL, TA and OPTP measurements, in this work greater attention is applied to the OPTP measurements. The OPTP measurements are also compared to mathematical models of the carrier dynamics, which is presented in Chapter 5.

4.3.2 Sample Fabrication

The data reported in this thesis includes measurements on samples from two repeat batches. The second batch included perovskite layers with two different thicknesses, and CTLs with two different thicknesses, referred to as thick and thin (see section 4.3.3.1). The C_{60} layers were deposited by thermal evaporation by Anjana Wijesakara at the University of Warwick. The perovskite, PCBM and Spiro-OMeTAD layers were fabricated by Imalka Jayawardena at the University of Surrey using the following protocol.

4.3.2.1 Solution Preparation

Perovskite precursors were prepared such that the (FA + MA): Pb molar ratio was 1:1.1 for both compositions.

For the mixed I-Br composition, 1.1 mmol of PbI_2 (from TCI) was added to a DMF:DMSO mix (1 ml, 4:1 ratio by volume), followed by 1 mmol of FAI (Greatcell solar), 0.22 mmol of $PbBr_2$ (TCI), and then 0.2 mmol of MABr (Greatcell Solar). A CsI solution was prepared by dissolving 78 mg of CsI (Sigma Aldrich) in 200 μl of DMSO. 42 μl of this was added to the solution of PbI_2 + FAI + $PbBr_2$ + MABr in DMF/DMSO.

For the pure I_3 composition, 1.32 mmol of PbI_2 (TCI) was added to a DMF:DMSO mix (1 ml, 4:1 ratio by volume), followed by 1 mmol of FAI (Greatcell solar) and mmol of MAI (Greatcell Solar). A CsI solution was prepared by dissolving 78 mg of CsI (Sigma Aldrich) in 200 μl of DMSO. 42 μl of this was added to the solution of PbI_2 + FAI + MAI in DMF/DMSO.

For Spiro, 72.3 mg of Spiro-OMeTAD (from Borun) was dissolved in chlorobenzene (CB). Separately, a 300 mg/ml solution of FK209 (in acetonitrile) and a 520 mg/ml solution of Li-TFSi (in acetonitrile) was prepared. To the Spiro solution, 28.8 μl of tBP solution, 17.5 μl of Li-TFSi solution and 29 μl of FK209 solution were added.

For $PC_{60}BM$, 20 mg of the powder (from Nano-C) was dissolved in 1 ml of CB.

For the thinner perovskite layers, 100 μl of the perovskite solutions were added to 500μl of DMF:DMSO 4:1 mix. For the thinner CTLs, 50μl of the Spiro-OMeTAD and $PC_{60}BM$ solutions were added to 150μl of CB.

4.3.2.2 Deposition

The perovskite layers were formed by spin-coating on quartz substrates using an anti-solvent method. The perovskite solution was dropped onto the substrate prior to spinning. The spinning was divided into two steps. First, the substrate was accelerated up to 1000rpm at a rate of 200rpm/sec, then after 8 seconds it was accelerated up to 6000rpm at a rate of 1000rpm/sec. 150 μl of CB was dropped onto the spinning substrate 30 seconds into the second step. The sample was then annealed at 100°C for 1 hour.

To form the Spiro-OMeTAD layer, the perovskite sample was accelerated to 4000rpm at a rate of 2000rpm/sec, and the Spiro-OMeTAD solution was dropped onto the spinning perovskite sample 5 seconds after starting (spinning stopped at 25 seconds).

To form the $PC_{60}BM$ layer, the $PC_{60}BM$ solution was dropped onto the stationary perovskite sample, which was then accelerated to 1000rpm at a rate of 1000rpm/sec (spinning stopped at 30 seconds).

All processing was carried out in an N_2 glove box with both O_2 and H_2O levels below 0.1 ppm.

4.3.3 Sample Characterisation

4.3.3.1 Scanning Electron Microscopy

The samples were imaged using scanning electron microscopy (SEM) (performed by Stephen York at the University of Warwick). Images taken at normal incidence to the layers ("top-down") for batch 2 showed that the thick perovskite layers had complete coverage of the quartz substrate (see Fig.4.3), with grain diameters of a few hundred nanometres, whereas the thin perovskite samples consisted of isolated islands of small crystals. The thick PCBM layers had complete coverage over the perovskite underneath, however the thick Spiro layers had some small pinholes. These may have grown in the months between taking optical measurements and SEM images, as humidity has been show to induce pinholes. The topography of the C_{60} layers on quartz was measured with AFM (by Ziyi Hu at the University of Warwick), and the C_{60} molecules showed a tendency to aggregate, so layers with thicknesses greater than ~15nm were required to ensure complete coverage (30 nm was used for thick C_{60}).

For cross-sectional images, a diamond saw was used to score a line on the underside of the quartz substrate that penetrated most of the way through its thickness, and then the samples were snapped along this line (performed by Tom Orton at the University of Warwick). The cross-section images confirmed complete coverage of the substrate by the thick perovskite for both batch 1 and 2, with the vast majority of grains penetrating the whole thickness of the layer, which was approximately 600 nm thick for batch 1 and 370nm thick for batch 2. Cross-sectional images of the thick PCBM and thick Spiro layers for batch 2 also confirmed complete coverage over both the quartz substrate and the perovskite. The thick PCBM and Spiro layers both had a thickness of ~120nm on quartz, but on the thick perovskite the thickness of PCBM and Spiro was thinner in some areas due to the surface roughness of the perovskite underlayer.

Batch 1	Batch 2			
I-Br	I-Br thick	PCBM thick	Spiro thick	C_{60} thick
600 nm	370 nm	120 nm	120 nm	30 nm

Table 4.1: Average layer thicknesses from SEM cross-sections.

4.3.3.2 Absorption

For the time resolved optical measurements, it is important to know the number of carriers photogenerated in the sample by the optical pump. To determine the actual fraction of the incident intensity that is absorbed in the sample, both the reflectance and transmittance must be measured, with the remaining fraction attributed to absorption. For bilayer samples, some of this absorption may be in the CTL. Measuring transmittance alone is not an accurate way to determine the absorbed fraction because reflectance accounts for 10-30% of the attenuation of transmittance. An integrating sphere is used for these measurements in order to account for scattered light, and the results for the mixed I-Br compositions are shown in Figs.4.4 and 4.5, with the pump wavelengths used in this work (405/410nm, 460nm, 633nm, 700nm) indicated by vertical dashed lines. For the pure I_3

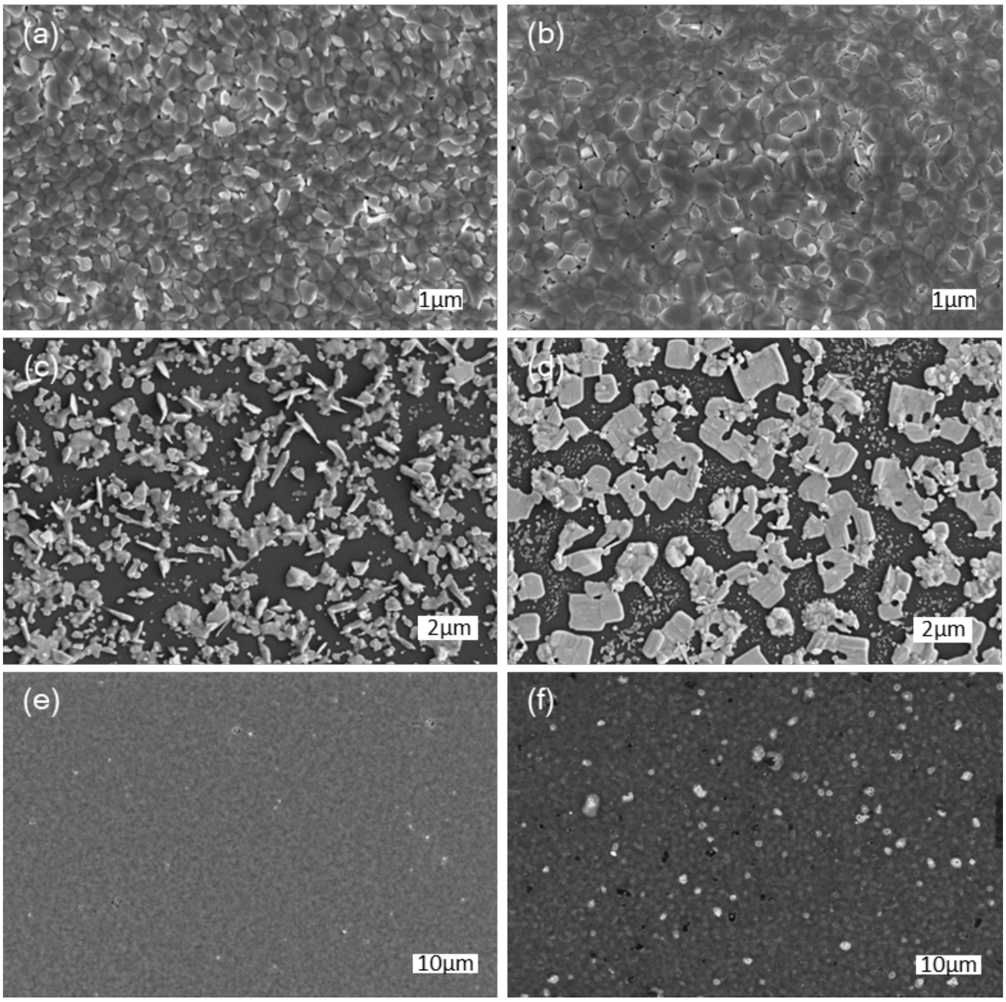

Figure 4.2: Top down SEM images of batch 2: a) mixed I-Br thick, b) pure I_3 thick, c) mixed I-Br thin, d) pure I_3 thin, e) thick PCBM on mixed I-Br thick, f) thick Spiro on mixed I-Br thick.

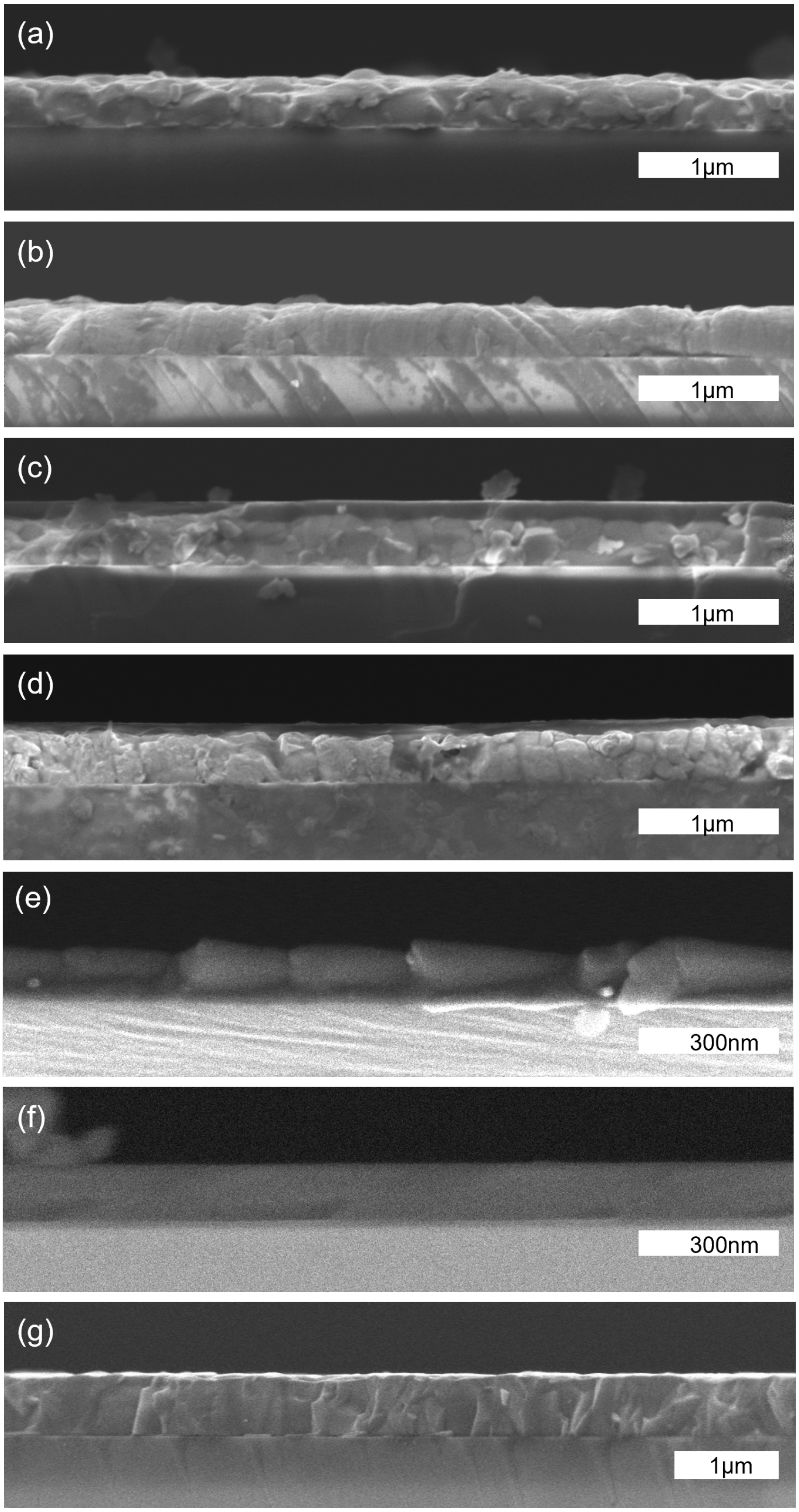

Figure 4.3: Cross-sectional SEM images of batch 2, except g) which is batch 1: a) mixed I-Br thick, b) pure I_3 thick, c) thick PCBM on mixed I-Br thick, d) thick Spiro on mixed I-Br thick e) thick PCBM on quartz, f) thick Spiro on quartz, g) mixed I-Br from first batch.

compositions, the absorption spectrum is redshifted but is otherwise similar.

It can be seen that below the bandgap of the perovskite layer, the transmittance and reflectance were dominated by thin film interference fringes. These interference fringes were almost completely removed when the absorption fraction was calculated $1 - T - R$ (where T and R are the transmittance and reflectance fractions).

For the following time-resolved spectroscopy experiments, it is important to know not only the total number of pump photons absorbed, but also the initial distribution of the photogenerated carriers within the perovskite layer. Therefore the absorption depth, δ, or absorption coefficient $\alpha = 1/\delta$, need to be determined, which are related to the imaginary component of the refractive index. The absorption coefficient is sometimes calculated from ellipsometry measurements, but these were not available. To determine the complex refractive index from transmittance and reflectance measurements, the transmittance and

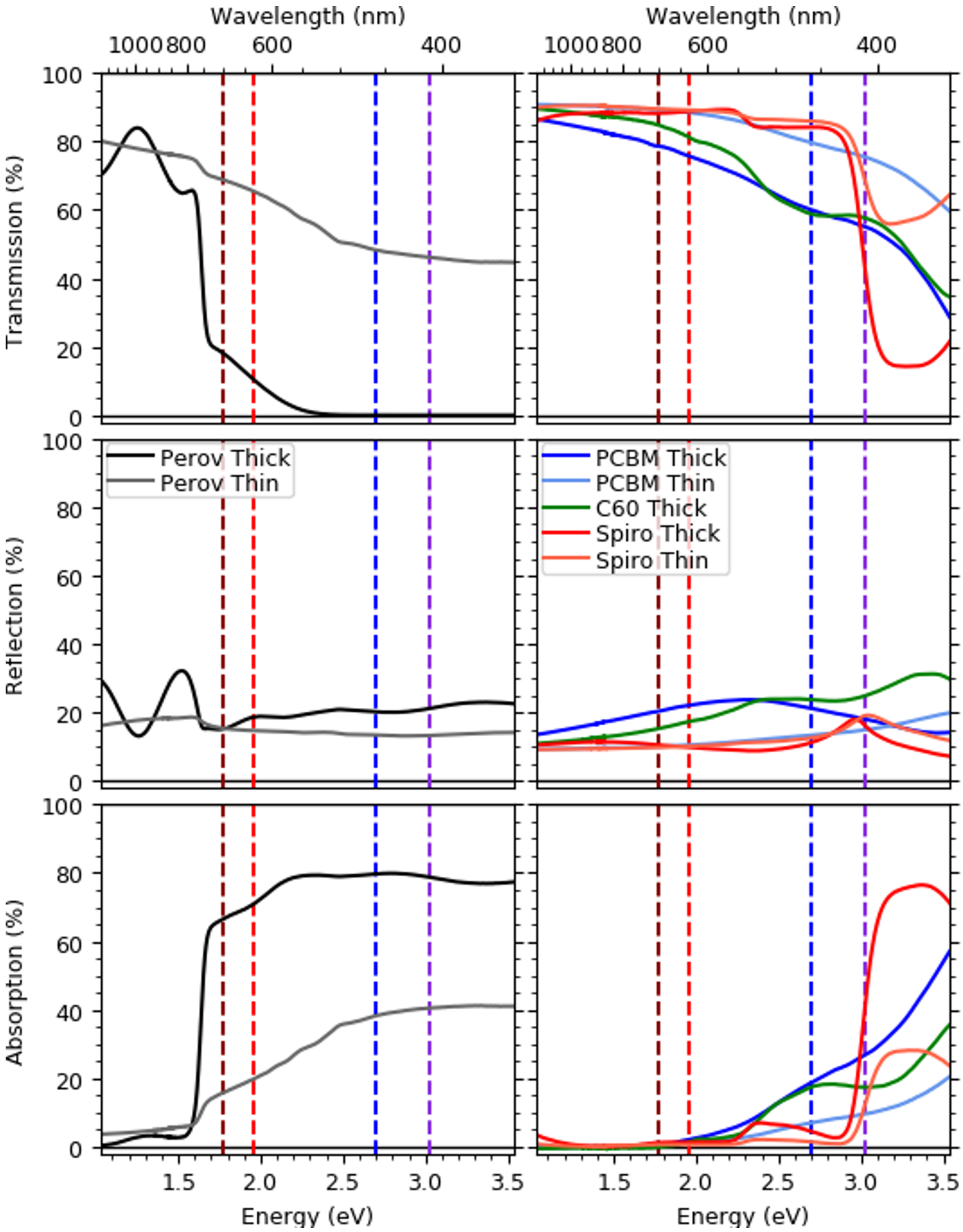

Figure 4.4: The measured transmitted fraction (T), reflected fraction (R) and absorbed fractions ($1 - T - R$) of the incident intensity, for single layers of either the perovskite (perov) or the CTLs on quartz substrates (batch 2). The pump wavelengths used in this work are shown by vertical dashed lines at 410nm, 460nm, 633nm, and 700nm.

reflectance can be written in terms of the complex refractive indices and thicknesses of the layers in the measurement, and then inverted to find the unknown parameter. This requires that all other parameters are known, i.e. the complex refractive indices and thicknesses of the other layers (e.g. the substrate). This expression is also very complicated as there is an infinite sum of possible propagation paths through the sample due to different combinations of internal reflections, and the expression becomes particularly complicated when there is more than one layer. This makes it very hard to invert the expressions to find the unknown parameter, and so simplifications are required, as was done for relating THz transmission and the sample's permittivity (section 2.2.2). Therefore, a simplified

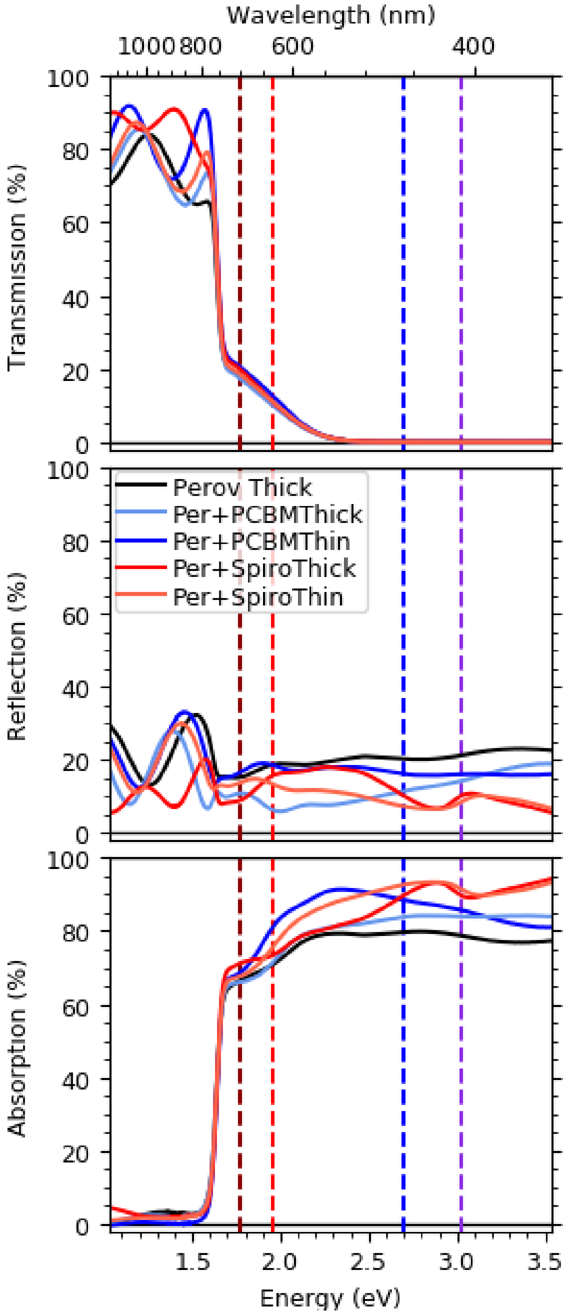

Figure 4.5: The measured transmitted fraction (T), reflected fraction (R) and absorbed fractions ($1 - T - R$) of the incident intensity, for a thick perovskite (per) layer on quartz substrates, with different thicknesses of CTLs on top (batch 2). The pump wavelengths used in this work are shown by vertical dashed lines at 410nm, 460nm, 633nm, and 700nm.

approximation was made here to estimate the absorption coefficient of the perovskite layer.

For the thick perovskite layer it was assumed that the transmittance was only attenuated by reflection at the air-perovskite interface and then absorption of the non-reflected light by the perovskite layer. In this case, the reflected intensity is entirely due to reflection at the air-perovskite interface. In other words, it was approximated that the light intensity that reaches the buried perovskite-quartz interface and then the rear quartz-air interface was entirely transmitted without reflection. This is reasonable since the intensity of light reaching these interfaces is already attenuated, and the intensities that are reflected are even smaller and so are small compared to the transmission losses due to the first two processes (reflection at the front interface and absorption within the perovskite). Thin film interference within the perovskite layer was also neglected. This approximation for the measured transmittance and reflectance, T_{thick} and R_{thick}, was expressed as

$$T_{thick} = (1 - R_p)e^{-\alpha L_{thick}} \tag{4.1}$$

$$R_{thick} = R_p$$

where α is the (Naperian) absorption coefficient, and R_p is the reflected fraction (reflectance) at the air-perovskite interface. The fraction of light that is absorbed when propagating through a layer will be referred to as internal transmittance, $T^* = e^{-\alpha L}$. α can be calculated for the thick perovskite sample since the other parameters in Eq. 4.1 are known (i.e. L_{thick}, $R_p = R_{thick}$ and T_{thick}).

Unfortunately, for the thick perovskite layers, the amount of transmittance for light with energy >2.5eV, is below the sensitivity of the equipment, so the absorption coefficient for 410nm and 460nm excitation could not be determined. Therefore, thinner perovskite samples with greater transmittance were fabricated (batch 2), but these were found to result in small crystals that only partially covered the quartz substrate with a thickness that cannot be measured accurately. Without a known thickness the absorption coefficient cannot be calculated. However, for layers of different thicknesses, e.g. $L_{thick} = nL_{thin}$, their internal transmittances are related by

$$\begin{aligned} T^*_{thick} &= e^{-\alpha n L_{thin}} && (4.2) \\ &= (T^*_{thin})^n && (4.3) \end{aligned}$$

It is also common to compare the decadic absorbance (optical density) of materials, so the decadic internal absorbance is $A^* = -\log_{10}(T^*)$ so

$$A^*_{thick} = nA^*_{thin}$$

Therefore, if the internal transmittances of the two different thicknesses can be determined, the ratio of their thicknesses, n, can be found, and hence the thickness of the thin sample. Since the individual crystals probably have a range of thicknesses, finding the ratio of internal transmittance determines an *average* thickness of the crystals relative to the thick film. With a known average thickness for the thin sample, the absorption coefficient for energies >2.5eV can be found. However, the thin sample had only partial coverage so calculation of the internal transmittance must take this into account. The ratio n should

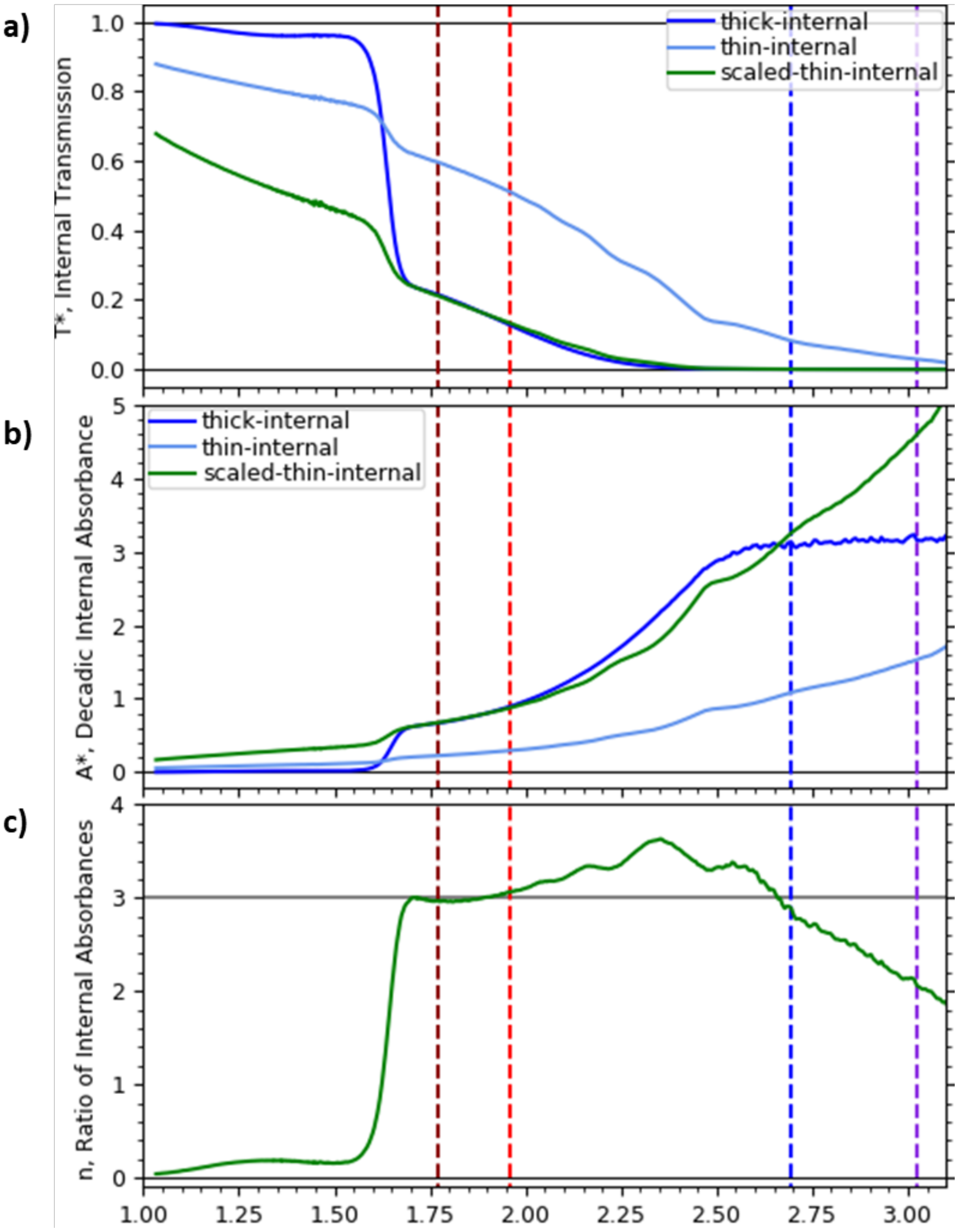

Figure 4.6: a) The internal transmittance $T^* = e^{-\alpha L}$ for the thick and thin perovskite samples (batch 2), where α is the absorption coefficient and L is the thickness of the layer. T^* for the thin perovskite scaled by the ratio $n \sim 3$ is also plotted. b) The decadic internal absorbance $A^* = -log_{10}(T^*)$ for the thick and thin perovskite samples, plus A^* for the thin perovskite scaled by the ratio $n \sim 3$. c) The ratio $n = A^*_{thick}/A^*_{thin}$.

be the same for all energies, and this uniformity can be used to check if the internal transmittance for the partially covered thin sample is calculated reliably.

In summary, the internal transmittance/absorbance for both thick and thin need to be calculated and compared. The internal transmittance/absorbance for the thick sample is easily calculated as described above. The internal transmittance/absorbance for the thin sample is now calculated.

The measured transmittance fraction for the thin sample, T_{thin}, is a sum of the transmittance fraction for the perovskite islands, T_p, and for the bare quartz gaps, T_q, weighted by their area fractions, W_p, and W_q. So

$$T_{thin} = W_p T_p + W_q T_q$$

For the regions covered by perovskite, the transmittance is approximated as for the thick perovskite sample, i.e.

$$\begin{aligned} T_p &= (1 - R_p) e^{-\alpha L_{thin}} & (4.4) \\ &= (1 - R_p) T^*_{thin} & (4.5) \end{aligned}$$

For the bare quartz regions, the transmittance is similarly approximated as

$$T_q = (1 - R_q)$$

where R_q is the measured reflected fraction when incident on a quartz slab (which actually includes the effect of reflection at the back interface as well as the front). So

$$\begin{aligned} T_{thin} &= W_p T_p + W_q T_q \\ &= W_p (1 - R_p) T^*_{thin} + W_q (1 - R_q) \end{aligned}$$

which can be rearranged to give:

$$T^*_{thin} = e^{-\alpha L_{thin}} = \frac{T_{thin} - W_q (1 - R_q)}{W_p (1 - R_p)}$$

To calculate the internal transmittances T^*_{thick} and T^*_{thin}, values for R_p, R_q, W_p, W_q, T_{thick}, and T_{thin} are required. T_{thick} and T_{thin} are just the transmittance measurements for the two samples. R_p and R_q, are reflectance measurements for the thick perovskite sample and a bare quartz sample, respectively. For the bare quartz, R_q ~0.1, and for the thick perovskite, R_p ~0.2. W_p and W_q are estimated as ~ 0.5 from the SEM image. This estimation can be checked by considering the formula for the measured reflectance off the thin sample, $R_{thin} = W_p R_p + W_q R_q$, which was measured as ~0.15. With $W_q = 1 - W_p$, this is rearranged to $W_p = (R_{thick} - R_q)/(R_p - R_q)$, which for $R_p \sim 0.2$, $R_q \sim 0.1$, gives $W_p \sim 0.5$, consistent with the SEM image.

The ratio, $n = A^*_{thick}/A^*_{thin}$ calculated by the above method is shown in Fig.4.6, and is approximately uniform in the energy range between the bandgap and 2.5eV, with a value ~3. Multiplying A^*_{thin} by the determined ratio $n \approx 3$ scales the internal absorbance of the thin layer up to the that of the thick layer, and can be used to extrapolate the internal absorbance of the thick layer beyond 2.5eV. For the thin sample, there are small wiggles in the transmission and absorption spectra for energies above 2.0eV (see Fig.4.4 or Fig.4.6), which is consistent with reports in the literature for mixed compositions, that attributed these to transitions between bands deeper in the bandstructure[299]. The absorption coefficient, α, for energies >2.5eV is calculated from $T^*_{thin} = e^{-\alpha L_{thick}/n}$ using $n \approx 3$.

The time resolved spectroscopy techniques employed in this work used a range of pump wavelengths (405/410nm, 460nm, 633nm, 700nm), which are indicated by the vertical dashed lines in the figures. The thin samples are not suitable for solar cell devices, and the spectroscopy signals were very small due to the weak absorption of the pump beam, so are not considered further.

For 700nm excitation, the internal transmittance T^* for the thick perovskite samples (batch 2) is ∼25% so the absorption depth δ is comparable to the thickness of the film (270nm vs 370nm). Therefore carriers will be generated throughout the thickness, varying by a factor of 4 from front to back. At the other end of the energy scale, 410nm excitation is estimated to have decadic internal absorbance of 4.7 for the thick sample (batch 2) giving an absorption depth of ∼35nm.

It is also important to understand how the CTLs affect the absorption in the perovskite layer. Adding a CTL on top of the perovskite will change the light absorption in the perovskite layer, not only by parasitic absorption of some of the pump light, but also by changing the set of interfaces and their reflectance and transmittance coefficients, i.e. the light in-coupling to the perovskite layer. Hence for the thick perovskite sample the reflected intensity can be seen to depend on the overlying CTL, and is generally reduced by the presence of CTLs. However, these are small differences, and the degree of parasitic absorption has the greatest impact on light absorption in the perovskite layer. This parasitic absorption can be estimated by measuring the transmittance and reflectance of CTLs on quartz, although the thickness of spin-coated layers may be slightly different for CTLs on quartz substrates compared to on top of perovskite layers, as they have different surface wettability and roughness. For 700nm and 633nm there will be negligible absorption of the pump light by any of the different CTLs. The Spiro layer will have very small absorption for 460nm excitation, but will absorb a large fraction of the 410nm pump light depending on the thickness. The fullerene layers will have slightly more absorption than Spiro-OMeTAD for 460nm pump, but half the absorption of Spiro-OMeTAD for 410nm pump.

4.3.3.3 Steady State PL

The steady state PL was performed at two of the pump wavelengths used for the other measurements, 410nm and 633nm, and was performed for illumination on either the quartz side or the CTL side. The slits for the monochromator were kept narrow to maximise spectral resolution (<5nm). The samples were illuminated at an incidence angle of 45°and the PL was detected on the illuminated side at an angle of 45°, so at 90°to the excitation.

All samples had the same normalised PL spectrum, for both pump wavelengths. In addition to the spectral shape, the steady state PL intensity is often used in the literature to check for PL quenching by the CTL, although there is large uncertainty in the PL intensity as it may either grow or shrink under illumination, depending on the atmosphere, wavelength, intensity and previous history of exposure (see sections 1.5.5 and 1.5.6). The PL intensity measured for illumination (and detection) on the two different sides of the sample, is expected to be different, as for the CTL side, the CTL may be parasitically absorbing the pump light. Also, for the two sides there are a different set of interfaces and thus different reflectance/transmittance coefficients, for both the incident pump beam and the emitted PL intensity. When comparing different samples, illumination on the quartz side has the same propagation path for all samples so offers the best comparison, and these

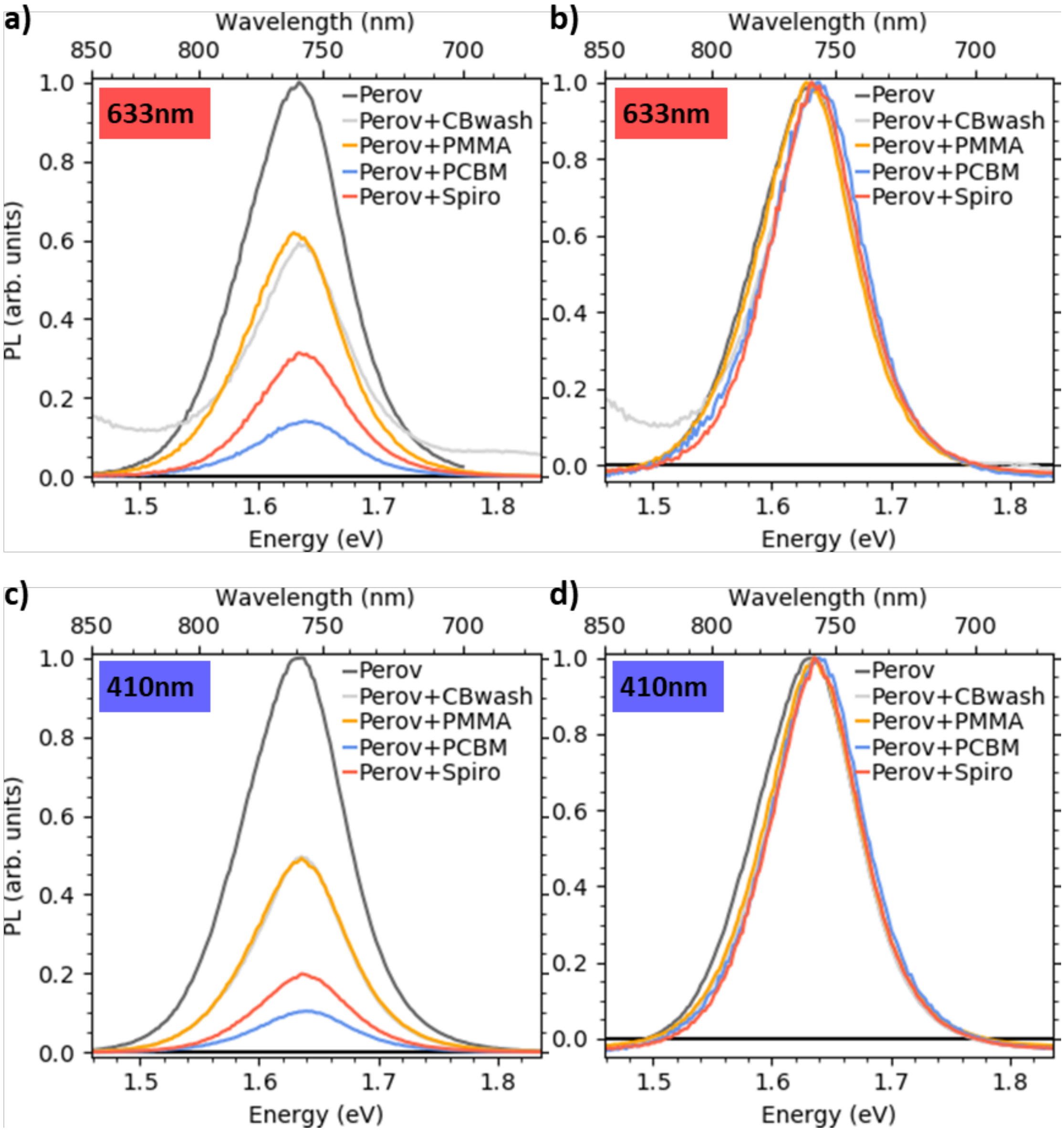

Figure 4.7: The steady state PL spectra measured on the quartz side of batch 1 samples. a)-b) 633nm excitation. c)-d) 405nm excitation. b) and d) are normalised after the background offset at the tail of the PL peaks was subtracted (background is not spectrally flat and differed between measurements).

spectra are shown in Fig.4.7 for batch 1. It should be noted however, that the out-coupling of emitted PL photons will depend on the set of adjacent layers, and so these layers may still effect the PL intensity.

The figure also shows the PL for a sample washed with chlorobenzene (CB), to simulate the deposition of the Spiro and PCBM molecules that are dissolved in CB, and a sample coated with PMMA, which is often used in the literature to protect the sample from the atmosphere (encapsulate). Whilst these samples appear to have different PL intensities compared to the plain perovskite sample, the time resolved measurements did not seem to be affected, except that for OPTP measurements, the absorption of the pump light by the perovskite layer appeared to be increased by the PMMA layer, possibly due to improved in-coupling of the pump light. A clear quenching of the PL is observed for CTL samples compared to the reference samples, for illumination with both wavelengths and including for illumination through the quartz side for which parasitic absorption of the pump beam can be discounted. It was observed that illumination through the CTLs with 410nm had even greater quenching (not shown), which was expected due to the parasitic absorption of the pump beam by the CTLs. For excitation through the quartz side, it can be seen that the Spiro layer does not quench the PL as much as PCBM does.

4.3.4 Time Resolved Measurements - Overview

Time resolved spectroscopy techniques are used to measure the carrier density in the perovskite layer as a function of time, and the behaviour of the observed transient signals can then be related to processes such as recombination in the bulk, extraction and recombination at the interface, and carrier transport. Each of these processes is happening simultaneously, meaning that relating the shape of the transients to the different processes is difficult. However, the relative contribution of each process and the delay time range for which a process dominates can be varied by using different experimental conditions, such as the initial spatial distribution of carriers. This results in transients with different shapes, and so parts of the transients can be associated to particular processes. For example, when carriers are initially photogenerated next to the quartz interface, extraction and/or recombination at the perovskite-CTL interface is delayed by the time it takes carriers to move to this interface, and this should be evident in the shape of the transient. Therefore, in this work the samples were illuminated with different pump wavelengths that have different absorption depths, and on different sides of the sample. This also beneficial for fitting the data with a mathematical model, as globally fitting different transients provides tighter constraints for the free parameters in the model.

4.3.5 TRPL

4.3.5.1 Methodology

As mentioned previously, TCSPC measurements are sensitive to a number of factors and must be performed carefully if reliable comparisons between samples are to be made. Here it was observed that the PL intensity and lifetime grow under illumination in ambient atmosphere, but when the sample chamber was flushed with N_2, the PL intensity and lifetime were decreased, and these changes were at least partially reversible (although some PL enhancement or quenching may persist). This is consistent with literature reports (see section 1.5.5). In this work, to study the differences between the CTLs, any differences in surface defect density should be minimised. Therefore, it was decided to measure the samples in ambient air, which passivates surface defects (degradation only occurs over timescales of days), so that all samples have the opportunity to reach similar densities of surface defects. Furthermore, this enhanced the PL intensity which made the measurements quicker and less noisy, and it enhanced the perovskite PL lifetime which may make any differences due to the CTL easier to distinguish. The PL lifetime was allowed to stabilise before recording the final data. For TCSPC, changes in the lifetime during the measurement are not apparent unless quick successive measurements are taken, which is not the standard method for this cumulative counting technique. When the PL lifetime is not stabilised, successive quick measurements showed decays which were close to monoexponential but with different lifetimes, and when accumulated together this results in a decay that is not monoexponential. This may explain why the TCSPC data is often reported as stretched exponential. It should be noted that the emission from samples with more stable PL decays could be accumulated over longer recording times, resulting in a better signal to noise ratio in the plotted data.

It was observed that the plain perovskite samples stabilised their PL lifetime over seconds, whereas samples covered in CTLs and illuminated with 633nm took longer to stabilise their lifetimes, presumably because the interaction with air was slowed down by the CTLs. Under 633nm illumination, the PL lifetime gradually increased, but did not change for 405nm. This shows some agreement with literature reports that shorter wavelengths do not enhance PL but rather decrease it (see section 1.5.5).

The TCSPC data usually shows a sharp decay in the PL intensity at the start of the decay (<10ns). Part of this intensity may be attributed to scatter of the excitation light, which can be minimised by adjusting the angle of the sample, but cannot be entirely removed. Using short measurement windows, which have higher temporal resolution, it can be seen that there is often a steep decay in the PL intensity over the first tens of nanoseconds (distinct from the spike due to scattered pump light), followed by a slow monoexponential decay. This behaviour has previously been attributed to carriers becoming trapped in long-lived defect states. The trapping results in a sharp decay in PL that then slows down as the traps are saturated and the population decay rate becomes limited by the rate at which these trapped carriers either escape back into the band, or recombine with the opposite carrier. A decay that is limited by a single step that is dependent on a single species, such as slow trap emission or slow capture of the second carrier, is expected to give a monoexponential decay. When N_2 is used instead of air, the initial sharp decay of the PL decays much further, consistent with a larger defect density trapping a larger fraction of the carrier density before the defects are saturated. Sometimes the slow decay does not become monoexponential, indicating the defects are not completely saturated.

Since there appears to be long-lived trapped carriers, the repetition rate of the pulsed excitation is also important. It is usually assumed that the carrier density has decayed

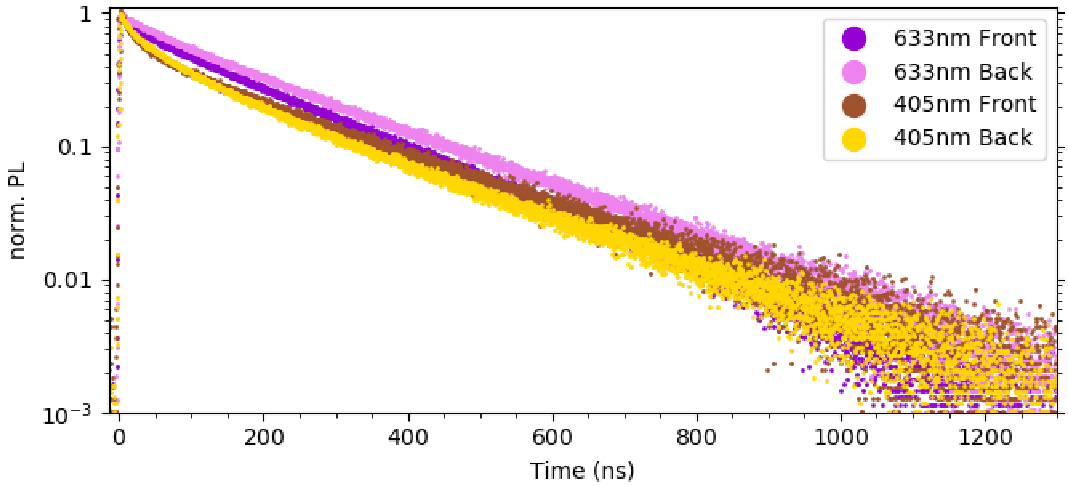

Figure 4.8: The normalised time resolved PL intensity measured by TCSPC, for the thick perovskite sample (batch 2) using 405nm and 633nm excitation on either the back side (through the quartz substrate) or the front side.

to zero before each pump pulse, but if trapped carriers have a long lifetime, a certain density of trapped carriers are present for the subsequent pulses. This will change the recombination dynamics for subsequent pulses, and the trapped population may increase over successive pulses, possibly until a cyclic steady state is reached in which the trapped density is the same at the start of each pulse. This has been studied in a number of papers (for example [178, 258]). This further emphasises why the PL behaviour must be allowed to stabilise before recording the final data.

As mentioned before, the absolute intensity of the PL signal is important, but to study the lifetimes it is easier to compare normalised data. The degree of pump scatter that gives the initial spike in PL intensity will vary between different samples (different reflectivity, roughness and mounting angles), so the PL is normalised to the intensity at the end of the initial spike (a few nanoseconds). Furthermore, since the level of the background intensity is different for each measurement, this should be subtracted before normalising.

In this work, TCSPC measurements used photoexcitation at 405nm and 633nm,

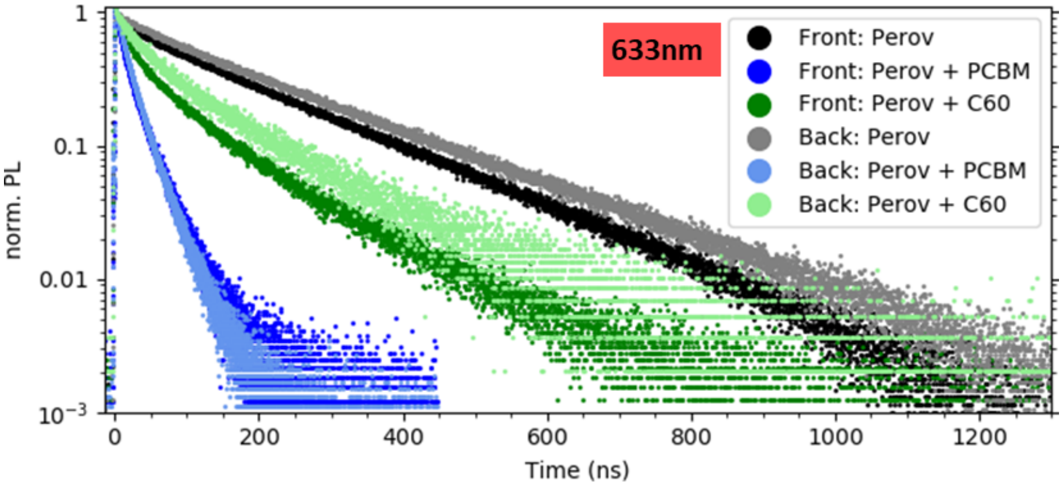

Figure 4.9: Normalised TCSPC curves for fullerene bilayers (batch 2, thick perovskite and thick CTL), using 633nm excitation on either the back side (quartz substrate) or the front side (CTL).

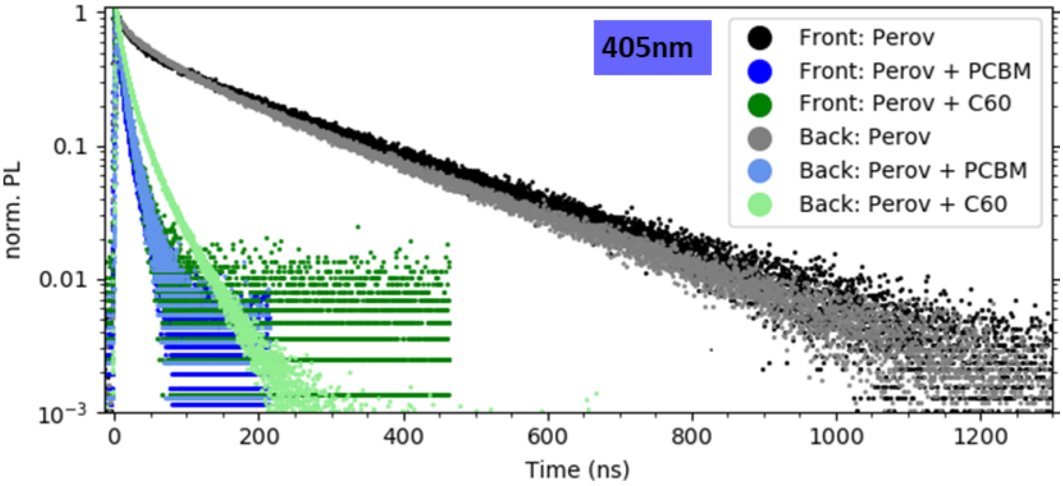

Figure 4.10: Normalised TCSPC curves for fullerene bilayers (batch 2, thick perovskite and thick CTL), using 405nm excitation on either the back side (quartz substrate) or the front side (CTL).

which had similar pulse fluences and spot sizes (see section 2.4.2). Since this measurement has temporal resolution of a few nanoseconds (depending on the time range studied), the carrier density following short wavelength excitation is expected to diffuse throughout the thickness of the film within the instrument response time (this is discussed in chapter 5). However, the initial difference in carrier distribution for different excitation wavelengths may still affect the decay dynamics beyond the first few nanoseconds for these asymmetric samples. For example, extraction into the CTL modifies the subsequent spatial distribution of carriers, so excitation on different sides may have different decay dynamics. It should be remembered that for 405nm excitation through the front, there will be significant parasitic absorption which reduces the number of photogenerated carriers in the perovskite layer, and thus potentially the decay curve.

4.3.5.2 Results

Figures 4.8 to 4.12 show TCSPC measurements of batch 2 samples with thick perovskite layers and thick CTLs. In Fig. 4.8, measurements of the reference plain perovskite sample

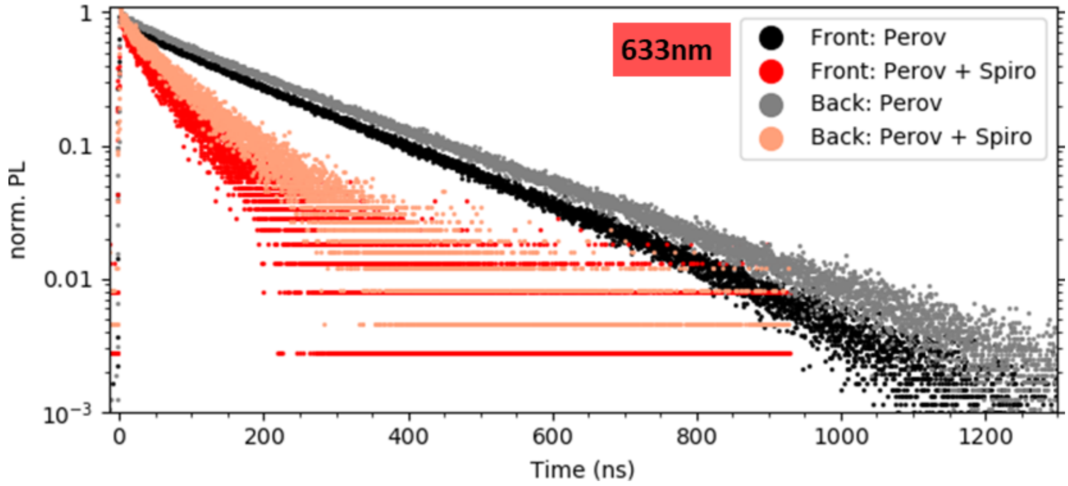

Figure 4.11: Normalised TCSPC curves for Spiro bilayers (batch 2, thick perovskite and thick CTL), using 633nm excitation on either the back side (quartz substrate) or the front side (CTL).

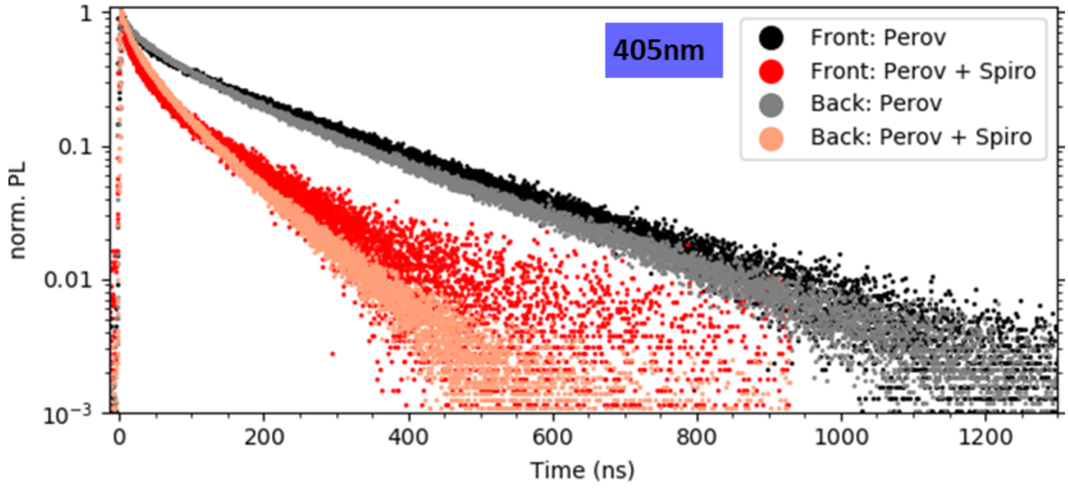

Figure 4.12: Normalised TCSPC curves for Spiro bilayers (batch 2, thick perovskite and thick CTL), using 405nm excitation on either the back side (quartz substrate) or the front side (CTL).

excited with 633nm on either side show a single monoexponential decay, whereas for 405nm excitation, the decay is slightly faster for the first hundred nanoseconds. This trend also appears to carry through for many of the other samples as well. This possibly suggests that the different initial distributions for 405nm and 633nm can affect the dynamics for the first ∼100ns.

The thick (∼120nm) PCBM layer significantly accelerates the PL decay compared to the reference, when excited with either wavelength and on either side (Fig.4.9 and 4.10). The side of excitation appears to make little difference, however 633nm excitation appears to result in slower decays. A thick C_{60} (∼30nm) layer also accelerates the decay (Fig.4.9 and 4.10). For 405nm excitation, the decay is accelerated by C_{60} almost as much as by PCBM, but for 633nm excitation, C_{60} has much less impact on the decay than PCBM does. This might be related to the observation that for 633nm excitation on C_{60} samples, the PL lifetime significantly increased during illumination (possibly due to easier penetration of this thinner layer by atmospheric gases).

A thin PCBM layer (not shown) does not accelerate the decay as much as a thick layer, and a thin C_{60} layer (not shown), which covers only a minority of the surface area, has very little effect on the decay. This emphasises that thin layers may not have complete surface coverage and thus CTL thickness is an important parameter to optimise in the full device stack.

For Spiro-OMeTAD bilayers (Fig.4.11 and 4.12), the decay is accelerated compared to the reference sample but not as much as the for fullerene bilayers. Excitation with either wavelength and on either side gave similar decay rates, except 633nm excitation gave a more monoexponential decay than 405nm, as was observed for the plain sample. A thin Spiro layer (not shown) gave a similar decay to a thick (∼120nm) Spiro layer.

Overall, there is a clear trend that the fullerenes accelerate the PL decay more than Spiro.

4.3.6 OPTP

4.3.6.1 Methodology

OPTP measures the photoconductivity transient for the first ∼3ns following photoexcitation by a ∼100fs pump pulse, and with sub-picosecond resolution. Carrier transport through the thickness of the film is expected to occur on sub-nanosecond timescales (validated in Chapter 5), and therefore the impact of the initial spatial distributions of the photoexcited carriers should be observed in the transients. This is in contrast to TRPL where the initial carrier distribution should spread throughout the thickness of the film within the instrument response time. Illuminating with short wavelengths generates carriers near the surface of incidence, so for excitation through the quartz side (back side), there is expected to be no extraction of carriers at the CTL interface until carriers have diffused through the perovskite layer. On the other hand, for excitation through the CTL, carriers are generated adjacent to the CTL interface and are available to be extracted immediately. Illuminating with long wavelengths generates carriers throughout the depth of the perovskite layer, so excitation on either side should both generate some carriers next to both interfaces, so there should be less difference in the decay dynamics.

A factor to keep in mind when interpreting OPTP measurements of selective carrier extraction, is that the signal measured by OPTP is proportional to the mobility of the carriers (at THz frequencies), which may not be the same for electron and holes. Therefore, extraction of one carrier type may cause a different reduction of the signal amplitude compared to extraction of the other type. Computational studies have suggested similar effective masses for both electrons and holes [300], but the ratio of their mobilities is harder to determine as mobility depends on the scattering rate as well. Some works have tried to find the individual mobilities by separately determining the THz sum mobility, and the ambipolar transport mobility. However, the transport mobility is for long distances and low frequencies, whereas the THz mobility is for high frequencies and short distances, and comparison of DC mobility measurements and THz mobility measurements show significant differences [271]. This means the ambipolar transport mobility and THz sum mobility cannot be used to find individual electron and hole mobilities.

Measurements using the electronically delayed OPTP setup developed in Chapter 6 show that at low fluences ($\sim 1\mu\text{Jcm}^{-2}$), the photoconductivity decayed monoexponentially with a lifetime of ~170ns. Using the standard OPTP setup, low pump fluences gave a flat decay over the 3ns pump-probe delay range. At higher fluences, the decay deviated from monoexponential indicating that non-linear processes, i.e. bimolecular recombination, started to contribute to the decay. OPTP measurements were performed using the lowest pump fluence that acheived a sufficient signal-to-noise ratio ($\sim 6\mu\text{J/cm}^2$) in order to minimise the amount of recombination during the 3ns window. Having negligible decay in the reference sample during the 3ns window significantly simplified the interpretation of any changes due to the presence of a CTL.

By using the same pump fluence for each measurement, the density in the perovskite layer and thus recombination dynamics should be the same. The pump laser power may drift slowly over time so it was carefully monitored between every measurement to ensure it was same when starting each measurement. This power drift was much more significant for 410nm and 460nm excitation, as these wavelengths were produced by a sequence of several non-linear interactions in the optical parametric amplifier, which will amplify any power and pointing instabilities of the main laser more than for 700nm excitation, which required fewer non-linear interactions. When using the same pump fluence, any difference in the initial amplitude of the signal could be due to either reduced absorption in the perovskite layer, or a decay process occurring within the instrument response time (the ~1ps rise time of the photoconductivity signal). Therefore, measuring the absorption and reflectance of the CTLs at the pump wavelengths is crucial to identify any reduced photogeneration in the perovskite, and thus distinguish this from very fast decay within the instrument response time. For example, for Spiro-OMeTAD there is severe parasitic absorption for 410nm only, and for fullerenes, parasitic absorption is more significant for the shorter wavelengths, 410nm and 460nm.

Measurements with 410nm and 700nm excitation were performed on samples from batch 1 (perovskite thickness ~600nm), and measurements with 460nm excitation were performed on samples from batch 2 (perovskite thickness ~370nm). For 460nm excitation, for the same incident laser power, different samples had slight differences in the initial amplitude of the photoconductivity, which are consistent with the CTLs changing the photon flux entering the perovskite layer. Therefore, the plain reference sample was measured with several slightly different laser powers in order to match the initial amplitude to that of the other samples, so that they all have the same initial carrier density and can be compared.

4.3.6.2 OPTP on PCBM and C_{60} bilayers

For the fullerene coated samples, there is a consistent trend of accelerated decay of the OPTP signal over the 3ns window relative to the reference sample, which is now discussed.

For 700nm excitation, there is negligible parasitic absorption by the fullerene, so the total number of photoexcited carriers and thus photoconductance should be the same when excited through either the fullerene or quartz side. The results for the PCBM bilayer are shown in Fig.4.13. Since the initial amplitude of the signal is the same for excitation through either side, this shows that any decay of the population during the instrument response time is smaller than the uncertainty in the measured amplitude. For this excitation wavelength, the decay of the signal is very similar for excitation through either side, which is not surprising since carriers are photogenerated throughout the film in both cases.

For excitation with 410nm and 460nm (Figs.4.14 and 4.15), the initial amplitude of the signal was found to be slightly lower for excitation through the fullerene layer compared to through the quartz substrate, but this reduction agrees with the amount of parasitic absorption by the fullerene, and so there is no clear evidence of extraction within the instrument response time (but also not clear evidence that this does not occur). For 460nm excitation, Fig.4.14 shows measurements of the bare perovskite with pump fluence adjusted to match the initial amplitude for the fullerene bilayer samples.

Excitation with 410nm and 460nm through the fullerene layer (front side) generates most carriers within 35nm and 50nm of the interface respectively, which explains why the signal decays immediately for excitation on the front side. On the other hand, excitation

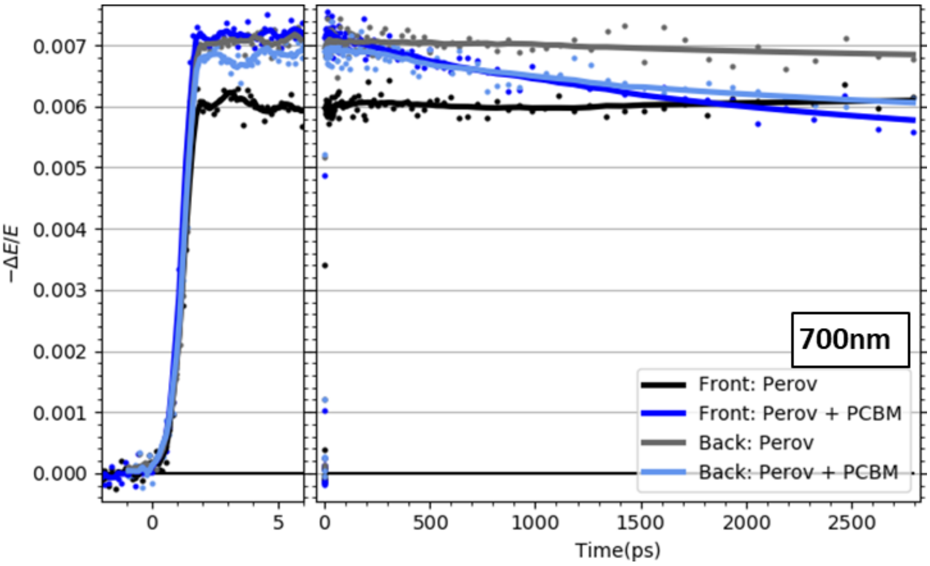

Figure 4.13: OPTP measurements of PCBM bilayers and the plain perovskite reference sample with 700nm excitation on either the front side or back (quartz) side (batch 1, perovskite thickness ~600nm).

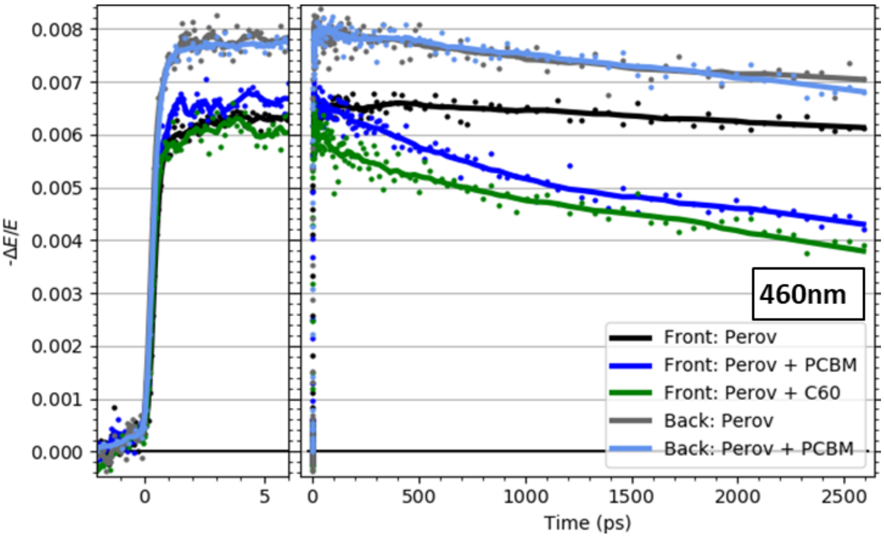

Figure 4.14: OPTP measurements of PCBM and C_{60} bilayers and the plain perovskite reference sample with 460nm excitation on either the front side or back (quartz) side (batch 2, perovskite thickness ~370nm).

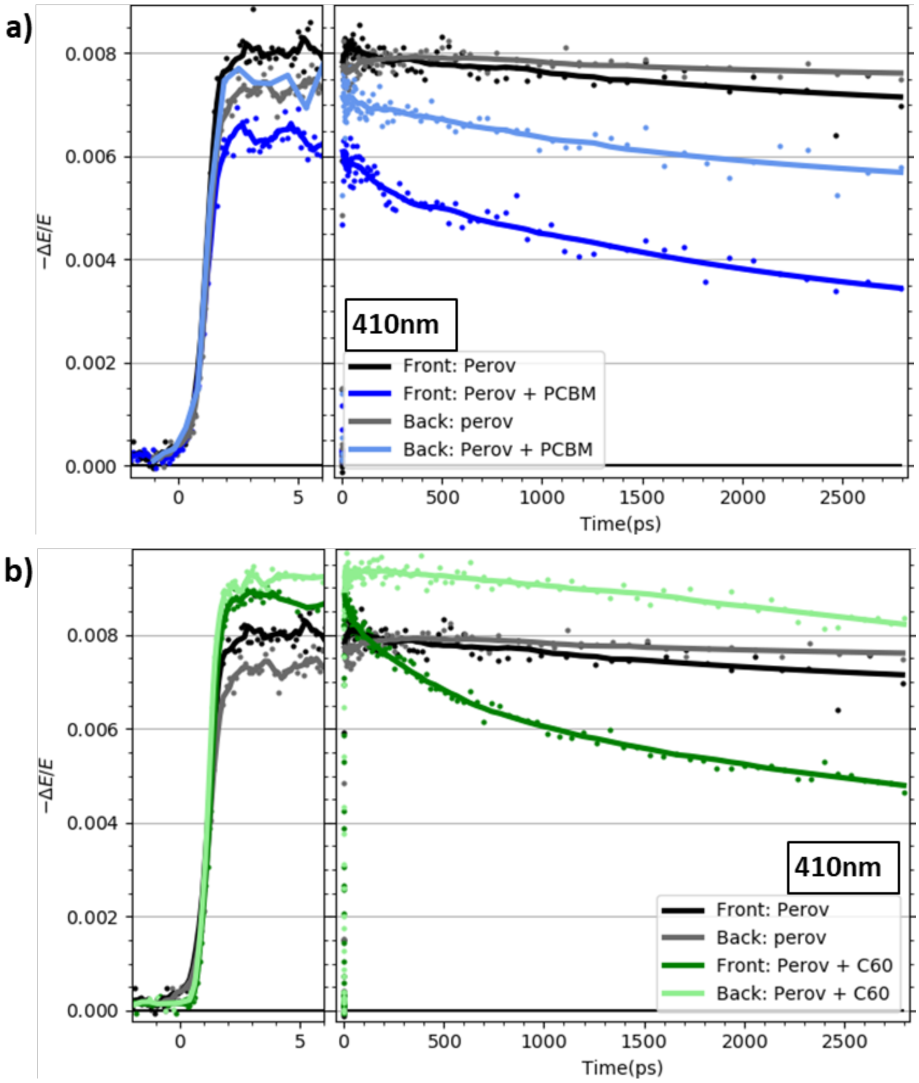

Figure 4.15: OPTP measurements of a) PCBM bilayers and b) C_{60} bilayers compared to the plain perovskite reference sample, using 410nm excitation on either the front side or back (quartz) side (batch 1, perovskite thickness ~600nm).

through the quartz substrate (back side) generates most carriers several hundred nanometres away from the CTL interface, and thus the decay is expected to be delayed as carriers must diffuse through the perovskite. For 410nm excitation on the back side of the C_{60} bilayer this delay is very clear. Even at late times, the decay for back excitation is still not quite as steep as for front excitation as there will still be fewer carriers near the interface. For 410nm excitation on the back side of the PCBM bilayer, the decay of the signal does not appear to be delayed very much, suggesting either that diffusion through the thickness of this sample is quicker, or that the solution deposited PCBM has penetrated closer to the quartz side, thus reducing the distance carriers must diffuse to reach the PCBM. Since for front side excitation C_{60} gives a similar decay rate to the PCBM bilayer, this suggests the effective surface recombination rates were similar for both CTLs. Therefore, the difference between the PCBM and C_{60} bilayers for back side excitation suggests that the vapour deposited C_{60} layer does not penetrate into the grain boundaries like the solution deposited PCBM does. Indeed, AFM topography maps (performed by Ziyi Hu at the University of Warwick) of thin C_{60} layers on quartz show that the molecules aggregate into clusters rather than forming complete monomolecular layers (C_{60} layers of sufficient thickness to ensure complete coverage were used in this work).

For 460nm excitation on the back side, the PCBM and C_{60} layers do not introduce any additional decay compared to the bare perovskite sample, suggesting that very few carriers diffuse to the ETL interface within 3ns. The samples for 460nm excitation were from batch 2, which were thinner than the batch 1 samples used for the measurements 410nm excitation. The lack of decay for the C_{60} bilayer from batch 2 suggests that the diffusion through the thickness was slower for this batch of samples, possibly related to the size of the grains - smaller grains would result in more grain boundaries normal to the diffusion through the thickness. The lack of decay for the PCBM bilayer from batch 2 suggests that the PCBM did not penetrate the perovskite layer as much, possibly due to closer packing of the perovskite grains and fewer pinholes.

4.3.6.3 OPTP on Spiro Bilayers

A universal trend for the Spiro coated samples is that there is no decay of the OPTP signal over the 3ns window for excitation on either side of the sample and with any of the pump wavelengths used (410nm, 460nm, 700nm). The only differences are in the initial amplitude of the signal relative to the bare perovskite reference sample.

For excitation on the quartz side, the intensity being absorbed in the perovskite layer should be the same for all samples since the propagation path is the same. Therefore, the observation that the initial amplitude is found to be the same (within measurement uncertainty) for both the plain perovskite and Spiro coated samples for excitation on the quartz side with any wavelength, indicates that the Spiro layer did not induce decay within the instrument response time, even when carriers were generated near the Spiro interface by using 700nm excitation. The carriers generated by 410nm and 460nm excitation through the quartz side, which have shorter absorption depths, are also expected to diffuse to the Spiro interface within 3ns, as evidenced by the fullerene measurements. Therefore, the lack of photoconductance decay for any of these wavelengths suggest interface processes are slow.

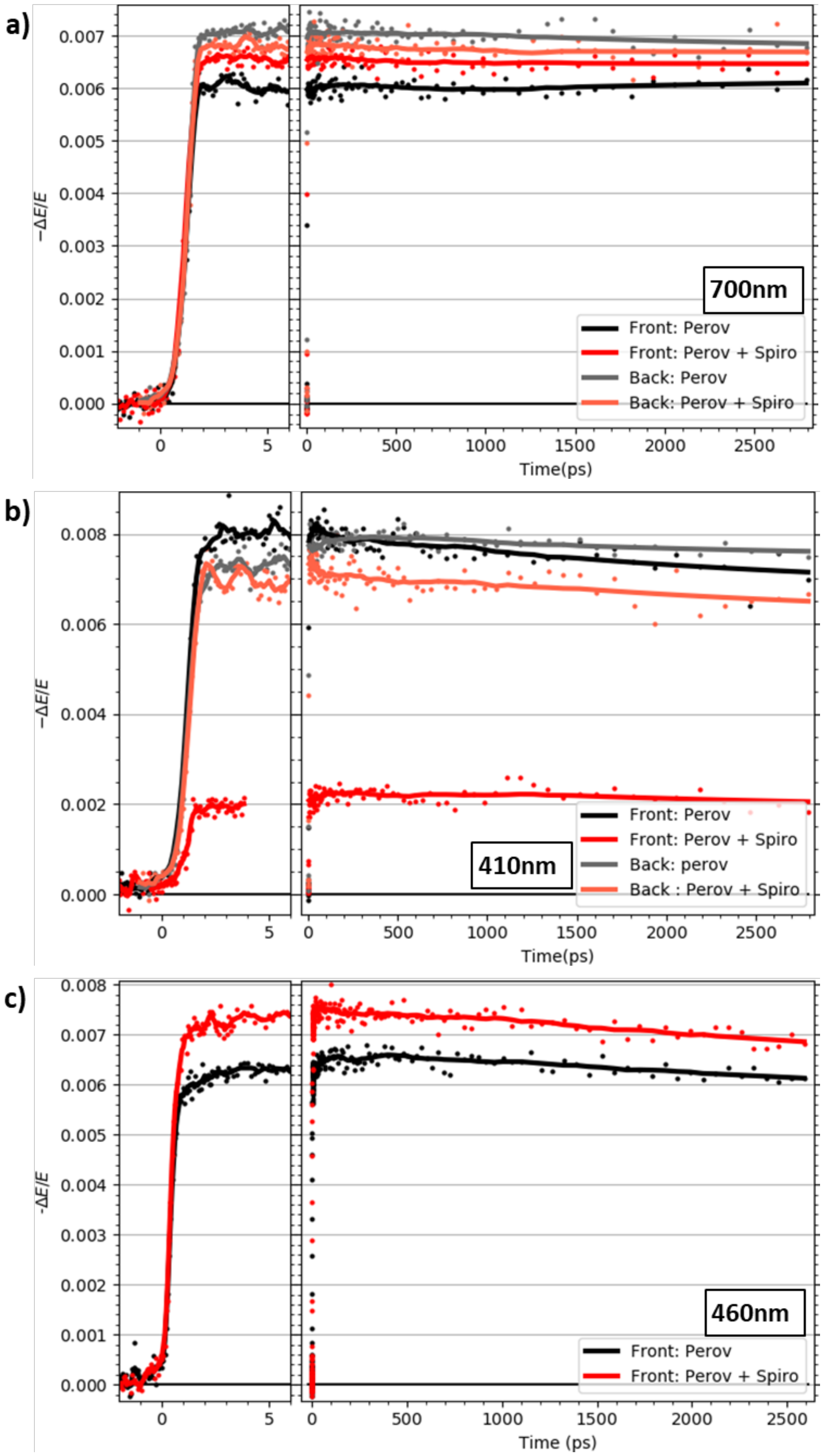

Figure 4.16: OPTP measurements of Spiro bilayers and the plain perovskite reference sample on either the front side or back (quartz) side. a) 700nm excitation b) 410nm excitation (both batch 1, perovskite thickness ∼600nm). c) 460nm excitation (batch 2, perovskite thickness ∼370nm).

Furthermore, for 700nm excitation through the Spiro layer (front side) instead of the quartz, since 700nm has no parasitic absorption in the Spiro, the observation of the same initial amplitude as the reference sample indicates there is also no extraction within the instrument response time for this measurement. Again, there is no decay over the 3ns window.

None of these measurements (Fig.4.16a-c) show any evidence of hole extraction within the 3ns window. The only possible evidence for hole extraction could be for 410nm excitation through the Spiro (front side), for which the initial amplitude is reduced to 1/3 of the amplitude for the plain reference sample. This has previously been attributed (see section 4.2.2) to fast extraction of one carrier within the instrument response time (IRT), followed by slow decay of the remaining carrier population, as the signal is flat over the 3ns window. For Fig.4.16b, attributing the reduction of the initial amplitude to hole extraction, would imply the THz mobility of the remaining electrons is half that of the holes, as the amplitude is reduced to 1/3. Observations of band bending at the Spiro interface or in the Spiro layer itself have been reported in the literature [107–109], which would favour fast hole extraction, although it was discussed in section 1.4.5 that these observations are not necessarily applicable to other samples. It should be noted that the hypothesis of fast hole extraction followed by slow cross-interface recombination of extracted holes and remaining electrons, requires that the rate constant for the cross-interface recombination is extremely low, since the simulations in chapter 5 show that selective extraction of one carrier will actually attract the other carrier to the interface, increasing the density of both carriers at the interface.

However, 410nm excitation is strongly parasitically absorbed by the Spiro layer with ~50% of the incident light being absorbed (there's a large uncertainty as the pump's spectrum overlaps with a steep absorption edge), which will reduce the initial amplitude of the perovskite's photoconductance, and can thus explain the significant amplitude reduction. Furthermore, excitation with 460nm (2.70eV) through the Spiro layer, which has a similar absorption depth in the perovskite layer (50nm vs 35nm for 410nm excitation), did not show reduced initial amplitude compared to the reference. This is consistent with the Spiro layer having negligible absorption at 460nm (in fact the initial amplitude was slightly larger than the reference, which is consistent with the Spiro layer actually reducing the reflectance at this wavelength). Due to the similar absorption depths of 410nm and 460nm, this suggests the reduced initial amplitude for 410nm is due to parasitic absorption rather than fast extraction of carriers concentrated at the interface. Furthermore, for 410nm excitation the parasitic absorption in the Spiro layer is expected to actually inhibit hole extraction from the perovskite, as the absorption will cause QFL splitting in the Spiro layer and reduce the QFL splitting in the perovskite layer, and thus reduce the hole QFL difference between the layers that is the driving force for extraction. This makes fast hole extraction for 410nm excitation seem less likely.

A possible alternative explanation for the difference between 410nm and 460nm excitation, is that 410nm excites holes at deeper positions in the perovskite's VB, i.e. "hot holes", and then it could be hypothesised that they are extracted at a much faster rate due to better energy alignment of these hot holes with the Spiro-OMeTAD energy levels, and a few papers have considered this hot hole extraction mechanism [285, 288, 293]. When exciting on the quartz side (back side), the hot holes generated near the quartz interface may relax to the VB edge before reaching the Spiro interface, and thus do not have fast extraction. One possible way of identifying differences between the holes generated by 410nm and 460nm excitation is to consider the absorption spectrum of the perovskite layer, as a sharp change in absorption strength between these two wavelengths may indicate photogeneration in different parts of the bandstructure. However, between these two photon energies (wavelengths), the absorption spectrum of the thin perovskite sample shows no steep changes that might suggest holes are photogenerated in very different positions in the band structure.

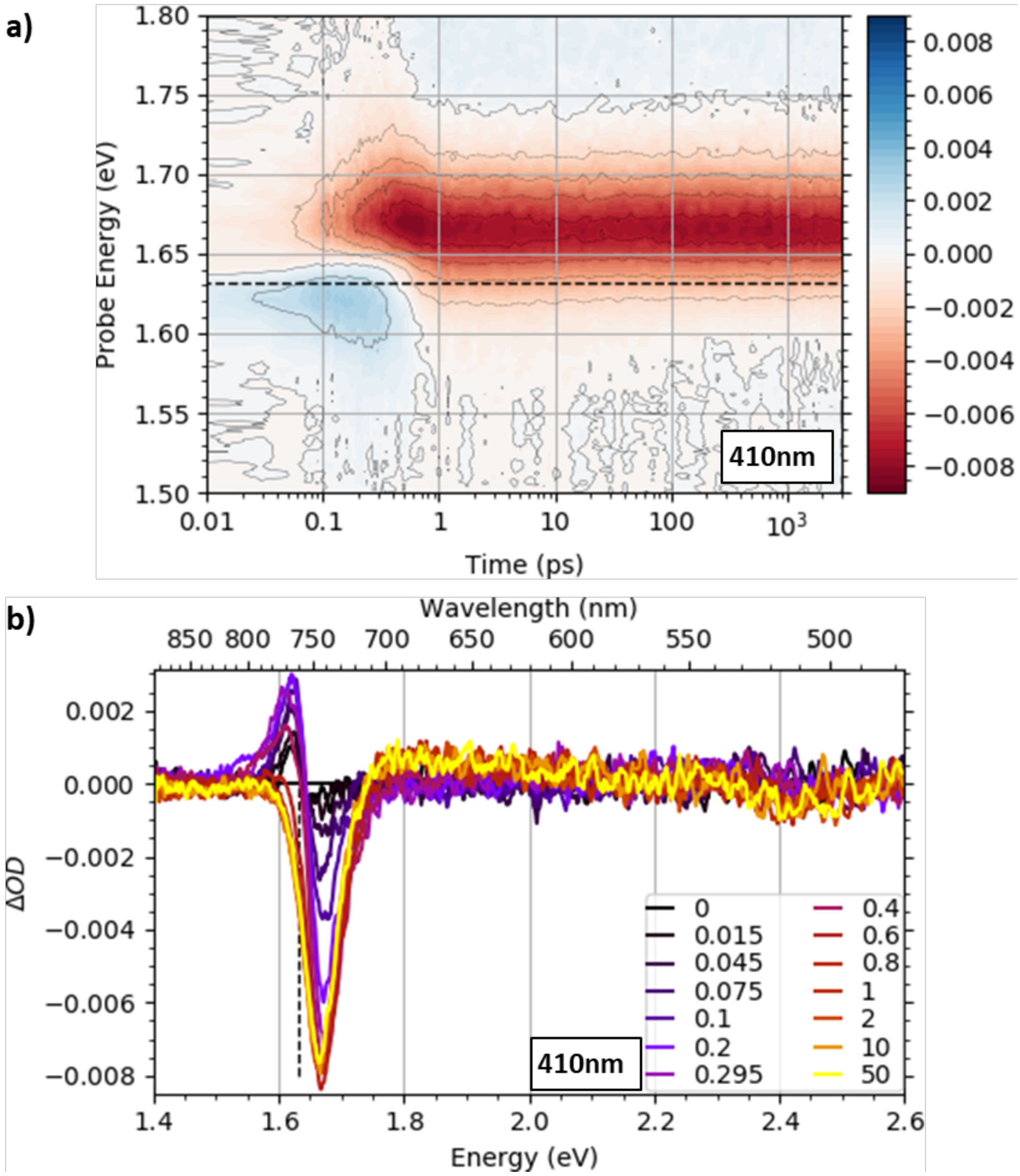

Figure 4.17: TA measurements of a bare perovskite sample (batch 1) with 410nm excitation on the front side (perovskite side). a) 2D colour map of the photoinduced change in optical density ΔOD, plotted as a function of probe energy and pump-probe delay time (logarithmic axis). Red indicates a bleach i.e. a reduction in absorption, and blue represents an increase in absorption. The peak of the PL spectrum is indicated by the black dashed line. b) The TA difference spectra at a selection of pump-probe delay times (ps).

Overall, the reduced initial amplitude for 410nm excitation through the Spiro layer can mostly be attributed to the parasitic absorption, and the other measurements show no signs of hole extraction within the 3ns window. If fast extraction of hot holes generated next to the Spiro interface does occur, it would not be relevant for standard perovskite solar cell architectures, since Spiro is used as the p-type layer in n-i-p cells, in which illumination is through the opposite side to the Spiro layer. In this case there will be negligible absorption of short wavelength photons near the Spiro interface and thus the possible mechanism of fast hot hole extraction would be insignificant in working devices.

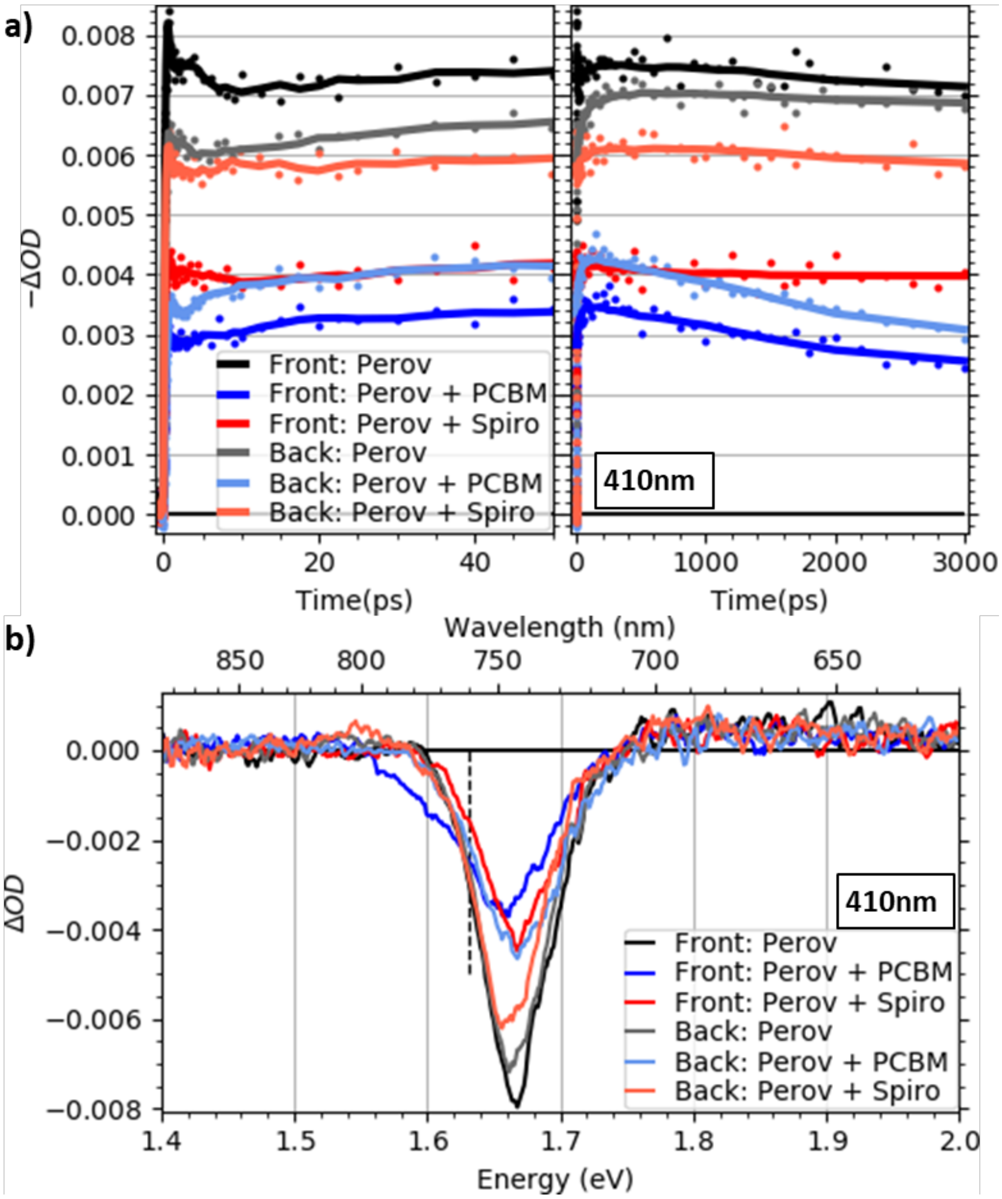

Figure 4.18: TA data for different samples (batch 1) excited with 410nm on either the front or back (quartz) side. a) For each sample, the amplitude at a single wavelength corresponding to the peak of the GSB at late times, is shown as a function of time. b) The TA difference spectra at pump-probe delay = 200ps for each sample.

4.3.7 Transient Absorption

TA measurements were performed with 410nm excitation and a 2D contour map of the time resolved difference spectra for the plain perovskite sample is shown in Fig.4.17a. The peak of the PL spectrum is indicated by the black dashed line, which emphasises that the PL is Stokes-shifted with respect to the absorption. The features in the TA difference spectra, which are shown at a selection of pump-probe delay times in Fig.4.17b, are consistent with the literature as described in section 4.2.3. There is a GSB at ∼1.67eV (∼745nm), a high energy bleach feature at ∼2.45eV(∼510nm), and a broad PIA in between. A sharp PIA just below the GSB energy appears within the instrument response time and then decays over the first picosecond. The high energy side of the GSB can be seen to shift to lower energies over the first ∼1ps as carriers cool.

TA measurements of the perovskite-CTL bilayers showed the same trends as for OPTP. The amplitude at a single wavelength and the integral over a range of wavelengths were both checked. The amplitude at a single wavelength corresponding to the peak of the GSB at late times is shown as a function of time in Fig.4.18a. For early times shown on the left plot, a sharp decrease and slower rise can be seen for all samples, which is due to the shape of the GSB changing over the first few picoseconds. For TA measurements, the initial amplitude of the signal was more difficult to control than for OPTP, partly due to the overlap of the pump and probe beams being more sensitive to alignment due to their smaller spot sizes and non-collinear alignment. As was observed for OPTP, the presence of Spiro does not accelerate the decay of the signal for excitation on either side, but the presence of PCBM does accelerate the decay for excitation on either side. This agreement between TA and OPTP transients confirms that the decay of the photoconductance signal is due to carrier recombination rather than changes in mobility. Fig.4.18b shows the TA difference spectra for all the samples at pump-probe delay = 200ps, confirming they all have similar spectral shapes.

4.4 Conclusion

The time resolved measurements presented in this chapter indicate that the decay of the carrier population in the perovskite layer is significantly accelerated by the addition of a PCBM or C_{60} layer, and if carriers are photoexcited near the interface then this accelerated decay is evident within the first tens of picoseconds after photoexcitation. The fact that the initial amplitude of the OPTP signal $\Delta E/E$ is not reduced (to within measurement uncertainty of ∼5-10% for short wavelengths, less for long wavelengths) implies that the fullerene layers do not significantly reduce the population within the rise time of ∼ 1ps.

The addition of a Spiro layer does not accelerate the decay of the population as much as for fullerene layers, and any difference compared to the bare perovskite sample is only evident after a pump-probe delay of several 10s of nanoseconds (which can only be observed by TCSPC). Similar to the fullerene layers, the initial amplitude of the OPTP signal $\Delta E/E$ for Spiro is not reduced, except when the pump pulse is parasitically absorbed by the Spiro layer for 410nm excitation, suggesting that the Spiro layers do not cause any detectable extraction or recombination of carriers within the rise time of ∼ 1ps.

Since fullerenes have been shown to passivate surface defects [99, 101, 103] and improve the performance of devices, they are not expected to increase the defect density at the interface (organic molecules do not suffer from dangling bonds in the same way that inorganic crystalline semiconductors do). The fullerenes are expected to extract electrons from the CB of the perovskite as they function well in solar cell devices, and the expected band alignment should allow extraction [104]). Therefore, for samples coated with fullerenes, the strong decay of the carrier population in the perovskite layer immediately following photoexcitation could be attributed to extraction of electrons. The numerical simulations of the carrier dynamics presented in the next section show that this separation of charge would quickly prevent further extraction of electrons and the carrier density in the perovskite would stop decaying, in contrast to what is observed. This is discussed in the next chapter.

Chapter 5

Modelling of Charge-Carrier Dynamics in Perovskite-CTL Bilayers

5.1 Introduction

Understanding of the observed population dynamics can be improved by comparing the data to a mathematical model. This can provide qualitative information about what processes are controlling the decay dynamics, but also quantitative information about properties such as rate constants and diffusion coefficients, that can be used in simulations of devices. Previous works on perovskite-CTL bilayers have included recombination and extraction processes, and sometimes diffusion processes, but have not considered the Coulombic force between electrons and holes. When charge carriers of one polarity are selectively transferred across an interface, this results in charge separation which may lead to Coulombic forces having a significant impact on carrier dynamics. Therefore, in this chapter the impact of the Coulombic forces is assessed.

Coulombic forces are included in more sophisticated simulation packages published in the literature or distributed commercially. Some simulation packages developed by academics are available for free such as PC1D/3D and Quokka2/3 for silicon solar cells, SCAPS1D for thin film solar cells and Solcore for quantum well solar cells. All these programs only consider steady state simulation, or sweeps across a range of conditions, finding the steady state solution for each condition. Some simulation packages have been specifically designed for perovskite solar cells, by including ion migration, such as Ion-Monger and Driftfusion (both use the finite element method and MATLAB routines). However, these are focussed on simulating full devices and particularly experiments such as *J*-*V* curves or *C*-*V* curves and are not designed to simulate transients on picosecond timescale following pulsed illumination. Although ion migration occurs much more slowly than the picosecond timescales considered here, ion migration will influence the electric fields that exist at equilibrium. There are also commercial packages that can be used to simulate solar cells such as Advanced Semiconductor Analysis (ASA) (only steady state), COMSOL, SETFOS by Fluxim, and Sentaurus by Synopsys.

In this chapter, a mathematical model for the spatially and temporally dependent carrier densities that includes Coulombic forces is employed. It is not possible to solve this analytically, so a numerical method is used. The numerical method will be introduced, the choice of method will be justified, and the accuracy of the method will be explained. The results of numerical solutions to the model are compared to the experimental data and the impact of charge separation is assessed. Following this, analytical solutions of a simplified model that is valid in the absence of charge separation, is used to fit the experimental data and estimate the interface recombination rate constant and the diffusion coefficient.

5.2 Numerical Methods and their Accuracy

5.2.1 Numerical Analysis

Common to all numerical methods is the discretisation of the dependent and independent variables, so that they can be stored in a computer. Most methods therefore require the domain to be divided into a mesh of edges and nodes. Problems of analysis, involving continuous variables and operations such as derivative and integrals, can only be tackled by a computer by formulating algebraic problems that approximate them.

5.2.2 Choice of Numerical Methods

Three of the main numerical methods are finite difference (FD), finite volume (FV) and finite element (FE) methods, where this classification distinguishes the conceptual approach to deriving algebraic approximations to the differential equation [254, 256, 257, 301, 302]. Finite element methods are the most complex to implement and are usually only worth doing if the resultant code will be heavily used. From practical experience (but not in a rigorous mathematical sense), finite difference methods have been found to be better for semiconductor equations than finite element[254]. For the semiconductor equations, the same algebraic approximations can be derived from the finite difference or finite volume method [254]. The main difference is in treating discontinuities or implementing Neumann boundary conditions.

For differential equations, finite differences is the conceptually simplest method, and the easiest to implement. The continuous variables are sampled at discrete points called nodes on a mesh (see Fig.5.1), and the differential equation at each node is expressed in terms of these nodal values. Derivatives are approximated by difference formulae, e.g. $\left.\frac{df}{dx}\right|_a = \frac{f(a+h)-f(a)}{h}$, which are derived from Taylor expansions [303]. So the differential equation at each node becomes an algebraic equation containing the values at neighbouring nodes, and so the equations at neighbouring nodes will be coupled.

The finite volume method divides the domain into contiguous volumes (see Fig.5.1), and an integral form of the differential equation is used so that it is expressed in terms of fluxes between volumes. Each “control volume” (CV) is associated with a value of the variable, which can be viewed as an average value for the volume. The fluxes at the boundaries are estimated with finite difference formulae, which invoke the values in the volumes on either side of the boundary.

For conservative equations, finite volume is the most popular approach, as it is the best at conserving quantities because it is based on a balance equation for each volume.

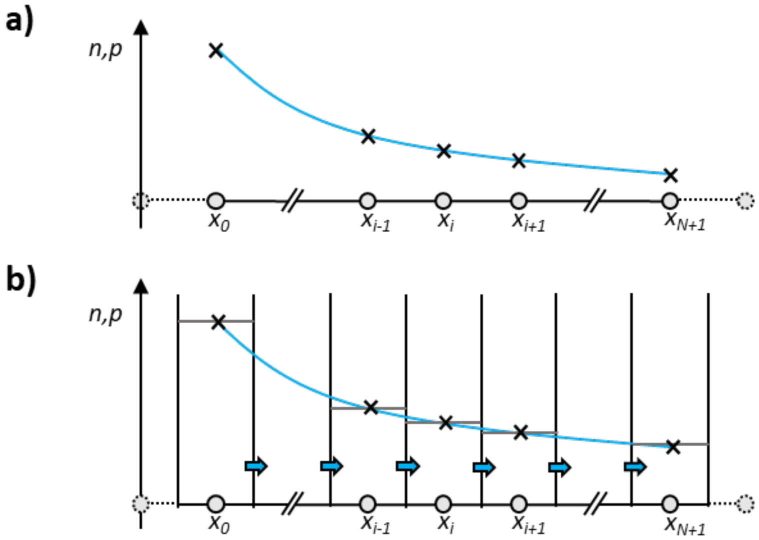

Figure 5.1: Schematic of a) finite difference (FD) discretisation and b) finite volume (FV) discretisation, for one spatial dimension (the time dimension is not shown). The FD approach samples the continuous function e.g. the carrier densities $n(x)$ and $p(x)$, at a series of nodes, whereas the FV approach treats these samples as averages over the control volumes (indicated black horizontal lines), which are the volumes between the midpoints indicated by vertical lines. FV conserves the flux across the boundaries between control volumes (CVs). So called ghost nodes outside the domain boundary are shown with dashed lines.

This approach is necessary to deal with discontinuities, for example changes in the permittivity and diffusion coefficient at an interface. The FV method can be referred to by many other names, such as FD, cell centred difference, box method, balance method, or discontinuous FE [302].

5.2.3 Performance

To assess the accuracy of a numerical approximation, the differences between exact values and the numerical approximations, i.e the errors, can be analysed quantitatively. Furthermore, it should be checked that the numerical approximation imposes conditions that reflect the real problem, such as the carrier density must always be positive.

There are two types of error, those that are due to the numerical method, and those that are due to the finite precision of the representation of numbers in a computer, called roundoff error [253]. The former type includes discretisation/truncation errors due to approximating a derivative as a difference. Roundoff errors occur due to the finite significant figures of floats, or due to the inability of binary to represent decimals. For most differential equation problems, the discretisation/truncation error dominates (unless the step size is made very small). The local error is the difference between the exact value and the numerical approximation of the dependent variable at a node (or the control volume average for FV method). The local Truncation error of the algebraic approximation can be determined by inserting Taylor expansions of the exact solution into the algebraic equation.

The global error is the norm of the local errors in the domain, for example the sum of the local errors or the maximum local error. For the time dependent problems considered here, the global error accumulates as time increases. The stability of a numerical solution is whether this global error is bounded as time tends to infinity, although it has different definitions in different contexts [253]. A desired property is convergence, that the numerical solution tends to the analytical solution as the size of the discretisation step tends to zero, so the (global) error should be proportional to the step size (raised to a positive power). Determining the stability and convergence properties is not a trivial process and becomes very difficult for differential equations that are not simple ODEs. In this work, the semiconductor equations form a stiff problem: one general definition of stiffness is that very small step sizes are required for stability, in particular that the choice of step size is limited by the need for stability rather than the desired accuracy.[253]

Time dependent PDEs (i.e. initial value problems) can be solved using an Explicit or an Implicit method (also called Forward and Backward Euler methods – see section 5.3.2), and for simple ODEs it can be shown they both have convergence of order 1 (i.e. global error is proportional to step size). However, the Explicit method is only stable for small time steps, whereas the Implicit method is stable for much larger step sizes. There are also methods that are neither fully explicit nor fully implicit, that have higher order convergence.

5.2.4 Additional Considerations for Semiconductor equations

For a numerical solution to accurately replicate the physical solution, it must be able to resolve the steepest possible variations of a dependent variable with respect to the independent variables, time and space. For the semiconductor equations, the maximum rate of variation of the dependent variables with respect to time and space can be defined [304]. The Debye length is the characteristic length over which a net charge density varies for mobile charges e.g. the exponential decay of net charge density away from a charged region. The relaxation time is the time it takes for a perturbation to the equilibrium charge distribution to relax back to equilibrium. Therefore, in order to fully resolve all possible behaviours, the spatial steps should be smaller than the Debye length and time steps should be smaller than the relaxation time. Having small steps is computationally expensive so to minimise the total number of nodes, a non-uniform grid can be used, but this requires significantly more user effort that may outweigh the computational cost of using uniform steps.

5.3 Finite Differences

5.3.1 Finite Difference Expressions

In the finite difference method, the derivatives in the differential equations are approximated using difference formulae, which are derived from Taylor expansions about the point of interest.

The difference formula for a derivative at a node will invoke values at neighbouring nodes. The set of nodes used in a difference formula is called the stencil. For multidimensional problems, the difference equations are simplest if the set of discrete points are arranged along lines (mesh lines or edges) parallel to the axis.

The simplest difference formulae for first order derivatives are the forward, backward and central differences, which all only use two nodes in their stencil. The first two are derived from the Taylor expansion for the node that is forward or backward of the node of interest respectively. This is rearranged to give the first order derivative in terms of the function's value at two points, the step size, and higher order derivatives. The forward difference formula is

$$f(x_{i+1}) = f(x_i) + \delta x \left.\frac{\partial f}{\partial x}\right|_i + \frac{1}{2}(\delta x)^2 \left.\frac{\partial^2 f}{\partial x^2}\right|_i + ...$$

$$\left.\frac{\partial f}{\partial x}\right|_i = \frac{f(x_{i+1}) - f(x_i)}{\delta x} + O(\delta x)$$

The backward difference formula is

$$f(x_{i-1}) = f(x_i) - \delta x \left.\frac{\partial f}{\partial x}\right|_i + \frac{1}{2}(\delta x)^2 \left.\frac{\partial^2 f}{\partial x^2}\right|_i + ...$$

$$\left.\frac{\partial f}{\partial x}\right|_i = \frac{f(x_i) - f(x_{i-1})}{\delta x} + O(\delta x)$$

The higher order derivative terms are neglected and the neglected term with the lowest order of step size gives the order of accuracy, in this case $O(\delta x)$. These are "one sided" formulae. The central difference formula comes from subtracting these two expansions, and rearranging for the first derivative. The central difference formula is

$$\left.\frac{\partial f}{\partial x}\right|_i = \frac{f(x_{i+1}) - f(x_{i-1})}{2\delta x} + O(\delta x^2)$$

or

$$\left.\frac{\partial f}{\partial x}\right|_i = \frac{f(x_{i+\frac{1}{2}}) - f(x_{i-\frac{1}{2}})}{\delta x} + O(\delta x^2)$$

This is a "two-sided" formula. The lowest order term that is neglected is O(δx^2). Therefore, central differences are preferred.

For second order derivatives, a difference formula can be derived by adding the forward and backward expansions, and the first term that is neglected is O(δx^2).

$$\left.\frac{\partial^2 f}{\partial^2 x}\right|_i = \frac{f(x_{i+1}) - 2f(x_i) + f(x_{i-1})}{\delta x^2} + O(\delta x^2)$$

This can also be derived by applying the central difference formula twice, but using midpoints either side rather than nodes either side.

For nodes on domain boundaries, the difference formula for the derivatives at these nodes may invoke nodes that are outside the domain so do not exist (this may also be a problem for nodes that are near the boundary if the difference formula invokes nodes further than just nearest neighbours). For example if the right side boundary is at node x_N, a central difference formula in the differential equation at this boundary node is

$$\left.\frac{\partial f}{\partial x}\right|_N = \frac{f(x_{N+1}) - f(x_{N-1})}{2\delta x} + O(\delta x^2)$$

where x_{N+1} is a ghost node. In this case, reference to these non-existent nodes (ghost nodes) will need to be eliminated by modifying the difference formulae. For example, the difference formula at the boundary node could be changed to invoke interior points only, i.e. become a one-sided formula, but this will have lower order accuracy. Alternatively, the non-existent nodes can be eliminated by another equation that also invokes the ghost nodes. For example, for Neumann boundary conditions the value of the derivative is specified at the boundary node, $\left.\frac{\partial f}{\partial x}\right|_N$, and this can be equated to a difference formula for the derivative at the boundary node that invokes the ghost node, e.g. a central difference formula.

For a Dirichilet condition, it is the value (not derivative) of the dependent variable that is specified at the boundary nodes, so the differential equation at the boundary node does not need to be solved, and so no ghost nodes are invoked.

In this work, Gauss's law has one Dirichilet and one Neumann boundary condition for the potential V. The continuity equations have Neumann boundary conditions for the carrier densities n and p.

5.3.2 Explicit and Implicit Methods for Open Boundary Problems

When finite differences are applied to ordinary or partial differential equations (ODEs and PDEs) with one open dimension (defined below), such as the time dimension in the continuity equation, there are two different approaches to solving the ODE/PDE along the open (time) dimension, called the explicit and implicit methods (alternatively named Forward Euler and Backward Euler methods).

For an ODE with an open boundary, the boundary condition is specified at one position and so its information propagates outward. This allows the algebraic equations at each node to be solved successively in order away from that point. If the derivative is approximated with a two node difference formula, the information at the initial time step (initial BC) is enough to find the value at the second time step (rearrange for this one unknown value).

For an ODE with a closed boundary, the boundary condition is specified at both ends of the domain, and it is not possible to solve at each position successively in order from one boundary to the other, as this does not account for the condition at the other boundary. The equations at each node can only be solved by solving the equations at all points simultaneously, i.e. a matrix problem. For N nodes there are N simultaneous equations. The 1D Gauss's law and the stationary (time independent) 1D continuity equation are ODEs with closed boundaries. The 2D Gauss's law is a PDE (two spatial dimensions) with closed boundaries.

The time dependent 1D continuity equation is a PDE (time and space dimensions) with an open boundary in the time dimension, but a closed boundary in the space dimension. An initial condition for the open dimension (time) is provided by specifying the 3 variables (n, p, V) over the entire spatial domain at the initial time. Then at each time step, spatial boundary conditions are provided.

In the case of a PDE with one open dimension (such as the continuity equation), there are different approaches to solving the PDE successively along the open (time) dimension. The finite difference formulae for the spatial derivatives will contain values at neighbouring spatial nodes, and these can be chosen to be either the values at the earlier time (k), which are known, or the later time ($k+1$), which are not known – this choice distinguishes explicit and implicit methods respectively. For example, for the continuity equations at the spatial node i, the explicit method is

$$\frac{n_i^{k+1} - n_i^k}{\delta t} = \frac{1}{q} \frac{J_n|_{i+\frac{1}{2}}^k - J_n|_{i-\frac{1}{2}}^k}{\delta x} \tag{5.1}$$

$$\frac{p_i^{k+1} - p_i^k}{\delta t} = -\frac{1}{q} \frac{J_p|_{i+\frac{1}{2}}^k - J_p|_{i-\frac{1}{2}}^k}{\delta x} \tag{5.2}$$

The superscript k indexes the time of the node, the subscript i indexes the spatial position of the node. The implicit method is

$$\frac{n_i^{k+1} - n_i^k}{\delta t} = \frac{1}{q} \frac{J_n|_{i+\frac{1}{2}}^{k+1} - J_n|_{i-\frac{1}{2}}^{k+1}}{\delta x} \tag{5.3}$$

$$\frac{p_i^{k+1} - p_i^k}{\delta t} = -\frac{1}{q} \frac{J_p|_{i+\frac{1}{2}}^{k+1} - J_p|_{i-\frac{1}{2}}^{k+1}}{\delta x} \tag{5.4}$$

In both cases, the values at time k are known but at time $k+1$ are not known. For the explicit method, there is only one unknown in each equation (which is the value for n or p at the spatial node of interest at time $k+1$), so the equation at each spatial node can be solved by itself. In contrast, in the implicit method there are multiple unknowns in the equation, and this equation cannot simply be rearranged. Therefore, the equation at each position can only be solved by solving it simultaneously with the equations at other spatial nodes, i.e. a matrix problem (N simultaneous equations for N spatial nodes). This is done for each time step.

For the semiconductor equations, an additional level of complexity is that there are 3 PDEs at each node, controlling the values of the 3 dependent variables (n, p, V), and these 3 equations are coupled (because more than one dependent variable appears in each equation). In order to solve one PDE for one variable, the values of the other variables must also be found. In the explicit method, the values at the earlier time step k are used, which are already known. In the implicit method, the values at the later time step $k+1$ are used, which are not known, so the equations can only be solved by solving all 3 equations simultaneously. This leads to a set of $3N$ simultaneous equations at each time step for the implicit method.

Clearly the two methods involve different solving processes. The explicit method is more intuitive, but is only stable for small time steps – the form of this stability condition depends on the differential equation, but for the continiuty equations, the time step must be in the order of the spatial step squared $O(\delta x^2)$ [254]. The diffusion equation has a stability condition of $\delta t < \delta x^2/2D$ [305] and was used as a rough guide in this work. The implicit method is stable for very large time steps, although time steps must be small enough for sufficient accuracy. The drawback is that large matrix problems must be solved at each time step. In summary, the implicit method requires fewer steps but each step is computationally expensive, whereas the explicit method requires many more steps, but each step is less computationally expensive. Both these methods use two point formulae for the time derivative and are first order accurate in time. There are methods that are second order accurate, such as Crank-Nicholson which uses a 3-point difference formula for the time dimension, but is difficult to implement for these equations [254].

In this work, an explicit method is used (Eq.5.1 and 5.2) since it is easier to implement and the cost of small time steps is acceptable for the situations under study. In the explicit method, the only set of simultaneous equations that must be solved is Gauss's law at each time step, once densities n and p at each spatial position have been calculated from the continuity equation. Using the natural variables n, p, V, Gauss's law is a linear equation with a tridiagonal matrix of coefficients which can be solved efficiently by the Thomas Algorithm (see section5.3.6). If quasi-Fermi level variables are used, Gauss's law is non-linear and an iterative method would be required to solve a set of simultaneous equations.

5.3.3 Scharfetter-Gummel Expression for Charge Current

After applying finite differences to the continuity equation, it is evident that values for the current at the midpoints, $J_n|_{i+\frac{1}{2}}$ and $J_n|_{i-\frac{1}{2}}$, are required to evaluate these expressions. The drift-diffusion expression for the electron charge current

$$J_n = q\mu nE + qD_e\frac{\partial n}{\partial x}$$

includes the mobility μ, the diffusion coefficient D_e, the electric field $E = -d\phi/dx$, the charge density n, and the gradient of the charge density $\frac{\partial n}{\partial x}$, which must all be evaluated at the midpoints. For example this could be done as follows:

$$J_n|_{i+\frac{1}{2}} = -q\mu n_{i+\frac{1}{2}}\frac{\phi_{i+1} - \phi_i}{\delta x} + qD_e\frac{n_{i+1} - n_i}{\delta x}$$

where

$$n_{i+\frac{1}{2}} = \frac{n_{i+1} + n_i}{2}$$

Here a central difference has been used for the derivatives and the midpoint has been estimated by linear interpolation. However this method can become unstable, which is because the drift term and diffusion term are not similar sizes [256]. A more stable scheme was put forward by Scharfetter and Gummel, which they interpreted as a finite difference method, but in multiple space dimensions it is more convenient to use a finite volume approach, which can aslo be called the box method [254]. When Boltzmann statistics is valid, the Scharfetter-Gummel (SG) method gives a thermodynamically consistent scheme for the system of semiconductor equations, which is convection (drift) dominated [256].

The Scharfetter-Gummel scheme is derived by treating the current as uniform between the two nodes. The particle current for species c is

$$\begin{aligned} j_c &= Zc\mu_c E - D_c\frac{\partial c}{\partial x} \\ &= v_c c - D_c\frac{dc}{dx} \end{aligned}$$

where $v_c = Z\mu_c E$, with $Z = 1$ for electrons and and $Z = -1$ for holes. If the terms $j_c(x)$, $E(x) \equiv -\frac{d\phi(x)}{dx}$ and μ_c are approximated as constant between x_i and x_{i+1}, then this is a first-order differential equation for $c(x)$, where the boundary conditions are $c(x_i)$ and $c(x_{i+1})$, shortened to c_i and c_{i+1}.

$$\frac{dc(x)}{dx} - \frac{v_c}{D_c}c(x) = -\frac{j_c}{D_c}$$

This can be solved for $c(x)$ between x_i and x_{i+1}.

$$c(x) = c_i e^{\frac{v_c(x-x_i)}{D_c}} + \frac{j_c}{v_c}\left[1 - e^{\frac{v_c(x-x_i)}{D_c}}\right]$$

Evaluating at the x_{i+1} boundary

$$c_{i+1} = c_i e^{\frac{v_c\delta}{D_c}} + \frac{j_c}{v_c}\left[1 - e^{\frac{v_c\delta}{D_c}}\right]$$

where $\delta = x_{i+1} - x_i$. Then rearranging for j_c (uniform between x_i and x_{i+1})

$$j_c = \frac{D_c}{\delta}\frac{v_c\delta}{D_c}\left(\frac{c_{i+1}}{1-e^{\frac{v_c\delta}{D_c}}} + \frac{c_i}{1-e^{\frac{-v_c\delta}{D_c}}}\right)$$

$$j_c = \frac{D_c}{\delta}\left[c_{i+1}(-)B\left(\frac{v_c\delta}{D_c}\right) + c_i B\left(\frac{-v_c\delta}{D_c}\right)\right]$$

where $B(x) = \frac{x}{e^x-1}$ is the Bernoulli function. The evaluation of the Bernoulli function by a computer will break down near $x = 0$, so is approximated with $B(x) = 1 - \frac{x}{2}$.

For electrons $\frac{v\delta}{D} = \frac{\phi_{i+1}-\phi_i}{\phi_T}$ and for holes $\frac{v\delta}{D} = \frac{\phi_i-\phi_{i+1}}{\phi_T}$, where $\phi_T = k_BT/q$ is the thermal voltage. Remembering $J_n = -qj_n$, $J_p = qj_p$, the expressions for the electron and hole charge currents densities at $x_{i+\frac{1}{2}}$ are

$$J_n|_{i+\frac{1}{2}} = q\frac{D_e}{\delta}\left[n_{i+1}B\left(\frac{\phi_{i+1}-\phi_i}{\phi_T}\right) - n_i B\left(\frac{\phi_i-\phi_{i+1}}{\phi_T}\right)\right]$$

$$J_p|_{i+\frac{1}{2}} = -q\frac{D_h}{\delta}\left[p_{i+1}B\left(\frac{\phi_i-\phi_{i+1}}{\phi_T}\right) - p_i B\left(\frac{\phi_{i+1}-\phi_i}{\phi_T}\right)\right]$$

Similarly at $x_{i-\frac{1}{2}}$

$$J_n|_{i-\frac{1}{2}} = q\frac{D_e}{\delta}\left[n_i B\left(\frac{\phi_i-\phi_{i-1}}{\phi_T}\right) - n_{i-1}B\left(\frac{\phi_{i-1}-\phi_i}{\phi_T}\right)\right]$$

$$J_p|_{i-\frac{1}{2}} = -q\frac{D_h}{\delta}\left[p_i B\left(\frac{\phi_{i-1}-\phi_i}{\phi_T}\right) - p_{i-1}B\left(\frac{\phi_i-\phi_{i-1}}{\phi_T}\right)\right]$$

5.3.4 Finite Differences Discretisation of Gauss's Law

For the perovskite-CTL bilayers, the photoexcited charge densities have much greater extent in the in-plane dimensions y and z, than in the depth dimension x, and the density is assumed to vary slowly with respect to the in-plane y and z dimensions, so is treated as uniform over a certain in-plane area. This means for distances away from the layer that are much smaller than width of this uniform area, the electric potential is modelled as that due to an infinite sheet of uniform charge density, i.e. Gauss's law is considered in

1D only.

$$\frac{d}{dx}\left(\epsilon_r(x)\frac{dV(x)}{dx}\right) = -\frac{\rho(x)}{\epsilon_0}$$

This means that the electric potential due to a sheet of charge (uniform in the in-plane dimension) varies linearly with respect to out-of-plane distance x, for distances from the sheet that are much less than the in-plane extent of the sheet. This also means that the electric field from a sheet of charge is constant with respect to x for distances from the sheet that are much less than the in-plane extent of the sheet. Therefore for a point outside the sheet of charge, the electric field only depends on the net sheet charge density (integral over the x dimension), not on the distribution of charge density with respect to x. In other words, the charge densities at each x position contribute with equal weight to the field at a particular point, because the field is not a function of distance. For example, outside a sample that is net neutral, the electric field is zero, regardless of the distribution of the charges with respect to x (the out-of-plane dimension).

Gauss's law includes the relative permittivity of the material as a parameter, which in general may be a function of position $\epsilon_r(x)$. When $\epsilon_r(x)$ is spatially varying (for example, in this work the ϵ_r in the CTL is different to the perovskite), the finite volume method is more suitable. The electric field in the perovskite due to the net charge in the CTL is not affected by the ϵ_r in the CTL, only the ϵ_r in the perovskite affects the electric field in the perovskite (i.e. the ϵ_r only modifies the electric field locally). The only effect that the ϵ_r in the CTL has on the perovskite, is that it influences the carrier distribution in the CTL and thus may affect cross-interface recombination, which is proportional to the carrier density next to the interface. However, in this work, since the mobility in the CTL is much lower than in the perovskite, it can be assumed that any carriers extracted into the CTL from the perovskite will remain close to the interface within the 3ns time window of the measurement, so can all contribute to cross-interface recombination. Therefore, the spatial distribution of carriers in the CTL can be neglected, and for calculating the rate of cross-interface recombination, the total number of carriers in the CTL can be used. Consequently, the 3 PDEs only need to be solved in the perovskite layer, and the permittivity ϵ_r is uniform over this domain.

When the permittivity ϵ_r is uniform, Gauss's law takes the form of the Poisson equation, and the finite difference formula for the Poisson equation in 1D is

$$\frac{\phi_{i+1} - 2\phi_i + \phi_{i-1}}{(\delta x)^2} = -\frac{\rho_i}{\epsilon_0 \epsilon_r}$$

The finite difference equations for each node are a set of simultaneous equations that can be written as a matrix equation $\mathbf{A}\ \mathbf{V} = \mathbf{d}$. The 1D spatial domain is divided into $N+1$ nodes indexed from 0 to N.

$$\begin{pmatrix} b_0 & c_0 & 0 & ... & & & \\ a_1 & b_1 & c_1 & ... & & & \\ ... & ... & ... & ... & ... & ... & ... \\ & & & ... & a_{N-1} & b_{N-1} & c_{N-1} \\ & & & ... & 0 & a_N & b_N \end{pmatrix} \begin{pmatrix} \phi_0 \\ \phi_1 \\ ... \\ \phi_{N-1} \\ \phi_N \end{pmatrix} = \begin{pmatrix} d_0 \\ d_1 \\ ... \\ d_{N-1} \\ d_N \end{pmatrix}$$

The matrix is tridiagonal, with the elements along the diagonal represented by a vector **b** of length $N + 1$, and the elements along the lower and upper diagonals represented by the vectors **a** and **c** respectively, both with length N. In the algorithm used to solve this matrix problem, the vectors are all given length $N+1$, so the elements a_0 and c_N are zero. For $1 \leq i \leq N - 1$,

$$a_i = 1 \tag{5.5}$$

$$b_i = -2 \tag{5.6}$$

$$c_i = 1 \tag{5.7}$$

$$d_i = \frac{-\rho_i \delta x^2}{\epsilon_0 \epsilon_r} \tag{5.8}$$

$$= \rho_i' \tag{5.9}$$

5.3.5 Boundary Conditions for Gauss's Law

Dirichilet boundary conditions specify the value of the dependent variable at the boundary node and are the easiest to implement. For example, using the notation $\phi_0 = \alpha$ or $\phi_N = \beta$ for Dirichilet BCs on the left and right boundaries respectively gives

$$\begin{pmatrix} 1 & 0 & 0 & ... & & & \\ 1 & -2 & 1 & ... & & & \\ ... & ... & ... & ... & ... & ... & ... \\ & & & ... & 1 & -2 & 1 \\ & & & ... & 0 & 0 & 1 \end{pmatrix} \begin{pmatrix} \phi_0 \\ \phi_1 \\ ... \\ \phi_{N-1} \\ \phi_N \end{pmatrix} = \begin{pmatrix} \alpha \\ \rho_1' \\ ... \\ \rho_{N-1}' \\ \beta \end{pmatrix}$$

A Neumann boundary condition specifies the derivative of ϕ at the boundary node normal to the boundary, $\frac{d\phi}{dx} = \gamma$. Gauss's law at the boundary node invokes a point outside the domain boundary, i.e. a ghost node, and the boundary condition can be written as a central difference derivative at the boundary node, and thus also invokes the ghost node. This boundary condition can be substituted into Gauss's law at the boundary node to eliminate the ghost node. For example for the left boundary node (so 0th equation), Gauss's law is:

$$\frac{\phi_1 - \phi_{-1}}{2\delta x} = \gamma_L$$

and the Neumann boundary condition is

$$\frac{\phi_1 - 2\phi_0 + \phi_{-1}}{\delta x^2} = \rho_0'$$

so

$$\phi_1 - \phi_0 = \frac{\rho_0'}{2} + \gamma_L \delta x$$

At the right boundary node (so Nth equation):

$$\frac{\phi_{N+1} - \phi_{N-1}}{2\delta x} = \gamma_R$$

and

$$\frac{\phi_{N+1} - 2\phi_N + \phi_{N-1}}{\delta x^2} = \rho_N'$$

so

$$\phi_{N-1} - \phi_N = \frac{\rho'_N}{2} - \gamma_R \delta x$$

Neumann boundary conditions on both sides would give the matrix equation:

$$\begin{pmatrix} -1 & 1 & 0 & ... & & & \\ 1 & -2 & 1 & ... & & & \\ ... & ... & ... & ... & ... & ... & ... \\ & & & ... & 1 & -2 & 1 \\ & & & ... & 0 & 1 & -1 \end{pmatrix} \begin{pmatrix} \phi_0 \\ \phi_1 \\ ... \\ \phi_{N-1} \\ \phi_N \end{pmatrix} = \begin{pmatrix} \frac{\rho'_0}{2} + \gamma_L \delta x \\ \rho'_1 \\ ... \\ \rho'_{N-1} \\ \frac{\rho'_N}{2} - \gamma_R \delta x \end{pmatrix}$$

The value of the derivative of the potential at the boundaries, $\gamma = \frac{d\phi}{dx}$, is now considered. The electric field due to a sheet of charge σ, where σ is signed, on the right side of the sheet is given by

$$\mathbf{E}_R = \frac{\sigma}{2\epsilon_0\epsilon_r}\hat{x}$$

and on the left side of the sheet is given by

$$\mathbf{E}_L = -\frac{\sigma}{2\epsilon_0\epsilon_r}\hat{x}$$

The field at any position x is a sum of the fields due to the sheets of charge on either side, so the fields at the boundaries are due to the total charge sheet density in the domain.

Since

$$\mathbf{E} = -\frac{d\phi(x)}{dx}\hat{x} = -\gamma\hat{x}$$

then γ on the right boundary is

$$\gamma_R = -\frac{\sigma}{2\epsilon_0\epsilon_r}$$

and γ on the left boundary is

$$\gamma_L = \frac{\sigma}{2\epsilon_0\epsilon_r}$$

In this work, the CTL is always considered to be on the left of the perovskite layer. Therefore, at the right boundary of the perovskite, the field should be zero as the total sheet charge density of the perovskite-CTL bilayer is zero.

$$\mathbf{E}_R = -\gamma_R\hat{x} = 0$$

On the left boundary of the perovksite layer (i.e. at the interface with the CTL), the electric field is the sum of the electric fields due to the sheet charge density in the perovskite and in the CTL outside the left boundary.

$$\mathbf{E}_L = -\frac{\sigma_{per}}{2\epsilon_0\epsilon_r}\hat{x} + \frac{\sigma_{CTL}}{2\epsilon_0\epsilon_r}\hat{x} \tag{5.10}$$

The sheet charge density in the CTL is equal in magnitude but opposite in sign to the sheet charge density in the perovskite, giving an electric field at the boundary that points in the same direction.

$$\sigma_{CTL} = -\sigma_{per}$$

so

$$\mathbf{E}_L = -\gamma_L \hat{x} = -\frac{\sigma_{per}}{\epsilon_0 \epsilon_r}\hat{x} = \frac{\sigma_{CTL}}{\epsilon_0 \epsilon_r}\hat{x}$$

The net sheet charge density in the perovskite, σ_{per} is an integral of the charge density over the thickness of the layer, which can be estimated by summing up the density at each node along the depth dimension and multiplying by the step size. More accurate numerical integration (such as Simpson's method) will increase computational expense and slow down the evaluation. Since it is the electric field outside the right surface that is zero for a net neutral sample, the boundary condition is implemented by introducing a node just outside the sample, referred to as a vacuum node, and expressing the electric field at this node with a central difference formula, and setting it to zero. This node will always have zero charge.

5.3.6 Thomas Algorithm for Tridiagonal Matrices

The finite differences discretisation of Gauss's law results in a tridiagonal matrix problem which can be solved efficiently by a tridiagonal matrix algorithm (TDMA). One method for solving such a matrix problem is to convert the matrix to Row Echelon form by Gaussian elimination, which can then be solved by back substitution. The pivot is the first non-zero element in every row when reading from left to right, and in row echelon form the pivot in each row is to the right of the pivot in the row above (the elements in the upper triangle can take any value). It can be chosen to perform operations such that the pivots are equal to 1

$$\begin{pmatrix} 1 & ... & ... & ... & ... \\ 0 & 1 & ... & ... & ... \\ 0 & 0 & 1 & ... & ... \\ 0 & 0 & 0 & 1 & ... \\ 0 & 0 & 0 & 0 & 1 \end{pmatrix} \begin{pmatrix} ... \\ ... \\ ... \\ ... \\ ... \end{pmatrix} = \begin{pmatrix} ... \\ ... \\ ... \\ ... \\ ... \end{pmatrix}$$

The row echelon form means that by starting with the N^{th} equation in the bottom row (which simply states the value of the N^{th} unknown) and working up the rows, the i^{th} equation can be solved for the i^{th} unknown, as all the other unknowns in the i^{th} equation have been found by solving the equations in lower rows.

A tri-diagonal matrix has non-zero elements on the main diagonal and the diagonal either side. It can be made into Row Echelon form with fewer steps then the general algorithm for Gaussian elimination, due to it being sparse and only one diagonal of elements needs to be reduced to zeros (i.e. the a coefficients). In the forward sweep of Gaussian elimination steps, we can choose to make the pivots, i.e. the b coefficients, =1. In the following derivation, coefficients converted to final form are denoted with $'$, coefficients in intermediate form are denoted $*$. The i^{th} row is denoted by R_i.

First, convert the 0^{th} row, R_0, to $b = 1$ form, by dividing R_0 by b_0 to give $b'_0 = 1$, $c'_0 = c_0/b_0$ and $d'_0 = d_0/b_0$.

$$\begin{pmatrix} 1 & c'_0 & 0 & ... & & & \\ a_1 & b_1 & c_1 & ... & & & \\ ... & ... & ... & ... & ... & ... & ... \\ & & & ... & a_{N-1} & b_{N-1} & c_{N-1} \\ & & & ... & 0 & a_N & b_N \end{pmatrix} \begin{pmatrix} \phi_0 \\ \phi_1 \\ ... \\ \phi_{N-1} \\ \phi_N \end{pmatrix} = \begin{pmatrix} d'_0 \\ d_1 \\ ... \\ d_{N-1} \\ d_N \end{pmatrix}$$

For the next row, R_1, convert the a_1 coefficient to 0, knowing that the b'_0 coefficient directly above it is now = 1:

$$R_1^* = R_1 - a_1 R'_0$$

and then convert the b_1 coefficient to 1 by dividing the row by the intermediate b_1^* coefficient:

$$R'_1 = \frac{R_1^*}{b_1^*} = \frac{R_1^*}{b_1 - a_1 c'_0}$$

So overall,

$$R'_1 = \frac{R_1 - a_1 R'_0}{b_1 - a_1 c'_0}$$

$$\begin{aligned} a'_1 &= 0 \\ b'_1 &= 1 \\ c'_1 &= \frac{c_1}{b_1 - a_1 c'_0} \\ d'_1 &= \frac{d_1 - a_1 d'_0}{b_1 - a_1 c'_0} \end{aligned}$$

Giving the matrix equation:

$$\begin{pmatrix} 1 & c'_0 & 0 & ... & & & \\ 0 & 1 & c'_1 & ... & & & \\ ... & ... & ... & ... & ... & ... & ... \\ & & & ... & a_{N-1} & b_{N-1} & c_{N-1} \\ & & & ... & 0 & a_N & b_N \end{pmatrix} \begin{pmatrix} \phi_0 \\ \phi_1 \\ ... \\ \phi_{N-1} \\ \phi_N \end{pmatrix} = \begin{pmatrix} d'_0 \\ d'_1 \\ ... \\ d_{N-1} \\ d_N \end{pmatrix}$$

This is repeated for each row, giving a recursive relation

$$R'_i = \frac{R_i - a_i R'_{i-1}}{b_i - a_i c'_{i-1}}$$

$$\begin{aligned} a'_i &= 0 \\ b'_i &= 1 \\ c'_i &= \frac{c_i}{b_i - a_i c'_{i-1}} \\ d'_i &= \frac{d_i - a_i d'_{i-1}}{b_i - a_i c'_{i-1}} \end{aligned}$$

Overall this yields the Row Echelon form

$$\begin{pmatrix} 1 & c'_0 & 0 & ... & & & \\ 0 & 1 & c'_1 & ... & & & \\ ... & ... & ... & ... & ... & ... & ... \\ & & & ... & 0 & 1 & c'_{N-1} \\ & & & ... & 0 & 0 & 1 \end{pmatrix} \begin{pmatrix} \phi_0 \\ \phi_1 \\ ... \\ \phi_{N-1} \\ \phi_N \end{pmatrix} = \begin{pmatrix} d'_0 \\ d'_1 \\ ... \\ d'_{N-1} \\ d'_N \end{pmatrix}$$

Having performed the forward sweep to give the Row Echelon form, the back substitution sweep is performed, starting from the bottom row and working upwards:

$$\phi_N = d'_N$$

then

$$\phi_{N-1} + c'_{N-1}\phi_N = d'_{N-1}$$

so

$$\phi_{N-1} = d'_{N-1} - c'_{N-1}\phi_N$$

This is repeated for each row giving a recursive relation:

$$\phi_{i-1} = d'_{i-1} - c'_{i-1}\phi_i$$

5.4 Modelling Results

The ultimate aim of measuring the carrier dynamics in perovskite-CTL bilayers is to understand the different processes such as transport, extraction and recombination, so that performance bottlenecks can be identified and improved. The suitability of the model can be assessed by comparing the measured dynamics to simulated dynamics. With a suitable model, the magnitudes of the different possible processes can be quantified by this comparison. For the perovskite-CTL bilayer samples, any selective extraction at the interface will result in charge separation and the resulting electric fields may have a large impact on carrier dynamics. This effect has mostly been neglected in previously reported studies of perovskite-CTL bilayers, but is modelled in this work to determine its significance.

In the first part of this section, a mathematical model for the spatially and temporally dependent carrier densities that includes Coulombic forces is employed. It is not possible to solve this analytically, so a numerical method is used. The numerical method will be introduced, the choice of method will be justified, and the accuracy of the method will be explained. The results of numerical solutions to the model are compared to the experimental data and the impact of charge separation is assessed. Following this, analytical solutions of a simplified model that is valid in the absence of charge separation, is used to fit the experimental OPTP data and estimate the interface recombination rate constant and the diffusion coefficient. The two models will be referred to as the drift-diffusion/numerical model and the ambipolar/analytical model respectively. In all cases, recombination within the perovskite bulk is ignored, as there was negligible decay of the carrier population in the bare perovskite sample over the 3ns window of OPTP or TA.

The numerical model allows one type of carrier to be extracted from the interface node at x_0 with a rate that is proportional to the density of the carrier at this node. For example, for an ETL bilayer

$$R_{extract} = k_{extract} n(x_0)$$

Extraction can also be allowed to occur from nodes deeper into the perovskite, which is referred to as smearing the interface. The numerical model also allows for the extracted charge carrier to recombine with the opposite polarity carrier that remains in the perovskite. This rate is proportional to the remaining carrier's density at the interface node, and the extracted carrier's density in the CTL, which is assumed to be concentrated next to the interface. This process is referred to as cross-interface or back recombination. For example, for an ETL bilayer

$$R_{inter} = k_{inter} n_{CTL} p(x_0)$$

Prior to comparing the experimental data and mathematical simulations, the accuracy of the numerical modelling was assessed by considering scenarios for which analytical solutions can be found.

5.4.1 Assessing the Accuracy of the Numerical Solution

For the drift-diffusion equations formed by the system of 3 coupled PDEs, there is no analytical solution that can be used to check the numerical solution, unless the neutrality approximation is made and recombination processes are assumed to be monomolecular only. The neutrality approximation is that the photoexcited electron and hole densities are assumed to be equal at all positions $n_e(x) = p_e(x)$, meaning that the carrier distribution can be described with a continuity equation for just a single species, either $n_e(x,t)$ or $p_e(x,t)$, called the ambipolar continuity equation. The electrons and holes diffuse together with a common ambipolar diffusion coefficient. In the absence of an externally applied field, the ambipolar continuity equation is equivalent to the diffusion equation with an additional term for monomolecular recombination. The analytical solution of this ambipolar continuity equation with monomolecular bulk or surface recombination is discussed in sections 3.6.4 and 3.6.5.

The code used to numerically solve the drift-diffusion equations can be used to numerically solve the ambipolar continuity equation. For the case that there is no carrier extraction or surface recombination ($S = 0$), this is done by simply setting the electron and hole mobilities to be equal. The case where $S > 0$ will be discussed further below. For the numerical solution, positions at which the carrier density varies steeply with respect to position will introduce the greatest errors. Therefore, since the initial photogenerated density decays exponentially through the thickness of the sample, the greatest errors will be near the illuminated surface. The rate of surface recombination is proportional to this density so will be impacted by these errors.

A comparison of numerical and analytical solutions for $S = 0$ is shown in Fig.5.2, and for $S > 0$ is shown in Figs.5.3 and 5.4. The perovskite layer thickness is $L_z = 600$nm, and to simplify the derivation of the analytical solution, photogeneration is assumed to be instantaneous rather than using the actual pump pulse duration of ~50fs (which could

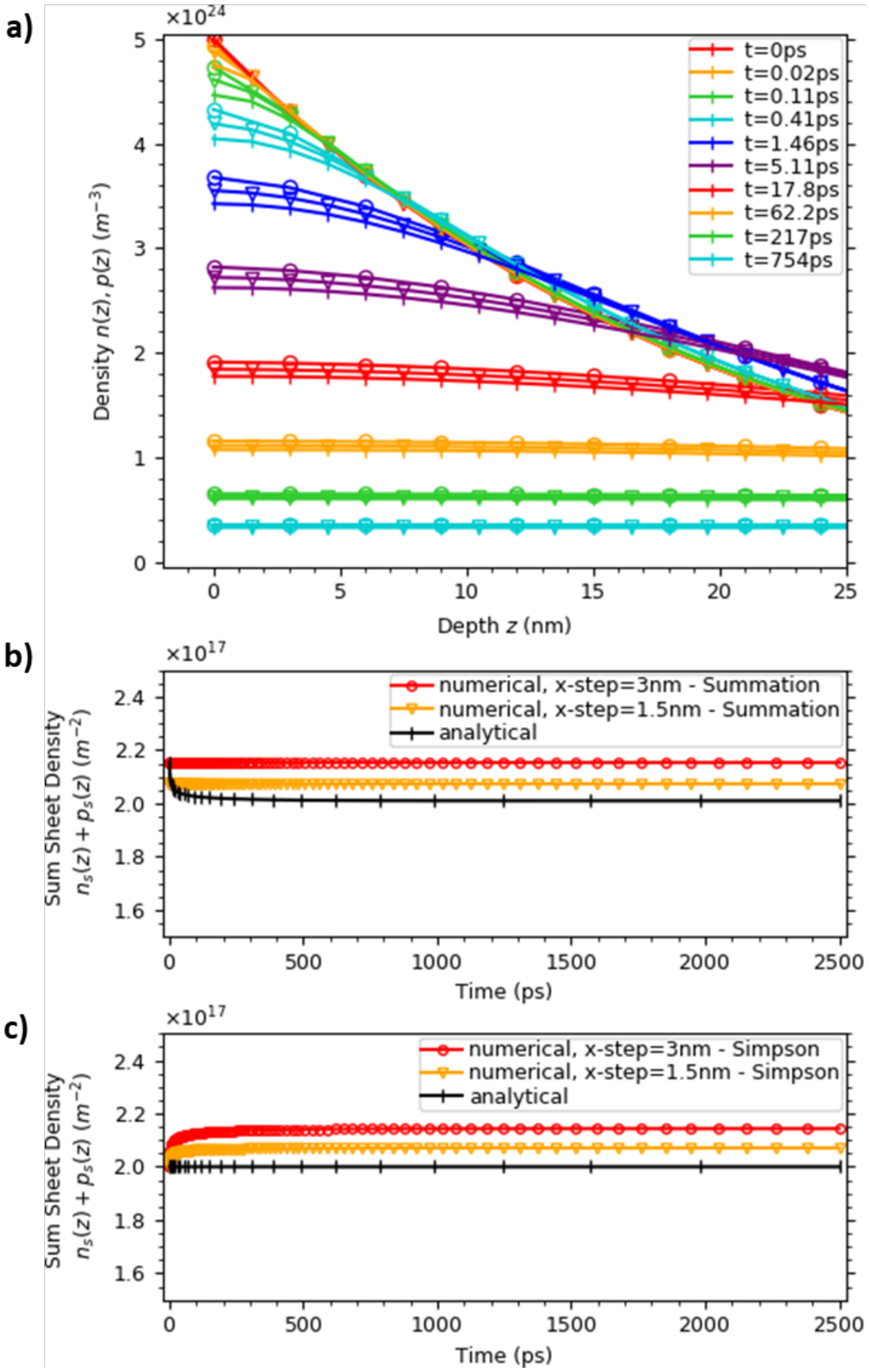

Figure 5.2: A comparison of the numerical solution (circles and triangles) and the analytical solution of the ambipolar continuity equation with surface recombination velocity $S = 0$. Two different spatial step sizes for the numerical solution are shown. a) Carrier density ($n(z) = p(z)$) as a function of depth for different pump-probe delay times. The positions of the nodes used in the numerical solutions are indicated by the markers, and the analytical solution is evaluated at the marker positions. b), c) Sheet density of electrons plus holes as a function of pump-probe delay, calculated by simple summation of nodal densities b), or by Simpson integration c).

easily be implemented in the numerical solution). Population decay within the ∼50fs pump pulse duration would reduce the initial amplitude of the signal so would need to be accounted for, but the measured photoconductance decays suggest that there is negligible decay within the ∼50fs pump pulse. Similarly, the simulations show there is negligible diffusion within this time, so overall an instantaneous photogeneration will accurately replicate the dynamics. Also the decay is much slower than the 1ps IRF of the THz probe, so convolution of the simulated decay with the IRF will have no effect on the decay curve, so is not necessary. The spatial distribution of the simulated charge density is shown as a function of position for a selection of pump-probe delay times. It can be seen that for $S = 0$, the numerical solution underestimates diffusion away from the interface compared to the analytical solution, and a smaller step size for the numerical solution reduces this error. This dependence on step size is expected since the truncation error for the finite difference approximations of the analytical derivatives has been been shown in section 5.3.1 to be $O(\delta x)$ and therefore increases proportionally to the step size. However, reducing the step size increases the computational expense - halving the spatial step size means the time step size must be reduced by a factor of 4 to maintain stability, so the total number of nodes increases by a factor of 8 - so the largest step size that achieves the required accuracy should be used. It can be seen that the truncation error is mostly introduced at the earliest times when the density profile is very steep.

The OPTP signal, $\Delta T/T$, is proportional to the sum of the electron and hole sheet densities (integral of density over thickness) so this is plotted as a function of time in Figs.5.2-5.4. The OPTP signal is actually proportional to the sum of the sheet densities weighted by their mobilities at THz frequencies. However, the individual electron and hole mobilities at THz frequencies cannot be determined from these measurements alone and there is no consensus on their ratio in the literature. Here it is assumed they are equal, but if they were unequal then extraction of the carrier with higher THz mobility would cause the photoconductivity signal to decay further, and vice versa.

The analytical solution for the density can be integrated over thickness to give an analytical expression for the sheet density, but the numerical solution for the density can only be integrated numerically. For the comparisons in Figs.5.2-5.4, a numerical integration is performed for both the analytical and numerical solutions. The simplest integration is a sum of the densities at each node, multiplied by the spatial step size. With this simple method, the sheet density for the numerical solution with $S = 0$ is found to be constant (since the finite difference/finite volume method should conserve the nodal values/cell average values), but the sheet density for the analytical solution for $S = 0$ drops over the first 10s of picoseconds because the simple integration overestimates the integral at the early times. Alternatively the integration can be performed using Simpson's rule, which yields a constant sheet density for the analytical solution, but for the numerical solution the sheet density rises over the first tens of picoseconds. This emphasises that there are numerical errors introduced when simulating the photoconductivity, but they are relatively small and should not change any conclusions.

To numerically simulate the ambipolar continuity equation with $S > 0$, the numerical simulation includes electron extraction across the interface (with a rate that is proportional to electron density at the interface), plus an interface recombination constant that is extremely large so that the extracted electrons instantaneously recombine with perovskite holes across the interface. When this back recombination constant is very high, no charge accumulates in the CTL so it does not matter whether the Coulomb force

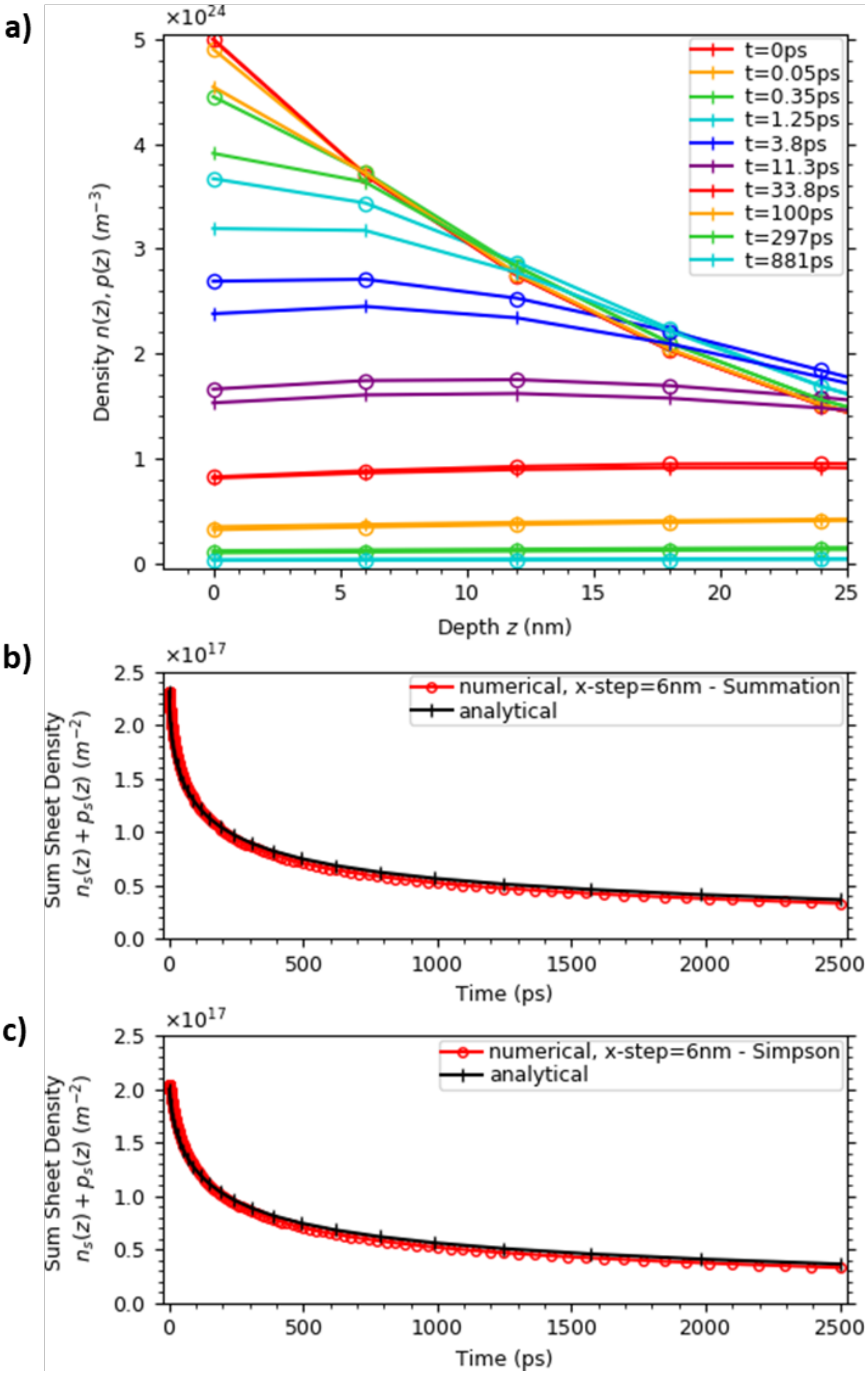

Figure 5.3: A comparison of the numerical solution (circles) and the analytical solution of the ambipolar continuity equation with a large surface recombination velocity $S > 0$. a) Carrier density ($n(z) = p(z)$) as a function of depth for different pump-probe delay times. The positions of the nodes used in the numerical solution are indicated by the markers, and the analytical solution is evaluated at the marker positions. b), c) Sheet density of electrons plus holes as a function of pump-probe delay, calculated by simple summation of nodal densities b), or by Simpson integration c).

is included or not (the Coulomb force can be turned off by fixing the potential as uniform instead of solving Gauss's law at each time step). The recombination rate for this two step process is limited by the first step (extraction), so is proportional to the electron density and is thus monomolecular, as is required for comparison to the analytical solution with

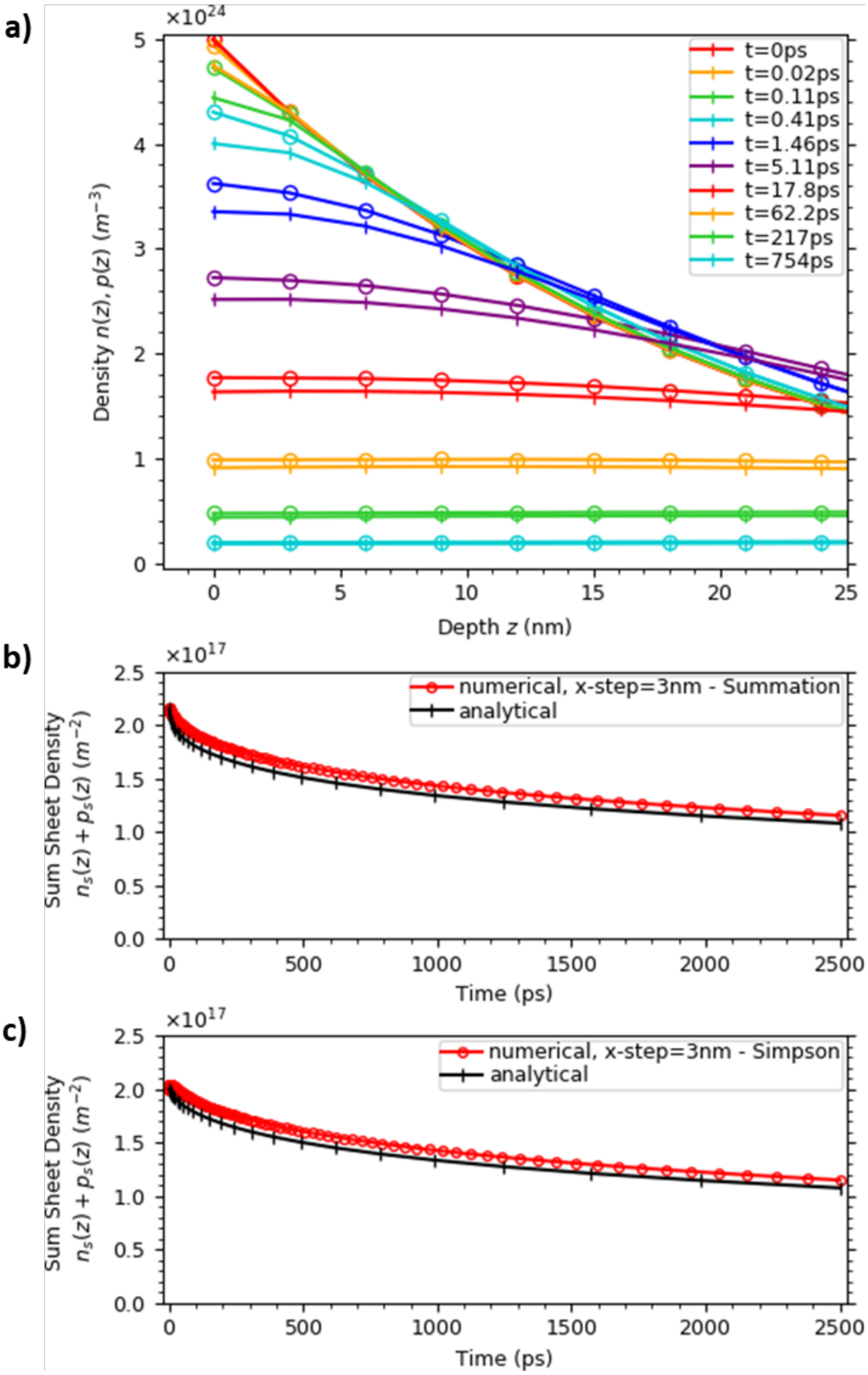

Figure 5.4: A comparison of the numerical solution (circles) and the analytical solution of the ambipolar continuity equation with a small surface recombination velocity $S > 0$. a) Carrier density ($n(z) = p(z)$) as a function of depth for different pump-probe delay times. The positions of the nodes used in the numerical solution are indicated by the markers, and the analytical solution is evaluated at the marker positions. b), c) Sheet density of electrons plus holes as a function of pump-probe delay, calculated by simple summation of nodal densities b), or by Simpson integration c).

monomolecular surface recombination. Alternatively monomolecular surface recombination can be replicated by additionally extracting holes with a rate that is proportional to the hole density. To make a comparison to the analytical solution for $S > 0$, a value for the extraction rate constant in the numerical solution is chosen which results in a decay curve that is similar to the analytical solution.

The comparison of the analytical and numerical solutions for $S > 0$ (Figs.5.3 and 5.4), shows that the density near the interface appears to be slightly different (most noticeably at early times). This difference is similar to the difference observed for $S = 0$, suggesting it is mostly due to errors in estimating the diffusion. Despite this, the photoconductance decay for the numerical and analytical solutions match quite closely, even for a large S and a large step size of 6nm.

Although the surface recombination process is monomolecular the photoconductance decay is not monoexponential. An instantaneous monoexponential/monomolecular lifetime, $\tau(t)$, can be defined for each time t in a decay even if the decay is not monoexponential

$$\frac{dn(t)}{dt} = \frac{-n(t)}{\tau(t)}$$

This is equivalent to the gradient of the logarithm of the signal versus time

$$\frac{d\ln(n(t))}{dt} = \frac{-1}{\tau(t)}$$

The photoconductance decay will only be monoexponential over time ranges for which the carrier density at the interface decays monoexponentially, which is not the case when carriers are diffusing away from the surface, as well as recombining. The monoexponential lifetime increases at later times because carriers have diffused away from the interface, which reduces the recombination rate at the interface below what it would have been without this diffusion. At late times when the diffusion current away from the surface has diminished, then the decay may become monoexponential. These considerations highlight that the ratio of the absorption depth and sample thickness can effect the decay shape, and so can the mobility. It should be noted that slow diffusion of carriers towards the surface where the population is being depleted, can reduce the decay lifetime below what would be observed when diffusion is extremely fast. With fast diffusion, the decay is recombination limited, and with slow diffusion it is transport limited, and the decay rate is a function of the diffusion coefficient.

5.4.2 Impact of the Coulomb Force

Having established the accuracy of the numerical solution with Coulomb forces excluded, Coulomb forces are now introduced. The numerical simulations consider electron extraction, but the results are equivalent for hole extraction instead. A finite duration of the photogeneration is included in the numerical solution, although it is much faster than the timescales for density decay so should not impact the simulated dynamics.

Figure 5.5 shows the carrier dynamics with Coulomb forces included, but without any back-recombination. Two different extraction rate constants are considered, and the grey lines show the carrier distribution when there is no extraction. With the Coulomb force included, the extracted electrons accumulate in the ETL and repel the electrons remaining in the perovskite, whilst attracting the holes in the perovskite. This forms a charge distribution akin to an electrical double layer. This reduces the density of perovskite electrons near the interface and thus slows down the extraction rate, so the transient decay curve plateaus. The level of this plateau is found to depend on the strength of the extraction rate constant, as shown in Fig. 5.5. Simulations with smaller step sizes confirm that this double layer is not an artefact of large step sizes. This extraction bottleneck

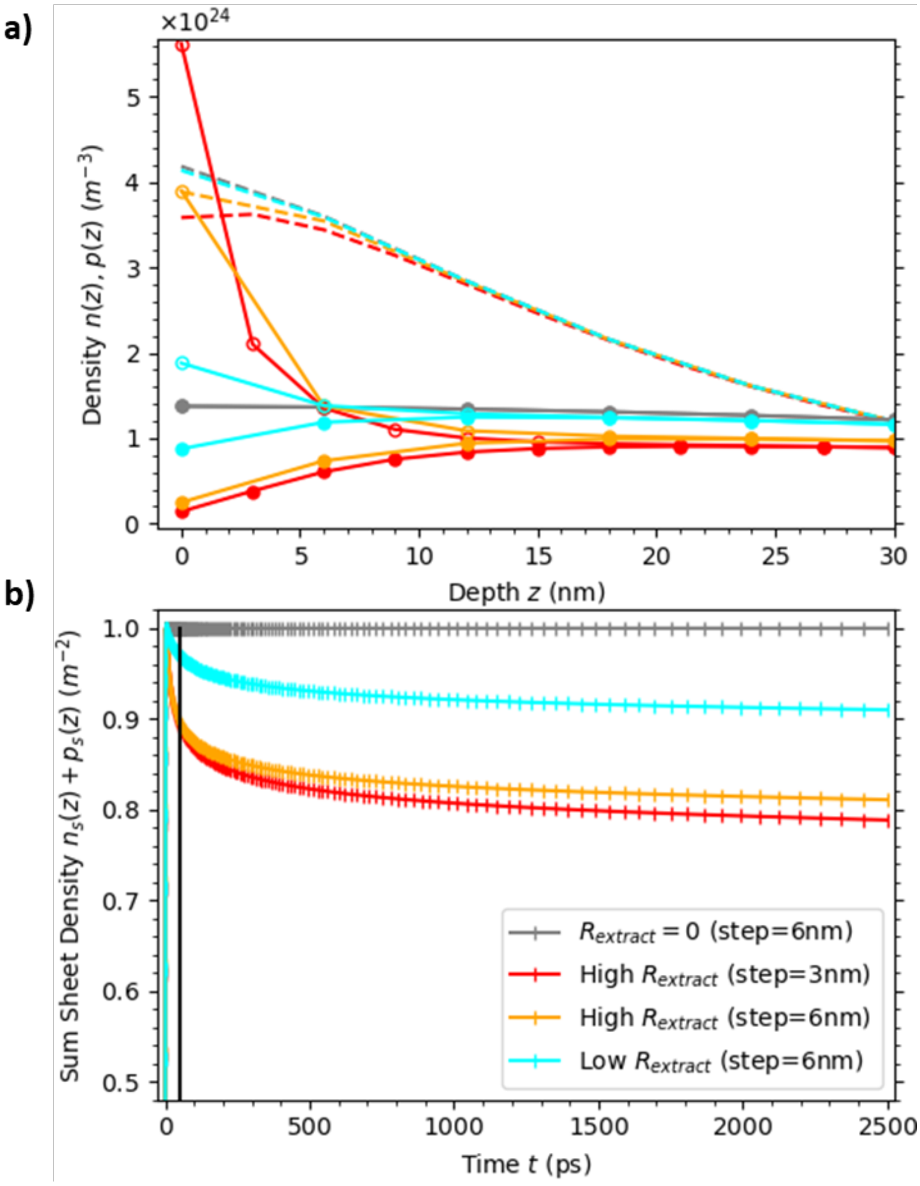

Figure 5.5: Numerical simulations of the drift-diffusion equations including the Coulombic force, but without any back-recombination, for an ETL-perovskite bilayer. The simulation is for 410nm excitation on the ETL side of a 600nm thick perovskite layer. a) The carrier distribution at t=50ps. The empty circles indicate the hole distribution and the filled circles indicate the electron distribution. The dashed lines indicate the distributions at the time of maximum sheet density. b) The sum of the electron and hole sheet densities, where the integral over depth is calculated by a simple summation of the nodal densities.

can be modified by allowing electrons to be extracted from deeper into the perovskite layer (here referred to as smearing the interface), or by increasing the permittivity to reduce the electric fields. If electrons can be extracted from deeper into the perovskite, where the electron density is not as greatly reduced as at the interface, then the extraction rate will not be so greatly diminished by the double layer formation, and the plateau in the photoconductivity decay will be less severe. Increasing the permittivity will reduce the depletion of the electron population at the interface (although the double layer will be wider), and so the extraction rate at late times will not be reduced as much, i.e. the plateau in the photoconductivity decay will be less severe. However, even extreme smearing of the interface or extreme permittivity values are not sufficient to reduce the plateau to the extent observed in the experimental data in sections 4.3.6.2 and 4.3.6.3.

The difference between the simulated decay curves and the experimental decay curves implies that the formation of such a double layer at the interface must be inhibited by processes that reverse charge separation, either returning electrons to the perovskite or extracting holes into the ETL. The possible processes are illustrated in Fig.5.6, which shows photoexcitation followed by the formation of the double layer as electrons are extracted into the ETL. One possible processes is that electrons extracted into the LUMO of the ETL can recombine with a hole in the VB of the perovskite, possibly via an interface state (process (a)). Alternatively, a hole may be extracted from the perovskite VB into

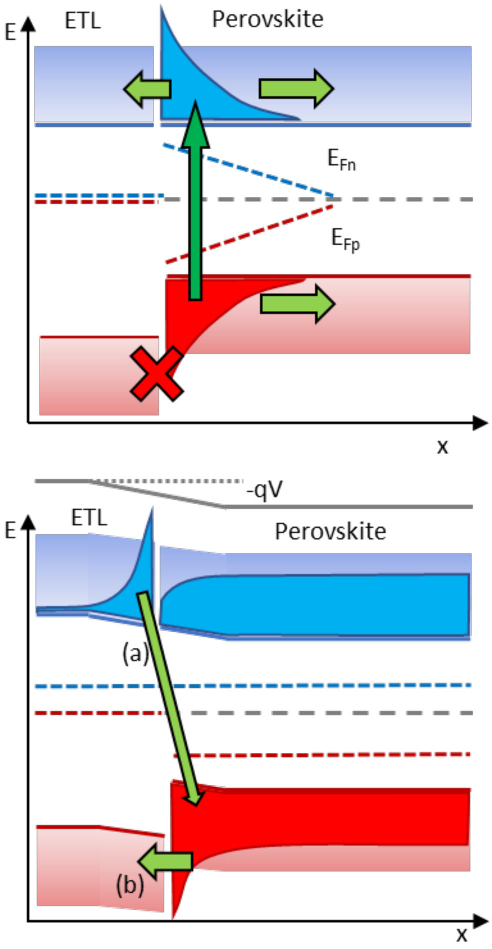

Figure 5.6: The distributions of CB electrons (blue) and VB holes (red) are superimposed on the energy level diagrams for two different times. Top: The initial distributions resulting from illumination through the ETL layer. The horizontal arrows indicate diffusion into the perovskite, or extraction of electrons into the ETL. Bottom: A double layer has formed with perovskite electrons repelled from the interface, but perovskite holes and ETL electrons are both attracted to the interface. When the quasi-Fermi Levels E_{F_n} and E_{F_p} are uniform, there is no net extraction of electrons. Extraction can only proceed further if other processes occur. Process (a) is recombination of ETL electrons and perovskite holes, called back recombination. Process (b) is extraction of perovskite holes into the ETL.

the HOMO of the ETL (process (b)), which is equivalent to an electron moving from the ETL HOMO to the perovskite VB and recombining with a hole. It has been shown [104] that fullerene molecules have a tail of states above the valence band, that means the VB offset between fullerene and perovskite is not very large and thus hole extraction may not be blocked very effectively.

The process of an electron in the LUMO of the ETL returning to the CB of the perovskite does not reduce the carrier density in the perovskite (unlike recombination of an electron and hole), so cannot contribute to decay of the photoconductance. It should also be noted that recombination within the ETL does not change the net charge of this layer, so cannot reduce the repulsion.

5.4.2.1 Cross-Interface Recombination

Cross-interface or "back" recombination of extracted electrons is introduced into the model as a means of inhibiting the formation of the double layer, and the resulting carrier dynamics are shown in Fig.5.7. Two different values of the extraction rate constant are shown (with the same back recombination constant), and also two different step sizes to confirm sufficient accuracy of the larger step size. The dynamics with and without back recombination are directly compared in Fig.5.8, showing that the plateau in the decay is removed by including a large back recombination rate constant.

In Fig.5.7 it can be seen that even with back recombination included, there is a small splitting of the electron and hole densities near the interface (i.e. a small double layer), and there is an overall excess of holes in the perovskite and electrons in the CTL. This charge separation rises quickly, saturates and then slowly declines. This is because initially the excess electron density in the CTL, n_{CTL}, and thus the interface recombination rate, $R_{int} = k_{int} n_{CTL} p_{per}$, are zero, so only extraction $R_{ex} = k_{ex} n_{per}$ occurs. As extraction proceeds, n_{CTL} and R_{int} increase until the interface recombination and extraction rates are similar, at which point n_{CTL} and the net charge density in the perovskite, $n_{per} - p_{per}$, saturate. These two rates will then continue to be similar to each other. so the net densities change very slowly. The rates R_{int} and R_{ex}, remain similar, but both decreasing, because extraction decreases the extraction rate (by decreasing n_{per}) and interface recombination decreases the interface recombination rate (by decreasing p_{per}), so both decrease at similar speeds. When R_{int} has increased to match R_{ex}, this is equivalent to any extracted electron immediately undergoing interface recombination, so n_{CTL} doesn't change. A larger interface recombination rate constant, k_{int}, means that recombination and extraction balance at a lower value of n_{CTL}, so the separation of charge density saturates at a lower density, i.e. the double layer is smaller. In the perovskite layer, not only extraction but the transport of carriers also determines the carrier density at the interface, making the dynamics more complicated.

5.4.3 Modelling with Effective Surface Recombination

Whenever interface recombination and extraction rates are similar $R_{int} \sim R_{ex}$, then this two-step process - extraction then immediate back recombination - will be equivalent to a surface recombination of perovskite electrons and holes, with a rate that is proportional the electron density, i.e. monomolecular. Therefore, this can be modelled with the ambipolar

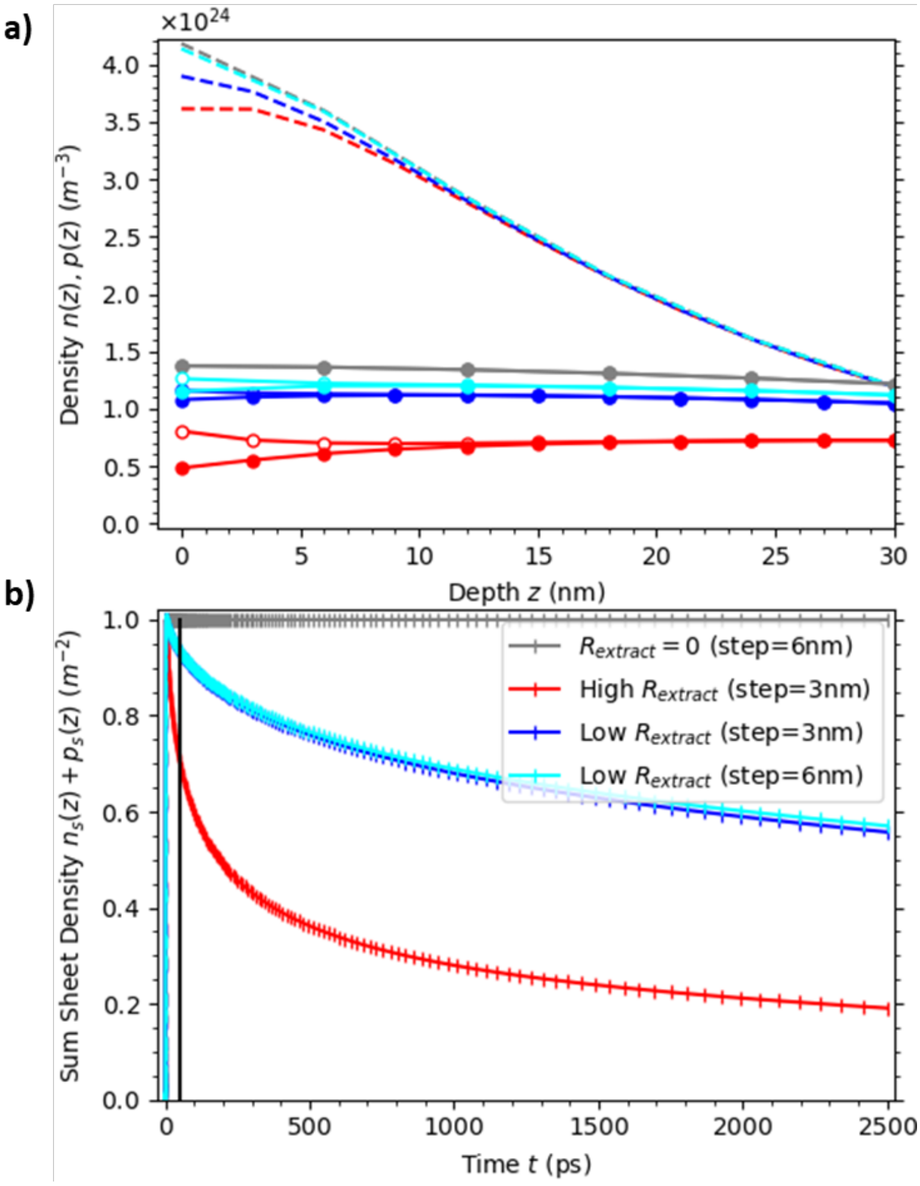

Figure 5.7: Numerical simulations of the drift-diffusion equations including the Coulombic force and a large back-recombination rate constant, for an ETL-perovskite bilayer. The simulation is for 410nm excitation on the ETL side of a 600nm thick perovskite layer. a) The carrier distribution at t=50ps. The empty circles indicate the hole distribution and the filled circles indicate the electron distribution. The dashed lines indicate the distributions at the time of maximum sheet density. b) The sum of the electron and hole sheet densities, where the integral over depth is calculated by a simple summation of the nodal densities.

continuity equation with monomolecular surface recombination. The analytical solution of the ambipolar continuity equation with surface recombination, can be solved much more quickly than the numerical solution, meaning fitting the solution to the data (iteratively varying the input parameters of the model to minimise the difference from the data) can be performed on reasonable timescales.

Iteratively fitting the analytical solution to the data is performed by least squares fitting. The square of the difference between the simulated decay curve and the experimental decay curve at each delay point, called the residual squared, is summed up for all the delay points to give the cost function. Some of the parameters in the model (the

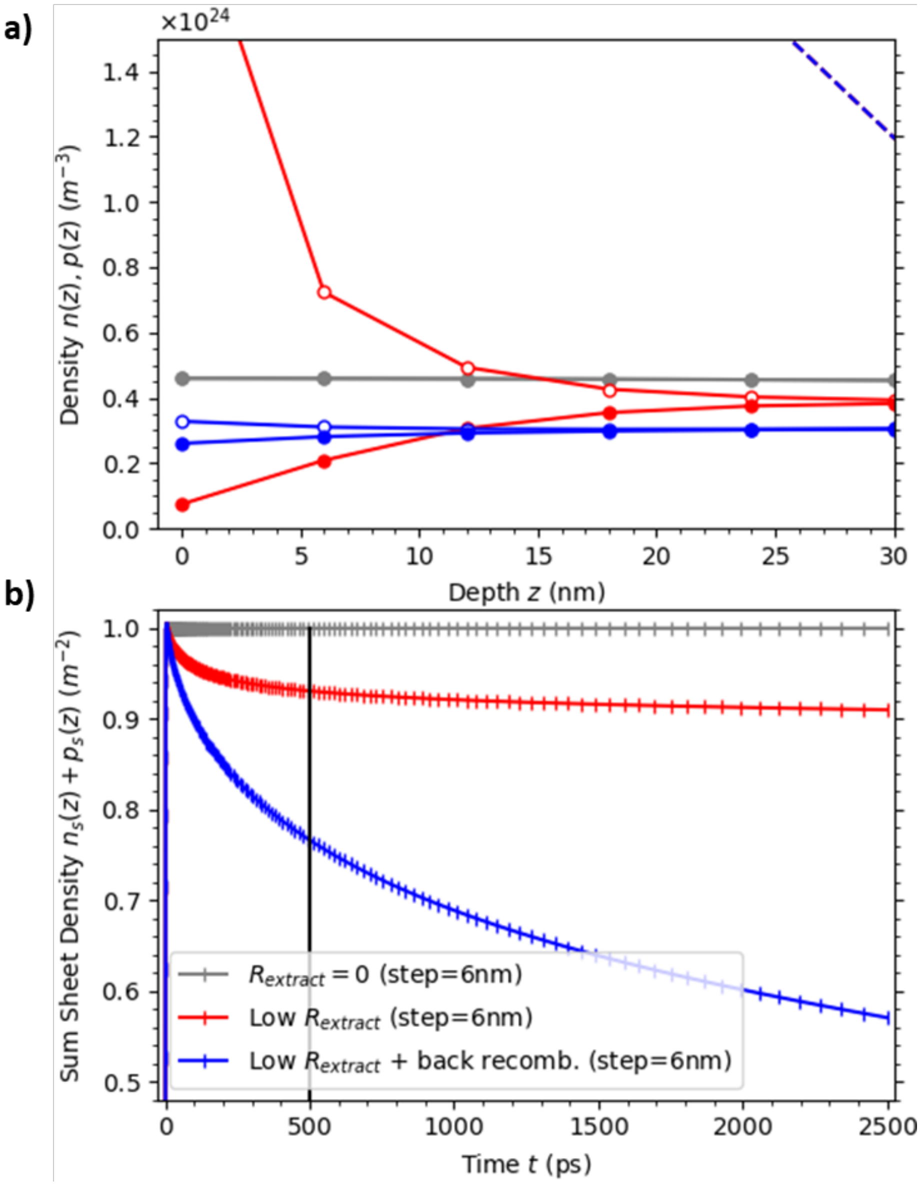

Figure 5.8: Numerical simulations of the drift-diffusion equations including the Coulombic force and either with (blue) or without (red) a large back-recombination rate constant, for an ETL-perovskite bilayer. The simulation is for 410nm excitation on the ETL side of a 600nm thick perovskite layer. a) The carrier distribution at t=500ps. The empty circles indicate the hole distribution and the filled circles indicate the electron distribution. The dashed lines indicate the distributions at the time of maximum sheet density. b) The sum of the electron and hole sheet densities, where the integral over depth is calculated by a simple summation of the nodal densities.

free parameters) are iteratively varied to find the parameter values that give the smallest value of the cost function (the "best fit" parameters). When each residual squared term in the summation is weighted by the inverse of its standard error squared, then the cost function is called χ^2 [306]

$$\chi^2 = \sum_{i=1}^{N} \frac{(y_i - f_i)^2}{\alpha_i^2} \tag{5.11}$$

where y_i is the data value, f_i is the simulated value. The standard error (in the mean) $\alpha_i = \sigma_{N-1}/\sqrt{N}$, where σ_{N-1} is the standard deviation of the N repeat measurements. When the standard errors are known, the minimisation algorithm can calculate 1σ uncertainties in the best fit parameters that it finds (in this work fitting was performed with the lmfit python package using the Levenberg-Marquardt algorithm).

The number of free parameters should be minimised to find a sharp minimum of the cost function with respect to the free parameters. Global fitting involves simultaneously fitting a set of decay curves for different experimental conditions, by comparing them to the set of corresponding simulated curves for each condition, all of which use the same values of the free parameters. The sum of the residuals squared for all these curves (the global cost function) can have a sharper minimum with respect to the free parameters, than for just a single curve, which corresponds to lower uncertainty on the best fit parameters. The decay curves should be for different experimental conditions in order to provide the additional constraint. In this work this was achieved by photoexciting using different wavelengths and thus different absorption depths, and by photoexciting on different sides of the sample.

The analytical model requires parameters describing the initial condition, the boundary conditions and the bulk processes of transport and recombination. The perovskite thickness is also required. In the scenarios considered here, bulk recombination in the perovskite is ignored, as the bare perovskite samples showed very little photoconductance decay over the 3ns window of the OPTP and TA experiments (indeed in chapter 6 E-OPTP measurements showed the perovskite layer had a monoexponential decay lifetime of ~170ns).

The initial condition (i.e. the initial carrier distribution) is determined by the incident photon flux, the front surface reflection, the absorption coefficient and the photogeneration yield (Φ). The first three can be measured, but Φ cannot hence $\Phi = 1$ was assumed. It is important to note that the ambipolar continuity equation is linear, so the normalised decay shape is the same regardless of the sheet density. Therefore, any errors in the estimation of the initial sheet density will not have any impact on the decay dynamics. The initial sheet density must be converted to a sheet photoconductance and then a fractional transmission change $\Delta T/T$ (via Eq.2.4) in order to compare it to the data. The conversion to photoconductance involves a product of the sheet densities and the THz mobilities of electrons and holes. The THz mobilities are not known, so the mobility values that are required to match the initial sheet density to the initial $\Delta E/E$ amplitude (see Eq.2.4) provide an estimate of these mobilities. The initial amplitude of $\Delta E/E$ could be allowed to be a free parameter e.g. allowing the THz sum mobility to be free. However, it is preferable to reduce the number of free parameters, and instead fix the initial amplitude of the simulated signal such that it matches the data.

The boundary conditions are specified by the surface recombination velocity, which is completely unknown so is set as a free parameter to be extracted by fitting the model to the data.

The parameter describing transport is the ambipolar diffusion coefficient. The term mobility refers to drift transport, but since a diffusion coefficient is related to mobility by the Einstein relation, a diffusion mobility may sometimes be referred to. The mobility for long range DC transport and is likely to be different to the THz mobility which is for short range transport at THz frequencies, so these are considered to be distinct and independent of each other. The ambipolar diffusion coefficient (or diffusion mobility) is an unknown so is set as a free parameter to be extracted by fitting the model to the data.

The only other parameter, perovskite thickness, can be measured from SEM images. Overall, the free parameters are just the ambipolar diffusion coefficient/mobility and the surface recombination velocity (for the particular CTL). Excitation on the back side (quartz) will give a strong constraint on the possible values for the ambipolar mobility, as the shape of the decay will be strongly influenced by the time taken to diffuse through the perovskite to the CTL interface.

5.4.4 Global Fitting of the Analytical Solution

Measurements of the same sample with different excitation conditions can be globally fitted. Samples from different batches should not be globally fit as the free parameters of ambipolar mobility and surface recombination velocity may be different for the different batches. For the C_{60} bilayers, global fitting was done for the measurements using 410nm excitation on the front side and on the back side, so the absorption coefficient is set to

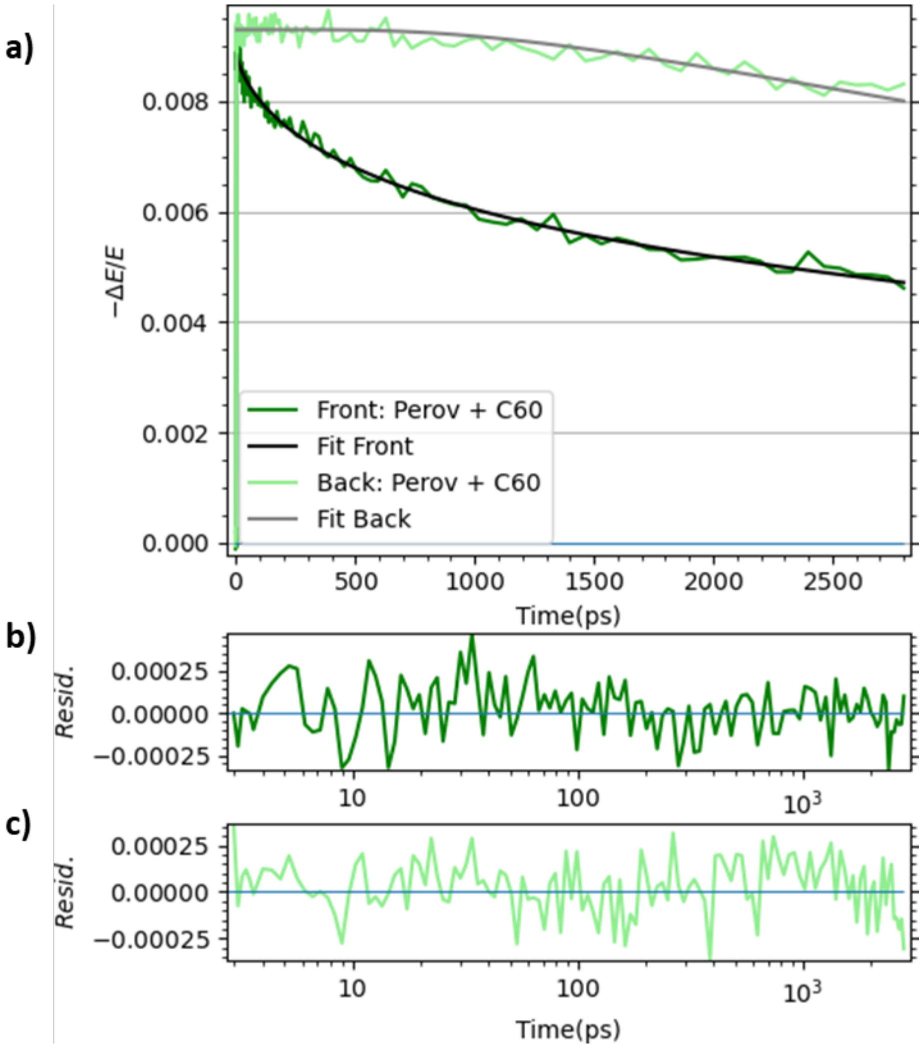

Figure 5.9: Global fitting of the analytical solution of the ambipolar continuity equation including surface recombination, to the OPTP transients for the C_{60} bilayer (batch 1) excited with 410nm on either the C_{60} side (front) or the quartz side (back). The best fit parameters are $\mu = 15 \pm 0.6 \times 10^{-4}\,\mathrm{m^2V^{-1}s^{-1}}$ and $S = 90 \pm 2\,\mathrm{ms^{-1}}$.

$3\times10^7\ \mathrm{m}^{-1}$ (batch 2 with perovskite thickness $\sim$ 370nm). The results are shown in Fig.5.9 and the residuals can be seen to be quite symmetrically distributed about zero. The values of the best fit parameters with their 1σ uncertainties are $\mu = 15 \pm 0.6 \times 10^{-4}\,\mathrm{m}^2\mathrm{V}^{-1}\mathrm{s}^{-1}$ and $S = 90 \pm 2\,\mathrm{ms}^{-1}$.

The measurements of the C_{60} bilayer with 410nm excitation show a clear delay in the decay of the signal when exciting on the Back (quartz) side, corresponding to the time it takes for carriers to diffuse from near the quartz interface to the C_{60} interface. However, for the PCBM bilayers (see Fig.5.10, it can be seen that with 410nm excitation on the back (quartz) side, whilst the decay is slower compared to excitation on the front (PCBM) side, it does not show a distinct delay to the start of the decay. As discussed

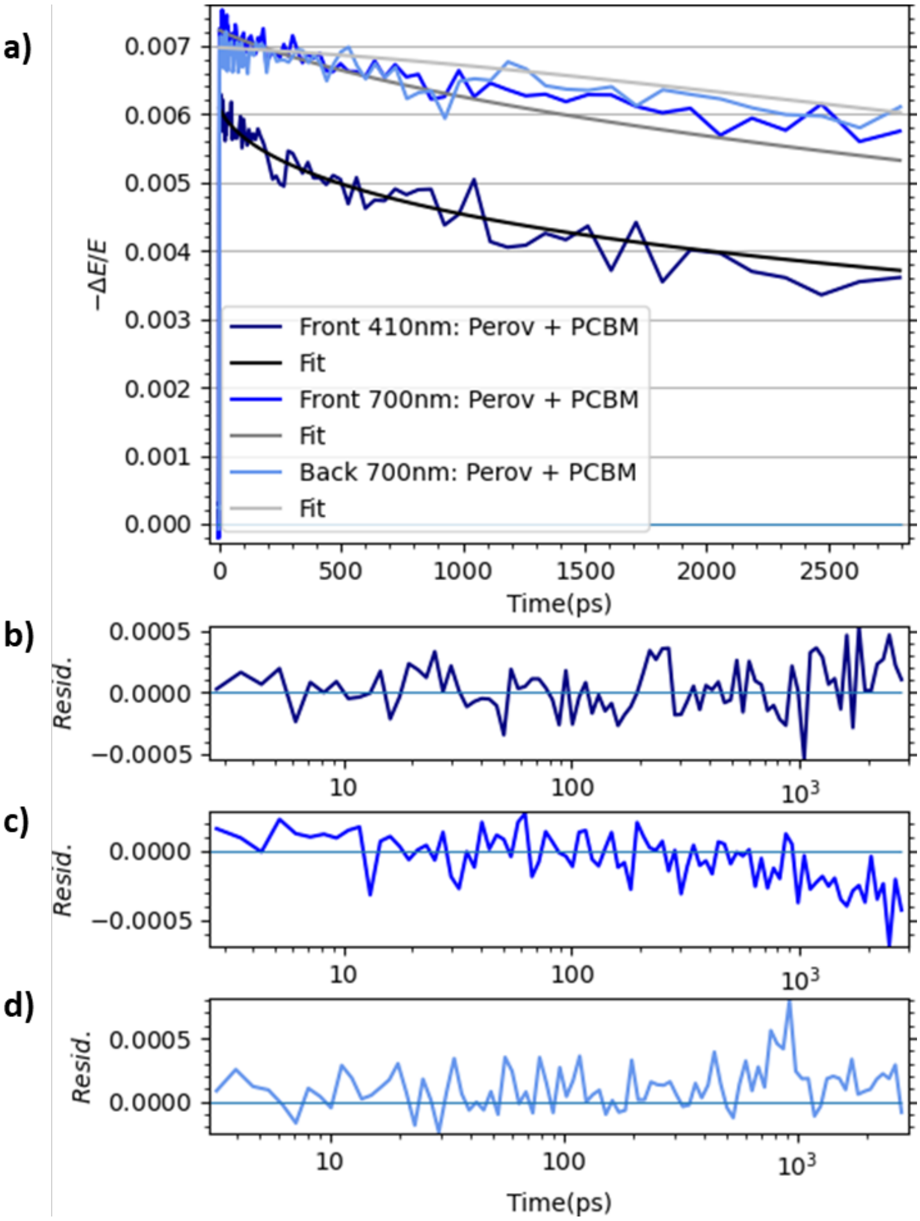

Figure 5.10: Global fitting of the analytical solution of the ambipolar continuity equation including surface recombination, to the OPTP transients for the PCBM bilayer (batch 1) for three different excitation conditions: 410nm excitation on the PCBM side (front), and 700nm excitation on either the front (PCBM) or back (quartz) side. The best fit parameters are $\mu = 12 \pm 1 \times 10^{-4}\,\mathrm{m}^2\mathrm{V}^{-1}\mathrm{s}^{-1}$ and $S = 61 \pm 2\,\mathrm{ms}^{-1}$.

before, this suggests that at least some PCBM is closer to the quartz substrate than the 600nm thickness of the perovskite layer. This could be because the thickness is actually smaller in the measured region, or that the solution deposited PCBM has penetrated into grain boundaries or small gaps. It is therefore difficult to globally fit the curves for the PCBM bilayers with the surface recombination model. If the PCBM molecules are closer to the quartz substrate than the full 600nm thickness of the perovskite layer, then a smaller thickness of the perovskite layer could be used in the analytical model of surface recombination. When a thickness of 300nm is used in the model instead of 600nm, the best fit values for μ and S are both reduced, but the fit is not noticeably improved.

Fitting of all the PCBM measurements except for excitation with 410nm on the back, yields reasonable fits. This is because it is the decay curves for 410nm excitation on the back that is most sensitive to the possible penetration of PCBM into the perovskite layer. The best fit parameters and their 1σ uncertainties are $\mu = 12 \pm 1 \times 10^{-4}\,\mathrm{m}^2\mathrm{V}^{-1}\mathrm{s}^{-1}$ and $S = 61 \pm 2\,\mathrm{ms}^{-1}$. However, it should be remembered that modelling the decay using 600nm thick perovskite with recombination at the surface only, is just an approximation of a more complex scenario for the PCBM bilayers.

5.5 Conclusions

The mathematical simulations of carrier dynamics presented in this chapter have provided greater understanding of the carrier dynamics in perovskite-CTL bilayers that were measured by optical spectroscopy in the previous chapter. Firstly, by employing a more detailed model that includes Gauss's law, it was shown that the Coulombic forces arising from selective carrier extraction induce a "double layer" distribution of electrons and holes near the interface, which reduces the carrier extraction rate as the carriers that can be extracted are repelled from the interface. This would result in the photoconductance decay plateauing within the 3ns measurement range of the OPTP and TA measurements, which was not observed. Since the fullerene layers are known to extract electrons efficiently (see section 1.4.4), this leads to the conclusion that the persistent decay of the photoconductance (and GSB) observed for the fullerene bilayers in chapter 4 must be due to a process that reverses the charge separation. The possible processes include recombination of electrons in the fullerene with holes in the perovskite, or extraction of perovskite holes into the fullerene. The two step process of electron extraction followed by recombination or hole extraction can be equivalent to a surface recombination process, which can be modelled using the ambipolar continuity equation. The analytical solutions of this model very accurately reproduced the OPTP measurements of the C_{60} bilayers. The difficulty in simulating the OPTP measurements for PCBM is consistent with a difference in the morphology of the two materials, as the vapour deposited C_{60} sits on the surface of the perovskite whilst the solution deposited PCBM penetrates into grain boundaries and gaps, and thus modelling the interface as a single flat plane is not appropriate. This work confirms that the morphology of the ETL material is an important parameter.

The observation of a significant effective surface recombination at the fullerene-perovskite, as just described, will undermine the performance of the cell. However, for closed circuit conditions in a full device the attracted carriers will be pulled away from the interface towards their respective electrodes, which will reduce the degree of charge accumulation, but will not entirely remove the double layer as the CTL will still accumulate a net charge at steady state due to the selective extraction. It has been shown that using layers which have wide bandgaps (e.g. BCP[105] or metal oxides[68, 95–97]) as additional layers between the fullerene layer and the metal contact improves performance, which is likely due to their efficient hole blocking making up for the poor hole blocking of the fullerene. Using these hole blocking layers without fullerene layers results in lower performance, suggesting they lack the fast electron extraction ability of the fullerene.

For Spiro-OMeTAD, the measurements in chapter 4 suggest that there is no extraction of holes (or recombination) within the first few nanoseconds after photoexcitation, and a faster decay of the density compared to the bare perovskite sample is only apparent over longer time scales (measured by TCSPC). However, Spiro has a large bandgap and its CB has a large energy offset relative to the perovskite CB [106], so is expected to be a good electron blocker. Therefore there is a possibility that Spiro could extract a fraction of holes that is not detectable within the measurement uncertainty (possibly due to smaller THz mobility for holes than electrons), which then strongly inhibits further extraction. Then in contrast to fullerenes, this charge separation could be maintained for a long time since Spiro is a good electron blocker, resulting in a slow signal decay. However, the simplest explanation appears to be that Spiro extracts holes more slowly than the fullerenes extract electrons.

The high performance of Spiro relative to other HTLs is not questioned by this conclusion, as other HTLs may be even slower hole extractors or worse electron blockers or leave more interface defects. The slow population decays observed in this work also suggest that there must be a relatively low density of defect states at the Spiro interface, which also contributes to its high performance.

Overall, the interface dynamics for fullerenes and spiro-OMeTAD have been shown to be very different, which will have a significant impact on device operation (as discussed in section 1.3.2.7). Furthermore, modelling has revealed that charge separation across the interface has the potential to leave a clear fingerprint on the decay dynamics, and the absence of this fingerprint is revealing.

Chapter 6

Electronically Delayed Optical Pump Terahertz Probe Spectroscopy

As has been demonstrated in Chapter 4, optical pump terahertz probe spectroscopy (OPTP) is a powerful technique for measuring transient photoconductance decays in a contactless manner and with femtosecond temporal resolution. The transient photoconductance decay of a material after pulsed photoexcitation gives valuable information about charge carrier mobilities and recombination lifetimes, which are critical properties for electronic device performance.

However, a limitation of using OPTP to study semiconductors used in electronic devices, particularly photovoltaics, is that the carrier lifetimes are often much longer than the time range of the technique. This chapter presents an electronically delayed OPTP technique (E-OPTP) that gives almost unlimited time range whilst maintaining sub-nanosecond resolution. The capabilities of this technique are demonstrated by examining the photoconductance decays of semiconductors with lifetimes ranging over six orders of magnitude: III-Vs, metal halide perovskites, germanium and silicon. The temporal performance of this setup is characterised, and an efficient method to sample photoconductance decays longer than the laser repetition period is presented. This method was used to study the impact of surface passivation on the carrier dynamics in silicon, and by comparing these measurements to those using an established technique (PCD), the superior spatial and temporal resolution of E-OPTP is highlighted, that allows in-plane and out-of-plane diffusion to be studied. This chapter was published in Butler-Caddle et al., “Terahertz photoconductance dynamics of semiconductors from sub-nanosecond to millisecond timescales”, Appl. Phys. Lett. 122, 012101 (2023) [307].

6.1 Introduction

In a typical OPTP setup, both the pump and probe pulses are derived from the same laser using a beam-splitter so that the pump-probe delay (i.e. the difference between the arrival times of the pump and probe pulses at the sample) can be varied with femtosecond precision by changing the path length of the one of the beams with micrometre precision, yielding femtosecond temporal steps. In this setup, the path for one of the beams includes a retro-reflecting mirror that is positioned on a mechanical translation stage that moves the mirror collinearly with the incident beam. Unfortunately, this is limited to a change in path length on the order of one metre which corresponds to a change in arrival time of only ∼3ns. So for samples with effective monomolecular lifetimes [1] longer than a few hundred picoseconds, only the earliest part of the decay can be measured. However, as much information as possible is required to discriminate the different possible mechanisms causing the signal decay, and measuring the full decay provides additional information that simply changing the excitation conditions (such as direction, fluence or wavelength) cannot.

The alternative to mechanically delaying fractions of a beam, is to generate the pump and probe beams from different sources, and vary the time delay between the pulses from the two sources. This can be done in different ways (e.g. asynchronous optical sampling, typically for femtosecond resolution over nanosecond ranges [308]), but for an OPTP setup using an amplified femtosecond laser, the simplest extension for measuring slow decays (so not requiring femtosecond resolution) is to choose the additional laser to be an electronically triggered laser for generating the pump pulses, and vary the timing of the electronic trigger. The femtosecond master laser generates an electronic signal that is synchronised to its optical emission, and this is sent to the pump laser via a delay generator, allowing the pump-probe delay to be varied. This method allows pump-probe delays from sub-nanosecond to beyond milliseconds to be measured, and does not suffer from the beam walk-off that occurs when the beam is not perfectly collinear with the mechanical stage, that results in artefacts/distortions.

6.1.1 Previous Versions

The concept of electronically delayed OPTP, hereafter named E-OPTP, has been reported previously[309, 310]. In a scheme that generated THz radiation using a laser oscillator[309], the probe was a series of consecutive THz pulses with a FWHM of 95 ns, limiting the temporal resolution, and the pump-probe delay range was limited to 200 μs. In contrast, for the amplified laser system used here, the probe is a single THz pulse, that is resolved down to tens of femtoseconds, so the temporal resolution is instead limited by the electronic jitter of the delay generator, which is tens of picoseconds. Lin et al. performed E-OPTP with an amplified laser to examine photoconductance decays in metal halide perovskites over a time range of only $\sim$ 100 ns[310], but no characterisation of temporal resolution was provided. Here we study semiconductors with carrier lifetimes ranging from nanoseconds to milliseconds, by employing a method for efficiently measuring photoconductance decays that exceed the 1 ms repetition period of the probe. Furthermore, the factors limiting temporal resolution are characterised.

6.1.2 Alternative Techniques

Other techniques that measure photoconductance decays in a non-contact manner include time resolved microwave conductivity (TRMC),[22–25] which measures the transmission

---

[1] Effective monomolecular lifetime is defined by $d(\Delta n)/dt = -\Delta n/\tau(\Delta n)$ where Δn is the excess carrier density.

(or reflection) of a continuous wave AC electric field at GHz frequencies, and inductively coupled photoconductance decay (PCD),[26–28] which induces and measures eddy currents at radio frequencies. Since these techniques probe at different frequencies, the properties that they measure may differ as both the conductivity response of a material and the penetration depth of the probing field are a function of frequency.[28, 231] For example, in polycrystalline materials, the carrier motion driven by probing fields may be impeded by grain boundaries, and this effect will be greater for lower frequencies and higher field strengths, which induce larger displacement meaning that more carriers will be impeded by the boundaries. This grain size dependent and frequency dependent mobility has been reported in MHPs [163, 231].

Of the three techniques, OPTP has the highest spatial resolution, with diffraction-limited spot sizes around 1 mm, whereas TRMC and PCD setups probe areas with dimensions of centimetres. When it comes to spatially mapping a sample, using a small probe spot is much preferred to using a small photoexcitation spot within a large probe area [311]. This is because when using a small photoexcitation spot, the photoexcited carriers may diffuse in the plane of the sample, reducing the spatial resolution, and this diffusion out of the probed region also complicates the interpretation of the signal decay, particularly if the sample is inhomogeneous and/or the wide area probe's sensitivity is spatially non-uniform. Instead, mapping using a small probe spot with wide field photoexcitation does not suffer from these diffusion related complications since there will be no in-plane diffusion in a uniformly illuminated area. Furthermore, if a small photoexcitation spot is deliberately chosen, a small probe spot allows in-plane diffusion (following localised photoexcitation) to be mapped, as will be shown in this work. In addition to superior spatial resolution, OPTP also has the best time resolution (down to tens of fs), in comparison to the typically ns and μs resolution of TRMC and PCD, respectively.

6.2 Experimental Implementation: delays < 1ms

E-OPTP was implemented with two different lasers and two different delay generators. One laser is a master oscillator power amplifier (MOPA) laser from Ikeos Research, with a centre wavelength of 1550nm and a pulse duration of ∼200ps FWHM. The other is a pulsed diode laser (Thorlabs NPL45C) that has a centre wavelength of 450nm and a pulse duration that can be varied from 6-129ns (16 discrete values), with an approximately square temporal profile. The two delay generators were either a Quantum Composers (QC) 9530 or a Stanford Research Systems (SRS) DG645.

First, results using the pulse scheme introduced previously (see section 2.2.6) are presented. This is referred to as normal mode E-OPTP and can be used for decays shorter than 1ms. Figure 6.1b reports $\Delta T/T$ transients obtained on a variety of indirect and direct bandgap semiconductors, and which could not have been measured using a mechanical delay line. An unpassivated n-type Ge wafer ($n_0 \leq 10^{14}\,\mathrm{cm}^{-3}$) and InSb or InAs epitaxial layers were excited with the 1550 nm laser, while a passivated Si wafer and a film of the triple cation lead halide perovskite[136, 312] $\mathrm{Cs_{0.05}(FA_{0.83}MA_{0.17})_{0.95}Pb(I_{0.83}Br_{0.17})_3}$ were excited with the 450 nm laser. The InAs, InSb and perovskite were fitted with mono-exponential decays (dashed lines) yielding lifetimes of 1 ns, 6 ns and 170 ns respectively.

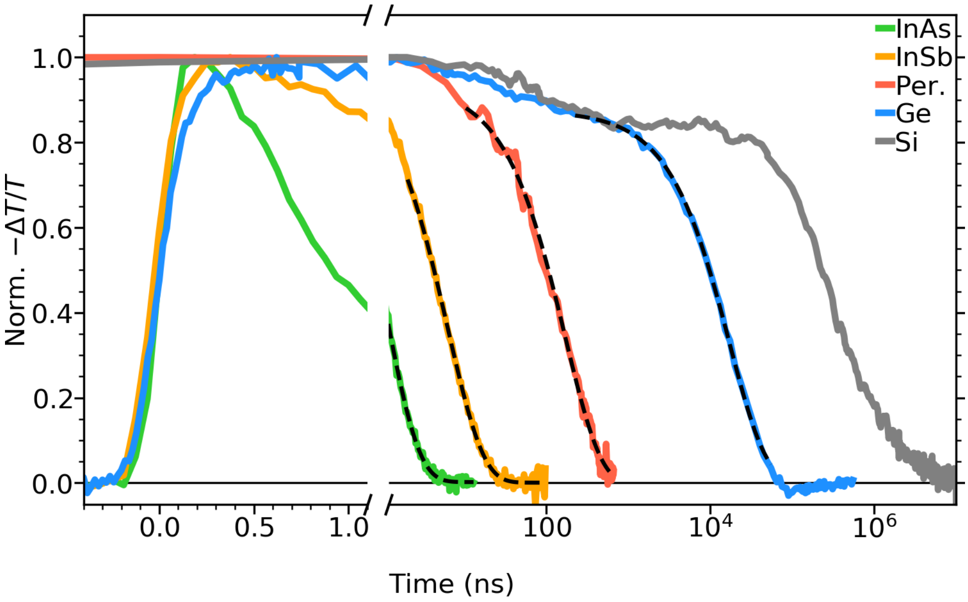

Figure 6.1: Normalised photoconductance decays for Ge, InSb and InAs excited by the 1550 nm laser, and a lead-halide perovskite (Per.) film or a passivated Si wafer excited by the 450 nm laser. Single-exponential fits are indicated by dashed lines. All curves were acquired with the usual 4 pulse scheme (see section 2.2.6), except for the data on Si, which required the "extended mode" scheme discussed with regard to Fig. 6.3.

For Ge, $\Delta T/T$ had a faster decay over the first few hundred nanoseconds, followed by a slower monoexponential decay (20 μs lifetime) commensurate with its indirect bandgap and low trap density, and consistent with lifetimes from TRMC.[313] Results for Si are discussed later.

6.3 Assessing the Temporal Resolution

The factors that affect the precision and accuracy of the temporal resolution in E-OPTP are now discussed. First regarding the precision, in both electronic and mechanical delay schemes the ultimate temporal resolution (precision) of the probe for a single shot is set by the response function of electro-optic sampling, *i.e.* the optical gate pulse duration (40 fs) and response of the non-linear crystal.[314] However, the temporal resolution (precision) is poorer for E-OPTP than for mechanical delay: the minimum delay step is greater (5 ps for the SRS and 250 ps for the QC delay generators compared to ~10 fs for mechanical delay stage), and the pump-probe delay jitter (shot-to-shot fluctuations in delay time) is larger. The jitter for the mechanically delayed method is from the vibrations of the optical components and possibly fluctuations in the refractive index of the atmosphere along the beam path. Jitter broadens the temporal response function for the mean of multiple repeats compared to the response function for a single repeat.The jitter between the input and output signals for each component can be assessed using an oscilloscope to measure the distribution of arrival times for the output signal relative to the input signal. It was found that the QC 9530 delay generator had a peak-to-peak jitter of 2.4 ns, whereas the SRS DG645 delay generator and all other components had jitters smaller than 0.4 ns (the sampling precision of the oscilloscope).

To provide context for the following discussion it should be clarified that the full

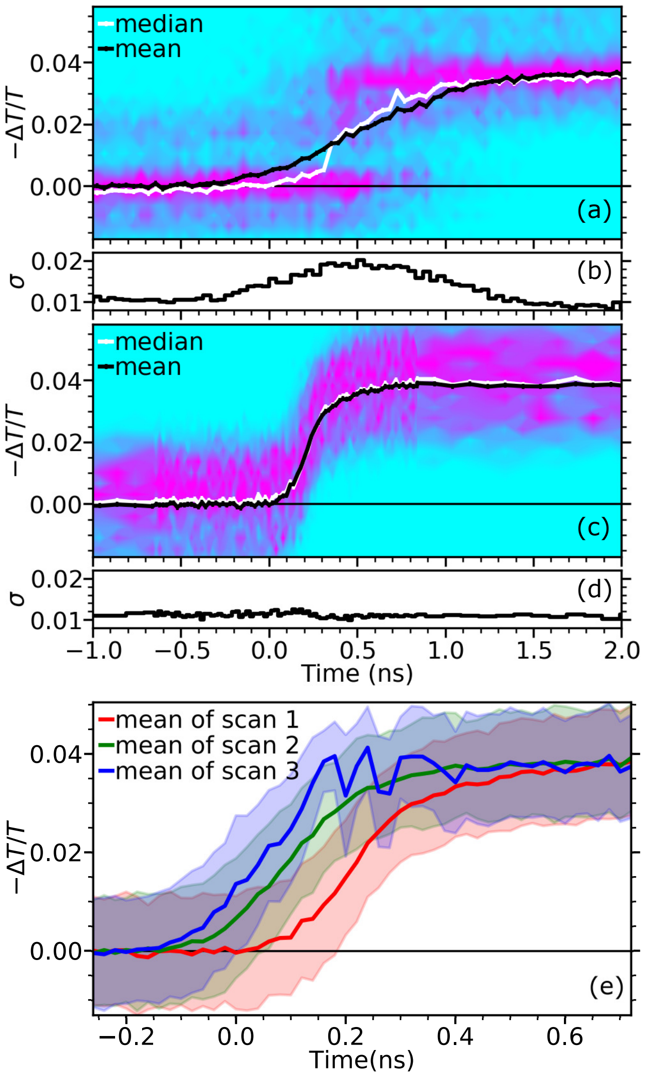

Figure 6.2: (a) 2D histogram of 200 repeat measurements of $\Delta T/T$ for Ge wafer excited at 1550 nm, plotted against nominal pump-probe delay set using the QC 9530 delay generator. Purple indicates more counts while cyan represents zero counts. (b) Standard deviation, σ, of $\Delta T/T$ from (a). (c)-(d) As (a) and (b) but using the SRS DG645 delay generator. (e) The mean (lines) and standard deviation (shaded) of $\Delta T/T$ obtained from 200 repeat measurements at each pump-probe delay, for three different sweeps (scans 1-3) over the delay range, taken at 5 minute intervals. Scan 1 data also shown in (c)-(d). (Ge wafer; 1550 nm excitation; SRS DG645 delay generator).

range of delays is swept over to form one "scan", and for each delay position in this sweep, 200 consecutive repeats of the 4 pulse scheme are recorded before moving to the next delay position. The impact of timing jitter in E-OPTP was further quantified using the histograms and statistics of one scan (200 repeat measurements) of $\Delta T/T$ for the photoconductance rise of a Ge wafer pumped with the 1550 nm laser, as shown in Fig. 6.2 (brighter purple representing more counts). For the QC 9530 delay generator (Fig. 6.2a) the temporal resolution, as assessed from the duration of the rise in signal, was dominated by the 2.4 ns jitter of the delay generator. The increase in signal spread at delay times where the signal is changing rapidly, such as at zero pump-probe delay (around 0.5 ns in panel (a)), is caused by temporal jitter. This is evident by the increase in its standard deviation σ (Fig. 6.2b). This occurs because for multiple repeats at a particular nominal delay, a range of different actual delays are being measured. In particular, when the signal is changing between two relatively constant values (i.e. like a step function), temporal jitter will result in a bimodal distribution, as seen in 6.2a at about 0.2ns.

The smaller jitter of the SRS DG645 improved the temporal resolution such that a unimodal distribution was observed (see Fig.6.2c - this is only possible if the jitter is smaller than the photoconductance rise time), and a signal spread that is independent of pump-probe delay (see Fig.6.2d) which implies that the spread due to temporal jitter is smaller than the spread in the measurement of the signal's amplitude. The SRS DG645's timing jitter increases linearly as a function of delay time at a rate of 10^{-8} s/s from a minimum of 20-30 ps, and hence would only reach 130 ps even with electronic delays of 10 ms. The rise of the signal instead tracked the shape of the 200 ps-long pump pulse of the Ikeos laser, showing that the temporal resolution of the E-OPTP spectrometer was sufficient to resolve the photoconductance rise.

An additional consideration in E-OPTP is the accuracy with which the delay time is set. For the SRS delay generator, the accuracy is specified by the manufacturer to have a minimum of 1 ns increasing at 5×10^{-6} s/s per year. For a time resolved measurement a systematic delay offset is not a problem, only if the offset changes as a function of delay will it cause distortions. In OPTP experiments, the full range of pump-probe delays is often scanned multiple times. Here, repeated scans of $\Delta T/T$ were found to be shifted in delay time with respect to each other by a maximum of ~200 ps (Fig. 6.2e). This is potentially caused by the finite stability of the delay generator's internal clock (specified at 2×10^{-6}), creating a drift in delay for long data acquisition times. These small offsets are only noticeable where the signal changes rapidly, such as at time zero. The drift during the time for a single scan is evidently small (maximum of ~200 ps), so is not distorting the decay over nanosecond to millisecond timescales. Furthermore, during the time taken to measure just the signal rise section of the scan, the drift is even less, so is also not distorting the fast signal rise. The only consequence is that the scans appear uniformly offset, and so these small offsets between successive scans can be readily subtracted before averaging the repeated scans. Otherwise, averaging over scans that are offset will reduce the temporal resolution of the average in the same way that jitter does (for example, the average signal will have a longer rise time, with greater standard deviation).

6.4 Experimental Implementation: delays > 1ms

An efficient method for measuring decays over times longer than the 1ms repetition period of the master femtosecond laser, will now be presented. First, the normal method is briefly restated to provide context.

In OPTP, to account for any background offset in the electro-optic signal, the magnitude of the transmitted THz field is calculated from the difference between the signal measured with and without the THz pulse present at the detector, preferably using consecutive shots of the detection beam. This pair of measurements is performed both with and without the pump beam incident on the sample, resulting in a scheme of four consecutive detection (gate) pulses labelled A, B, C, D (see Fig.2.3). $\Delta T/T$ was calculated from:

$$\frac{\Delta T}{T} \equiv \frac{E_{\text{on}} - E_{\text{off}}}{E_{\text{off}}} = \frac{(A - B) - (C - D)}{C - D}. \tag{6.1}$$

where $E_{\text{on}} \propto A - B$ and $E_{\text{off}} \propto C - D$, are the transmitted THz field strengths with and without the pump incident on the sample. In the limit of small $\Delta T/T$, adopted herein, the sheet photoconductance $\Delta\sigma \propto -\Delta T/T$.[315] In contrast to double-demodulation based on lock-in amplifiers,[228] recording the electro-optic signal of these 4 pulses (the balanced photodiodes output) with an oscilloscope permits a shot-by-shot analysis of the statistics (*e.g.* standard deviation; median) of the data set.

For any pump-probe measurement, the signal should decay to zero before the next pump pulse excites the sample. In the normal 4 pulse scheme, pulse B has pump on, so the photoconductance should decay to zero in the time between pulse A and B, i.e. 1ms. So to use the normal 4 pulse scheme it would have to be scaled to have longer periods between the A, B, C, D pulses, (i.e. pulse A and B separated by a multiple of 1ms).Alternatively, a decay range of 2ms can be achieved by choosing the pump pulse to be off in pulse B, so that the photoconductance is only required to decay to zero before pulse C, i.e. 2ms. In this case, the B and D pulses are equivalent (both are THz off, pump off). For longer decays, scaling of the 4-pulse scheme to longer repetition periods, with A, B, C, D separated by $N \times 1$ms, would be required. However, this throws away a significant fraction of THz pulses (fixed 1ms repetition period). Here we devise a scheme that makes use of all the THz pulses, which is made possible by using an oscilloscope to record the data rather than lock-in amplifiers. The pulse scheme that is used is shown in Fig.6.3. The use of an electronically triggered pump laser makes it much easier to modify the pulse sequence for the pump laser, than with mechanical choppers.

Since the amplitude of each individual THz pulse is recorded by the oscilloscope (rather than the average recorded by lock-in amplifier techniques), multiple THz probe pulses can be recorded during a single photoconductance decay, allowing E_{on} to be sampled at multiple delay times during a single photoconductance decay (see the crosses at delay times τ_1 and τ_2 in Fig. 6.3). Also, only 2ms are required to measure $E_{\text{off}} = C - D$ rather

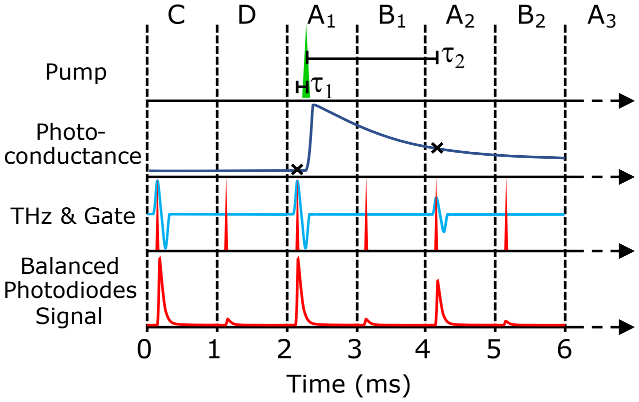

Figure 6.3: The "extended mode" data acquisition scheme, used to record dynamics at delays exceeding the master laser's repetition period (1 ms), with a single pump and multiple THz probes. E_{on} was sampled at multiple pump-probe delay times for each pump pulse (*e.g.* at τ_1 and $\tau_2 = \tau_1 + 2\,\text{ms}$) , and $\Delta T/T$ was calculated using Eq. 6.2.

than $N \times 2$ms for scaling the 4-pulse scheme. This "extended mode" method significantly reduces the time required to perform a certain number of $\Delta T/T$ samples, compared to using a scaled 4-pulse scheme.

The $\Delta T/T$ for the different sample points was calculated from:

$$\left.\frac{\Delta T}{T}\right|_i \equiv \frac{E_{\text{on},i} - E_{\text{off}}}{E_{\text{off}}} = \frac{(A_i - B_i) - (C - D)}{C - D}, \tag{6.2}$$

where i indexes the pair of A, B pulses used to calculate $E_{\text{on},i}$ at the sample point i (see Fig. 6.3).

The one difference from the 4-pulse scheme is that a measurement with pump on but THz off (to check for THz emission from the sample due to photoexcitation) is not performed, but the THz emission due to pumping the sample is usually negligible and can be checked separately.

6.5 Carrier Dynamics in Silicon Wafers

The capability of the extended mode was demonstrated by studying pieces of passivated silicon wafers for which the photoconductance decay can be significantly longer than the 1ms repetition period of the master laser. Two silicon samples were studied (see Fig.6.4): one with passivation applied to both surfaces (called "double passivated"), and one with the passivation removed from one surface by etching (called "single passivated").

The silicon wafers were Czochralski-grown and p-type with a resistivity of 2000 Ωcm. They were 700 μm thick and cut into pieces 5 cm×5 cm across. A rigorous pre-cleaning procedure was used before processing.[316] Both surfaces of the wafers were passivated by 20 nm-thick Al_2O_3 layers, formed by 160 cycles of atomic layer deposition (ALD) with O_2 plasma. Al_2O_3 provides chemical passivation (passivating surface defect states) and also field-effect passivation [317, 318], in which fixed negative charges in the Al_2O_3 layer repel electrons away from the surface and attract holes (so locally p-type). This means that near the surface the np product is reduced and thus all recombination processes, particularly surface defect mediated recombination, are reduced. For the "single passivated" sample, the passivation on one side was removed by HF etching, whilst the passivation on the other side was protected by depositing a layer of HfO_2 on one side prior to etching (deposited by ALD with O_2 plasma for 100 cycles, corresponding to 10 nm deposited). The "double passivated" sample kept passivation on both sides, but a HfO_2 layer was also deposited on one side of this sample for consistency with the single passivated sample. The passivation is activated by annealing the samples in air at 460 °C .[319, 320]

6.5.1 Impact of Surface Passivation

E-OPTP transients using the 450 nm laser are reported in Fig. 6.5 for the double passivated and single passivated silicon wafers, the latter of which was excited on either the passivated or the etched side. The pump beam's intensity profile in one direction was Gaussian with a sigma of 1mm at the sample (so D4σ = 4 mm), and in the other direction was a top hat with a diameter of D4σ = 4 mm. This was determined using a RaspberryPi camera as well as knife edge measurements. This intensity profile is due to the source being a diode laser.

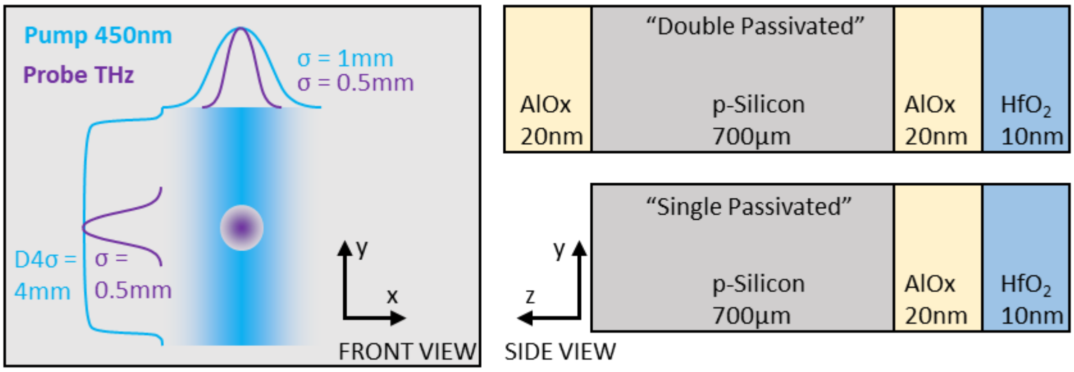

Figure 6.4: Schematic of the intensity profile of the 450nm pump and the field profile of the THz probe (left), and cross-sections of the two silicon samples (right).

The shallow absorption depth (0.4 μm [321]) when pumped at 450 nm meant carriers were initially concentrated near the illuminated surface. Hence the single passivated sample had faster recombination kinetics when excited on the etched side than on the passivated side (Fig. 6.5b).

The high temporal range of the E-OPTP enables the rate of diffusion into the depth of the wafer to be studied. While the magnitude of $\Delta T/T$ at a particular pump-probe delay time is not sensitive to the depth dependence of the photoconductivity (the transmission change is dominated by the absorption by free carriers, and so is proportional to the total carrier density along the propagation path, regardless of the distribution), the $\Delta T/T$ decay rate varies depending on the carrier density's depth profile. When illuminated on its passivated side, the transient for the single passivated sample was almost identical to the decay for the double passivated sample for delay times up to 25-30 μs, whereupon $\Delta T/T$ started to decay more quickly for the single passivated sample (Fig. 6.5b). This is the time required for carriers to diffuse to the unpassivated side of the wafer, where the surface recombination constant is higher.

This assertion is supported by the time-dependent carrier profile calculated using an analytical solution of the 1D ambipolar continuity equation for Si, as reported in Fig. 6.6a. In this simulation, recombination and transport were assumed to be negligible during the pump pulse, so the initial distribution was given by the measured generation profile. Literature values of electron and hole mobility were used to provide the ambipolar mobility for this simulation (the mobility calculator on the PV lighthouse website uses the Klaassen model [322]). To highlight the effect of diffusion, the simulation does not include recombination. For the timescale considered (100 μs), in-plane diffusion was neglected as it proceeds at a slower rate due to its smaller concentration gradient (it can be easily included in a 3D simulation). It can be seen that following excitation on the passivated side, an appreciable carrier density only arrives at the etched surface (at 700 μm depth) after 20-30 μs, and hence the population decay accelerates after this time.

The experimental decay curves for excitation of the single passivated sample on either of its two opposite surfaces both become monoexponential after about 100 μs delay, with approximately the same monoexponential lifetime of $\sim 110\,\mu$s (which is similar to the lifetimes measured by PCD shown in Fig.6.7). This is consistent with the carrier density diffusing to similar distributions following excitation on different sides, and indeed

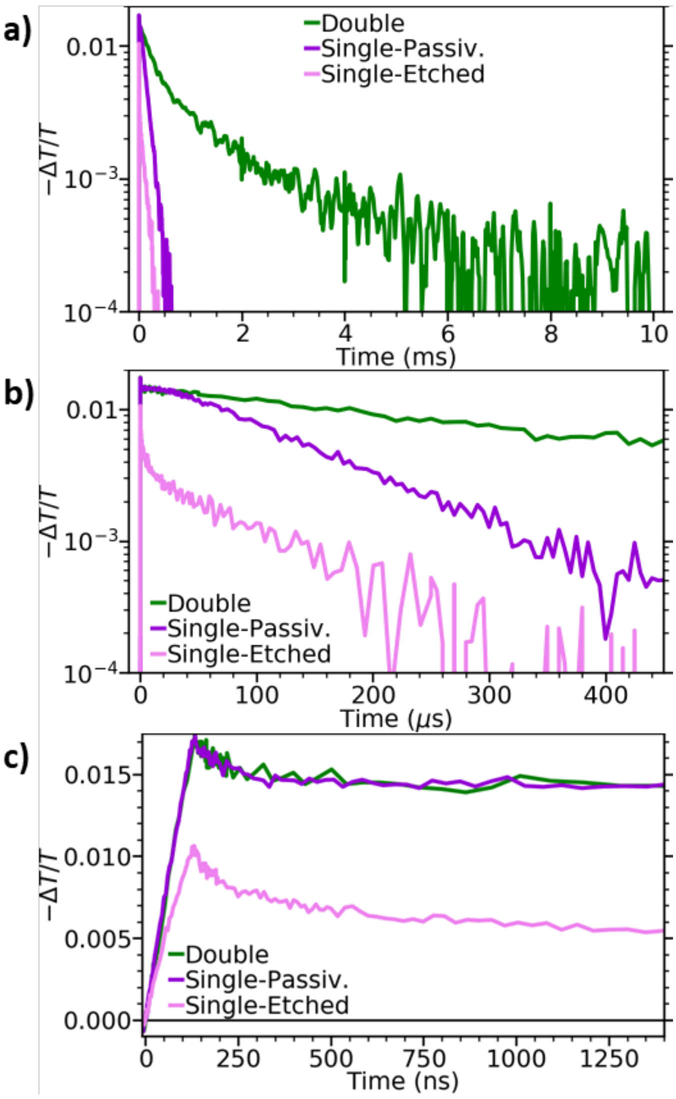

Figure 6.5: Photoconductance decays under 450 nm excitation for double-side passivated and single-side passivated Si wafers (illuminated either on its passivated side or on its etched side). a) Full time-window from data acquired in extended mode. b) and c) are the data from a), but highlighting the earlier times.

the simulation (Fig.6.6) shows that the carriers form a flat distribution (recombination is neglected) after about 100 μs delay, with concentration $\simeq 2 \times 10^{13}\,\mathrm{cm}^{-3}$. A monoexponential decay for the population can occur if the recombination process is monoexponential everywhere, but since the recombination rate constants are not uniform - they are higher at the surface than in the bulk - a monoexponential population decay can only occur if a stationary distribution is formed: the shape of the distribution does not change with time, only the amplitude.

In addition to the large temporal range, the E-OPTP technique has sufficient temporal resolution to observe faster changes. For excitation on passivated surfaces it can be seen that the photconductance decays rapidly over the first 100ns after the pump pulse is terminated, before slowing down (see Fig.6.5c). This can be attributed to the carrier density being concentrated in a short absorption depth immediately after photogeneration, resulting in a high recombination rate constant (either due to higher order processes such as Auger, or due to an enhanced monomolecular recombination constant near the surface).

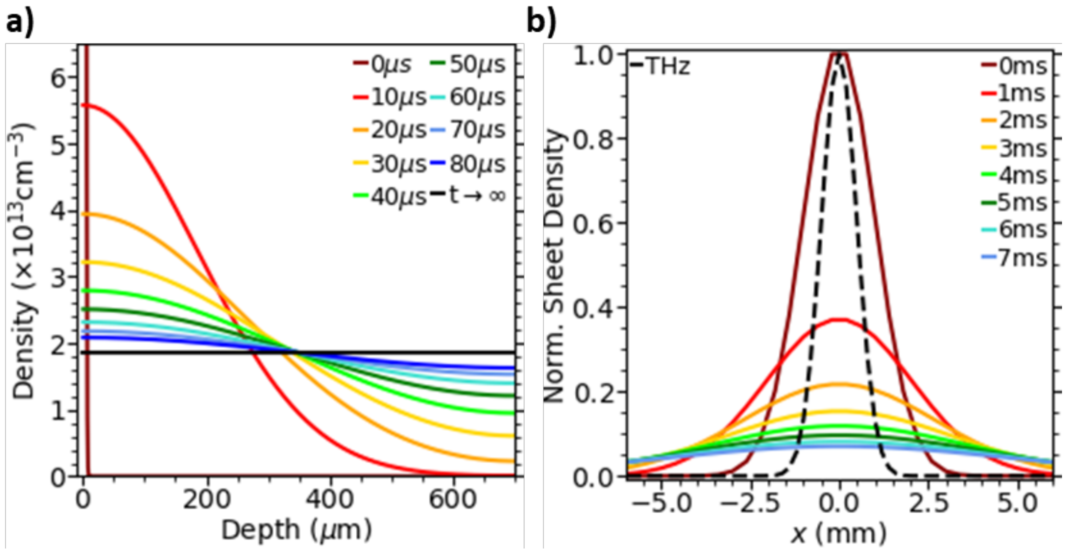

Figure 6.6: Carrier density profiles from analytical solutions to the ambipolar continuity equation, ignoring recombination since it is over longer timescales. a) Excess carrier density, Δn, versus depth at the centre of the pump spot, from solving the 1D case (in-plane diffusion was neglected). b) Profile of the sheet carrier density in the plane of the wafer, from solving the 2D problem. The THz probe (profile in black, dashed line) samples lower density at later times owing to in-plane diffusion.

This recombination is slowed as the carrier density is depleted and as carriers diffuse away from the surface. The field effect passivation likely assists in spatially separating electrons and holes, and reducing the recombination rate.

6.5.2 Comparison with PCD

The double passivated sample can be used to compare the E-OPTP technique with the established PCD method, which was implemented using a Sinton Instruments WCT-120 with white light illumination and a 2 cm spatial resolution (defined by the coil diameter). For PCD, a calibration converted the photoconductance signal into the excess carrier density, Δn, under the assumption that carriers had sufficient time to spread through the depth of the wafer to reach a stationary spatial distribution [323]. The density-dependent effective lifetime,[2] $\tau(\Delta n)$, was calculated from $\tau(\Delta n) = -\Delta n/d(\Delta n)/dt$[27, 323, 324]. Fig.6.7 shows the effective lifetimes measured by PCD. The lifetime for the double passivated sample was $\tau \sim$10 ms at the highest density $\Delta n = 5 \times 10^{15}\,\mathrm{cm}^{-3}$, and $\sim$20 ms for lower densities $\Delta n = 10^{15}\,\mathrm{cm}^{-3}$ to $10^{13}\,\mathrm{cm}^{-3}$. The shorter lifetime at higher densities is consistent with Auger recombination beginning to contribute.[325] For E-OPTP (Fig. 6.5a), an excess $\Delta n \simeq 2 \times 10^{13}\,\mathrm{cm}^{-3}$ was reached following out-of-plane diffusion into the wafer (around 100 μs, Fig.6.5b), and in contrast to PCD, the effective lifetime for the double passivated sample at this density was $\tau < 1$ ms, lengthening to ~ 1.3 ms by the end of the decay.

Therefore, there is a significant disagreement in the lifetime measured by E-OPTP and PCD at comparable densities ($10^{13}\,\mathrm{cm}^{-3}$). The faster E-OPTP dynamic can be ex-

---

[2] This effective monomolecular lifetime incorporates the rates from both bulk and surface recombination, and hence depends on the carrier profile versus depth.

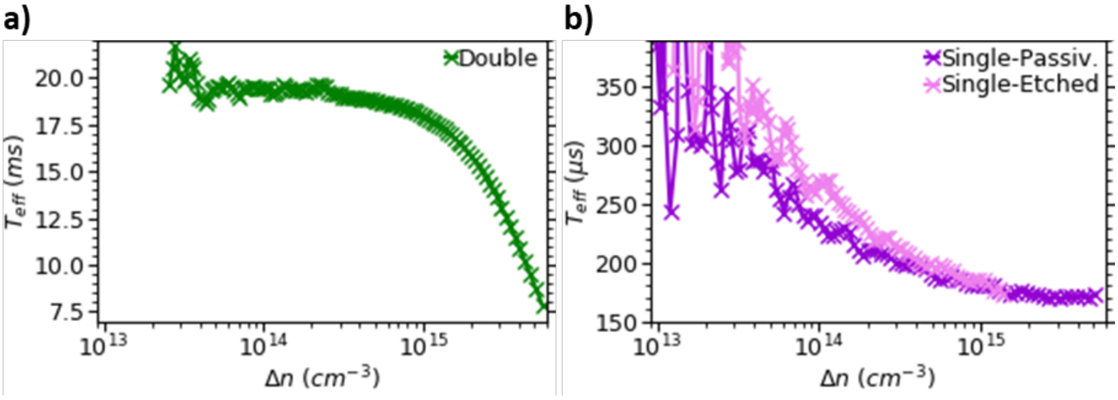

Figure 6.7: The effective lifetime as a function of excess density for a) the double passivated and b) the single passivated silicon wafer illuminated on either its passivated or etched sides, as measured by photoconductance decay (PCD).

plained by the in-plane diffusion of carriers away from the region probed by the THz pulse, which reduces the carrier density in the probed region, resulting in a decay of the signal. The flux from in-plane diffusion is greatest at early times when the in-plane concentration gradient is greatest, and reduces at later times when the gradient is shallower, consistent with $\Delta T/T$ decaying more slowly at late times. This explanation was further supported by analytical solutions to the 2D ambipolar continuity equation, reported in Fig. 6.6b for parameters matching the E-OPTP experiments. The calculated sheet density (the concentration integrated over the thickness of the wafer) in the probed region (dashed line in Fig. 6.6b) drops rapidly over the first couple of picoseconds, before slowing down (coloured lines), consistent with the data. Bulk and surface recombination were neglected in these calculations to highlight the effect of diffusion. The PCD measurements are also performed on the single passivated samples, and good agreement with the E-OPTP lifetimes is found, as in-plane diffusion is a less significant effect when recombination rates are much higher. Overall, the measurements of the Double Passivated sample demonstrate that the small probe spot size in E-OPTP makes the study of in-plane diffusion effects possible in semiconductors with long diffusion lengths.

6.6 Conclusion

In summary, this work develops and characterises an electronically-delayed optical pump terahertz probe (E-OPTP) setup with virtually unlimited delay range, allowing the full photoconductance decay of an optically excited material to be measured in a non-contact manner with sub-nanosecond resolution. The factors determining temporal resolution were discussed, and an efficient method to sample photoconductance decays longer than the laser repetition period was found.

It is noted that frequency-resolved conductivity spectra can be obtained with this method, but are averaged over a small range of pump-probe delays because of the timing jitter. The E-OPTP technique is highly complementary to existing methods to measure photoconductance decays, such as TRMC and PCD, while the superior spatial resolution of the THz probe enables photoconductance mapping and studies of carrier diffusion.

Chapter 7

Conclusion

This thesis has reported optical measurements and analysis of the charge-carrier dynamics in semiconductor materials and structures that are used in photovoltaic cells. Observing the carrier dynamics in these materials and structures is crucial for understanding what properties are limiting the efficiency of photovoltaic cells, so that improvements in performance can be achieved more quickly through design, rather than trial and error. The time resolved optical measurements were complemented by mathematical modelling of the charge carrier dynamics, which helped to interpret the experimental measurements. As well as studying interfaces in the rapidly improving class of solar cells based on metal halide perovskites, this work presented an extension of the optical pump terahertz probe spectroscopy technique that allowed the charge-carrier dynamics of these materials and others, such as silicon, to be studied over greater time ranges. This chapter summarises the work in this thesis, highlighting the key results and conclusions, and finishes by proposing opportunities for extension of this work.

Chapter 1 summarised the theoretical operation of photovoltaic cells, highlighting that in perovskite solar cells, the charge transport layers (CTLs) on either side of the light absorbing perovskite layer, and specifically the interfaces between these layers, provide the asymmetry that generates a photovoltage and photocurrent in solar cells. It was explained that optimising the charge-carrier extraction selectivity of these interfaces, and minimising non-radiative recombination at the interfaces and in the bulk, are necessary to improve performance. Therefore, these processes must be studied and understood, which was the aim of this work. This chapter also summarised the properties of metal halide perovskites and different CTL materials, providing justification for the choice of materials studied in this work (specifically triple cation perovskite compositions, with spiro-OMeTAD, C_{60} and PCBM as the CTLs). This also provided the background necessary to interpret the measurements in later chapters.

Chapter 2 presented the capabilities of different time resolved spectroscopy techniques used in this work, and explained how charge carrier dynamics could be deduced from the measured signals.

Chapter 3 summarised the mathematical model that describes charge-carrier dynamics in semiconductors, and discussed the conditions for which this model can be solved analytically. Analytical solutions can be evaluated much more quickly than numerical solutions which allows the model to be iteratively fit to data in reasonable timescales. This was exploited in chapter 5. Analytical solutions also do not suffer from the discretisation errors that occur in numerical solutions, although to derive analytical solutions the model must be simplified, which means its applicability may be limited, which was discussed in chapter 5.

Chapter 4 presented the experimental measurements of the perovskite-CTL bilayers. The constituent layers were first measured by a range of static techniques to characterise their geometry and morphology, and their optical properties, all of which are crucial for analysing the time resolved optical measurements. The time resolved measurements presented in this chapter indicated that the decay of the carrier population in the perovskite layer is significantly accelerated by the addition of a PCBM or C_{60} layer. Since fullerenes have been shown to passivate surface defects [99, 101, 103] and improve the performance of devices, they are not expected to increase the defect density at the perovskite surface and are instead expected to extract electrons from the conduction band of the perovskite.

For the addition of a spiro-OMeTAD layer, the initial amplitude of the OPTP signal ($\Delta E/E$) was not reduced in comparison to the bare perovskite, except when the pump pulse was parasitically absorbed by the spiro-OMeTAD layer for 410nm excitation. This suggested that the spiro-OMeTAD layer did not cause any detectable extraction or recombination of carriers within the rise time of $\sim$ 1ps. Furthermore, any difference in the carrier dynamics compared to the bare perovskite sample is only evident after a pump-probe delay of several 10s of nanoseconds rather than 10s of picoseconds for fullerenes, showing that extraction or recombination of carriers is much slower than for fullerene layers. This has significant implications for the distribution of carries within the solar cell during steady state operation, as transport bottlenecks lead to carrier accumulation that may increase non-radiative recombination rates, and in perovskite cells may even induce degradation.

Chapter 5 presented the results of mathematical simulations of carrier dynamics that provided greater understanding of the carrier dynamics in perovskite-CTL bilayers that were measured by optical spectroscopy in the previous chapter. Two models of charge carrier dynamics were employed: one which included the Coulombic forces and can only be solved numerically; and another which considered ambipolar carrier densities and can be solved analytically. The numerical model was shown to accurately reproduce the analytical model for the case of ambipolar carrier densities. The numerical model showed that charge separation across the interface has the potential to leave a clear fingerprint on the decay dynamics, and the absence of this fingerprint is revealing. This showed that the persistent decay of the photoconductance (and ground state absorption bleach) observed for the fullerene bilayers in chapter 4 must be due to a process that reverses the charge separation. The possible processes include recombination of electrons in the fullerene with holes in the perovskite, or extraction of perovskite holes into the fullerene, which is thought to be likely due to the small energy barrier for hole extraction [104]. This scenario can be simulated with the analytical model and then iteratively fit to the data, which showed excellent agreement with the OPTP measurements of C_{60} bilayers. The difficulty in simulating the OPTP measurements for PCBM is consistent with a difference in the morphology of the two materials, highlighting the importance of this property.

Chapter 6 presented an improvement to OPTP, called electronically delayed OPTP

(E-OPTP), that allowed photoconductance dynamics to be measured over an unlimited time range rather than just the first few nanoseconds, whilst maintaining sub-nanosecond resolution. This temporal range is necessary to measure the full photoconductance decay of many semiconductors, and thus gain more complete information about carrier dynamics. The temporal performance of this technique was characterised, and an efficient method for measuring decays longer than the laser repetition period was presented, which allowed passivated silicon wafers to be studied. Measurements of silicon wafers showed a difference between the photoconductance decays measured by E-OPTP and by PCD. This difference was understood using analytical solutions of ambipolar charge-carrier diffusion, which showed that the E-OPTP signal was sensitive to in-plane diffusion in the wafer due to its higher spatial resolution. Therefore, E-OPTP is paticularly useful for spatial mapping of photoconductance and for studying carrier diffusion.

7.1 Future work

This work has demonstrated the capability of time-resolved optical spectroscopy to measure charge-carrier dynamics in semiconductor materials and heterostructures. In particular, transient absorption (TA) and optical pump terahertz probe (OPTP) have sufficient temporal resolution to observe processes at the perovskite-fullerene interfaces, but their temporal range is too limited to measure the full decay or observe processes at perovskite-spiro-OMeTAD interfaces. Therefore, future work could investigate these dynamics using the extended time range of the electronically delayed OPTP (E-OPTP) technique introduced in chapter 6. Measurements of bare perovskite layers were reported in chapter 6, but with the low power laser used in that work, the signal was very low and not practical for measuring perovskite-CTL bilayers. Since this work was performed, a laser with higher pulse energy has been installed and so this could be used to study perovskite-CTL bilayers. This would directly complement the TCSPC technique, which also has a sufficiently large time range to measure the full carrier density decay, but photoexcites lower charge carrier densities in the sample. Electronically delayed TA setups already exist, but E-OPTP measurements would benefit from simpler data interpretation, as described in this work.

Three of the most common CTL materials have been studied in this work, but bilayer samples using different CTLs could be investigated in future work using this combination of time-resolved optical measurements and mathematical modelling. It would also be interesting to extend the study of bilayers to samples with charge transport layers on both sides of the perovskite layer (trilayers), to see if the behaviours observed at the interfaces in bilayers can be used to understood the more complicated scenario of a trilayer.

The diffusion of carriers in silicon wafers shown in chapter 6 could be further investigated by varying the spatial profile of the photoexcitation (i.e. a smaller or wider photoexcitation area), or by displacing the photoexcited region and the region probed by the THz. This would allow more accurate measurements of the diffusion coefficients. Spatial mapping of the decay dynamics or in plane diffusion of carriers would be particularly useful for studying patterned wafers.

Appendix A

J-V Curve and Equivalent Circuit

A.1 J-V curve

How the current and voltage vary as the load is varied between zero and infinity is the $J-V$ curve (see Fig. A.1).

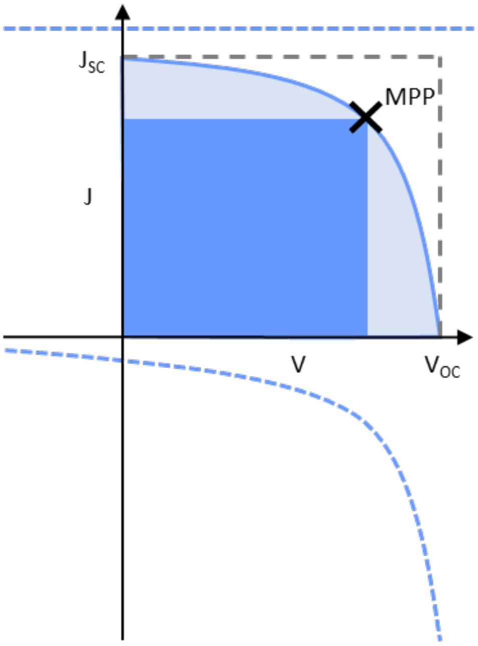

Figure A.1: The dashed blue lines represent the $J-V$ curve of an ideal current generator and a p-n diode respectively, which are superposed to give the $J-V$ curve of a solar cell (solid blue line). The current due to a forward bias applied to p-n diode is defined as a negative current for a solar cell. The blue shaded area is the value of the power output when operated at the maximum power point (MPP). The ratio of the total area under the curve (both blue and grey areas combined) to the total area of the dashed square, represents the fill factor.

At the limit of zero load i.e. short circuit, the voltage is zero (because no population accumulation) and the current is maximum (because minimal recombination). This maximum current is called J_{SC} and is determined only by the illumination intensity. At the limit of infinite load i.e. open circuit, there is no current flow (photogeneration and recombination balanced), but the population accumulation and thus photovoltage is a maximum, called V_{OC}. Therefore the J-V curve intersects the current axis (zero voltage) at J_{SC}, and intersects the voltage axis (zero current) at V_{OC}. Since these are the maximum values of J and V, the curve must fall within the square defined by these two limits. The maximum power that can be extracted is when the product JV is maximum and is called the maximum power point (MPP). The largest possible value of the MPP is at the corner of the square, with value $J_{SC}V_{OC}$, so a J-V curve which passes/lies closer to this corner will give higher MPP. The fill factor FF expresses the MPP as a percentage of the largest possible value. FF=100 occurs when the MPP is at $J = J_{SC}$,$V = V_{OC}$, and the J-V curve is a rectangle – in this case all electron hole pairs are extracted (i.e. no recombination occurs) until the load reaches infinity and blocks the current.

A.2 Equivalent Circuit

The photovoltage between the electrodes drives a current through the circuit, but also drives a current through the device in the opposite direction[39]. Therefore, the $J - V$ behaviour of the cell can be approximated as a superposition of the current that occurs under illumination with negligible load and thus negligible photovoltage, and a current in the opposite direction due to the emergence of a photovoltage when there is a finite load, which represents the recombination current within the device. This recombination current often has roughly exponential dependence on the photovoltage, because the rate of recombination is proportional to np, where n and p are exponentially dependent on the Quasi Fermi Levels (QFLs), so $np \propto e^{\frac{E_{F_n} - E_{F_p}}{k_B T}}$, where the difference in QFLs between the contacts is the photovoltage. Hence this recombination current has exponential dependence on voltage like for a p-n diode, even if the cell has no p-n junction. Therefore the behaviour of the cell is decomposed into a current generator and a diode. For a quantitative description, we use ideal components i.e. an ideal current generator and an ideal diode. Deviations from ideal diode behaviour can be included through a non-ideality factor and series and shunt resistances.

Appendix B

Shockley-Read-Hall Recombination Rate

The SRH rate can be derived as follows [29, 39]. For hole capture into a defect state, the rate is proportional to the density of occupied defect states, $N_T f_T$ (where $f_T = f(E_T)$ and E_T is the energy of the trap state), and the density of unoccupied VB states, p, with capture coefficient $C_p = v\sigma_p$

$$r^p_{cap} = C_p p N_T f_T$$

The rate of electron emission into the CB is proportional to the density of occupied traps $N_T f_T$ and the density of unoccupied states in the CB $N_C(1 - f(E_C)$, which is approximately constant so is absorbed into the coefficient E_n.

$$g^n_{emiss} = E_n N_T f_T$$

The rate of hole emission into the VB is proportional to the density of unoccupied traps and the density of occupied states in the VB $N_V f(E_V)$, which is approximately constant so is absorbed into the coefficient E_p.

$$g^p_{emiss} = E_p N_T (1 - f_T)$$

At steady state, $g^n_{emiss} = r^n_{cap}$, so

$$E_n = C_n n \frac{1 - f_T}{f_T} = C_n n e^{\frac{E_T - E_F}{k_B T}}$$

Since $n = N_c e^{-\frac{E_c - E_F}{k_B T}}$, then

$$E_n = C_n N_c^{-\frac{E_c - E_T}{k_B T}} = C_n n_T$$

where $n_T = N_c e^{-\frac{E_c - E_T}{k_B T}}$ is the electron density if $E_F = E_T$.

Similarly, $g^p_{emiss} = r^p_{cap}$, so

$$E_p = C_p p \frac{f_T}{1 - f_T} = C_p p e^{\frac{E_F - E_T}{k_B T}}$$

Since $p = N_V e^{-\frac{E_F - E_v}{k_B T}}$, then

$$E_p = C_p N_v^{-\frac{E_T - E_v}{k_B T}} = C_p p_T$$

where $p_T = N_v^{-\frac{E_T - E_v}{k_B T}}$ is the hole density if $E_F = E_T$.

The net capture rates are

$$r^n_{cap} - g^n_{emiss} = C_n N_T (n(1 - f_T) - n_T f_T)$$

$$r^p_{cap} - g^p_{emiss} = C_p N_T (p f_T - p_T (1 - f_T)$$

At steady state, the net capture rates are balanced which gives

$$f_T = \frac{C_n N_T n + C_p N_T p_T}{C_p N_T (p + p_T) + C_n N_T (n + n_T)}$$

Substituting this into $r^n_{cap} - g^n_{emiss}$ or $r^p_{cap} - g^p_{emiss}$ and noting $n_T p_T = n_i^2$ gives

$$r_{SRH} = r^n_{cap} - g^n_{emiss} = r^p_{cap} - g^p_{emiss} = \frac{(np - n_i^2)}{\frac{1}{N_T C_p}(n + n_T) + \frac{1}{N_T C_n}(p + p_T)}$$

where $\frac{1}{N_T C_p} = \tau^n_c$ and $\frac{1}{N_T C_n} = \tau^p_c$.

Appendix C

Equivalence of Methods for Calculating Sheet Density

The 2D sheet density is found by integrating the 3D solution over thickness. In the case that there is no surface recombination, the solution of the 2D diffusion equation is sufficient, and can be shown to be equivalent to the 3D solution integrated over thickness.

C.1 Integral Over Depth of the Solution to the 3D Diffusion Equation

In this work, the experiment measures a signal that is proportional to the integral over depth (z-dimension) of the carrier density. So the solution Eq. 3.29:

$$n(t,x,y,z) = \sum_{p=0}^{\infty} \cos(l_p x) \sum_{q=0}^{\infty} \cos(m_q y) \sum_{r=0}^{\infty} \cos(n_r z) e^{-t(l_p^2+m_q^2+n_r^2)D} c_{pqr}$$

becomes

$$n_{sh}(x,y,t) = \sum_{p=0}^{\infty} \cos(l_p x) \sum_{q=0}^{\infty} \cos(m_q y) e^{-t(l_p^2+m_q^2)D} L_z c_{pq0} \tag{C.1}$$

This is because the depth (z) integral $\int_0^{L_z} \cos(\frac{r\pi z}{L_z})dz = 0$ except for $r = 0$ which gives $= L_z$. So the summation over the depth dimension is replaced by a factor L_z.

In Eq C.1,

$$c_{pq0} = A \frac{2}{L_x} I_x(j) \frac{2}{L_y} I_y(k) \frac{1}{L_z} I_z(0) \tag{C.2}$$

where $I_z(0) = \int_0^{L_z} \cos(0) e^{-\alpha z} dz = \frac{1-e^{-\alpha L_z}}{\alpha}$ which cancels $\frac{\alpha}{1-e^{-\alpha L_z}}$ inside A (the amplitude of the initial distribution).

So in Eq.C.1,

$$L_z c_{pq0} = \frac{N_T}{w\sqrt{2\pi}\sigma erf(\frac{L_x}{2\sqrt{2}\sigma})} . \frac{2}{L_x} I_x(j) \frac{2}{L_y} I_y(k)$$

C.2 2D Diffusion Equation

This 2D sheet density can also be derived by considering the 2D diffusion equation.

$$n(x,y,t) = \sum_{p=0}^{\infty} \cos(l_p x) \sum_{q=0}^{\infty} \cos(m_q y) e^{-t(l_p^2+m_q^2)D} c_{pq}$$

$$c_{pq} = A_{sh} \frac{2}{L_x} I_x(j) \frac{2}{L_y} I_y(k) \tag{C.3}$$

In this case the product solution is for 2 dimensions only, and the initial distribution is a sheet density with amplitude A_{sh} such that the integral over area gives the total absorbed number, N_T. The factor c_{pq} takes the place of the factor $= L_z c_{pq0}$ in the previous derivation, Eq. C.1

A_{sh} is derived:

$$\begin{aligned} N_T &= \int_0^{L_x} \int_0^{L_y} n(x,y,z,0) dx dy \\ &= A_{sh} \int_0^{L_x} e^{-\frac{(x-x_0)^2}{2\sigma^2}} dx \int_{\frac{L_y}{2}-\frac{w}{2}}^{\frac{L_y}{2}+\frac{w}{2}} dy \\ &= A_{sh} \sqrt{\frac{\pi}{2}} \sigma (\mathrm{erf}(\frac{x_0}{\sqrt{2}\sigma}) - \mathrm{erf}(\frac{x_0 - L_x}{\sqrt{2}\sigma})).w \end{aligned}$$

For $x_0 = \frac{L_x}{2}$, the erfs simplify to $2\mathrm{erf}(\frac{L_x}{2\sqrt{2}\sigma})$. So:

$$A_{sh} = \frac{N_T}{w\sqrt{2\pi}\sigma \mathrm{erf}(\frac{L_x}{2\sqrt{2}\sigma})} \tag{C.4}$$

Therefore, Eq.C.3 is

$$c_{pq} = \frac{N_T}{w\sqrt{2\pi}\sigma \mathrm{erf}(\frac{L_x}{2\sqrt{2}\sigma})} . \frac{2}{L_x} I_x(j) \frac{2}{L_y} I_y(k)$$

which $= L_z c_{pq0}$ from Eq C.1 as required.

Bibliography

1. Gibon, T., Hertwich, E. G., Arvesen, A., Singh, B. & Verones, F. Health benefits, ecological threats of low-carbon electricity. *Environmental Research Letters* **12,** 034023. ISSN: 17489326 (Mar. 2017).
2. Green, M. A. Photovoltaic technology and visions for the future. *Progress in Energy* **1,** 13001. ISSN: 25161083 (2019).
3. Creutzig, F. *et al.* The underestimated potential of solar energy to mitigate climate change. *Nature Energy* **2,** 1–9. ISSN: 20587546. arXiv: `1710.05957` (Aug. 2017).
4. Green, M. A. Commercial progress and challenges for photovoltaics. *Nature Energy* **1,** 1–4. ISSN: 20587546 (Jan. 2016).
5. Kost, C. *et al. Levelized Cost of Electricity Renewable Energy Technologies, June 2021* (Fraunhofer ISE, June 2021).
6. Lazard. *Lazard's Levelized Cost of Energy Analysis—Version 15.0* (Lazard, Oct. 2021).
7. International Renewable Energy Agency (IRENA). *Renewable Power Generation Costs in 2021 - Executive Summary* (International Renewable Energy Agency, 2021).
8. National Renewable Energy Laboratory. *Interactive Best Research-Cell Efficiency Chart* (National Renewable Energy Laboratory (NREL), Jan. 2023).
9. Lee, B., Fan, D. & Forrest, S. R. A high throughput, linear molecular beam epitaxy system for reduced cost manufacturing of GaAs photovoltaic cells: Will GaAs ever be inexpensive enough? *Sustainable Energy and Fuels* **4,** 2035–2042. ISSN: 23984902 (Mar. 2020).
10. Woodhouse, M. *et al. On the Path to SunShot. The Role of Advancements in Solar Photovoltaic Efficiency, Reliability, and Costs* ISBN: NREL/TP-6A20-65800 (National Renewable Energy Laboratory (NREL), Golden, CO, May 2016).
11. Kavlak, G., McNerney, J. & Trancik, J. E. Evaluating the Changing Causes of Photovoltaics Cost Reduction. *SSRN Electronic Journal* (Aug. 2017).
12. Kojima, A., Teshima, K., Shirai, Y. & Miyasaka, T. Organometal halide perovskites as visible-light sensitizers for photovoltaic cells. *Journal of the American Chemical Society* **131,** 6050–6051. ISSN: 00027863 (May 2009).
13. Boyd, C. C., Cheacharoen, R., Leijtens, T. & McGehee, M. D. Understanding Degradation Mechanisms and Improving Stability of Perovskite Photovoltaics. *Chemical Reviews* **119,** 3418–3451. ISSN: 15206890 (2019).
14. Kirchartz, T. & Rau, U. What Makes a Good Solar Cell? *Advanced Energy Materials* **8,** 1703385. ISSN: 16146840 (Oct. 2018).

15. Vidal, R., Alberola-Borràs, J.-A., Sánchez-Pantoja, N. & Mora-Seró, I. Comparison of Perovskite Solar Cells with other Photovoltaics Technologies from the Point of View of Life Cycle Assessment. *Advanced Energy and Sustainability Research* **2,** 2000088. ISSN: 2699-9412 (May 2021).
16. De Wolf, S. *et al.* Organometallic halide perovskites: Sharp optical absorption edge and its relation to photovoltaic performance. *Journal of Physical Chemistry Letters* **5,** 1035–1039. ISSN: 19487185 (Mar. 2014).
17. Davies, C. L. *et al.* Bimolecular recombination in methylammonium lead triiodide perovskite is an inverse absorption process. *Nature Communications* **9.** ISSN: 20411723 (2018).
18. Baranowski, M. & Plochocka, P. Excitons in Metal-Halide Perovskites. *Advanced Energy Materials* **10,** 1903659. ISSN: 16146840 (Feb. 2020).
19. Stranks, S. D. *et al.* Electron-hole diffusion lengths exceeding 1 micrometer in an organometal trihalide perovskite absorber. *Science* **342,** 341–344. ISSN: 10959203 (Oct. 2013).
20. Shockley, W. & Queisser, H. J. Detailed balance limit of efficiency of p-n junction solar cells. *Journal of Applied Physics* **32,** 510–519. ISSN: 00218979 (1961).
21. Guillemoles, J. F., Kirchartz, T., Cahen, D. & Rau, U. Guide for the perplexed to the Shockley–Queisser model for solar cells. *Nature Photonics* **13,** 501–505. ISSN: 17494893 (July 2019).
22. De Haas, M. P. & Warman, J. M. Photon-induced molecular charge separation studied by nanosecond time-resolved microwave conductivity. *Chemical Physics* **73,** 35–53. ISSN: 03010104 (Dec. 1982).
23. Kunst, M. & Beck, G. The study of charge carrier kinetics in semiconductors by microwave conductivity measurements. *Journal of Applied Physics* **60,** 3558–3566. ISSN: 00218979 (June 1986).
24. Kunst, M. & Beck, G. The study of charge carrier kinetics in semiconductors by microwave conductivity measurements. II. *Journal of Applied Physics* **63,** 1093–1098. ISSN: 00218979 (Aug. 1988).
25. Savenije, T. J., Ferguson, A. J., Kopidakis, N. & Rumbles, G. Revealing the dynamics of charge carriers in polymer:fullerene blends using photoinduced time-resolved microwave conductivity. *Journal of Physical Chemistry C* **117,** 24085–24103. ISSN: 19327447 (Nov. 2013).
26. Yablonovitch, E. & Gmitter, T. J. A contactless minority lifetime probe of heterostructures, surfaces, interfaces and bulk wafers. *Solid State Electronics* **35,** 261–267. ISSN: 00381101 (Mar. 1992).
27. Sinton, R. A. & Cuevas, A. Contactless determination of current-voltage characteristics and minority-carrier lifetimes in semiconductors from quasi-steady-state photoconductance data. *Applied Physics Letters* **69,** 2510–2512. ISSN: 00036951 (1996).
28. Ahrenkiel, R. K. & Johnston, S. Contactless measurement of recombination lifetime in photovoltaic materials. *Solar Energy Materials and Solar Cells* **55,** 59–73. ISSN: 09270248 (July 1998).
29. McKelvey, J. P. *Solid state and semiconductor physics* (Harper & Row, New York, Jan. 1966).

30. Even, J., Pedesseau, L. & Katan, C. Analysis of multivalley and multibandgap absorption and enhancement of free carriers related to exciton screening in hybrid perovskites. *Journal of Physical Chemistry C* **118,** 11566–11572. ISSN: 19327455 (June 2014).

31. Leguy, A. M. *et al.* Experimental and theoretical optical properties of methylammonium lead halide perovskites. *Nanoscale* **8,** 6317–6327. ISSN: 2040-3372 (Mar. 2016).

32. Würfel, P. & Würfel, U. *Physics of solar cells: from basic principles to advanced concepts* 2nd. English. ISBN: 978-3-527-40857-3 (Wiley-VCH, Weinheim, 2009).

33. Chen, L.-Q. *Thermodynamic Equilibrium and Stability of Materials* ISBN: 9789811386916 (Springer Singapore, 2022).

34. Wurfel, P. The chemical potential of radiation. *Journal of Physics C: Solid State Physics* **15,** 3967–3985. ISSN: 00223719 (1982).

35. Wurfel, U., Cuevas, A. & Wurfel, P. Charge carrier separation in solar cells. *IEEE Journal of Photovoltaics* **5,** 461–469. ISSN: 21563381 (Jan. 2015).

36. Green, M. A. Photovoltaic principles. *Physica E: Low-Dimensional Systems and Nanostructures* **14,** 11–17. ISSN: 13869477 (Apr. 2002).

37. Lipovšek, B., Smole, F., Topič, M., Humar, I. & Sinigoj, A. R. Driving forces and charge-carrier separation in p-n junction solar cells. *AIP Advances* **9,** 055026. ISSN: 21583226 (May 2019).

38. Hara, K. O. & Usami, N. Theory of open-circuit voltage and the driving force of charge separation in pn-junction solar cells. *Journal of Applied Physics* **114,** 153101. ISSN: 00218979 (2013).

39. Nelson, J. *The Physics of Solar Cells* ISBN: 9781860943409 (Imperial College Press, London, May 2003).

40. Sze, S. & Ng, K. K. *Physics of Semiconductor Devices* 3rd. ISBN: 9780470068328 (John Wiley & Sons, Inc., Oct. 2006).

41. König, D. *et al.* Non-equilibrium dynamics, materials and structures for hot carrier solar cells: a detailed review. *Semiconductor Science and Technology* **35,** 073002. ISSN: 0268-1242 (June 2020).

42. Wells, H. L. Über die Cäsium- und Kalium-Bleihalogenide. *Zeitschrift für anorganische Chemie* **3,** 195–210. ISSN: 1521-3749 (Jan. 1893).

43. Weber, D. CH3NH3PbX3, ein Pb(II)-System mit kubischer Perowskitstruktur / CH3NH3PbX3, a Pb(II)-System with Cubic Perovskite Structure. *Zeitschrift fur Naturforschung - Section B Journal of Chemical Sciences* **33,** 1443–1445. ISSN: 18657117 (Dec. 1978).

44. Mitzi, D. B. in *Progress in Inorganic Chemistry* (ed Karlin, K. D.) 1–121 (John Wiley & Sons, Inc., Jan. 1999). ISBN: 9780470166499.

45. Mitzi, D. B., Chondroudis, K. & Kagan, C. R. Organic-inorganic electronics. *IBM Journal of Research and Development* **45,** 29–45. ISSN: 00188646 (2001).

46. Jena, A. K., Kulkarni, A. & Miyasaka, T. Halide Perovskite Photovoltaics: Background, Status, and Future Prospects. *Chemical Reviews* **119,** 3036–3103. ISSN: 15206890 (Mar. 2019).

47. Miyasaka, T. Perovskite photovoltaics: Rare functions of organo lead halide in solar cells and optoelectronic devices. *Chemistry Letters* **44,** 720–729. ISSN: 13480715 (2015).
48. Kojima, A., Teshima, K., Miyasaka, T. & Shirai, Y. Novel Photoelectrochemical Cell with Mesoscopic Electrodes Sensitized by Lead-Halide Compounds (2). *ECS Meeting Abstracts* **MA2006-02,** 397. ISSN: 2151-2043 (June 2006).
49. Kojima, A., Teshima, K., Shirai, Y. & Miyasaka, T. Novel Photoelectrochemical Cell with Mesoscopic Electrodes Sensitized by Lead-halide Compounds (5). *ECS Meeting Abstracts* **MA2007-02,** 352. ISSN: 2151-2043 (Sept. 2007).
50. Im, J. H., Lee, C. R., Lee, J. W., Park, S. W. & Park, N. G. 6.5% efficient perovskite quantum-dot-sensitized solar cell. *Nanoscale* **3,** 4088–4093. ISSN: 2040-3372 (Oct. 2011).
51. Kojima, A., Teshima, K., Shirai, Y. & Miyasaka, T. Novel Photoelectrochemical Cell with Mesoscopic Electrodes Sensitized by Lead-halide Compounds (11). *ECS Meeting Abstracts* **MA2008-02,** 27. ISSN: 2151-2043 (Aug. 2008).
52. Lee, M. M., Teuscher, J., Miyasaka, T., Murakami, T. N. & Snaith, H. J. Efficient hybrid solar cells based on meso-superstructured organometal halide perovskites. *Science* **338,** 643–647. ISSN: 10959203 (Nov. 2012).
53. Ball, J. M., Lee, M. M., Hey, A. & Snaith, H. J. Low-temperature processed meso-superstructured to thin-film perovskite solar cells. *Energy & Environmental Science* **6,** 1739–1743. ISSN: 1754-5706 (May 2013).
54. Liu, M., Johnston, M. B. & Snaith, H. J. Efficient planar heterojunction perovskite solar cells by vapour deposition. *Nature* **501,** 395–398. ISSN: 00280836. arXiv: `arXiv:1011.1669v3` (2013).
55. Dänekamp, B. *et al.* Perovskite-Perovskite Homojunctions via Compositional Doping. *Journal of Physical Chemistry Letters* **9,** 2770–2775. ISSN: 19487185 (June 2018).
56. Cui, P. *et al.* Planar p–n homojunction perovskite solar cells with efficiency exceeding 21.3%. *Nature Energy* **4,** 150–159. ISSN: 20587546 (Feb. 2019).
57. Kirchartz, T. & Cahen, D. Minimum doping densities for p–n junctions. *Nature Energy* **5,** 973–975. ISSN: 20587546 (Oct. 2020).
58. Calado, P. & Barnes, P. R. Ionic screening in perovskite p–n homojunctions. *Nature Energy* **6,** 589–591. ISSN: 20587546 (May 2021).
59. Euvrard, J., Yan, Y. & Mitzi, D. B. *Electrical doping in halide perovskites* Mar. 2021.
60. Abdelhady, A. L. *et al.* Heterovalent Dopant Incorporation for Bandgap and Type Engineering of Perovskite Crystals. *Journal of Physical Chemistry Letters* **7,** 295–301. ISSN: 19487185 (Jan. 2016).
61. Nayak, P. K. *et al.* Impact of Bi3+ Heterovalent Doping in Organic-Inorganic Metal Halide Perovskite Crystals. *Journal of the American Chemical Society* **140,** 574–577. ISSN: 15205126 (Jan. 2018).
62. Pérez-del-Rey, D. *et al.* Strontium Insertion in Methylammonium Lead Iodide: Long Charge Carrier Lifetime and High Fill-Factor Solar Cells. *Advanced Materials* **28,** 9839–9845. ISSN: 1521-4095 (Nov. 2016).

63. Mosconi, E., Merabet, B., Meggiolaro, D., Zaoui, A. & De Angelis, F. First-Principles Modeling of Bismuth Doping in the MAPbI3 Perovskite. *Journal of Physical Chemistry C* **122,** 14107–14112. ISSN: 19327455 (June 2018).

64. Juarez-Perez, E. J. *et al.* Role of the selective contacts in the performance of lead halide perovskite solar cells. *Journal of Physical Chemistry Letters* **5,** 680–685. ISSN: 19487185 (Feb. 2014).

65. Zhang, Y. *et al.* Charge selective contacts, mobile ions and anomalous hysteresis in organic–inorganic perovskite solar cells. *Materials Horizons* **2,** 315–322. ISSN: 2051-6355 (Apr. 2015).

66. Kim, G. W. *et al.* Hole Transport Materials in Conventional Structural (n–i–p) Perovskite Solar Cells: From Past to the Future. *Advanced Energy Materials* **10,** 1903403. ISSN: 16146840 (Feb. 2020).

67. Peña-Camargo, F. *et al.* Revealing the doping density in perovskite solar cells and its impact on device performance. *Applied Physics Reviews* **9.** ISSN: 19319401. arXiv: `2201.09664` (2022).

68. Wojciechowski, K. *et al.* C60 as an efficient n-type compact layer in perovskite solar cells. *Journal of Physical Chemistry Letters* **6,** 2399–2405. ISSN: 19487185 (June 2015).

69. Rueda-Delgado, D. *et al.* Solution-processed and evaporated C60 interlayers for improved charge transport in perovskite photovoltaics. *Organic Electronics* **77,** 105526. ISSN: 15661199 (Feb. 2020).

70. Lee, K. M. *et al.* Thickness effects of thermally evaporated C60 thin films on regular-type CH3NH3PbI3 based solar cells. *Solar Energy Materials and Solar Cells* **164,** 13–18. ISSN: 09270248 (May 2017).

71. Mohamad Noh, M. F. *et al.* The architecture of the electron transport layer for a perovskite solar cell. *Journal of Materials Chemistry C* **6,** 682–712. ISSN: 20507526 (2018).

72. Jiang, Q., Zhang, X. & You, J. SnO2: A Wonderful Electron Transport Layer for Perovskite Solar Cells. *Small* **14.** ISSN: 16136829 (Aug. 2018).

73. Bach, U. *et al.* Solid-state dye-sensitized mesoporous TiO2 solar cells with high photon-to-electron conversion efficiencies. *Nature* **395,** 583–585. ISSN: 00280836 (Oct. 1998).

74. Docampo, P. *et al.* Lessons learned: From dye-sensitized solar cells to all-solid-state hybrid devices. *Advanced Materials* **26,** 4013–4030. ISSN: 15214095 (June 2014).

75. Hawash, Z., Ono, L. K. & Qi, Y. Recent Advances in Spiro-MeOTAD Hole Transport Material and Its Applications in Organic–Inorganic Halide Perovskite Solar Cells. *Advanced Materials Interfaces* **5.** ISSN: 21967350 (Jan. 2018).

76. Calió, L., Kazim, S., Grätzel, M. & Ahmad, S. Hole-Transport Materials for Perovskite Solar Cells. *Angewandte Chemie - International Edition* **55,** 14522–14545. ISSN: 15213773 (Nov. 2016).

77. Saragi, T. P., Spehr, T., Siebert, A., Fuhrmann-Lieker, T. & Salbeck, J. Spiro compounds for organic optoelectronics. *Chemical Reviews* **107,** 1011–1065. ISSN: 00092665 (Apr. 2007).

78. Abate, A. *et al.* Lithium salts as "redox active" p-type dopants for organic semiconductors and their impact in solid-state dye-sensitized solar cells. *Physical Chemistry Chemical Physics* **15,** 2572–2579. ISSN: 1463-9084 (Jan. 2013).
79. Hawash, Z., Ono, L. K. & Qi, Y. Moisture and Oxygen Enhance Conductivity of LiTFSI-Doped Spiro-MeOTAD Hole Transport Layer in Perovskite Solar Cells. *Advanced Materials Interfaces* **3.** ISSN: 21967350 (July 2016).
80. Krüger, J. *et al.* High efficiency solid-state photovoltaic device due to inhibition of interface charge recombination. *Applied Physics Letters* **79,** 2085. ISSN: 0003-6951 (Sept. 2001).
81. Boschloo, G., Häggman, L. & Hagfeldt, A. Quantification of the effect of 4-tert-butylpyridine addition to I -/I3- redox electrolytes in dye-sensitized nanostructured TiO2 solar cells. *Journal of Physical Chemistry B* **110,** 13144–13150. ISSN: 15206106 (July 2006).
82. Wang, S. *et al.* Role of 4-tert-Butylpyridine as a Hole Transport Layer Morphological Controller in Perovskite Solar Cells. *Nano Letters* **16,** 5594–5600. ISSN: 15306992 (Sept. 2016).
83. Habisreutinger, S. N., Noel, N. K., Snaith, H. J. & Nicholas, R. J. Investigating the Role of 4-Tert Butylpyridine in Perovskite Solar Cells. *Advanced Energy Materials* **7.** ISSN: 16146840 (Jan. 2017).
84. Kim, G. W., Kang, G., Malekshahi Byranvand, M., Lee, G. Y. & Park, T. Gradated Mixed Hole Transport Layer in a Perovskite Solar Cell: Improving Moisture Stability and Efficiency. *ACS Applied Materials and Interfaces* **9,** 27720–27726. ISSN: 19448252 (Aug. 2017).
85. Hawash, Z., Ono, L. K., Raga, S. R., Lee, M. V. & Qi, Y. Air-exposure induced dopant redistribution and energy level shifts in spin-coated Spiro-Meotad films. *Chemistry of Materials* **27,** 562–569. ISSN: 15205002 (Jan. 2015).
86. Ono, L. K. *et al.* Pinhole-free hole transport layers significantly improve the stability of MAPbI3-based perovskite solar cells under operating conditions. *Journal of Materials Chemistry A* **3,** 15451–15456. ISSN: 2050-7496 (July 2015).
87. Li, W. *et al.* Montmorillonite as bifunctional buffer layer material for hybrid perovskite solar cells with protection from corrosion and retarding recombination. *Journal of Materials Chemistry A* **2,** 13587–13592. ISSN: 2050-7496 (July 2014).
88. Malinauskas, T. *et al.* Enhancing thermal stability and lifetime of solid-state dye-sensitized solar cells via molecular engineering of the hole-transporting material spiro-OMeTAD. *ACS Applied Materials and Interfaces* **7,** 11107–11116. ISSN: 19448252 (June 2015).
89. Burschka, J. *et al.* Tris(2-(1 H -pyrazol-1-yl)pyridine)cobalt(III) as p-type dopant for organic semiconductors and its application in highly efficient solid-state dye-sensitized solar cells. *Journal of the American Chemical Society* **133,** 18042–18045. ISSN: 00027863 (Nov. 2011).
90. Noh, J. H. *et al.* Nanostructured TiO2/CH3NH3PbI3 heterojunction solar cells employing spiro-OMeTAD/Co-complex as hole-transporting material. *Journal of Materials Chemistry A* **1,** 11842–11847. ISSN: 2050-7496 (Sept. 2013).

91. Dang, M. T., Hirsch, L. & Wantz, G. P3HT:PCBM, best seller in polymer photovoltaic research. *Advanced Materials* **23,** 3597–3602. ISSN: 09359648 (Aug. 2011).
92. Hummelen, J. C. *et al.* Preparation and Characterization of Fulleroid and Methanofullerene Derivatives. *Journal of Organic Chemistry* **60,** 532–538. ISSN: 15206904 (1995).
93. Troshin, P. A. *et al.* Material Solubility-Photovoltaic Performance Relationship in the Design of Novel Fullerene Derivatives for Bulk Heterojunction Solar Cells. *Advanced Functional Materials* **19,** 779–788. ISSN: 1616-3028 (Mar. 2009).
94. Larson, B. W. *et al.* Thermal [6,6] → [6,6] isomerization and decomposition of PCBM (phenyl-C61-butyric acid methyl ester). *Chemistry of Materials* **26,** 2361–2367. ISSN: 15205002 (Apr. 2014).
95. Tao, C. *et al.* 17.6% stabilized efficiency in low-temperature processed planar perovskite solar cells. *Energy & Environmental Science* **8,** 2365–2370. ISSN: 1754-5706 (July 2015).
96. Kegelmann, L. *et al.* It Takes Two to Tango - Double-Layer Selective Contacts in Perovskite Solar Cells for Improved Device Performance and Reduced Hysteresis. *ACS Applied Materials and Interfaces* **9,** 17245–17255. ISSN: 19448252 (May 2017).
97. Ke, W. *et al.* Cooperative tin oxide fullerene electron selective layers for high-performance planar perovskite solar cells. *Journal of Materials Chemistry A* **4,** 14276–14283. ISSN: 2050-7496 (Sept. 2016).
98. Ryu, S. *et al.* Fabrication of metal-oxide-free CH3NH3PbI3 perovskite solar cells processed at low temperature. *Journal of Materials Chemistry A* **3,** 3271–3275. ISSN: 2050-7496 (Feb. 2015).
99. Shao, Y., Xiao, Z., Bi, C., Yuan, Y. & Huang, J. Origin and elimination of photocurrent hysteresis by fullerene passivation in CH3NH3PbI3 planar heterojunction solar cells. *Nature Communications* **5,** 1–7. ISSN: 20411723 (Dec. 2014).
100. Shao, Y. *et al.* Grain boundary dominated ion migration in polycrystalline organic–inorganic halide perovskite films. *Energy & Environmental Science* **9,** 1752–1759. ISSN: 1754-5706 (May 2016).
101. Xu, J. *et al.* Perovskite-fullerene hybrid materials suppress hysteresis in planar diodes. *Nature Communications* **6,** 1–8. ISSN: 20411723 (May 2015).
102. Tajima, Y. *et al.* Surface free energy and wettability determination of various fullerene derivative films on amorphous carbon wafer. *Japanese Journal of Applied Physics* **47,** 5730–5733. ISSN: 00214922 (2008).
103. Shao, Y., Yuan, Y. & Huang, J. Correlation of energy disorder and open-circuit voltage in hybrid perovskite solar cells. *Nature Energy* **1,** 1–6. ISSN: 20587546 (Jan. 2016).
104. Schulz, P. *et al.* Electronic Level Alignment in Inverted Organometal Perovskite Solar Cells. *Advanced Materials Interfaces* **2,** 1400532. ISSN: 2196-7350 (May 2015).
105. Chen, C. *et al.* Effect of BCP buffer layer on eliminating charge accumulation for high performance of inverted perovskite solar cells. *RSC Advances* **7,** 35819–35826. ISSN: 2046-2069 (July 2017).

106. Schulz, P. *et al.* Interface energetics in organo-metal halide perovskite-based photovoltaic cells. *Energy and Environmental Science* **7,** 1377–1381. ISSN: 17545706 (2014).

107. Hellmann, T. *et al.* The Electronic Structure of MAPI-Based Perovskite Solar Cells: Detailed Band Diagram Determination by Photoemission Spectroscopy Comparing Classical and Inverted Device Stacks. *Advanced Energy Materials* **10,** 2002129. ISSN: 16146840 (Nov. 2020).

108. Wussler, M. *et al.* Tapered Cross-Section Photoelectron Spectroscopy of State-of-the-Art Mixed Ion Perovskite Solar Cells: Band Bending Profile in the Dark, Photopotential Profile Under Open Circuit Illumination, and Band Diagram. *Advanced Functional Materials* **30,** 1910679. ISSN: 16163028 (July 2020).

109. Byeon, J. *et al.* Charge Transport Layer-Dependent Electronic Band Bending in Perovskite Solar Cells and Its Correlation to Light-Induced Device Degradation. *ACS Energy Letters* **5,** 2580–2589. ISSN: 23808195 (Aug. 2020).

110. Edri, E. *et al.* Elucidating the charge carrier separation and working mechanism of CH 3 NH 3 PbI 3-x Cl x perovskite solar cells. *Nature Communications* **5,** 1–8. ISSN: 20411723 (Mar. 2014).

111. Hermes, I. M., Hou, Y., Bergmann, V. W., Brabec, C. J. & Weber, S. A. The Interplay of Contact Layers: How the Electron Transport Layer Influences Interfacial Recombination and Hole Extraction in Perovskite Solar Cells. *Journal of Physical Chemistry Letters* **9,** 6249–6256. ISSN: 19487185 (Nov. 2018).

112. Bergmann, V. W. *et al.* Real-space observation of unbalanced charge distribution inside a perovskite-sensitized solar cell. *Nature Communications* **5,** 1–9. ISSN: 20411723 (Sept. 2014).

113. Bergmann, V. W. *et al.* Local Time-Dependent Charging in a Perovskite Solar Cell. *ACS Applied Materials and Interfaces* **8,** 19402–19409. ISSN: 19448252 (Aug. 2016).

114. Cai, M. *et al.* Control of Electrical Potential Distribution for High-Performance Perovskite Solar Cells. *Joule* **2,** 296–306. ISSN: 2542-4351 (Feb. 2018).

115. Jiang, C. S. *et al.* Carrier separation and transport in perovskite solar cells studied by nanometre-scale profiling of electrical potential. *Nature Communications* **6,** 1–10. ISSN: 20411723 (Sept. 2015).

116. Weber, S. A. *et al.* How the formation of interfacial charge causes hysteresis in perovskite solar cells. *Energy & Environmental Science* **11,** 2404–2413. ISSN: 1754-5706 (Sept. 2018).

117. Garrett, J. L. *et al.* Real-Time Nanoscale Open-Circuit Voltage Dynamics of Perovskite Solar Cells. *Nano Letters* **17,** 2554–2560. ISSN: 15306992 (Apr. 2017).

118. Saparov, B. & Mitzi, D. B. Organic-Inorganic Perovskites: Structural Versatility for Functional Materials Design. *Chemical Reviews* **116,** 4558–4596. ISSN: 15206890 (Apr. 2016).

119. Filip, M. R. & Giustino, F. The geometric blueprint of perovskites. *Proceedings of the National Academy of Sciences of the United States of America* **115,** 5397–5402. ISSN: 10916490. arXiv: `1805.08250` (May 2018).

120. Whitfield, P. S. *et al.* Structures, Phase Transitions and Tricritical Behavior of the Hybrid Perovskite Methyl Ammonium Lead Iodide. *Scientific Reports* **6.** ISSN: 20452322 (2016).
121. Stoumpos, C. C., Malliakas, C. D. & Kanatzidis, M. G. Semiconducting tin and lead iodide perovskites with organic cations: Phase transitions, high mobilities, and near-infrared photoluminescent properties. *Inorganic Chemistry* **52,** 9019–9038. ISSN: 00201669 (Aug. 2013).
122. Eames, C. *et al.* Ionic transport in hybrid lead iodide perovskite solar cells. *Nature Communications* **6,** 1–8. ISSN: 20411723 (June 2015).
123. Goldschmidt, V. M. Die Gesetze der Krystallochemie. *Die Naturwissenschaften* **14,** 477–485. ISSN: 00281042 (May 1926).
124. Megaw, H. D. & Barber, J. *Crystal structures: a working approach* English. ISBN: 9780721662602 (Saunders, Philadelphia, 1973).
125. Li, Z. *et al.* Stabilizing Perovskite Structures by Tuning Tolerance Factor: Formation of Formamidinium and Cesium Lead Iodide Solid-State Alloys. *Chemistry of Materials* **28,** 284–292. ISSN: 15205002 (2016).
126. Eperon, G. E. *et al.* Inorganic caesium lead iodide perovskite solar cells. *Journal of Materials Chemistry A* **3,** 19688–19695. ISSN: 2050-7496 (Sept. 2015).
127. Eperon, G. E., Hörantner, M. T. & Snaith, H. J. Metal halide perovskite tandem and multiple-junction photovoltaics. *Nature Reviews Chemistry* **1,** 95. ISSN: 23973358 (Nov. 2017).
128. Wang, R. *et al.* Prospects for metal halide perovskite-based tandem solar cells. *Nature Photonics* **15,** 411–425. ISSN: 17494893 (May 2021).
129. Koh, T. M. *et al.* Formamidinium-containing metal-halide: An alternative material for near-IR absorption perovskite solar cells. *Journal of Physical Chemistry C* **118,** 16458–16462. ISSN: 19327455 (July 2014).
130. Lee, J. W., Seol, D. J., Cho, A. N. & Park, N. G. High-Efficiency Perovskite Solar Cells Based on the Black Polymorph of HC(NH2)2PbI3. *Advanced Materials* **26,** 4991–4998. ISSN: 1521-4095 (Aug. 2014).
131. Eperon, G. E. *et al.* Formamidinium lead trihalide: A broadly tunable perovskite for efficient planar heterojunction solar cells. *Energy and Environmental Science* **7,** 982–988. ISSN: 17545692 (2014).
132. Conings, B. *et al.* Intrinsic Thermal Instability of Methylammonium Lead Trihalide Perovskite. *Advanced Energy Materials* **5,** 1500477. ISSN: 16146840 (June 2015).
133. Binek, A., Hanusch, F. C., Docampo, P. & Bein, T. Stabilization of the trigonal high-temperature phase of formamidinium lead iodide. *Journal of Physical Chemistry Letters* **6,** 1249–1253. ISSN: 19487185 (Apr. 2015).
134. Lee, J. W. *et al.* Formamidinium and Cesium Hybridization for Photo- and Moisture-Stable Perovskite Solar Cell. *Advanced Energy Materials* **5,** 1501310. ISSN: 1614-6840 (Oct. 2015).
135. Yi, C. *et al.* Entropic stabilization of mixed A-cation ABX3 metal halide perovskites for high performance perovskite solar cells. *Energy & Environmental Science* **9,** 656–662. ISSN: 1754-5706 (Feb. 2016).

136. Saliba, M. *et al.* Cesium-containing triple cation perovskite solar cells: Improved stability, reproducibility and high efficiency. *Energy and Environmental Science* **9,** 1989–1997. ISSN: 17545706 (June 2016).

137. Kubicki, D. J. *et al.* Phase Segregation in Cs-, Rb- and K-Doped Mixed-Cation (MA)x(FA)1-xPbI3 Hybrid Perovskites from Solid-State NMR. *Journal of the American Chemical Society* **139,** 14173–14180. ISSN: 15205126 (Oct. 2017).

138. Møller, C. K. Crystal structure and photoconductivity of cæsium plumbohalides. *Nature* **182,** 1436. ISSN: 00280836 (1958).

139. Vaynzof, Y. The Future of Perovskite Photovoltaics—Thermal Evaporation or Solution Processing? *Advanced Energy Materials* **10,** 2003073. ISSN: 16146840 (Dec. 2020).

140. Chen, Q. *et al.* Planar heterojunction perovskite solar cells via vapor-assisted solution process. *Journal of the American Chemical Society* **136,** 622–625. ISSN: 00027863 (2014).

141. Park, N. G. & Zhu, K. Scalable fabrication and coating methods for perovskite solar cells and solar modules. *Nature Reviews Materials* **5,** 333–350. ISSN: 20588437 (Feb. 2020).

142. Jeon, N. J. *et al.* Solvent engineering for high-performance inorganic–organic hybrid perovskite solar cells. *Nature Materials* **13,** 897–903. ISSN: 1476-4660 (July 2014).

143. Jung, M., Ji, S. G., Kim, G. & Seok, S. I. Perovskite precursor solution chemistry: From fundamentals to photovoltaic applications. *Chemical Society Reviews* **48,** 2011–2038. ISSN: 14604744 (Apr. 2019).

144. Williams, S. T. *et al.* Role of chloride in the morphological evolution of organolead halide perovskite thin films. *ACS Nano* **8,** 10640–10654. ISSN: 1936086X (Oct. 2014).

145. Buin, A. *et al.* Materials processing routes to trap-free halide perovskites. *Nano Letters* **14,** 6281–6286. ISSN: 15306992 (Nov. 2014).

146. McMeekin, D. P. *et al.* Crystallization Kinetics and Morphology Control of Formamidinium–Cesium Mixed-Cation Lead Mixed-Halide Perovskite via Tunability of the Colloidal Precursor Solution. *Advanced Materials* **29,** 1607039. ISSN: 1521-4095 (Aug. 2017).

147. Li, J. *et al.* Perovskite Single Crystals: Synthesis, Optoelectronic Properties, and Application. *Advanced Functional Materials* **31,** 2008684. ISSN: 1616-3028 (Mar. 2021).

148. Shi, D. *et al.* Low trap-state density and long carrier diffusion in organolead trihalide perovskite single crystals. *Science* **347,** 519–522. ISSN: 10959203 (Jan. 2015).

149. Turedi, B. *et al.* Perovskite Single-Crystal Solar Cells: Going Forward. *ACS Energy Letters* **6,** 631–642. ISSN: 23808195 (Feb. 2021).

150. Kubicki, D. J., Stranks, S. D., Grey, C. P. & Emsley, L. NMR spectroscopy probes microstructure, dynamics and doping of metal halide perovskites. *Nature Reviews Chemistry* **5,** 624–645. ISSN: 23973358 (Aug. 2021).

151. Prochowicz, D. *et al.* Mechanosynthesis of the hybrid perovskite CH3NH3PbI3: characterization and the corresponding solar cell efficiency. *Journal of Materials Chemistry A* **3,** 20772–20777. ISSN: 2050-7496 (Oct. 2015).

152. Brivio, F., Butler, K. T., Walsh, A. & Van Schilfgaarde, M. Relativistic quasiparticle self-consistent electronic structure of hybrid halide perovskite photovoltaic absorbers. *Physical Review B* **89,** 155204. ISSN: 1550235X. arXiv: `1401.6993` (2014).

153. Even, J., Pedesseau, L., Jancu, J. M. & Katan, C. Importance of spin-orbit coupling in hybrid organic/inorganic perovskites for photovoltaic applications. *Journal of Physical Chemistry Letters* **4,** 2999–3005. ISSN: 19487185 (Sept. 2013).

154. Du, M. H. Density functional calculations of native defects in CH3NH3PbI3: Effects of spin - Orbit coupling and self-interaction error. *Journal of Physical Chemistry Letters* **6,** 1461–1466. ISSN: 19487185 (2015).

155. Meggiolaro, D. & De Angelis, F. First-Principles Modeling of Defects in Lead Halide Perovskites: Best Practices and Open Issues. *ACS Energy Letters* **3,** 2206–2222. ISSN: 23808195 (2018).

156. Abdi-Jalebi, M. *et al.* Maximizing and stabilizing luminescence from halide perovskites with potassium passivation. *Nature* **555,** 497–501. ISSN: 14764687 (Mar. 2018).

157. Noel, N. K. *et al.* Enhanced Photoluminescence and Solar Cell Performance via Lewis Base Passivation of Organic–Inorganic Lead Halide Perovskites. *ACS Nano* **8,** 9815–9821. ISSN: 1936-0851 (Oct. 2014).

158. Dequilettes, D. W. *et al.* Photoluminescence Lifetimes Exceeding 8 μs and Quantum Yields Exceeding 30% in Hybrid Perovskite Thin Films by Ligand Passivation. *ACS Energy Letters* **1,** 438–444. ISSN: 23808195 (Aug. 2016).

159. Zohar, A. *et al.* What is the Mechanism of MAPbI3 p-Doping by I2? Insights from Optoelectronic Properties. *ACS Energy Letters* **2,** 2408–2414. ISSN: 23808195 (Oct. 2017).

160. Senocrate, A. *et al.* The Nature of Ion Conduction in Methylammonium Lead Iodide: A Multimethod Approach. *Angewandte Chemie International Edition* **56,** 7755–7759. ISSN: 1521-3773 (June 2017).

161. Leijtens, T. *et al.* Carrier trapping and recombination: The role of defect physics in enhancing the open circuit voltage of metal halide perovskite solar cells. *Energy and Environmental Science* **9,** 3472–3481. ISSN: 17545706 (Nov. 2016).

162. Hutter, E. M., Eperon, G. E., Stranks, S. D. & Savenije, T. J. Charge Carriers in Planar and Meso-Structured Organic-Inorganic Perovskites: Mobilities, Lifetimes, and Concentrations of Trap States. *Journal of Physical Chemistry Letters* **6,** 3082–3090. ISSN: 19487185 (Aug. 2015).

163. Reid, O. G., Yang, M., Kopidakis, N., Zhu, K. & Rumbles, G. Grain-Size-Limited Mobility in Methylammonium Lead Iodide Perovskite Thin Films. *ACS Energy Letters* **1,** 561–565. ISSN: 23808195 (2016).

164. Sadoughi, G. *et al.* Observation and Mediation of the Presence of Metallic Lead in Organic-Inorganic Perovskite Films. *ACS Applied Materials and Interfaces* **7,** 13440–13444. ISSN: 19448252 (June 2015).

165. Minns, J. L., Zajdel, P., Chernyshov, D., Van Beek, W. & Green, M. A. Structure and interstitial iodide migration in hybrid perovskite methylammonium lead iodide. *Nature Communications* **8,** 1–5. ISSN: 20411723 (May 2017).

166. Kiermasch, D., Rieder, P., Tvingstedt, K., Baumann, A. & Dyakonov, V. Improved charge carrier lifetime in planar perovskite solar cells by bromine doping. *Scientific Reports* **6,** 1–7. ISSN: 20452322 (Dec. 2016).

167. Tian, Y. *et al.* Mechanistic insights into perovskite photoluminescence enhancement: Light curing with oxygen can boost yield thousandfold. *Physical Chemistry Chemical Physics* **17,** 24978–24987. ISSN: 14639076 (Sept. 2015).

168. Galisteo-López, J. F., Anaya, M., Calvo, M. E. & Míguez, H. Environmental effects on the photophysics of organic-inorganic halide perovskites. *Journal of Physical Chemistry Letters* **6,** 2200–2205. ISSN: 19487185 (June 2015).

169. Brenes, R. *et al.* Metal Halide Perovskite Polycrystalline Films Exhibiting Properties of Single Crystals. *Joule* **1,** 155–167. ISSN: 25424351 (2017).

170. Brenes, R., Eames, C., Bulović, V., Islam, M. S. & Stranks, S. D. The Impact of Atmosphere on the Local Luminescence Properties of Metal Halide Perovskite Grains. *Advanced Materials* **30,** 1706208. ISSN: 15214095 (Apr. 2018).

171. Meggiolaro, D., Mosconi, E. & De Angelis, F. Mechanism of Reversible Trap Passivation by Molecular Oxygen in Lead-Halide Perovskites. *ACS Energy Letters* **2,** 2794–2798. ISSN: 23808195 (Dec. 2017).

172. Aristidou, N. *et al.* The Role of Oxygen in the Degradation of Methylammonium Lead Trihalide Perovskite Photoactive Layers. *Angewandte Chemie - International Edition* **54,** 8208–8212. ISSN: 15213773 (July 2015).

173. Aristidou, N. *et al.* Fast oxygen diffusion and iodide defects mediate oxygen-induced degradation of perovskite solar cells. *Nature Communications* **8,** 1–10. ISSN: 20411723 (May 2017).

174. Leguy, A. M. *et al.* Reversible hydration of CH3NH3PbI3 in films, single crystals, and solar cells. *Chemistry of Materials* **27,** 3397–3407. ISSN: 15205002 (May 2015).

175. Yang, J., Siempelkamp, B. D., Liu, D. & Kelly, T. L. Investigation of CH3NH3PbI3 degradation rates and mechanisms in controlled humidity environments using in situ techniques. *ACS Nano* **9,** 1955–1963. ISSN: 1936086X (Feb. 2015).

176. Quitsch, W. A. *et al.* The Role of Excitation Energy in Photobrightening and Photodegradation of Halide Perovskite Thin Films. *Journal of Physical Chemistry Letters* **9,** 2062–2069. ISSN: 19487185 (Apr. 2018).

177. Wang, S., Jiang, Y., Juarez-Perez, E. J., Ono, L. K. & Qi, Y. Accelerated degradation of methylammonium lead iodide perovskites induced by exposure to iodine vapour. *Nature Energy* **2.** ISSN: 20587546 (2017).

178. Motti, S. G. *et al.* Controlling competing photochemical reactions stabilizes perovskite solar cells. *Nature Photonics* **13,** 532–539. ISSN: 17494893 (May 2019).

179. Barker, A. J. *et al.* Defect-Assisted Photoinduced Halide Segregation in Mixed-Halide Perovskite Thin Films. *ACS Energy Letters* **2,** 1416–1424. ISSN: 23808195 (June 2017).

180. Hoke, E. T. *et al.* Reversible photo-induced trap formation in mixed-halide hybrid perovskites for photovoltaics. *Chemical Science* **6,** 613–617. ISSN: 20416539 (Dec. 2015).

181. Rehman, W. *et al.* Charge-Carrier Dynamics and Mobilities in Formamidinium Lead Mixed-Halide Perovskites. *Advanced Materials* **27,** 7938–7944. ISSN: 15214095 (Dec. 2015).

182. DeQuilettes, D. W. *et al.* Photo-induced halide redistribution in organic-inorganic perovskite films. *Nature Communications* **7,** 11683. ISSN: 20411723 (May 2016).

183. Azpiroz, J. M., Mosconi, E., Bisquert, J. & De Angelis, F. Defect migration in methylammonium lead iodide and its role in perovskite solar cell operation. *Energy & Environmental Science* **8,** 2118–2127. ISSN: 1754-5706 (July 2015).

184. Yang, J. H., Yin, W. J., Park, J. S. & Wei, S. H. Fast self-diffusion of ions in CH3NH3PbI3: the interstiticaly mechanism versus vacancy-assisted mechanism. *Journal of Materials Chemistry A* **4,** 13105–13112. ISSN: 2050-7496 (Aug. 2016).

185. Walsh, A. & Stranks, S. D. Taking Control of Ion Transport in Halide Perovskite Solar Cells. *ACS Energy Letters* **3,** 1983–1990. ISSN: 23808195 (Aug. 2018).

186. Mosconi, E. & De Angelis, F. Mobile Ions in Organohalide Perovskites: Interplay of Electronic Structure and Dynamics. *ACS Energy Letters* **1,** 182–188. ISSN: 23808195 (July 2016).

187. Rehman, W. *et al.* Photovoltaic mixed-cation lead mixed-halide perovskites: Links between crystallinity, photo-stability and electronic properties. *Energy and Environmental Science* **10,** 361–369. ISSN: 17545706 (2017).

188. Sutter-Fella, C. M. *et al.* Cation-Dependent Light-Induced Halide Demixing in Hybrid Organic-Inorganic Perovskites. *Nano Letters* **18,** 3473–3480. ISSN: 15306992 (June 2018).

189. Knight, A. J. & Herz, L. M. Preventing phase segregation in mixed-halide perovskites: A perspective. *Energy and Environmental Science* **13,** 2024–2046. ISSN: 17545706 (July 2020).

190. Draguta, S. *et al.* Rationalizing the light-induced phase separation of mixed halide organic-inorganic perovskites. *Nature Communications* **8,** 1–8. ISSN: 20411723 (Dec. 2017).

191. Bischak, C. G. *et al.* Origin of Reversible Photoinduced Phase Separation in Hybrid Perovskites. *Nano Letters* **17,** 1028–1033. ISSN: 15306992. arXiv: `1606.07366` (Feb. 2017).

192. Slotcavage, D. J., Karunadasa, H. I. & McGehee, M. D. Light-Induced Phase Segregation in Halide-Perovskite Absorbers. *ACS Energy Letters* **1,** 1199–1205. ISSN: 23808195 (Dec. 2016).

193. Brennan, M. C., Draguta, S., Kamat, P. V. & Kuno, M. Light-Induced Anion Phase Segregation in Mixed Halide Perovskites. *ACS Energy Letters* **3,** 204–213. ISSN: 23808195 (Jan. 2018).

194. Brivio, F., Caetano, C. & Walsh, A. Thermodynamic Origin of Photoinstability in the CH3NH3Pb(I1-xBrx)3 Hybrid Halide Perovskite Alloy. *Journal of Physical Chemistry Letters* **7,** 1083–1087. ISSN: 19487185 (Mar. 2016).

195. Yoon, S. J., Kuno, M. & Kamat, P. V. Shift Happens. How Halide Ion Defects Influence Photoinduced Segregation in Mixed Halide Perovskites. *ACS Energy Letters* **2,** 1507–1514. ISSN: 23808195 (July 2017).

196. Braly, I. L. *et al.* Current-Induced Phase Segregation in Mixed Halide Hybrid Perovskites and its Impact on Two-Terminal Tandem Solar Cell Design. *ACS Energy Letters* **2,** 1841–1847. ISSN: 23808195 (Aug. 2017).

197. Duong, T. *et al.* Light and Electrically Induced Phase Segregation and Its Impact on the Stability of Quadruple Cation High Bandgap Perovskite Solar Cells. *ACS Applied Materials and Interfaces* **9,** 26859–26866. ISSN: 19448252 (Aug. 2017).

198. Knight, A. J. *et al.* Electronic Traps and Phase Segregation in Lead Mixed-Halide Perovskite. *ACS Energy Letters* **4,** 75–84. ISSN: 23808195 (Jan. 2019).

199. Belisle, R. A. *et al.* Impact of surfaces on photoinduced halide segregation in mixed-halide perovskites. *ACS Energy Letters* **3,** 2694–2700. ISSN: 23808195 (2018).

200. Christians, J. A., Miranda Herrera, P. A. & Kamat, P. V. Transformation of the excited state and photovoltaic efficiency of CH3NH3PbI3 perovskite upon controlled exposure to humidified air. *Journal of the American Chemical Society* **137,** 1530–1538. ISSN: 15205126 (Feb. 2015).

201. Ahn, N. *et al.* Trapped charge-driven degradation of perovskite solar cells. *Nature Communications* **7,** 1–9. ISSN: 20411723 (Nov. 2016).

202. Domanski, K. *et al.* Not All That Glitters Is Gold: Metal-Migration-Induced Degradation in Perovskite Solar Cells. *ACS Nano* **10,** 6306–6314. ISSN: 1936086X (June 2016).

203. Yang, M. *et al.* Do grain boundaries dominate non-radiative recombination in CH3NH3PbI3 perovskite thin films? *Physical Chemistry Chemical Physics* **19,** 5043–5050. ISSN: 14639076 (2017).

204. DeQuilettes, D. W. *et al.* Impact of microstructure on local carrier lifetime in perovskite solar cells. *Science* **348,** 683–686. ISSN: 10959203 (Apr. 2015).

205. Li, J. J. *et al.* Microscopic Investigation of Grain Boundaries in Organolead Halide Perovskite Solar Cells. *ACS Applied Materials and Interfaces* **7,** 28518–28523. ISSN: 19448252 (Dec. 2015).

206. Yun, J. S. *et al.* Benefit of grain boundaries in organic-inorganic halide planar perovskite solar cells. *Journal of Physical Chemistry Letters* **6,** 875–880. ISSN: 19487185 (Mar. 2015).

207. Sherkar, T. S. *et al.* Recombination in Perovskite Solar Cells: Significance of Grain Boundaries, Interface Traps, and Defect Ions. *ACS Energy Letters* **2,** 1214–1222. ISSN: 23808195 (May 2017).

208. Stranks, S. D. *et al.* Recombination Kinetics in Organic-Inorganic Perovskites: Excitons, Free Charge, and Subgap States. *Physical Review Applied* **2,** 34007. ISSN: 23317019 (Sept. 2014).

209. Visoly-Fisher, I., Cohen, S. R., Ruzin, A. & Cahen, D. How Polycrystalline Devices Can Outperform Single-Crystal Ones: Thin Film CdTe/CdS Solar Cells. *Advanced Materials* **16,** 879–883. ISSN: 1521-4095 (June 2004).

210. Jiang, C. S. *et al.* Does the local built-in potential on grain boundaries of Cu(In,Ga)Se2 thin films benefit photovoltaic performance of the device? *Applied Physics Letters* **85,** 2625. ISSN: 0003-6951 (Sept. 2004).

211. Wang, Q. *et al.* Qualifying composition dependent p and n self-doping in CH3NH3PbI3. *Applied Physics Letters* **105,** 163508. ISSN: 0003-6951 (Oct. 2014).

212. Olthof, S. & Meerholz, K. Substrate-dependent electronic structure and film formation of MAPbI3 perovskites. *Scientific Reports* **7,** 1–10. ISSN: 20452322 (Jan. 2017).

213. Shin, D. *et al.* Mechanism and Timescales of Reversible p-Doping of Methylammonium Lead Triiodide by Oxygen. *Advanced Materials* **33,** 2100211. ISSN: 1521-4095 (June 2021).

214. Zu, F. *et al.* Unraveling the Electronic Properties of Lead Halide Perovskites with Surface Photovoltage in Photoemission Studies. *ACS Applied Materials and Interfaces* **11,** 21578–21583. ISSN: 19448252 (June 2019).

215. Walsh, A., Scanlon, D. O., Chen, S., Gong, X. G. & Wei, S. H. Self-regulation mechanism for charged point defects in hybrid halide perovskites. *Angewandte Chemie - International Edition* **54,** 1791–1794. ISSN: 15213773. arXiv: `1411.7606` (2015).

216. Steirer, K. X. *et al.* Defect Tolerance in Methylammonium Lead Triiodide Perovskite. *ACS Energy Letters* **1,** 360–366. ISSN: 23808195 (Aug. 2016).

217. Beard, M. C., Turner, G. M. & Schmuttenmaer, C. A. Terahertz spectroscopy. *Journal of Physical Chemistry B* **106,** 7146–7159. ISSN: 10895647 (July 2002).

218. Schmuttenmaer, C. A. Exploring dynamics in the far-infrared with terahertz spectroscopy. *Chemical Reviews* **104,** 1759–1779. ISSN: 00092665 (Apr. 2004).

219. Ulbricht, R., Hendry, E., Shan, J., Heinz, T. F. & Bonn, M. Carrier dynamics in semiconductors studied with time-resolved terahertz spectroscopy. *Reviews of Modern Physics* **83,** 543–586. ISSN: 15390756 (June 2011).

220. Jepsen, P. U., Cooke, D. G. & Koch, M. Terahertz spectroscopy and imaging - Modern techniques and applications. *Laser and Photonics Reviews* **5,** 124–166. ISSN: 18638880 (Jan. 2011).

221. Beard, M. C. & Schmuttenmaer, C. A. Using the finite-difference time-domain pulse propagation method to simulate time-resolved THz experiments. *Journal of Chemical Physics* **114,** 2903–2909. ISSN: 00219606 (Feb. 2001).

222. Beard, M. C., Turner, G. M. & Schmuttenmaer, C. A. Subpicosecond carrier dynamics in low-temperature grown GaAs as measured by time-resolved terahertz spectroscopy. *Journal of Applied Physics* **90,** 5915–5923. ISSN: 00218979 (Nov. 2001).

223. Němec, H., Kadlec, F. & Kužel, P. Methodology of an optical pump-terahertz probe experiment: An analytical frequency-domain approach. *Journal of Chemical Physics* **117,** 8454–8465. ISSN: 00219606 (Oct. 2002).

224. Nienhuys, H. K. & Sundström, V. Intrinsic complications in the analysis of optical-pump, terahertz probe experiments. *Physical Review B - Condensed Matter and Materials Physics* **71,** 235110. ISSN: 10980121 (June 2005).

225. Kužel, P., Kadlec, F. & Němec, H. Propagation of terahertz pulses in photoexcited media: Analytical theory for layered systems. *Journal of Chemical Physics* **127,** 024506. ISSN: 00219606 (July 2007).

226. Withayachumnankul, W. & Naftaly, M. Fundamentals of measurement in terahertz time-domain spectroscopy. *Journal of Infrared, Millimeter, and Terahertz Waves* **35,** 610–637. ISSN: 18666906 (Dec. 2014).

227. Lloyd-Hughes, J. & Jeon, T. I. A review of the terahertz conductivity of bulk and nano-materials. *Journal of Infrared, Millimeter, and Terahertz Waves* **33,** 871–925. ISSN: 18666892 (Sept. 2012).
228. Joyce, H. J., Boland, J. L., Davies, C. L., Baig, S. A. & Johnston, M. B. A review of the electrical properties of semiconductor nanowires: Insights gained from terahertz conductivity spectroscopy. *Semiconductor Science and Technology* **31,** 103003. ISSN: 13616641 (Sept. 2016).
229. Neu, J., Regan, K. P., Swierk, J. R. & Schmuttenmaer, C. A. Applicability of the thin-film approximation in terahertz photoconductivity measurements. *Applied Physics Letters* **113,** 233901. ISSN: 00036951 (Dec. 2018).
230. Glover, R. E. & Tinkham, M. Conductivity of superconducting films for photon energies between 0.3 and 40kTc. *Physical Review* **108,** 243–256. ISSN: 0031899X (Oct. 1957).
231. Hempel, H. *et al.* Predicting Solar Cell Performance from Terahertz and Microwave Spectroscopy. *Advanced Energy Materials* **12,** 2102776. ISSN: 16146840 (Feb. 2022).
232. Seifert, T. *et al.* Efficient metallic spintronic emitters of ultrabroadband terahertz radiation. *Nature Photonics* **10,** 483–488. ISSN: 17494893. arXiv: `1510.03729` (July 2016).
233. Seifert, T. *et al.* Ultrabroadband single-cycle terahertz pulses with peak fields of 300 kV cm-1 from a metallic spintronic emitter. *Applied Physics Letters* **110,** 252402. ISSN: 00036951. arXiv: `1703.09970` (2017).
234. Kampfrath, T. *et al.* Terahertz spin current pulses controlled by magnetic heterostructures. *Nature Nanotechnology* **8,** 256–260. ISSN: 17483395 (2013).
235. Klingshirn, C. F. & Kalt, H. *Semiconductor Optics 1: Linear Optical Properties of Semiconductors* 5th. ISBN: 9783030241520 (Springer Nature, 2019).
236. Yu, P. Y. & Cardona, M. *Fundamentals of Semiconductors: Physics and Materials Properties* 4th. ISBN: 9783642007101 (Springer-Verlag Berlin Heidelbeg, 2010).
237. Fox, M. *Optical Properties of Solids* 2nd. ISBN: 9780191576720 (Oxford University Press, 2010).
238. Mandl, F. *Quantum Mechanics* ISBN: 9781118728895 (John Wiley & Sons, Inc., Chichester, 1992).
239. Elliott, R. J. Intensity of Optical Absorption by Excitons. *Physical Review* **108,** 1384. ISSN: 0031899X (Dec. 1957).
240. Price, M. B. *et al.* Hot-carrier cooling and photoinduced refractive index changes in organic-inorganic lead halide perovskites. *Nature Communications* **6,** 1–8. ISSN: 20411723 (Sept. 2015).
241. Koch, S. W., Kira, M., Khitrova, G. & Gibbs, H. M. Semiconductor excitons in new light. *Nature Materials* **5,** 523–531. ISSN: 14764660 (2006).
242. D'Innocenzo, V. *et al.* Excitons versus free charges in organo-lead tri-halide perovskites. *Nature Communications* **5.** ISSN: 20411723. arXiv: `arXiv:0710.1245v2` (2014).
243. Valverde-Chávez, D. A. *et al.* Intrinsic femtosecond charge generation dynamics in single crystal CH3NH3PbI3. *Energy and Environmental Science* **8,** 3700–3707. ISSN: 17545706 (Dec. 2015).

244. Piatkowski, P. *et al.* Unraveling Charge Carriers Generation, Diffusion, and Recombination in Formamidinium Lead Triiodide Perovskite Polycrystalline Thin Film. *Journal of Physical Chemistry Letters* **7,** 204–210. ISSN: 19487185 (Jan. 2016).
245. Awasthi, K. *et al.* Electroabsorption Studies of Multicolored Lead Halide Perovskite Nanocrystalline Solid Films. *ACS Photonics* **5,** 2408–2417. ISSN: 23304022 (June 2018).
246. Ziffer, M. E., Mohammed, J. C. & Ginger, D. S. Electroabsorption Spectroscopy Measurements of the Exciton Binding Energy, Electron-Hole Reduced Effective Mass, and Band Gap in the Perovskite CH3NH3PbI3. *ACS Photonics* **3,** 1060–1068. ISSN: 23304022 (June 2016).
247. Miyata, A. *et al.* Direct measurement of the exciton binding energy and effective masses for charge carriers in organic-inorganic tri-halide perovskites. *Nature Physics* **11,** 582–587. ISSN: 17452481. arXiv: `1504.07025` (2015).
248. Jha, A. *et al.* Direct Observation of Ultrafast Exciton Dissociation in Lead Iodide Perovskite by 2D Electronic Spectroscopy. *ACS Photonics* **5,** 852–860. ISSN: 23304022 (Mar. 2018).
249. Saba, M. *et al.* Correlated electron-hole plasma in organometal perovskites. *Nature Communications* **5,** 1–10. ISSN: 20411723 (Sept. 2014).
250. Chen, K., Barker, A. J., Morgan, F. L., Halpert, J. E. & Hodgkiss, J. M. Effect of carrier thermalization dynamics on light emission and amplification in organometal halide perovskites. *Journal of Physical Chemistry Letters* **6,** 153–158. ISSN: 19487185 (Jan. 2015).
251. Monti, M. *et al.* Hot carriers in mixed Pb-Sn halide perovskite semiconductors cool slowly while retaining their electrical mobility. *Physical Review B* **102,** 245204. ISSN: 24699969 (Dec. 2020).
252. Whal, M. *Technical Note: Time-Correlated Single Photon Counting* (PcioQuant GmbH, 2014).
253. Soderlind, G. *Numerical Methods for Differential Equations: An Introduction to Scientific Computing* (Springer, 2017).
254. Selberherr, S. *Analysis and Simulation of Semiconductor Devices* ISBN: 9783709187548 (Springer Vienna, 1984).
255. Karakus, M. *et al.* Phonon-Electron Scattering Limits Free Charge Mobility in Methylammonium Lead Iodide Perovskites. *Journal of Physical Chemistry Letters* **6,** 4991–4996. ISSN: 19487185 (2015).
256. Farrell, P. *et al.* in *Handbook of Optoelectronic Device Modeling and Simulation* (CRC Press, Oct. 2017). ISBN: 9781315152318.
257. Farrell, P. *et al.* Numerical methods for drift-diffusion models. *Weierstrass Institute for Applied Analysis and Stochastics: Preprint 2263* (May 2016).
258. Kiligaridis, A. *et al.* Are Shockley-Read-Hall and ABC models valid for lead halide perovskites? *Nature Communications* **12,** 1–13. ISSN: 2041-1723. arXiv: `2009.04163` (June 2021).
259. Kunst, M. & Sanders, A. Transport of excess carriers in silicon wafers. *Semiconductor Science and Technology* **7,** 51–59. ISSN: 02681242 (Jan. 1992).
260. Blakemore, J. S. *Semiconductor Statistics* (Pergamon Press, Oxford, 1962).

261. Shockley, W. & Read, W. T. Statistics of the recombinations of holes and electrons. *Physical Review* **87,** 835–842. ISSN: 0031899X (Sept. 1952).
262. Hahn, D. W. & Özişik, M. N. *Heat Conduction: Third Edition* ISBN: 9780470902936 (John Wiley and Sons, Aug. 2012).
263. Sallenave, X. *et al.* Interfacial and bulk properties of hole transporting materials in perovskite solar cells: spiro-MeTAD versus spiro-OMeTAD. *Journal of Materials Chemistry A* **8,** 8527–8539. ISSN: 2050-7496 (May 2020).
264. Leijtens, T. *et al.* Hole transport materials with low glass transition temperatures and high solubility for application in solid-state dye-sensitized solar cells. *ACS Nano* **6,** 1455–1462. ISSN: 19360851 (Feb. 2012).
265. Poplavskyy, D. & Nelson, J. Nondispersive hole transport in amorphous films of methoxy-spirofluorene-arylamine organic compound. *Journal of Applied Physics* **93,** 341. ISSN: 0021-8979 (Dec. 2002).
266. Röhr, J. A., Shi, X., Haque, S. A., Kirchartz, T. & Nelson, J. Charge Transport in Spiro-OMeTAD Investigated through Space-Charge-Limited Current Measurements. *Physical Review Applied* **9.** ISSN: 23317019 (2018).
267. Shi, D. *et al.* Spiro-OMeTAD single crystals: Remarkably enhanced charge-carrier transport via mesoscale ordering. *Science Advances* **2.** ISSN: 23752548 (Apr. 2016).
268. Singh, T. B. *et al.* Correlation of crystalline and structural properties of C60 thin films grown at various temperature with charge carrier mobility. *Applied Physics Letters* **90,** 213512. ISSN: 0003-6951 (May 2007).
269. Cabanillas-Gonzalez, J. *et al.* Photoinduced transient stark spectroscopy in organic semiconductors: A method for charge mobility determination in the picosecond regime. *Physical Review Letters* **96.** ISSN: 00319007 (2006).
270. Priebe, G., Pietzak, B. & Könenkamp, R. Determination of transport parameters in fullerene films. *Applied Physics Letters* **71,** 2160–2162. ISSN: 00036951 (1997).
271. Herz, L. M. Charge-Carrier Mobilities in Metal Halide Perovskites: Fundamental Mechanisms and Limits. *ACS Energy Letters* **2,** 1539–1548. ISSN: 23808195 (July 2017).
272. Ponseca, C. S. *et al.* Mechanism of Charge Transfer and Recombination Dynamics in Organo Metal Halide Perovskites and Organic Electrodes, PCBM, and Spiro-OMeTAD: Role of Dark Carriers. *Journal of the American Chemical Society* **137,** 16043–16048. ISSN: 15205126 (Dec. 2015).
273. Ponseca, C. S. *et al.* Organometal halide perovskite solar cell materials rationalized: Ultrafast charge generation, high and microsecond-long balanced mobilities, and slow recombination. *Journal of the American Chemical Society* **136,** 5189–5192. ISSN: 15205126 (2014).
274. Hutter, E. M. *et al.* Charge Transfer from Methylammonium Lead Iodide Perovskite to Organic Transport Materials: Efficiencies, Transfer Rates, and Interfacial Recombination. *Advanced Energy Materials* **7,** 1602349. ISSN: 16146840 (July 2017).
275. Pydzińska-Białek, K., Szeremeta, J., Wojciechowski, K. & Ziółek, M. Insights into the Femtosecond to Nanosecond Charge Carrier Kinetics in Perovskite Materials for Solar Cells. *Journal of Physical Chemistry C* **123,** 110–119. ISSN: 19327455 (Oct. 2019).

276. Manser, J. S. & Kamat, P. V. Band filling with free charge carriers in organometal halide perovskites. *Nature Photonics* **8,** 737–743. ISSN: 17494893 (2014).

277. Muñoz, M. *et al.* Burstein-Moss shift of n-doped In0.53Ga0.47As/InP. *Physical Review B* **63,** 233302. ISSN: 1550235X (2001).

278. Deschler, F. *et al.* High photoluminescence efficiency and optically pumped lasing in solution-processed mixed halide perovskite semiconductors. *Journal of Physical Chemistry Letters* **5,** 1421–1426. ISSN: 19487185 (Apr. 2014).

279. Pydzińska, K. *et al.* Determination of Interfacial Charge-Transfer Rate Constants in Perovskite Solar Cells. *ChemSusChem* **9,** 1647–1659. ISSN: 1864564X (July 2016).

280. Liu, J., Leng, J., Wang, S., Zhang, J. & Jin, S. Artifacts in Transient Absorption Measurements of Perovskite Films Induced by Transient Reflection from Morphological Microstructures. *Journal of Physical Chemistry Letters* **10,** 97–101. ISSN: 19487185 (Jan. 2019).

281. Tamming, R. R. *et al.* Ultrafast Spectrally Resolved Photoinduced Complex Refractive Index Changes in CsPbBr 3 Perovskites. *ACS Photonics* **6,** 345–350. ISSN: 23304022 (Feb. 2019).

282. Ghosh, T., Aharon, S., Shpatz, A., Etgar, L. & Ruhman, S. Reflectivity Effects on Pump-Probe Spectra of Lead Halide Perovskites: Comparing Thin Films versus Nanocrystals. *ACS Nano* **12,** 5719–5725. ISSN: 1936086X (June 2018).

283. Braver, Y., Gelzinis, A., Chmeliov, J. & Valkunas, L. Application of decay- and evolution-associated spectra for molecular systems with spectral shifts or inherent inhomogeneities. *Chemical Physics* **525,** 110403. ISSN: 0301-0104 (Sept. 2019).

284. Brauer, J. C., Lee, Y. H., Nazeeruddin, M. K. & Banerji, N. Charge Transfer Dynamics from Organometal Halide Perovskite to Polymeric Hole Transport Materials in Hybrid Solar Cells. *Journal of Physical Chemistry Letters* **6,** 3675–3681. ISSN: 19487185 (Sept. 2015).

285. Brauer, J. C., Lee, Y. H., Nazeeruddin, M. K. & Banerji, N. Ultrafast charge carrier dynamics in CH3NH3PbI3: Evidence for hot hole injection into spiro-OMeTAD. *Journal of Materials Chemistry C* **4,** 5922–5931. ISSN: 20507526 (June 2016).

286. Horn, J., Minda, I., Schwoerer, H. & Schlettwein, D. Direct Observation of Charge Injection From CH3NH3PbI3xClx to Organic Semiconductors Monitored With sub-ps Transient Absorption Spectroscopy. *Physica Status Solidi (B) Basic Research* **256,** 1800265. ISSN: 15213951 (Mar. 2019).

287. Zhou, M., Sarmiento, J. S., Fei, C. & Wang, H. Charge Transfer and Diffusion at the Perovskite/PCBM Interface Probed by Transient Absorption and Reflection. *Journal of Physical Chemistry C* **123,** 22095–22103. ISSN: 19327455 (2019).

288. Xing, G. *et al.* Long-range balanced electron-and hole-transport lengths in organic-inorganic CH3NH3PbI3. *Science* **342,** 344–347. ISSN: 10959203 (2013).

289. Leng, J., Liu, J., Zhang, J. & Jin, S. Decoupling Interfacial Charge Transfer from Bulk Diffusion Unravels Its Intrinsic Role for Efficient Charge Extraction in Perovskite Solar Cells. *Journal of Physical Chemistry Letters* **7,** 5056–5061. ISSN: 19487185 (Dec. 2016).

290. Pasanen, H. P., Vivo, P., Canil, L., Abate, A. & Tkachenko, N. Refractive index change dominates the transient absorption response of metal halide perovskite thin

films in the near infrared. *Physical Chemistry Chemical Physics* **21,** 14663–14670. ISSN: 14639076 (July 2019).

291. Grancini, G. *et al.* Femtosecond Charge-Injection Dynamics at Hybrid Perovskite Interfaces. *ChemPhysChem* **18,** 2381–2389. ISSN: 14397641 (Sept. 2017).
292. Jiménez-López, J., Puscher, B. M., Guldi, D. M. & Palomares, E. Improved Carrier Collection and Hot Electron Extraction across Perovskite, C60, and TiO2 Interfaces. *Journal of the American Chemical Society* **142,** 1236–1246. ISSN: 15205126 (Jan. 2020).
293. Dursun, I. *et al.* Why are Hot Holes Easier to Extract than Hot Electrons from Methylammonium Lead Iodide Perovskite? *Advanced Energy Materials* **9,** 1900084. ISSN: 1614-6840 (June 2019).
294. Zhai, Y. *et al.* Ultrafast Spectroscopy of Photoexcitations in Organometal Trihalide Perovskites. *Advanced Functional Materials* **26,** 1617–1627. ISSN: 1616-3028 (Mar. 2016).
295. Makuta, S. *et al.* Photo-excitation intensity dependent electron and hole injections from lead iodide perovskite to nanocrystalline TiO2 and spiro-OMeTAD. *Chemical Communications* **52,** 673–676. ISSN: 1364548X (Dec. 2016).
296. Fantacci, S., De Angelis, F., Nazeeruddin, M. K. & Grätzel, M. Electronic and optical properties of the spiro-MeOTAD hole conductor in its neutral and oxidized forms: A DFT/TDDFT investigation. *Journal of Physical Chemistry C* **115,** 23126–23133. ISSN: 19327447 (Nov. 2011).
297. Marchioro, A. *et al.* Unravelling the mechanism of photoinduced charge transfer processes in lead iodide perovskite solar cells. *Nature Photonics* **8,** 250–255. ISSN: 17494885 (Mar. 2014).
298. Piatkowski, P. *et al.* Direct monitoring of ultrafast electron and hole dynamics in perovskite solar cells. *Physical Chemistry Chemical Physics* **17,** 14674–14684. ISSN: 14639076 (June 2015).
299. Brauer, J. C. *et al.* Comparing the excited-state properties of a mixed-cation-mixed-halide perovskite to methylammonium lead iodide. *Journal of Chemical Physics* **152,** 104703. ISSN: 00219606 (Mar. 2020).
300. Giorgi, G., Fujisawa, J. I., Segawa, H. & Yamashita, K. Small photocarrier effective masses featuring ambipolar transport in methylammonium lead iodide perovskite: A density functional analysis. *Journal of Physical Chemistry Letters* **4,** 4213–4216. ISSN: 19487185 (Dec. 2013).
301. LeVeque, R. J. *Numerical Methods for Conservation Laws* ISBN: 9783034851169 (Birkhäuser Verlag, Basel, 1990).
302. Eymard, R., Gallouët, T. & Herbin, R. in *Handbook of Numerical Analysis* 713–1018 (Elsevier, Jan. 2000).
303. Evans, G. A., Blackledge, J. M. & Yardley, P. D. *Numerical Methods for Partial Differential Equations* ISBN: 9783540761259 (Springer London, London, 2000).
304. Vasileska, D., Goodnick, S. M. & Klimeck, G. *Computational electronics: Semi-classical and quantum device modeling and simulation* ISBN: 9781420064841 (CRC Press, 2017).

305. Press, W. H. *Numerical recipes in C: the art of scientific computing* 2nd. English. ISBN: 0521431085 (Cambridge University Press, Cambridge, 1992).

306. Hughes, I. & Hase, T. *Measurements and Their Uncertainties : A Practical Guide to Modern Error Analysis* ISBN: 9780191576560 (Oxford University Press, 2010).

307. Butler-Caddle, E. *et al.* Terahertz photoconductance dynamics of semiconductors from sub-nanosecond to millisecond timescales. *Applied Physics Letters* **122,** 012101. ISSN: 0003-6951 (Jan. 2023).

308. Stoica, V. A., Sheu, Y.-M., Reis, D. A. & Clarke, R. Wideband detection of transient solid-state dynamics using ultrafast fiber lasers and asynchronous optical sampling. *Optics Express* **16,** 2322. ISSN: 10944087 (Feb. 2008).

309. Neu, J. & Rahm, M. Terahertz time domain spectroscopy for carrier lifetime mapping in the picosecond to microsecond regime. *Optics Express* **23,** 12900. ISSN: 10944087 (May 2015).

310. Lin, R. *et al.* Monolithic all-perovskite tandem solar cells with 24.8% efficiency exploiting comproportionation to suppress Sn(ii) oxidation in precursor ink. *Nature Energy* **4,** 864–873. ISSN: 20587546 (Oct. 2019).

311. Glunz, S. W. & Warta, W. High-resolution lifetime mapping using modulated free-carrier absorption. *Journal of Applied Physics* **77,** 3243–3247. ISSN: 00218979 (Aug. 1995).

312. Bandara, R. M. *et al.* Tin(IV) dopant removal through anti-solvent engineering enabling tin based perovskite solar cells with high charge carrier mobilities. *Journal of Materials Chemistry C* **7,** 8389–8397. ISSN: 20507526 (July 2019).

313. Gaubas, E. & Vanhellemont, J. Dependence of carrier lifetime in germanium on resisitivity and carrier injection level. *Applied Physics Letters* **89,** 142106. ISSN: 00036951 (Oct. 2006).

314. Leitenstorfer, A., Hunsche, S., Shah, J., Nuss, M. C. & Knox, W. H. Detectors and sources for ultrabroadband electro-optic sampling: Experiment and theory. *Applied Physics Letters* **74,** 1516. ISSN: 0003-6951 (Mar. 1999).

315. Burdanova, M. G. *et al.* Giant Negative Terahertz Photoconductivity in Controllably Doped Carbon Nanotube Networks. *ACS Photonics* **6,** 1058–1066. ISSN: 23304022 (Apr. 2019).

316. Grant, N. E. *et al.* Superacid-Treated Silicon Surfaces: Extending the Limit of Carrier Lifetime for Photovoltaic Applications. *IEEE Journal of Photovoltaics* **7,** 1574–1583. ISSN: 21563381 (Nov. 2017).

317. Dingemans, G. & Kessels, W. M. M. Status and prospects of Al2O3 -based surface passivation schemes for silicon solar cells. *Journal of Vacuum Science & Technology A: Vacuum, Surfaces, and Films* **30,** 040802. ISSN: 0734-2101 (July 2012).

318. Black, L. E. *New Perspectives on Surface Passivation: Understanding the Si-Al2O3 Interface* ISBN: 978-3-319-32520-0 (Springer, Germany, 2016).

319. Grant, N. E. *et al.* Atomic level termination for passivation and functionalisation of silicon surfaces. *Nanoscale* **12,** 17332–17341. ISSN: 2040-3372 (Aug. 2020).

320. Pain, S. L. *et al.* Electronic Characteristics of Ultra-Thin Passivation Layers for Silicon Photovoltaics. *Advanced Materials Interfaces* **9,** 2201339. ISSN: 2196-7350 (Oct. 2022).

321. Green, M. A. Self-consistent optical parameters of intrinsic silicon at 300 K including temperature coefficients. *Solar Energy Materials and Solar Cells* **92,** 1305–1310. ISSN: 09270248 (Nov. 2008).

322. Klaassen, D. B. A unified mobility model for device simulation-I. Model equations and concentration dependence. *Solid State Electronics.* ISSN: 00381101 (1992).

323. Cuevas, A., Macdonald, D. & Sinton, R. A. in *Practical Handbook of Photovoltaics* (eds McEvoy, A., Markvart, T. & Castañer, L.) 2nd, 1011–1044 (Academic Press, Boston, 2012). ISBN: 978-0-12-385934-1.

324. Schroder, D. K. in *Semiconductor Material and Device Characterization* 389–464 (John Wiley & Sons, Ltd, Apr. 2005).

325. Niewelt, T. *et al.* Reassessment of the intrinsic bulk recombination in crystalline silicon. *Solar Energy Materials and Solar Cells* **235.** ISSN: 09270248 (Jan. 2022).